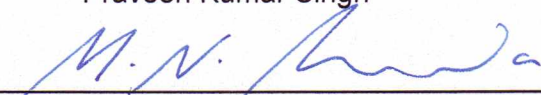


AN ENGINEERING STUDY TO INVESTIGATE THE METHANE HYDRATE  
RESOURCE POTENTIAL ASSOCIATED WITH THE BARROW GAS FIELDS IN  
ALASKA

By


Praveen Kumar Singh

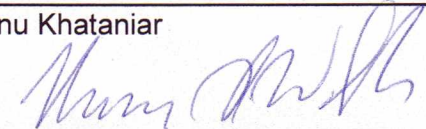
RECOMMENDED:

  
\_\_\_\_\_

  
\_\_\_\_\_

Mr. Peter J. Stokes

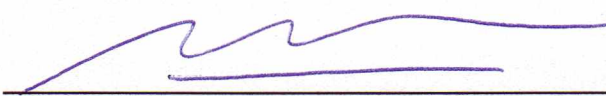
  
\_\_\_\_\_

  
\_\_\_\_\_

Mr. Thomas P. Walsh

  
\_\_\_\_\_

Dr. Shirish L. Patil, Advisory Committee Co-Chair

  
\_\_\_\_\_

Dr. Abhijit Y. Dandekar, Advisory Committee Co-Chair

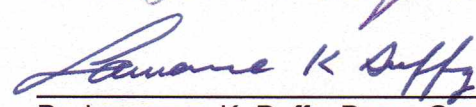
  
\_\_\_\_\_

Dr. Shirish L. Patil, Chair, Department of Petroleum Engineering

APPROVED:

  
\_\_\_\_\_

Dr. Douglas J. Goering, Dean, College of Engineering and Mines

  
\_\_\_\_\_

Dr. Lawrence K. Duffy, Dean, Graduate School

Nov 5, 2008

\_\_\_\_\_

Date

**AN ENGINEERING STUDY TO INVESTIGATE THE METHANE HYDRATE  
RESOURCE POTENTIAL ASSOCIATED WITH THE BARROW GAS FIELDS IN  
ALASKA**

A

THESIS

Presented to the Faculty  
of the University of Alaska Fairbanks

in Partial Fulfillment of the Requirements  
for the Degree of

MASTER OF SCIENCE

By

Praveen Kumar Singh, B. Tech.

Fairbanks, Alaska

December 2008



## ABSTRACT

Previous studies on the Barrow Gas Fields (BGF) in Alaska have suggested that accumulations of natural gas hydrates could exist within these reservoirs. In consideration of future energy challenges, and the potential of gas hydrates in meeting them, a comprehensive engineering study was undertaken to investigate the BGF for hydrates, and to recommend an optimal plan for future field development.

The methane hydrate resource potential of the BGF, viz. the East Barrow (EB), South Barrow (SB), and Walakpa (WAL) gas pools, was analyzed by developing gas hydrate stability models. Material balance studies were performed on the EB gas field to understand the reservoir drive mechanisms. Gas-water relative permeability experiments were conducted on a hydrate-saturated consolidated core sample, by maintaining the EB reservoir conditions, to model two-phase fluid flow behavior. Finally, field-scale dynamic reservoir simulation models were developed for the EB and WAL gas fields. Production history data were matched, reservoir drive mechanisms were confirmed, free gas and hydrate resources were quantified, hydrate dissociation patterns were examined, optimum locations for drilling infill wells were identified, and future production scenarios were simulated.

Findings from this work indicate that BGF are associated with hydrates that are constantly recharging the gas reservoir by dissociation.

## TABLE OF CONTENTS

	Page
<b>SIGNATURE PAGE</b> .....	i
<b>TITLE PAGE</b> .....	ii
<b>ABSTRACT</b> .....	iii
<b>TABLE OF CONTENTS</b> .....	iv
<b>LIST OF FIGURES</b> .....	ix
<b>LIST OF TABLES</b> .....	xvi
<b>LIST OF APPENDICES</b> .....	xviii
<b>DEDICATION</b> .....	xix
<b>ACKNOWLEDGMENTS</b> .....	xx
<b>DISCLAIMER</b> .....	xxi
<b>1. INTRODUCTION</b> .....	1
1.1 Background .....	1
1.2 Objectives.....	4
1.3 Tasks Performed .....	5
<b>2. LITERATURE REVIEW</b> .....	7
2.1 Gas Hydrates .....	7
<i>2.1.1 Historical Background</i> .....	7
<i>2.1.2 Structure</i> .....	9
<i>2.1.3 Properties</i> .....	11
2.2 Natural Gas Hydrates: An Untapped Resource.....	11
<i>2.2.1 Naturally Occurring Methane Hydrates</i> .....	11
<i>2.2.2 Geographic Occurrence</i> .....	13
<i>2.2.3 Methods of Quantifying Hydrate Resource</i> .....	14
<i>2.2.4 Gas Hydrate Stability Zones in Permafrost Location</i> .....	15
<i>2.2.5 Estimates of Hydrate-Associated Gas</i> .....	17
2.3 Alaska Gas Hydrate Resource Potential.....	19
2.4 Gas Hydrate Production Technology .....	22
<i>2.4.1 Thermal Injection</i> .....	23

	<b>Page</b>
2.4.2 Depressurization .....	24
2.4.3 Inhibitor Injection.....	26
2.5 Modeling Hydrate-Bearing Reservoirs .....	27
2.5.1 Classification of Gas Hydrate Deposits .....	27
2.5.2 Numerical Simulations .....	29
2.5.3 Data Requirements for Gas Hydrate Reservoir Simulation.....	30
2.5.4 Gas-Water Relative Permeability Studies.....	31
2.6 Global Methane Hydrate Research Activities .....	32
<b>3. METHODOLOGY FOR RESERVOIR ENGINEERING OF HYDRATE SYSTEMS ....</b>	<b>33</b>
3.1 Gas Hydrate Stability Modeling.....	33
3.1.1 Background and Objectives .....	33
3.1.2 Data and Assumptions .....	33
3.1.2.1 Gas Analysis Data.....	33
3.1.2.2 Formation Water Salinity Data.....	34
3.1.2.3 Pressure Gradient Data.....	34
3.1.2.4 Temperature Gradient Data.....	35
3.1.3 CSM-HYD Results Validation.....	35
3.1.4 Gas Hydrate Stability Model Development.....	38
3.2 Material Balance Study.....	38
3.2.1 Background and Objectives .....	38
3.2.2 Data and Assumptions .....	41
3.2.2.1 Reservoir Thickness.....	41
3.2.2.2 Reservoir Properties.....	42
3.2.2.3 Initial Reservoir Pressure and Temperature .....	43
3.2.2.4 Original Gas In-Place (OGIP) .....	44
3.2.2.5 Water Influx.....	44
3.2.2.6 Production Data.....	45
3.2.2.7 Summary.....	46
3.2.3 Methodology .....	47

	<b>Page</b>
3.2.3.1 Volumetric Model.....	47
3.2.3.2 Water Influx Model .....	49
3.2.3.3 Hydrate Model.....	51
3.2.3.4 CMG-STARs Simulation Model.....	53
3.3 Gas-Water Relative Permeability Study.....	54
3.3.1 Background and Objectives .....	54
3.3.2 Experimental Setup.....	57
3.3.3 Procedures.....	59
3.3.3.1 Porosity and Absolute Permeability Determination .....	59
3.3.3.2 Hydrate Formation and Dissociation Experiments .....	60
3.3.3.3 Unsteady-State Displacement Experiments.....	62
3.3.4 Tuning Relative Permeability Model .....	63
3.4 Reservoir Simulation Study .....	64
3.4.1 Background and Objectives .....	64
3.4.2 CMG-STARs Reservoir Simulator .....	64
3.4.2.1 Reservoir Grid .....	65
3.4.2.2 Reservoir Properties.....	65
3.4.2.3 Thermal Properties.....	66
3.4.2.4 Fluid/Component Properties.....	66
3.4.2.5 Relative Permeabilities and Capillary Pressure Functions .....	68
3.4.2.6 Production Well Modeling.....	69
3.4.3 Model Initialization.....	70
3.4.3.1 East Barrow Gas Field.....	70
3.4.3.2 Walakpa Gas Field .....	105
3.4.4 History Matching Study .....	117
3.4.4.1 East Barrow Gas Field.....	117
3.4.4.2 Walakpa Gas Field .....	123
3.4.5 Sensitivity Study.....	123
3.4.5.1 East Barrow Gas Field.....	123

	<b>Page</b>
3.4.5.2 <i>Walakpa Gas Field</i> .....	129
3.4.6 <i>Forecasting Study</i> .....	129
3.4.6.1 <i>East Barrow Gas Field</i> .....	129
3.4.6.2 <i>Walakpa Gas Field</i> .....	130
<b>4. RESULTS AND DISCUSSION</b> .....	<b>132</b>
4.1 <i>Gas Hydrate Stability Modeling</i> .....	132
4.1.1 <i>CSM-HYD Results Validation</i> .....	132
4.1.2 <i>Gas Hydrate Stability Models</i> .....	134
4.1.2.1 <i>South Barrow Gas Field</i> .....	134
4.1.2.2 <i>East Barrow Gas Field</i> .....	134
4.1.2.3 <i>Walakpa Gas Field</i> .....	134
4.2 <i>Material Balance Study</i> .....	137
4.2.1 <i>Volumetric Model</i> .....	138
4.2.2 <i>Water Influx Model</i> .....	140
4.2.3 <i>Hydrate Model</i> .....	142
4.2.4 <i>CMG-STARs Simulation Model</i> .....	146
4.3 <i>Gas-Water Relative Permeability Study</i> .....	152
4.3.1 <i>Porosity and Absolute Permeability Determination</i> .....	152
4.3.2 <i>Hydrate Formation and Dissociation Experiments</i> .....	154
4.3.3 <i>Unsteady-State Displacement Experiments</i> .....	156
4.3.4 <i>Tuning the Relative Permeability Model</i> .....	160
4.4 <i>Reservoir Simulation Study</i> .....	160
4.4.1 <i>History Matching</i> .....	160
4.4.1.1 <i>East Barrow Gas Field</i> .....	160
4.4.1.2 <i>Walakpa Gas Fields</i> .....	182
4.4.2 <i>Sensitivity Study</i> .....	187
4.4.2.1 <i>East Barrow Gas Field</i> .....	187
4.4.3 <i>Forecasting Study</i> .....	197
4.4.3.1 <i>East Barrow Gas Field</i> .....	197

	<b>Page</b>
4.4.3.2 <i>Walakpa Gas Field</i> .....	202
<b>5. CONCLUSIONS AND RECOMMENDATIONS</b> .....	<b>206</b>
5.1 Conclusions.....	206
5.1.1 <i>Gas Hydrate Stability Modeling</i> .....	206
5.1.2 <i>Material Balance Study</i> .....	207
5.1.3 <i>Gas-Water Relative Permeability Study</i> .....	208
5.1.4 <i>Reservoir Simulation Study</i> .....	208
5.1.4.1 <i>East Barrow Reservoir Model</i> .....	208
5.1.4.2 <i>Walakpa Reservoir Model</i> .....	210
5.2 Recommendations.....	210
<b>REFERENCES</b> .....	<b>212</b>
<b>GLOSSARY</b> .....	<b>219</b>
<b>APPENDICES</b> .....	<b>224</b>

## LIST OF FIGURES

	<b>Page</b>
Figure 1.1: BGF, Alaska .....	2
Figure 1.2: Summary and Sequence of Completed Tasks .....	5
Figure 2.1: Burning Sample of Methane Hydrate .....	8
Figure 2.2: Structures of Hydrate Crystal .....	10
Figure 2.3: Types of Natural Gas Hydrate Accumulations.....	12
Figure 2.4: Types of Gas Hydrate Deposits .....	13
Figure 2.5: Worldwide Hydrate Accumulations .....	14
Figure 2.6: Gas Hydrate Stability Zone in Permafrost .....	16
Figure 2.7: Hydrate Plays and Province in the U.S. ....	18
Figure 2.8: Extent of Stable Hydrate Zone in ANS.....	19
Figure 2.9: Cross Section Showing Lateral and Vertical Extent of Gas Hydrates and Free Gas Occurrences in Prudhoe Bay-Kuparuk River area of ANS.....	20
Figure 2.10: Map Showing Distribution of Hydrate Accumulations in Prudhoe Bay, Kuparuk River, and Milne Point Fields of the ANS .....	21
Figure 2.11: Gas Hydrate Production Methods: a) Thermal Injection, b) Depressurization, c) Inhibitor Injection .....	23
Figure 2.12: Pressure-Temperature Equilibrium Curve Showing Hydrate Production Mechanism for Depressurization Technique .....	25
Figure 2.13: Water-Hydrate-Gas Three-Phase Equilibrium Curve and Methods of Hydrate Decomposition .....	27
Figure 2.14: Class 1G (Water-Poor System) Accumulations.....	28
Figure 2.15: Class 2 Hydrate Deposit .....	29
Figure 3.1: Hydrate Equilibrium Pressure-Temperature Relationship .....	37
Figure 3.2: EB Gas Reservoir Performance Plot.....	39
Figure 3.3: Methodology Followed for Material Balance Study .....	40
Figure 3.4: Production History Chart for the EB Gas Pool.....	45
Figure 3.5: $P(t)/z(t)$ vs. Pressure, $P(t)$ Relationship.....	47
Figure 3.6: Gas-Water Relative Permeability Setup.....	58



**Page**

Figure 3.7: Flow Diagram - Gas-Water Relative Permeability Experiment .....	59
Figure 3.8: Reservoir Grid - 3D View .....	71
Figure 3.9: Reservoir Grid (K Layer 1) - IJ Plane View .....	71
Figure 3.10: Reservoir Grid (K Layer 12) - IJ Plane View .....	72
Figure 3.11: Reservoir Grid (K Layer 25) - IJ Plane View .....	72
Figure 3.12: Porosity Distribution, % - 3D View .....	73
Figure 3.13: Porosity - 5% (K Layer 16) - IJ Plane View .....	74
Figure 3.14: Permeability Distribution - I Direction, md - 3D View .....	75
Figure 3.15: Permeability Distribution - J Direction, md - 3D View .....	75
Figure 3.16: Permeability Distribution - K Direction, md - 3D View.....	76
Figure 3.17: Permeability - 5 md (K Layer 16) - IJ Plane View.....	76
Figure 3.18: Initial Temperature Distribution, °F (on Dec 01, 1981) - 3D View .....	77
Figure 3.19: Formula Editor - Initializing Temperature Distribution.....	78
Figure 3.20: Initial Pressure, psi (on Dec 01, 1981) - 3D View.....	79
Figure 3.21: Initial Condition - No Vertical Equilibrium Calculation.....	79
Figure 3.22: Pressure-Temperature Equilibrium Curve Showing Initial Thermodynamic Condition of the EB Reservoir .....	80
Figure 3.23: Formula Editor - Initializing Hydrate Saturation.....	82
Figure 3.24: Initial Hydrate Saturation, % (on Dec 01, 1981) - 3D View.....	82
Figure 3.25: Initial Hydrate Saturation, % (K Layer 1) - IJ Plane View .....	83
Figure 3.26: Initial HGC (on Dec 01, 1981) - IK Plane View.....	83
Figure 3.27: Formula Editor - Initializing Gas Saturation.....	85
Figure 3.28: Initial Gas Saturation, % (on Dec 01, 1981) - 3D View.....	85
Figure 3.29: Initial Gas Saturation, % (K Layer 1) - IJ Plane View .....	86
Figure 3.30: Initial HGC and GWC (on Dec 01, 1981) - IK Plane View .....	86
Figure 3.31: Formula Editor - Initializing Water Saturation.....	88
Figure 3.32: Initial Water Saturation, % (on Dec 01, 1981) - 3D View.....	88
Figure 3.33: Initial Water Saturation, % (K Layer 1) - IJ Plane View .....	89
Figure 3.34: Initial GWC (on Dec 01, 1981) - IK Plane View.....	89

	<b>Page</b>
Figure 3.35: Hydrate-Water Relative Permeability Curve (CMG Keyword *SWT) .....	91
Figure 3.36: Water Capillary Pressure (CMG Keyword *SWT) .....	92
Figure 3.37: Gas-Hydrate Relative Permeability Curve (CMG Keyword *SLT).....	93
Figure 3.38: Gas Capillary Pressure (CMG Keyword *SLT).....	93
Figure 3.39: Well Locations (IJ Plane View) .....	95
Figure 3.40: Step 1 - Choose the File Containing Well Production Data .....	97
Figure 3.41: Step 2 - Choose the File Option.....	98
Figure 3.42: Step 3 - Select Delimiters .....	99
Figure 3.43: Step 4 - Choose Column Details.....	100
Figure 3.44: Step 5 - Check Well Names and Primary Constraint.....	101
Figure 3.45: Gas Production Rate for EB #14 (Production Data vs. Model Output) .....	103
Figure 3.46: Gas Production Rate for EB #15 (Production Data vs. Model Output) .....	103
Figure 3.47: Gas Production Rate for EB #18 (Production Data vs. Model Output) .....	104
Figure 3.48: Gas Production Rate for EB #19 (Production Data vs. Model Output) .....	104
Figure 3.49: Gas Production Rate for EB #21 (Production Data vs. Model Output) .....	105
Figure 3.50: Reservoir Grid (SMALL Model) - 3D View.....	106
Figure 3.51: Porosity (SMALL Model) - 3D View.....	107
Figure 3.52: Permeability Distribution (SMALL Model) - 3D View .....	108
Figure 3.53: Initial Temperature, °F (SMALL Model) - 3D View .....	109
Figure 3.54: Initial Reservoir Pressure, psi (SMALL Model) - 3D View.....	110
Figure 3.55: Pressure-Temperature Equilibrium Curve Showing Initial Thermodynamic Condition of the WAL Reservoir.....	111
Figure 3.56: Initial Hydrate Saturation, % (SMALL Model) - 3D View.....	111
Figure 3.57: Initial HGC (SMALL Model) - JK Plane View.....	112
Figure 3.58: Initial Gas Saturation, % (SMALL Model) - 3D View.....	113
Figure 3.59: Initial HGC and GWC (SMALL Model) - JK Plane View .....	113
Figure 3.60: Initial Water Saturation, % (SMALL Model) - 3D View.....	114
Figure 3.61: Initial GWC (SMALL Model) - JK Plane View .....	115
Figure 3.62: Well Locations (SMALL Model) - IJ Plane View .....	117

## Page

Figure 3.63: Block 19,19,1 Representing Average Reservoir Pressure.....	119
Figure 3.64: Aquifer Options (CMG-STARS) .....	126
Figure 3.65: Initializing Bottom Aquifer (Infinite Size).....	127
Figure 3.66: Initializing Bottom Aquifer (Finite Size).....	127
Figure 3.67: Initializing Region Aquifer (Infinite Size).....	128
Figure 3.68: Initializing Region Aquifer (Finite Size).....	129
Figure 4.1: CSM-HYD Results Validation Study (99% Methane, 2% w/w Salinity) .....	132
Figure 4.2: CSM-HYD Results Validation Study (99% Methane, 4% w/w Salinity) .....	133
Figure 4.3: Hydrate Stability Model for the SB Gas Field .....	135
Figure 4.4: Hydrate Stability Model for the EB Gas Field .....	135
Figure 4.5: Structural Diagram Showing Hydrate Stability Zone.....	136
Figure 4.6: Hydrate Stability Model for the WAL Gas Field .....	136
Figure 4.7: Structural Diagram Showing Hydrate Stability Zone.....	137
Figure 4.8: Volumetric Model - Constant (Horizontal) $C$ vs. Time (Months) .....	138
Figure 4.9: Volumetric Model - $\frac{P(t)}{z(t)}$ vs. $G_p(t)$ Plot for the EB Reservoir .....	139
Figure 4.10: Volumetric Model - Pressure vs. Time Plot for the EB Reservoir.....	140
Figure 4.11: Water Influx Model for the EB Reservoir .....	141
Figure 4.12: Volumetric Gas Reservoir Performance Plot for Mechanistic Model .....	143
Figure 4.13: Pressure vs. Time Plot for Mechanistic (Gas Reservoir) Model .....	143
Figure 4.14: Volumetric Gas Reservoir Performance Plot for <i>Modified Hydrate Model</i> and the EB Production Data .....	144
Figure 4.15: Pressure vs. Time Comparison Plot for <i>Modified Hydrate Model</i> , CMG- STARS Model, and the EB Production Data.....	145
Figure 4.16: Pressure vs. Time Plot for Hydrate Model (Changing Hydrate Zone Size).....	146
Figure 4.17: Pressure vs. Time Comparison Plot for Hydrate and CMG-STARS Models (Hydrate vs. Aquifer Support) .....	148
Figure 4.18: Hydrate and Aquifer Supported Gas Reservoir Performance Plot (CMG- STARS Model) .....	148

	<b>Page</b>
Figure 4.19: The EB Production Data History Matching Plot.....	149
Figure 4.20: Sensitivity Analysis (Permeability) .....	150
Figure 4.21: Sensitivity Analysis (Gas Production Rates) .....	151
Figure 4.22: Sensitivity Analysis (Hydrate Zone/Free Gas Zone Ratio).....	151
Figure 4.23: Hydrate Formation Profile (Hydrate Saturation 38%) .....	154
Figure 4.24: Hydrate Dissociation Profile (Hydrate Saturation 38%) .....	156
Figure 4.25: Gas-Water Relative Permeability Curve (Hydrate Saturation 38%).....	157
Figure 4.26: Gas-Water Relative Permeability Curve (Hydrate Saturation 14%).....	157
Figure 4.27: Gas-Water Relative Permeability Curve (Hydrate Saturation 5%).....	158
Figure 4.28: Effective Permeability vs. Hydrate Saturation .....	159
Figure 4.29: Cumulative Gas Production (History Matching).....	162
Figure 4.30: Cumulative Water Production (History Matching).....	163
Figure 4.31: Average Reservoir Pressure (History Matching) .....	165
Figure 4.32: Water Production Rate (History Matching) - Well EB #14 .....	166
Figure 4.33: Water Production Rate (History Matching) - Well EB #15 .....	167
Figure 4.34: Water Production Rate (History Matching) - Well EB #18 .....	167
Figure 4.35: Water Production Rate (History Matching) - Well EB #19 .....	168
Figure 4.36: Water Production Rate (History Matching) - Well EB #21 .....	168
Figure 4.37: Hydrate Saturation Profile (Location 19, 19, and [K = 1 to 25]) .....	169
Figure 4.38: Gas Saturation Profile (Location 19, 19, and [K = 1 to 25]) .....	170
Figure 4.39: Water Saturation Profile (Location 19, 19, and [K = 1 to 25]) .....	171
Figure 4.40: Hydrate-Free Gas-Aquifer Zone (Location 29, 8, and [K =1 to 25]) .....	172
Figure 4.41: Hydrate Saturation Profile (Location 29, 8, and [K = 1 to 8]) .....	172
Figure 4.42: Gas Saturation Profile (Location 29, 8 and [K = 1 to 22]) .....	173
Figure 4.43: Water Saturation Profile (Location 29, 8, and [K = 1 to 22]) .....	174
Figure 4.44: Current Reservoir Pressure, psi (on Sep 01, 2007) - 3D View .....	175
Figure 4.45: Current Reservoir Temperature, °F (on Sep 01, 2007) - 3D View .....	175
Figure 4.46: Current Hydrate Saturation, % (on Sep 01, 2007) - 3D View .....	176
Figure 4.47: Current Gas Saturation, % (on Sep 01, 2007) - 3D View .....	176

**Page**

Figure 4.48: Current Water Saturation, % (on Sep 01, 2007) - 3D View .....	177
Figure 4.49: Initial HGC at 2050 ft (on Dec 01, 1981) .....	178
Figure 4.50: Current HGC at 2045 ft (on Sep 01, 2007).....	178
Figure 4.51: Initial GWC at 2080 ft (on Dec 01, 1981) .....	179
Figure 4.52: Current GWC at 2070 ft (on Sep 01, 2007).....	179
Figure 4.53: Possible Locations for Drilling Infill Wells.....	181
Figure 4.54: Cumulative Gas Production (History Matching Case <i>A</i> and <i>B</i> ) - SMALL Model .....	183
Figure 4.55: Average Reservoir Pressure (History Matching Case <i>A</i> ) - SMALL Model	184
Figure 4.56: Average Reservoir Pressure (History Matching Case <i>B</i> ) - SMALL Model	184
Figure 4.57: IJ Coordinates Representing Reservoir Pressure - SMALL Model .....	185
Figure 4.58: Cumulative Gas Production (Sensitivity - Free Gas Zone Size) .....	188
Figure 4.59: Cumulative Water Production (Sensitivity - Free Gas Zone Size) .....	188
Figure 4.60: Average Reservoir Pressure (Sensitivity - Free Gas Zone Size) .....	189
Figure 4.61: Cumulative Gas Production (Sensitivity - Hydrate Saturation) .....	190
Figure 4.62: Cumulative Water Production (Sensitivity - Hydrate Saturation) .....	191
Figure 4.63: Average Reservoir Pressure (Sensitivity - Hydrate Saturation) .....	192
Figure 4.64: Cumulative Gas Production (Sensitivity - Hydrate Zone Size).....	193
Figure 4.65: Cumulative Water Production (Sensitivity - Hydrate Zone Size).....	194
Figure 4.66: Average Reservoir Pressure (Sensitivity - Hydrate Zone Size) .....	194
Figure 4.67: Cumulative Gas Production (Sensitivity - Aquifer Strength and Size).....	195
Figure 4.68: Cumulative Water Production (Sensitivity - Aquifer Strength and Size)....	196
Figure 4.69: Average Reservoir Pressure (Sensitivity - Aquifer Strength and Size) .....	197
Figure 4.70: Average Reservoir Pressure (Forecasting Study) .....	198
Figure 4.71: Gas Production Rates (Forecasting Study) .....	199
Figure 4.72: Cumulative Water Production (Forecasting Study) .....	200
Figure 4.73: Percentage of Gas Recovery (Forecasting Study) .....	200
Figure 4.74: Cumulative Gas Production (Forecasting Study) - LARGE Model.....	203
Figure 4.75: Cumulative Gas Production Rate (Forecasting Study) - LARGE Model ...	204

	<b>Page</b>
Figure 4.76: Average Reservoir Pressure (Forecasting Study) - LARGE Model .....	204
Figure C.1: Waterdrive Mechanisms.....	228
Figure H.1: Wellbore Diagram of EB #14.....	242
Figure H.2: Wellbore Diagram of EB #15.....	243
Figure H.3: Wellbore Diagram of EB #18.....	244
Figure H.4: Wellbore Diagram of EB #19.....	245
Figure H.5: Wellbore Diagram of EB #21.....	246
Figure I.1: Wellbore Diagram of EB #14 (Completed in Horizontal Section).....	247
Figure I.2: Wellbore Diagram of EB #19 (Completed in Horizontal Section).....	248
Figure I.3: Wellbore Diagram of Vertical Well (New Test Well) .....	249
Figure I.4: Wellbore Diagram of Horizontal Well (New Test Well) .....	250
Figure J.1: Gas-Water Relative Permeability Curve (Hydrate Saturation 38%) .....	251
Figure J.2: Gas-Water Relative Permeability Curve (Hydrate Saturation 14%) .....	251
Figure J.3: Gas-Water Relative Permeability Curve (Hydrate Saturation 5%) .....	252

## LIST OF TABLES

	<b>Page</b>
Table 2.1: Summary of Simulator Data Requirements for Performing Hydrate Reservoir Simulation Studies.....	31
Table 3.1: Core Analysis Results for Wells EB #12 and #17.....	42
Table 3.2: Log Analysis Results for Wells EB #12, #14, #17, and #19.....	43
Table 3.3: Reservoir Properties Considered for the Material Balance Study.....	46
Table 3.4: Summary of Initial Condition for the EB Reservoir Model (Best Case) .....	90
Table 3.5: End-Point Saturation and Relative Permeability for Hydrate-Water System ..	91
Table 3.6: End-Point Saturation and Relative Permeability for Gas-Hydrate System .....	92
Table 3.7: Locations (Coordinates) and Dimensions of the EB Wells .....	95
Table 3.8: Summary of Initial Reservoir Condition (WAL Reservoir Model) .....	114
Table 3.9: Production History Data for the WAL Gas Field .....	116
Table 3.10: Locations (Coordinates) and Dimension of WAL Wells .....	116
Table 3.11: History Matching Cases .....	120
Table 3.12: Initial Condition for Case <i>A</i> (Only Gas Model) .....	121
Table 3.13: Initial Condition for Case <i>B</i> (Gas + Aquifer Model) .....	121
Table 3.14: Initial Condition for Case <i>C</i> (HYD + Gas + Aquifer Model) .....	121
Table 3.15: Initial Condition for Case <i>D</i> (Only HYD Model) .....	122
Table 3.16: Initial Condition for Case <i>E</i> (HYD + Gas Model) .....	122
Table 3.17: Initial Condition for Case <i>F</i> (HYD + Aquifer Model) .....	122
Table 3.18: Initial Condition for Case <i>A</i> (Gas + Aquifer Model) .....	123
Table 3.19: Initial Condition for Case <i>B</i> (HYD + Gas + Aquifer Model) .....	123
Table 3.20: Summary of Forecasting Runs.....	131
Table 4.1: Root Mean Square Error Analysis.....	133
Table 4.2: BS Sample Dimensions .....	152
Table 4.3: Results: Sample Porosity.....	152
Table 4.4: Results: Absolute Permeability .....	153
Table 4.5: System Parameters for Hydrate Formation .....	155



**Page**

Table 4.6: Effect of Hydrate Saturation on Irreducible Water Saturation and Gas-Water Effective Permeabilities .....	159
Table 4.7: Tuned Parameters of Relative Permeability Model .....	160
Table 4.8: Initial Estimates of Free Gas, Hydrate, and Water .....	161
Table 4.9: Initial Gas In-Place (Free Gas + Hydrate-Associated Gas) .....	161
Table 4.10: Cumulative Gas Production (on Sep 01, 2007) .....	162
Table 4.11: Cumulative Water Production (on Sep 01, 2007) .....	164
Table 4.12: Root Mean Square Error Analysis (Reservoir Pressure vs. Model Output) .....	165
Table 4.13: Hydrate Contribution in Recharging Gas Reservoir.....	180
Table 4.14: Possible Locations (Gridblock Coordinates) for Drilling Future Wells .....	181
Table 4.15: Initial Estimates of Free Gas, Hydrates, and Water (LARGE Model).....	182
Table 4.16: Initial Gas In-Place (Free Gas + Hydrate-Associated) (LARGE Model) .....	182
Table 4.17: Root Mean Square Error Analysis (Case A) - SMALL Model .....	185
Table 4.18: Root Mean Square Error Analysis (Case B) - SMALL Model .....	186
Table 4.19: Hydrate Contribution in Recharging Gas Reservoir (LARGE Model).....	186
Table 4.20: Cumulative Gas Production, Recovery, and Water Production from Dec 01, 1981 to Sep 01, 2037 (Forecasting Study) .....	201
Table 4.21: Summary of History Matching and Forecasting Results for the Best-Case .....	202
Table 4.22: Summary of History Matching and Forecasting Study for the Best-Case .....	203
Table 4.23: Initial Gas In-Place Estimates for WAL (LARGE Model).....	205
Table E.1: Summary of Displacement Experiment (Hydrate Saturation 38%) .....	233
Table E.2: Summary of Displacement Experiment (Hydrate Saturation 14%) .....	234
Table E.3: Summary of Displacement Experiment (Hydrate Saturation 5%) .....	236
Table G.1: Thermal Properties of Rock and Fluids .....	239
Table G.2: Fluid Properties for the EB and WAL Reservoir Model .....	240

**LIST OF APPENDICES**

	<b>Page</b>
APPENDIX A. Flowchart - Hydrate Stability Model Development .....	224
APPENDIX B. Volumetric Model.....	225
APPENDIX C. Water Influx Model .....	227
APPENDIX D. Hydrate Model.....	230
APPENDIX E. Summary of Displacement Experiments.....	233
APPENDIX F. NLREG Programs .....	238
APPENDIX G. Thermal and Fluid Component Properties.....	239
APPENDIX H. Wellbore Diagrams of the Existing EB Wells .....	242
APPENDIX I. Wellbore Diagrams of the Future EB Wells (Forecast) .....	247
APPENDIX J. NLREG Regression Model Results .....	251

DEDICATION

*In loving memory of my grandmother*

## ACKNOWLEDGMENTS

First, I would like to express my sincere gratitude to my advisors Dr. Shirish Patil and Dr. Abhijit Dandekar for their support throughout the course of this research. I would also like to thank my advisory committee members Mr. Thomas Walsh, Dr. Manmath Panda, Mr. Peter Stokes and Dr. Santanu Khataniar for their technical guidance and vital input. I would also like to take this opportunity to thank Ms. Melody Hughes, manager, petroleum engineering department, University of Alaska Fairbanks (UAF) for her assistance, whenever needed.

In addition, I wish to thank Computer Modeling Group Ltd. (CMG) for donating “unlimited gridblock” license of their commercial reservoir simulator “STARS” for this work and for providing technical assistance during the course of this study. Many thanks to the Arctic Region Supercomputing Center (ARSC) at UAF for enabling free access to their supercomputer’s processor time.

My sincere appreciation goes to Dr. George Moridis of the Lawrence Berkeley National Laboratory (LBNL) for providing the latest version of the LBNL’s hydrate simulator (TOUGH+HYDRATE). I am equally thankful to Thunderhead Engineering Group for donating the license of their pre- and post-processor “PetraSim.” Thanks are additionally extended to Mr. Scott Wilson (Ryder Scott Company) for sharing important information related to reservoir simulation studies. I sincerely thank Mr. Bob Hunter (ASRC Energy Group) and Dr. Timothy Collett, United States Geological Survey (USGS) for their timely suggestions.

I am grateful to the U.S. Department of Energy (USDOE), North Slope Borough (NSB), Petrotechnical Resources of Alaska (PRA), and Petroleum Development Laboratory (PDL) at UAF for their financial support in accomplishing this work.

Finally, I would like to deeply thank my family and friends. Without their unconditional love and support, I would not have accomplished this research.

**DISCLAIMER**

This thesis was prepared as an account of work sponsored by an agency of the United States (U.S.) Government. Neither the U.S. Government nor an agency thereof, nor any of their employees, makes any warranty, expressed or implied, or assumes any legal liability or responsibility for the accuracy, completeness, or usefulness of any information, apparatus, product, or process disclosed, or represents that its use would not infringe privately owned rights. References herein to any specific commercial product, process, or service by trade name, trademark, manufacture, or otherwise does not necessarily constitute or imply its endorsement, recommendation, or favoring by the U.S. Government or any agency thereof. The views and opinions of the author expressed herein do not necessarily state or reflect those of the U.S. Government or any agency thereof.

## 1. INTRODUCTION

### 1.1 Background

Barrow, Alaska, is a cold and remote city located in the northernmost land of the United States of America (U.S.). The city is the largest in the region and serves both as the economic and administrative center of the North Slope Borough (NSB). The NSB meets the energy demand of the city of Barrow and nearby villages through a natural gas supply from the Barrow Gas Fields (BGF). The BGF, comprised of East Barrow (EB), South Barrow (SB), and Walakpa (WAL) fields, have been producing natural gas for the last 25 years (Figure 1.1). It has been estimated that the proven gas reserves in these fields exceed 250 billion standard cubic feet (bcf) (Gruy, 1978; Darkwah and Allen, 1996). Assuming current demands for natural gas in the region, the BGF are capable of supplying natural gas for heating and generating electricity for another 100 years. However, the city of Barrow is expanding, thus increasing the demand for natural gas. Moreover, with rising oil and gas prices, the cost of energy being transported to nearby villages is also on the rise. Hence, there is an immediate need to enhance natural gas production and expand production facilities in order to provide an affordable and assured source of energy to the residents of Barrow and other areas.

The BGF are relatively shallow gas reservoirs, lying beneath a permafrost region. The pressure and temperature conditions are such that they provide a favorable environment for stable natural gas hydrates to exist. Given other favorable conditions (gas composition and availability of free water), gas hydrate is likely to be found in updip locations of the reservoirs. Previous engineering study supports this argument. The study on the EB (Stokes and Walsh, 2007) and WAL (Stokes et al., 2005) gas pools concluded that the gas recharge from dissociating hydrates could be one of the contributors to the drive mechanisms of these reservoirs. Glenn and Allen (1991) collected seismic, well log, gas chemistry, pressure gradient and temperature gradient data from the WAL gas field. Based on these data, Glenn and Allen (1991) were able to map possible gas hydrate distribution for WAL gas pool. They also estimated that the stable hydrate zone thickness lies within a depth range of 2000-2550 ft below sea level.

Seismic data, well log data, and correlation with nearby wells helped them in determining the extent of the reservoir.

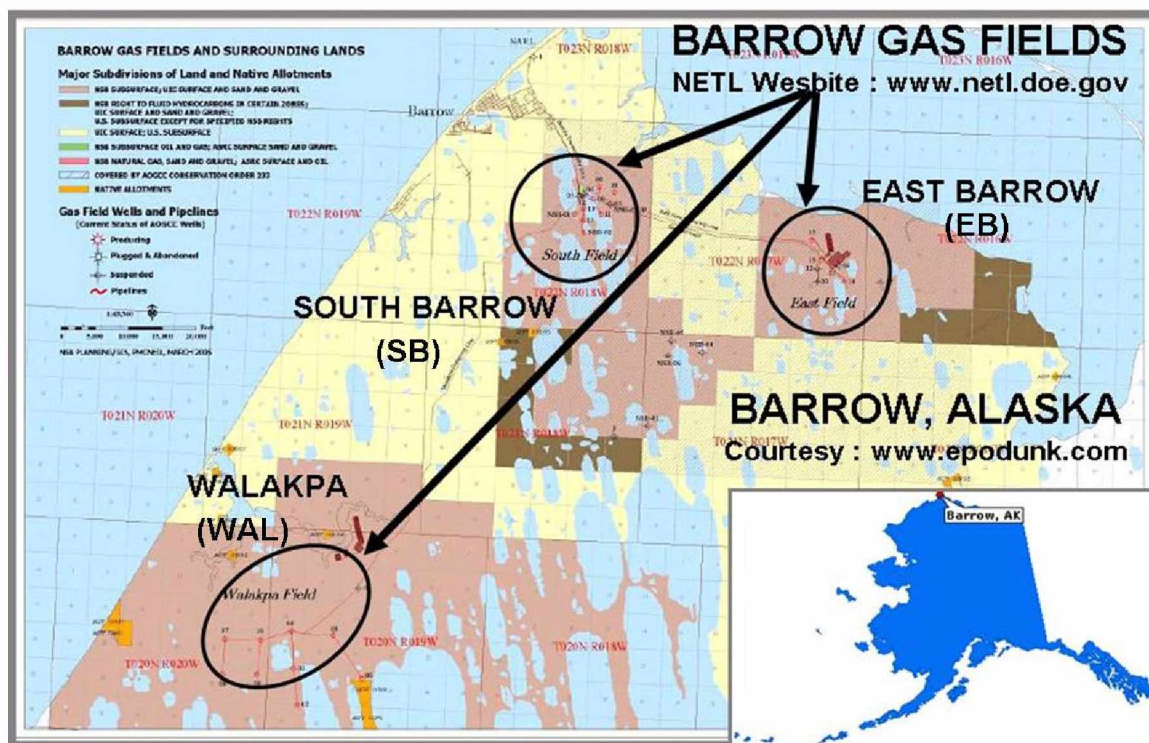


Figure 1.1: BGF, Alaska (Modified from NETL Website, [www.netl.doe.gov](http://www.netl.doe.gov))

Gas hydrates are solid crystalline compounds in which gas molecules are encased inside the lattices of ice crystals. These light non-polar gases are referred to as *guest*, whereas the ice crystals are called *hosts*. Such deposits exist in distinct geologic formations such as permafrost and deep marine sediments, where the thermodynamic conditions of low temperature and high-pressure allow hydrate formation. Methane is the primary gas found in the majority of naturally occurring hydrocarbon gas hydrates (Sloan and Koh, 2008). Upon dissociation, methane hydrates are capable of supplying abundant volumes of natural gas. Considering sheer magnitude of untapped gas in-place (as hydrates) and the environmentally friendly nature of the fuel (as compared to solid and liquid fuel), naturally occurring gas hydrates have now become an attractive resource that needs to be developed and produced in the future.



The existence of stable natural gas hydrates within the reservoir sediments of the Alaska North Slope (ANS) was reported in 1972, while the Northwest Eileen (NWE) No.-2 Well was being drilled in the Prudhoe Bay Unit (PBU). The volumes of gas trapped in gas hydrates of Prudhoe Bay-Kuparuk areas are estimated to be about 35-40 trillion standard cubic feet (tcf), which is twice the volume of known free gas reserves in PBU (Collett, 2002). However, Collett (2004) speculates that these figures could easily exceed 100 tcf for the two reservoirs. Knowing the significance of finding and developing this resource, several government and privately funded projects have been initiated in the past decade, primarily focusing on developing Alaska's gas hydrate resource. Of particular importance and interest is the currently active ANS gas hydrate program, jointly funded by the USDOE and BP Exploration, Alaska (BPXA). The primary objective of this project is to characterize and quantify ANS hydrate resource potential by performing laboratory, desktop-based, and field-based studies (USDOE/NETL and BPXA, 2001). Recently, successful drilling and coring operations were completed on Mt. Elbert-01 in the Milne Point Unit (MPU) where more than 430 ft of core sample were recovered, including 100 ft of hydrate-bearing sediments. The research team performed short-term production testing within the hydrate zone, the first time ever attempted on the ANS (Hunter et al., 2007). The acquired data are currently being analyzed, and research efforts are now underway to perform long-term production tests and determine reservoir deliverability under a variety of production and completion scenarios (Hunter et al., 2007). The success of this project marks the start of a new phase in hydrate research in Alaska.

Hydrate researchers around the world are currently performing production modeling/simulation studies and laboratory-scale experiments in order to fully understand the hydrate dissociation mechanism. Field-level tests are still a rarity, as they involve long-term planning, huge costs, a considerable level of risk, and a wide range of uncertainties. On the other hand, energy challenges associated with the BGF are realistic and need immediate evaluation. There is an urgent need to develop these reservoirs with the intention of tapping gas from possible hydrate accumulations. Realizing this, in 2006 the USDOE and NSB jointly funded a research program to characterize and quantify methane hydrate resource potential associated with the BGF

popularly known as the Barrow Gas Hydrate Project. The goal of this project is to investigate the BGF for hydrates and to develop the individual gas pools in order to meet the future energy demands of Barrow and other local communities (USDOE/NETL and NSB, 2006). The project's focus is directed toward delivering technical solutions to the NSB that will assist them in improving and sustaining long-term gas production.

The Barrow Gas Hydrate Project will provide an excellent opportunity to drill and perform long-term production tests within the hydrate sediments. In addition to this, it will offer a chance to closely monitor the reservoir drive mechanism and quantify the relative contribution of dissociating hydrates in recharging the free gas reservoir (Walsh and Stokes, 2007). The researchers involved with the Barrow project believe that the findings from this study will add an important source of data to global research efforts regarding the potential for methane hydrates to supplement conventional production in arctic regions. They are confident that the end result of their work has the potential to greatly benefit the community of Barrow and similar communities across the ANS by expanding the energy resources available for heating and electricity (Walsh and Stokes, 2007).

## **1.2 Objectives**

The work reported in this study was performed under the Barrow Gas Hydrate Project (USDOE/NETL and NSB, 2006), with a goal to evaluate the EB, SB, and WAL gas fields of the BGF for possible hydrate accumulations. The focus of this work was on applying engineering concepts and methodologies to identify any hydrate-bearing reservoirs, understand reservoir drive mechanisms, study two-phase fluid flow properties through lab scale experiments, develop dynamic reservoir models to match historical data, generate current reservoir conditions, and propose an optimal plan for future expansion (Figure 1.2). An evaluative procedure was followed for all three gas pools based on data availability and requirements.

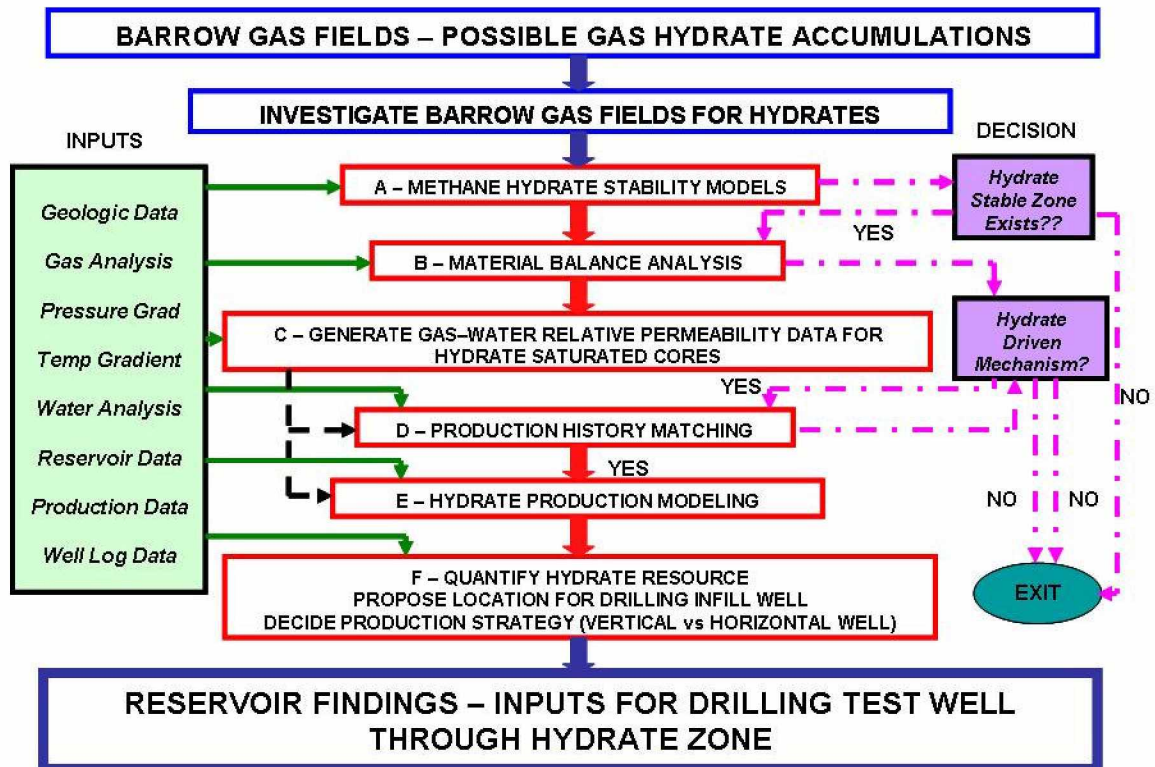


Figure 1.2: Summary and Sequence of Completed Tasks

### 1.3 Tasks Performed

The following tasks were performed to meet the objectives of this study:

- i. Validated the Colorado School of Mines-Hydrate (CSM-HYD) software predictions by comparing the results with experimental data (Westervelt, 2004) and empirical equations (Kamath and Holder, 1987; Moridis, 2003).
- ii. Developed gas hydrate stability models, using CSM-HYD software, for the EB, SB, and WAL gas fields, utilizing gas chemistry, formation water salinity, pressure and temperature gradient data.
- iii. Formulated a stepwise procedure, based on conclusions from hydrate stability studies, to apply the material balance technique and understand the reservoir drive mechanisms of the EB gas field.
- iv. Re-calibrated the relative permeability setup (Jaiswal, 2004) and performed gas-water displacement experiments on consolidated core sample at three

different hydrate saturations; generated corresponding gas-water relative permeability curves; and tuned mathematical models (Hong, 2003) using Non Linear Regression (NLREG) software to obtain relative permeability models, unique for each set of experimental data.

- v. Developed state-of-the-art full-field dynamic reservoir simulation models for the EB and WAL gas fields using the Computer Modeling Group-Steam Thermal and Advanced Processes Reservoir Simulator (CMG-STARS). These models are capable of representing current reservoir conditions and evaluating future prospects of reservoir development. The following subtasks were completed under this section:
  - a. Developed dynamic reservoir models and completed a detailed history matching analysis by following the top-down approach.
  - b. Quantified initial and current in-place hydrates and free-gas resource.
  - c. Mapped current reservoir conditions and proposed possible locations for drilling future infill wells.
  - d. Performed sensitivity studies by varying parameters, such as hydrate zone size, free gas zone size, hydrate saturation, and *numerical aquifer* strength and sizes.
  - e. Carried out forecasting (production modeling) runs to evaluate the performance of vertical and horizontal wells.
  - f. Proposed an optimal production plan (drilling option) for future reservoir development.

Chapter 2 of this thesis presents the background knowledge of gas hydrates, based on previously published work. The chapter point outs numerous challenges being faced by the hydrate research community. Chapter 3 shares the methodology followed in order to accomplish the individual tasks; it also gives a brief background and the objective of each task, and lists the data and assumptions wherever needed. Chapter 4 presents the results and discusses the findings from this study. The conclusions from this study are summarized in Chapter 5, which also suggests the future scope of work.

## 2. LITERATURE REVIEW

### 2.1 Gas Hydrates

Gas hydrates (also called clathrates) are crystalline compounds which occur when water forms a cage like structure (termed *host*) around smaller gas (referred to as *guest*) molecules. The word “clathrate” is derived from the Latin word “clathratus,” meaning to encage. Hydrate formation is a possibility at any place where water exists in the vicinity of gas molecules, both naturally and artificially, at near freezing temperatures and elevated pressures. Gases such as methane, ethane, propane, iso- and n-butane, nitrogen, carbon dioxide, and hydrogen sulfide form hydrates in the presence of water at temperature and pressure conditions different for each gas molecule. The hydrate formation reaction can be described by the general equation (Moridis et al., 2008a).



where  $g$  represents the gas and  $n_H$  is the hydration number.

Of particular interest are the methane (or natural gas) hydrates composed mainly of methane (or natural gas molecules including methane, ethane, propane, butane, and carbon dioxide) due to their potential energy value. It has been estimated that a single volumetric unit of hydrates can store approximately 184 volumetric units of natural gas at standard pressure and temperature (Yousif and Sloan, 1991). Figure 2.1 shows an example of a burning methane hydrate sample.

#### 2.1.1 Historical Background

Historically, the research on natural gas hydrates began when it was first reported by Sir Humphrey Davy in the year 1810 (Sloan and Koh, 2008). Since then, the research efforts on natural gas hydrates have seen several periods of growth. These periods have been broadly classified into three major categories (Sloan and Koh, 2008).

- i. The period from the year 1810 till today has seen researchers performing experiments and recording hydrate formation and the dissociation phenomenon at macroscopic (Kamath and Holder, 1987; Ullerich et al., 1987) and pore levels, (Ioannis and Lichtner, 2004; Seol et al., 2006).
- ii. Man-made gas hydrates hindered natural gas flow through pipelines in cold regions; thus the second phase of research (from 1934 until present) was directed toward investigating such a phenomenon (Hammerschmidt, 1934; Sloan et al., 1976; Song and Kobayashi, 1982).
- iii. Naturally occurring hydrates were first reported by Makagon and his team in the year 1965. Since then extensive research has been performed to detect, quantify, and develop in-situ hydrates as a potential source of energy (Collett et al., 1988; Kvenvolden, 1993; Collett, 2002; Moridis et al., 2008a).



Figure 2.1: Burning Sample of Methane Hydrate (Courtesy National Research Council, Canada, Website: [www.nrc-cnrc.gc.ca](http://www.nrc-cnrc.gc.ca))

### 2.1.2 Structure

The crystal structure of gas hydrates varies depending on the type of *guest* molecule trapped and the thermodynamic conditions existing during hydrate formation. Broadly, gas hydrate belongs to three crystal structures: cubic structure I (*sI*), cubic structure II (*sII*), or hexagonal structure H (*sH*).

Structure I and II are known to exist commonly in nature. Structure I is formed with *guest* molecules having diameters between 4.2 and 6 Å, such as methane, ethane, carbon dioxide, and hydrogen sulfide. A unit cell (the smallest repeatable element) of a structure I hydrate consists of 46 water molecules surrounding 2 small cavities and 6 medium-sized cavities. Nitrogen, hydrogen, and other smaller molecules (diameter < 4.2 Å) form structure II as single *guest*. Larger single *guest* molecules (6 Å < diameter < 7 Å), such as propane or iso-butane, also form structure II. The unit cell of structure II hydrates consists of 136 water molecules creating 16 small cavities and 8 large cavities (Sloan and Koh, 2008).

Molecules, such as iso-pentane or n-hexane, with diameters higher than 7 Å and less than 9 Å, can form structure H when accompanied by smaller molecules such as methane, hydrogen sulfide, or nitrogen. A unit cell of this new “double hydrate” consists of 34 water molecules producing 3 small cavities, 12 slightly larger cavities, and 1 relatively huge cavity. It is this large cavity that allows structure H hydrates to incorporate large molecules (such as butane and larger hydrocarbons), given the presence of other smaller gases to fill and support the remaining smaller cavities (Sloan and Koh, 2008).

Figure 2.2 describes the cavity types and the type of *guest* molecules for each hydrate structure. Hydrogen bonding between water molecules forms the basic building block for structure I and II called  $5^{12}$  because there are 12 faces of the pentagonally bonded water molecules in that cavity. The  $5^{12}$  building blocks are joined to others that are  $5^{12}$  either through the vertices (structure I) or through the  $5^{12}$  faces (structure II).  $5^{12}$  cavities are filled with other cavities that relieve the strain by incorporating 2 hexagonal faces in the  $5^{12}6^2$  cavity of structure I, and 4 hexagonal faces in the  $5^{12}6^4$  of structure II (Sloan, 2003). An irregular dodecahedron cavity ( $4^35^66^3$ ) represents the building block of



structure H. It has 3 square faces and 6 pentagonal faces, in addition to 3 hexagonal faces (Sloan and Koh, 2008).

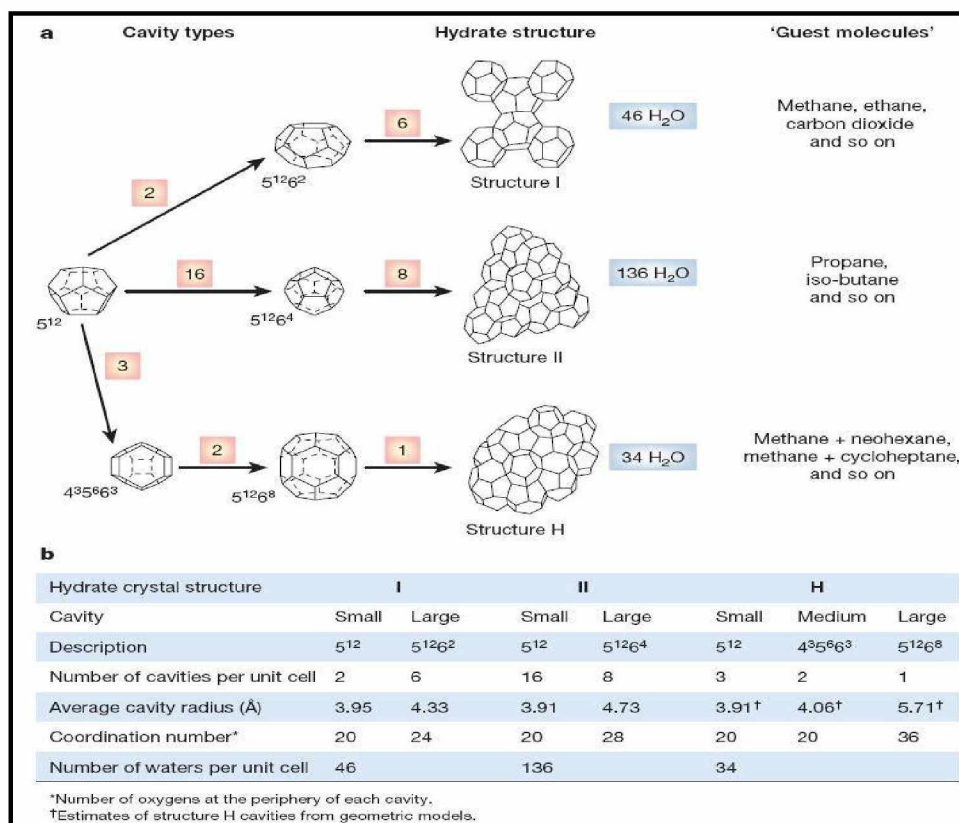


Figure 2.2: Structures of Hydrate Crystal (Modified from Sloan, 2003)

Predicting hydrate structure for gas mixtures requires extensive knowledge of hydrate thermodynamics. Sloan and his team at the Center for Hydrate Research, Colorado School of Mines, developed a software program, CSM-HYD, to predict stable hydrate structures that would form, given gas composition and water salinity data (Sloan, 1998). Information about hydrate structure assists in choosing valid hydrate properties. These properties are desired for studying the impact of gas hydrates on flow assurance through gas pipelines, energy recovery from in-situ hydrates, and the effect of dissociating hydrates on climate (Sloan, 2003).

Sloan (2003) and Sloan and Koh (2008) have reviewed and updated their work, discussing several technical papers which detail types of hydrate structure and the physics behind their stability. This literature provides information about the effect of hydrate crystal structure on physical and thermal properties.

### *2.1.3 Properties*

Due to the nonstoichiometric nature of hydrates, the mole fraction of water is invariably higher than 85%. Such high water content can be used as a basis of defining hydrate properties similar to ice. Sloan and Koh (2008) reviewed previous work done in this direction and concluded that the hydrate properties are different than ice due to the difference in water and hydrate structure. Comparing hydrate structure I and II, they concluded that since the  $5^{12}$  cavity is common to each hydrate structure, the differences in their properties are not appreciable.

## **2.2 Natural Gas Hydrates: An Untapped Resource**

### *2.2.1 Naturally Occurring Methane Hydrates*

Methane hydrate can form in rocks or sediments of any type, given suitable pressures, temperatures, and supplies of water and methane. Natural methane hydrate has been most commonly observed occurring as disseminated grains, nodules that grow and displace surrounding sediments, massive layers of pure hydrate up to 4 meters thick, veins filling small fractures, and thin layers along bedding planes (Figure 2.3, Dvorkin et al., 2000).

Hydrate formation in sediment pores depends on factors such as wettability of the sediment, phase saturation of free water, free gas in the pores, pore size, etc. Dvorkin et al. (2000) described the growth habit of hydrates in sediments as follows:

- i. Hydrate floating in the pore fluid
- ii. Hydrate as a load-bearing part of the solid phase
- iii. Hydrate cementing grain contacts
- iv. Hydrate acting as cement, forming only at grain contacts

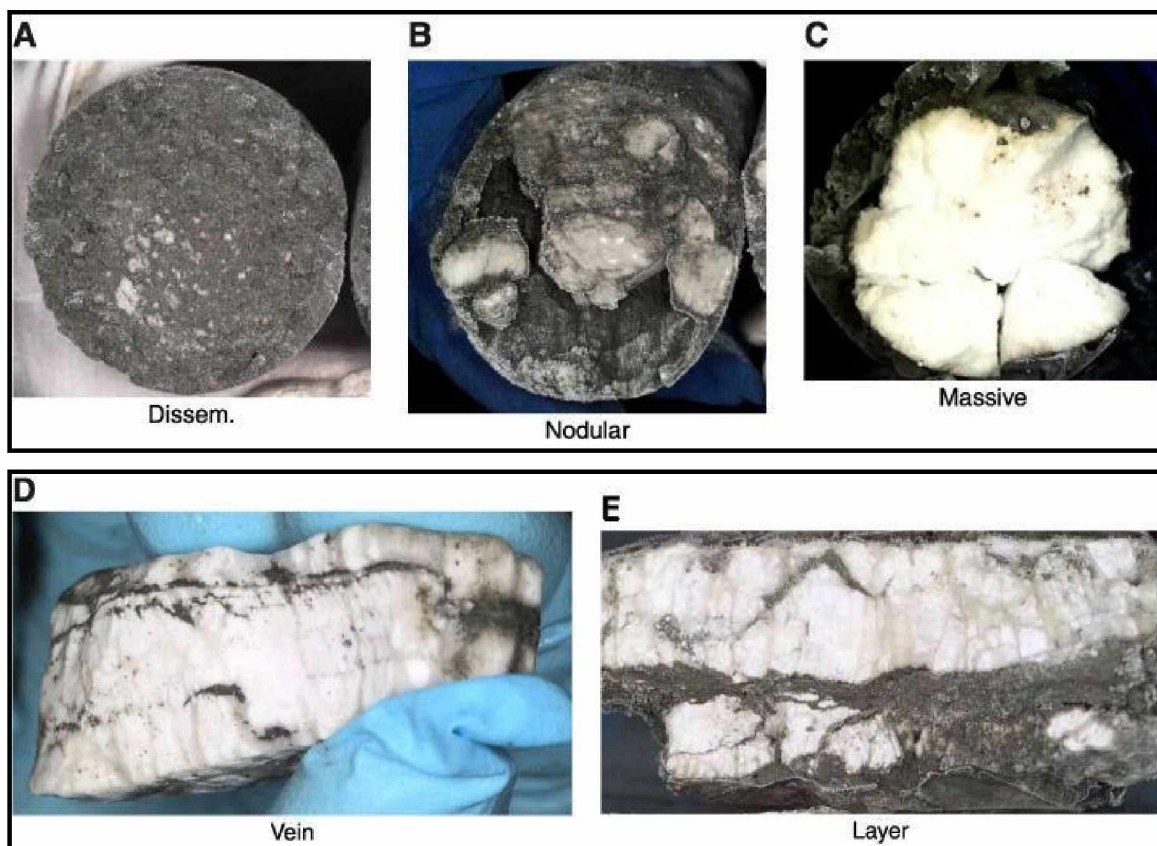


Figure 2.3: Types of Natural Gas Hydrate Accumulations (Modified from Open-File Report, 2007, Ocean Development Program <http://www-odp.tamu.edu/publications/>)

Based on geography, natural gas hydrates are commonly described as occurring in two distinct classes: “marine” hydrates and “permafrost” hydrates. Figure 2.4 shows the two geological environments where natural gas hydrate deposits have been found. The pressure and temperature conditions in permafrost and in a deep oceanic environment support hydrate formation. However, the amount and distribution of hydrates within these locations are mostly controlled by local geologic environments.

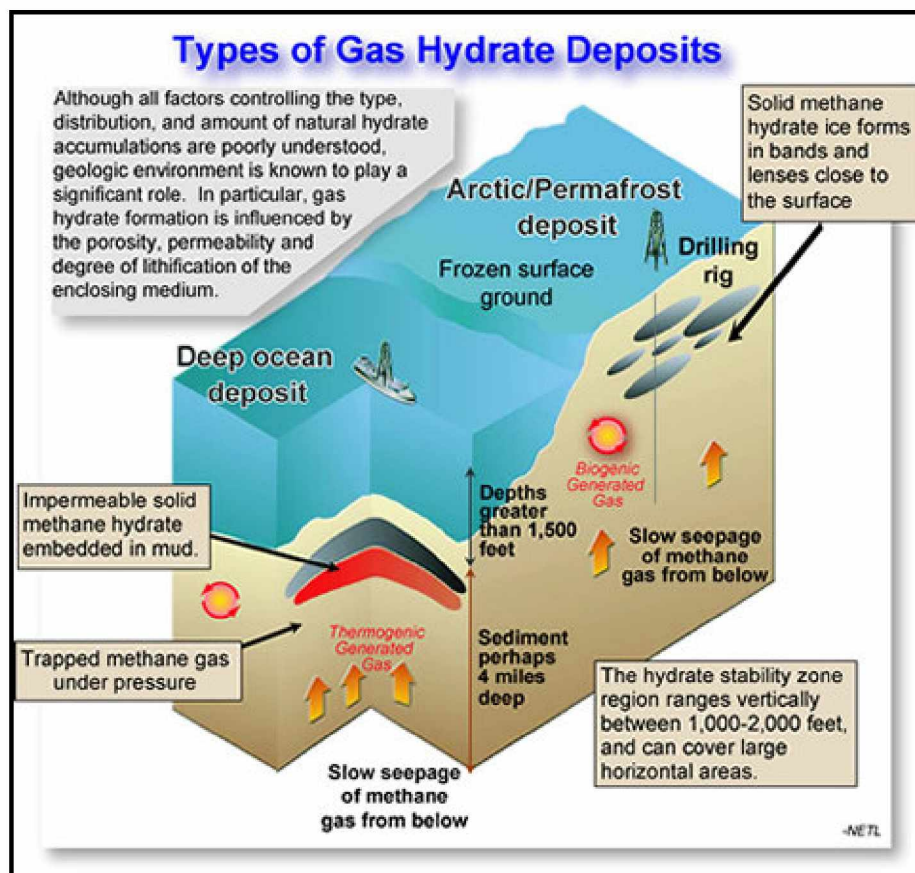


Figure 2.4: Types of Gas Hydrate Deposits (NETL Website: [www.netl.doe.gov](http://www.netl.doe.gov))

### 2.2.2 Geographic Occurrence

Naturally occurring gas hydrates have been reported in more than 89 locations worldwide (Kvenvolden and Rogers, 2005). Figure 2.5 shows the worldwide distribution of hydrates in both oceanic and permafrost environments. The amount of hydrates in the ocean exceeds that in the permafrost locations by two orders of magnitude (Sloan and Koh, 2008). Gas hydrates have been found within and beneath permafrost on the ANS, in the Canadian Arctic, and in northern Siberia. Oceanic hydrates have also been reported in the Blake Ridge, along the Cascadia continental margin off the Pacific coast of Canada, in the Nankai trough off the eastern coast of Japan, and in the offshore basins of India.

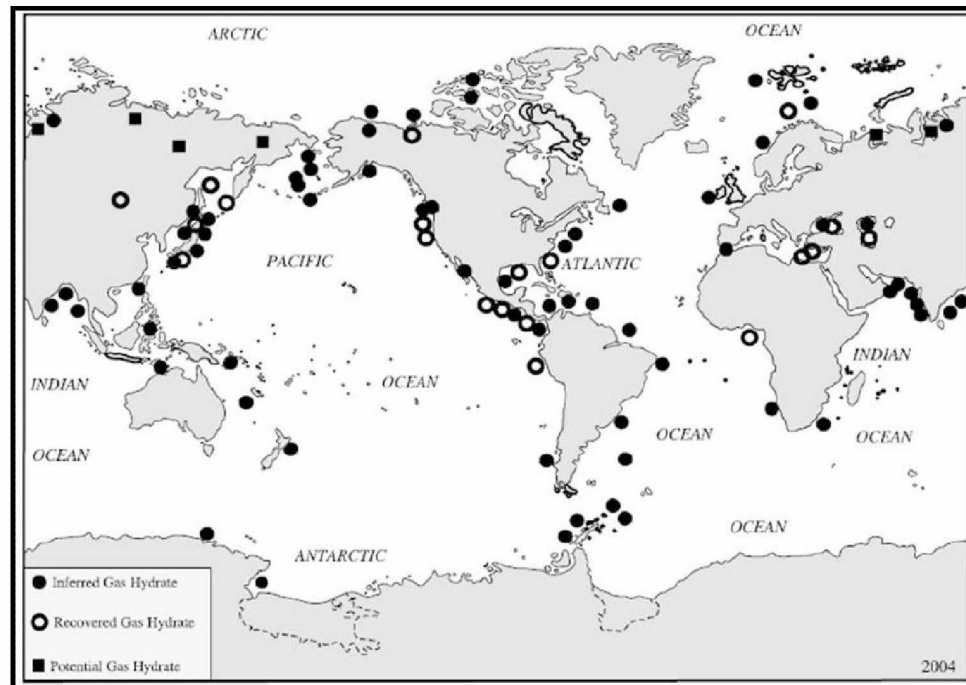


Figure 2.5: Worldwide Hydrate Accumulations (Kvenvolden and Rogers, 2005)

The hydrate locations were included in Figure 2.5 if hydrate samples were recovered from these locations (23 locations), or if hydrate accumulations were inferred from well logs, geophysical signatures of the bottom simulating reflectors (84 locations) or interpreted from geologic settings (6 locations). Some of the hydrate deposits were inferred by using combinations of these methods (Sloan and Koh, 2008).

### *2.2.3 Methods of Quantifying Hydrate Resource*

The extent of naturally occurring methane hydrates can be quantified by indirect (remote) and direct methods. The indirect methods can be broadly classified as follows (Sloan and Koh, 2008):

- i. Use of thermodynamic pressure-temperature stability data combined with the geothermal gradient, determining maximum hydrate stability depths.
- ii. Seismic methods such as Bottom Simulating Reflectors (BSR), providing approximate assessment of the area and maximum depth of stable hydrate formation.

- iii. Methane solubility to determine the top and bottom of the hydrate stability zone within pressure-temperature region as in case i.

Direct methods of estimating the hydrate resource provide improved assessment of hydrate gas amounts and assist in updating estimation methodologies applied under the indirect method. Drilling and coring methods are the direct and accurate methods of quantifying the resource; however, these methods are expensive and have associated risks.

- i. Logging tools, such as caliper, gamma ray, density, resistivity, neutron porosity, and Nuclear Magnetic Resonance (NMR) spectroscopy, determine hydrate depth and concentrations.
- ii. Core analysis tools, including Infrared (IR) temperature sensor, gas evolution from cores, pore-water chlorinity decrease, and Computed Tomography (CT) of cores, provide the extent and concentration of hydrates within the reservoir.

#### *2.2.4 Gas Hydrate Stability Zones in Permafrost Location*

The simplest and quickest method of identifying the zone of possible gas hydrate occurrence is to develop and examine the gas hydrate stability zone. The essential condition for gas hydrate stability at a given depth is that the actual earth temperature at that depth should be lower than the equilibrium temperature of hydrates corresponding to existing reservoir fluid (gas) composition and pressure conditions. The thickness of a potential hydrate zone can be an important variable in a drilling operation where drilling through hydrates needs additional precaution. Thickness also can be of significance in determining regions where hydrate occurrences might be sufficiently thick to justify gas recovery. The existence of a gas hydrate stability condition, however, does not ensure that hydrates exist in that region; but if gas and water coexist within the hydrate stability zone, then they must exist in gas hydrate form. Shallow hydrate reservoirs of the ANS are good examples of hydrate accumulations associated with permafrost regions. Hydrate stability studies must be supported by performing physical interpretation of subsurface geology. This can be achieved by conducting core and well log evaluations



and seismic surveys in order to confirm the presence of hydrates. Figure 2.6 shows the hydrate stability zone and phase envelope of a classic permafrost location. Factors affecting methane hydrate stability in arctic settings include (Collett et al., 1988):

- i. Mean annual soil surface temperatures
- ii. Geothermal gradients within and below the base of permafrost
- iii. Gas composition
- iv. Formation water salinity
- v. Reservoir rock-grain sizes
- vi. Subsurface pressures

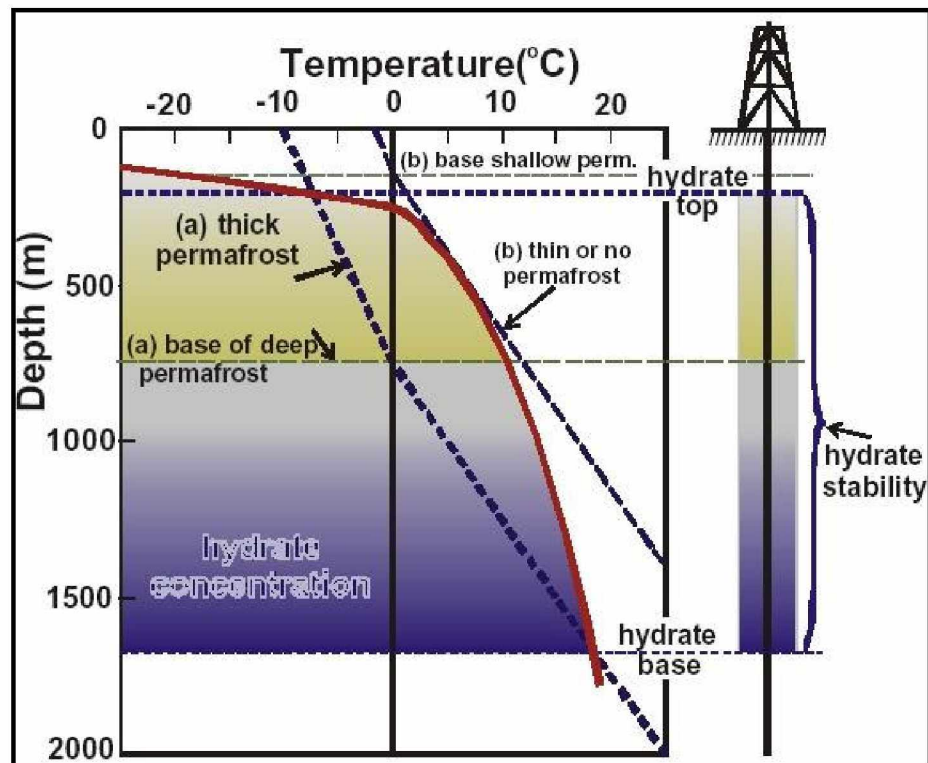


Figure 2.6: Gas Hydrate Stability Zone in Permafrost (Geologic Survey of Canada, [www.nrcan.gc.ca](http://www.nrcan.gc.ca))

Two critical factors that affect hydrate stability are gas chemistry and temperature gradient. Other factors are difficult to quantify and have little impact on hydrate stability (Collett et al., 1988).

Hydrate phase behavior study involves construction of a pressure-temperature equilibrium curve, primarily based on gas composition and water salinity data. ANS gas composition mainly contains a high percentage of methane (Collett et al., 1988), but the presence of heavier components increases the hydrate stability zone (Katz, 1945). On the other hand, higher water salinity tends to reduce the stability range (Sloan and Koh, 2008). Thus it is important to collect accurate gas compositions and water salinity data for hydrate stability calculations. Experimental modules (Westervelt, 2004; Sloan and Koh, 2008), empirical equations (Kamath and Holder, 1987; Moridis, 2003), and computer based software (Sloan, 1998) have been developed to predict the three-phase equilibrium curve. These models will be explained in detail in Chapter 3.

Geothermal gradient has a significant impact on a hydrate stability zone (Collett et al., 1988). Permafrost regions are associated with two types of geothermal gradient: one within the permafrost region and the other below the base of permafrost. Values in the ice-bearing permafrost sequence range from approximately 1.5 °C/100 m in the Prudhoe Bay area to approximately 4.5 °C/100 m in the east-central region of the ANS. Geothermal gradients below the ice-bearing permafrost sequence range from approximately 1.6 °C/100 m to approximately 5.2 °C/100 m (Collett, 1993). Lachenbruch et al. (1988) studied temperature profiles in ten wells located in the Kuparuk, Milne Point, and Prudhoe Bay oil fields. They reported significant variation in geothermal gradients within these reservoirs. Hence, taking an average geothermal gradient for the entire ANS will cause significant error in estimating hydrate potential of the region (Collett et al., 1988). Collett et al. (1988) calculated hydrate stability on a well-to-well basis before mapping hydrate stability for the entire field. Later on, based on three-dimensional (3D) seismic surveys and downhole well log data, Collett (2002) indicated a significant presence of in-situ hydrates.

### *2.2.5 Estimates of Hydrate-Associated Gas*

The volume of natural gas trapped in gas hydrates is enormous, but estimates of gas hydrate resources are highly speculative. Uncertainties in determining the extent of natural gas hydrate resource, especially in offshore basins, have presented the biggest



challenge in quantifying the worldwide estimate of hydrate-associated gas. Sloan and Koh (2008) have discussed and listed global estimates made by researchers in the past 25 years. These estimate ranges from a maximum value of  $108 \times 10^{18}$  cubic feet ( $\text{ft}^3$ ) of in-place natural gas to a minimum of  $0.007 \times 10^{18}$   $\text{ft}^3$  at standard conditions (STD). All estimates were made approximately the same way: i.e., the limited amount of good quality geological data was extrapolated on a worldwide scale. Interestingly, these estimates have shown a gradual decline in the past 25 years (Sloan and Koh, 2008).

In 1995, the USGS conducted an assessment of the in-place natural gas hydrate resources of the U.S. (Kleinberg, 2007). The study suggested that the amount of gas in the nation's hydrate accumulations could be more than 320,192 tcf (Figure 2.7). The USGS assessment also estimated that the permafrost-associated gas hydrates on the ANS may contain as much as 590 tcf of in-place gas (Collett, 2004). Figure 2.8 shows the areas of the ANS where subsurface conditions are conducive to the occurrence of gas hydrates. Figure 2.8 forms the basis of Collett's (2004) estimates.

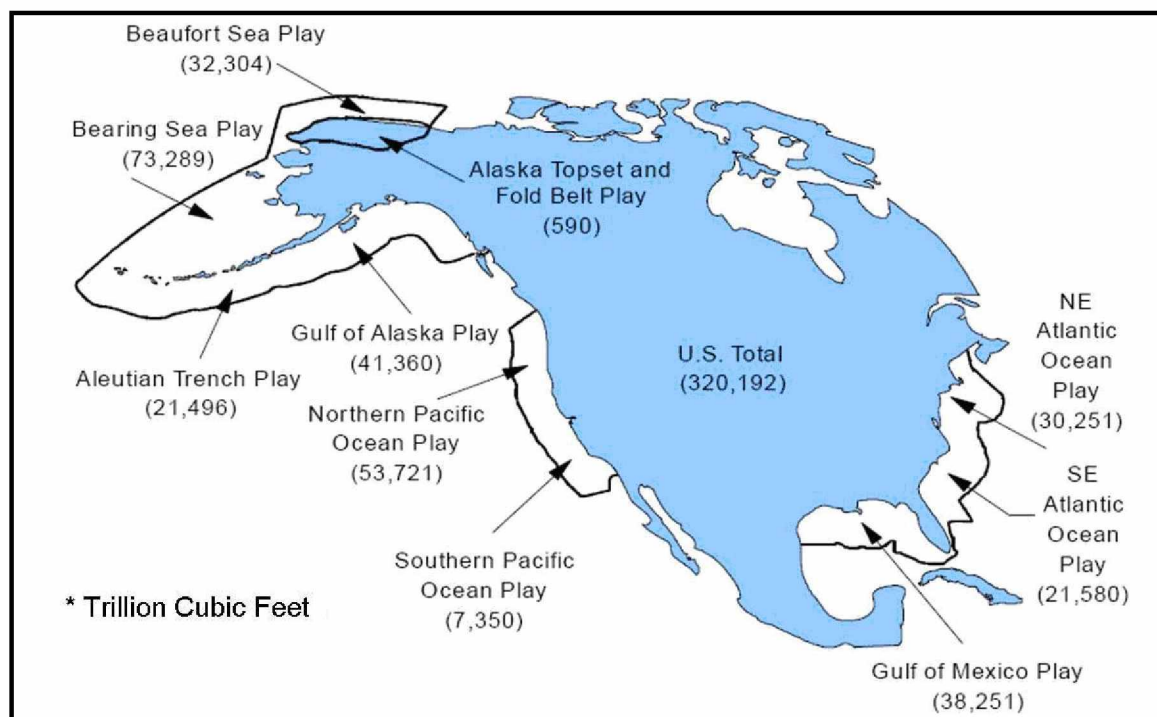


Figure 2.7: Hydrate Plays and Province in the U.S. (Kleinberg, 2007)

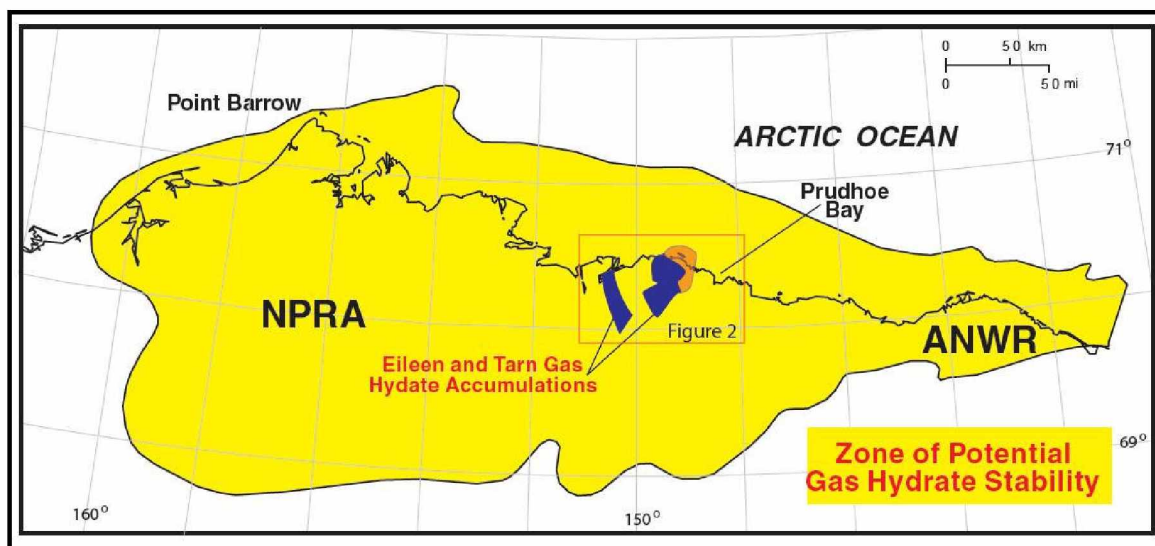


Figure 2.8: Extent of Stable Hydrate Zone in ANS (Collett, 2004)

### 2.3 Alaska Gas Hydrate Resource Potential

The occurrence of natural gas hydrates on the ANS was confirmed in 1972 with data from the ARCO/Exxon NWE No.-2 Well located in the northwest part of the PBU. Studies of pressurized core samples, and downhole logs, and the results of production testing have confirmed the occurrence of three gas hydrate-bearing stratigraphic units in the ARCO/Exxon NWE No.-2 Well (Collett, 1993). Gas hydrates were also inferred to occur in an additional 50 exploratory and production wells in northern Alaska, based on downhole log responses calibrated to the known gas hydrate occurrences in the ARCO/Exxon NEW No.-2 Well (Collett, 2002).

Most of the log-inferred gas hydrates occur in six laterally continuous sandstone and conglomerate units; all are geographically restricted to the area overlying the eastern part of the Kuparuk River field and the western part of the Prudhoe Bay field (Collett et al., 1988). Each of the six gas hydrate-bearing sedimentary units have been assigned a reference letter, units A to F, with unit A being the stratigraphically deepest (Figure 2.9). 3D seismic surveys and downhole logs from wells in the western part of the Prudhoe Bay field indicate the presence of several large free gas accumulations trapped stratigraphically downdip below four of the log-inferred gas hydrate units (Collett, 2002).

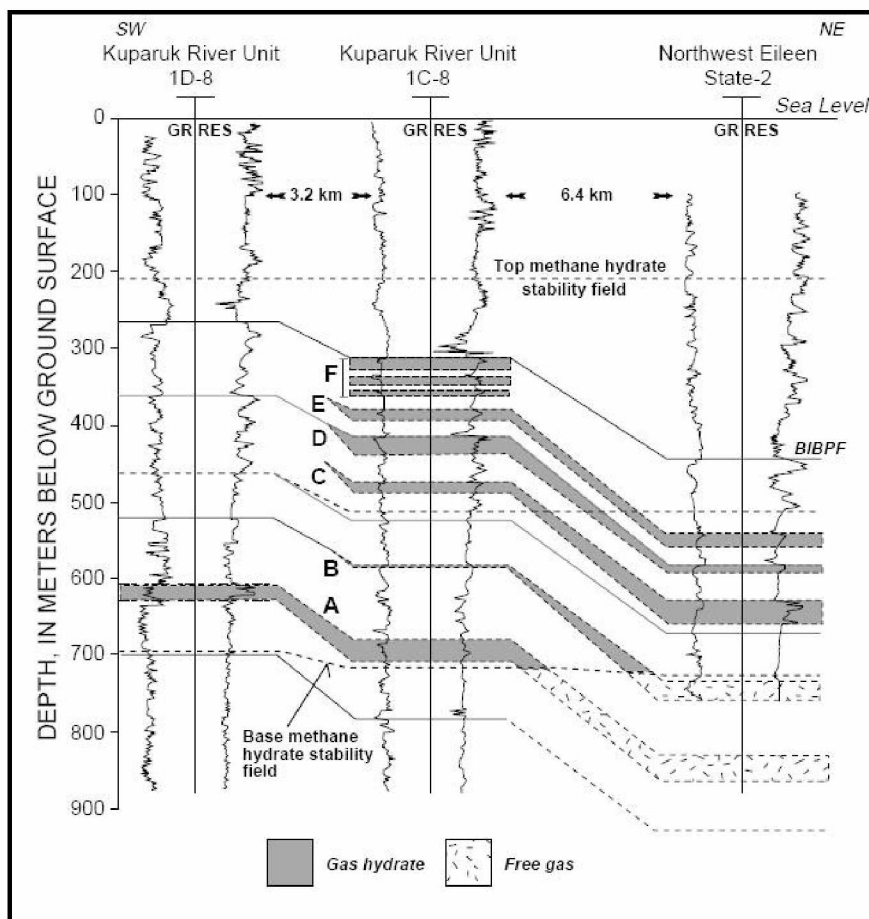


Figure 2.9: Cross Section Showing Lateral and Vertical Extent of Gas Hydrates and Free Gas Occurrences in Prudhoe Bay-Kuparuk River area of ANS (Modified from Collett, 2002)

Collett et al. (1988) performed detailed geological studies to understand the extent of the hydrate stability zone within the ANS. They collected local geothermal gradient, static pressure gradient, well logs and water salinity data, covering the entire ANS including the Barrow region. They studied the relative impact of each parameter on hydrate stability and also estimated the depth and thickness of hydrate stability. The report was later updated by Collett (1993) and Collett (2002). Collett et al. (1988) reported the well log evaluation procedures, reservoir properties, and hydrate distribution maps for the ANS. Further, Collett et al. (1988) explained the theoretical and ANS geologic models; explaining gas migration, trapping mechanisms, and hydrate formation events that may have taken place in geologic times. The report briefly discusses the source of methane

found in in-situ hydrates and related quantification methods. Interestingly, the study showed that the trapped methane hydrates contained both thermogenic and biogenic gases. Collett has performed substantial work in quantifying the hydrate resource potential of Alaska based on geological and geophysical data. He has updated his findings in the form of published papers and reports, some of which are Collett (1993), Collett (2002), and Collett (2004).

Recently concluded drilling, coring, and production testing operations on the hydrate-bound reservoir of MPU (Figure 2.10) have shown thick hydrate accumulations (Hunter et al., 2007), thus supporting the previous geologic estimations done by Collett and his team (Collett et al., 1988; Collett, 1993; Collett, 2002). Short-term production testing results showed high hydrate saturations and an absence of free gas availability within the reservoir (Hunter et al., 2007). The operation has verified a vast, untapped hydrate resource of the ANS that needs to be developed for future production. Figure 2.10 shows the distribution of gas hydrate accumulations over the Prudhoe Bay, Kuparuk River, and Milne Point fields of the ANS (Collett, 2004).

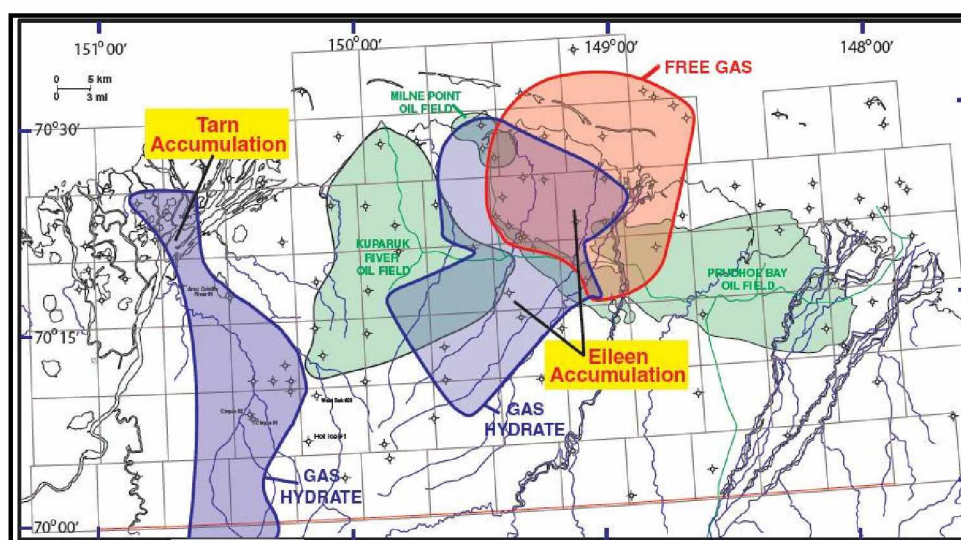


Figure 2.10: Map Showing Distribution of Hydrate Accumulations in Prudhoe Bay, Kuparuk River, and Milne Point Fields of the ANS (Modified from Collett, 2004)

## 2.4 Gas Hydrate Production Technology

The last decade has seen an increase in field-based experiments (Dallimore and Collett, 2005; Hunter et al., 2007) that were designed to investigate reservoir performance and well integrity issues while producing gas from hydrate-bound sediments. The majority of these field-based tests were performed in permafrost locations due to lower cost of operation, better geologic information and easier access. Unfortunately, these experiments were still very expensive, time-consuming, risky, and held a wide range of uncertainties. None of the field projects performed to date could verify the behavior of hydrate reservoirs. Nevertheless, scientists are still searching for suitable locations where they could perform long-term production tests. Potential production targets must have the following attributes (Moridis et al., 2008a):

- i. Presence of high hydrate saturation (inferred by performing coring and well logging or by geophysical methods)
- ii. Occurrence of hydrate within good reservoir quality sand in order to support well based production methods
- iii. Accesibility of field to existing infrastructure
- iv. Easy aces of produced gas to market through a pipeline system

Gas hydrate production schemes have been classified under three categories (Figure 2.11):

- i. Thermal Injection
- ii. Depressurization
- iii. Inhibitor Injection

Gas production from hydrates involves dissociation of in-situ hydrates. Upon dissociation, each molecule of methane hydrate produces approximately 1 molecule of methane and 6 molecules of formation water. Hence, the goal of each scheme is to destabilize hydrates and produce gas at optimum rates such that the gas production from hydrates should neither cause uncontrolled dissociation nor re-association of produced gas and water.



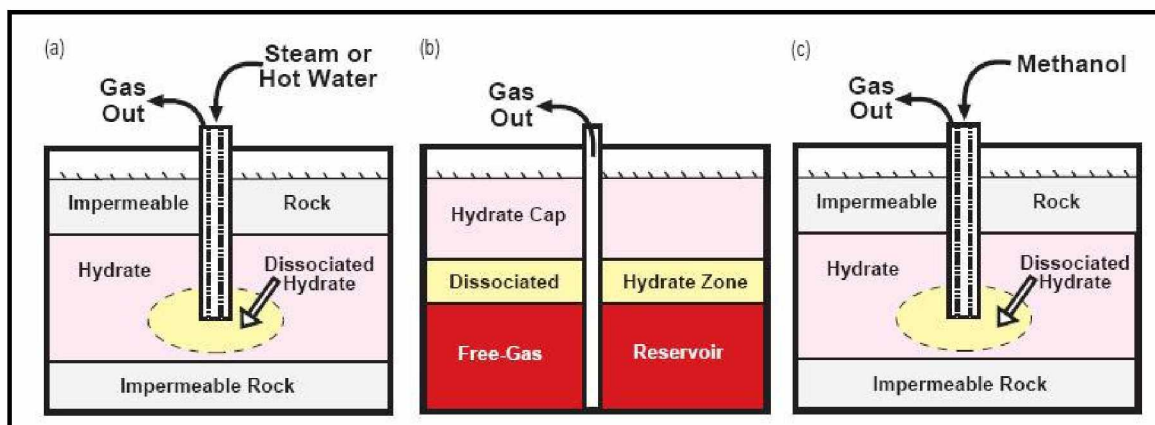


Figure 2.11: Gas Hydrate Production Methods: a) Thermal Injection, b) Depressurization, c) Inhibitor Injection (Modified from Collett, 2002)

The features of these mechanisms are as follows (Darvish, 2004):

- i. To bring pressure and temperature conditions of the reservoir outside the hydrate stability zone.
- ii. To sustain the energy required (naturally or artificially) for the hydrate dissociation (endothermic reaction).
- iii. To provide a means of transferring the products of decomposition to the production wells.

#### 2.4.1 Thermal Injection

In the thermal injection method, a constant heat source in the form of steam or hot water is injected into the reservoir causing an increase in reservoir temperature, thereby destabilizing in-situ hydrates (Figure 2.11). The introduction of thermal energy may also be achieved by downhole processes such as in-situ combustion, or electric, or electromagnetic heating.

The thermal injection method was applied on a field-scale during Mallik 2002 tests. Short-term depressurization tests were followed by a thermal stimulation run performed by circulating warm water through a highly concentrated hydrate zone. The thermal dissociation technique resulted in continuous gas production at variable rates, reaching a maximum rate of 1500 m<sup>3</sup>/day (Dallimore and Collett, 2005). Swinkles and Drenth

(2000) modeled the behavior of a hydrate-capped gas reservoir using a 3D thermal reservoir simulator. They simulated several gas production scenarios, and reported good recovery using the thermal injection technique. They were concerned, however, about the role of excessive water production, and suggested the need for setting up water-handling facilities.

The thermal injection technique has a major disadvantage: the variable cost of operation is substantially higher than depressurization method. The thermal efficiency of the system needs to be monitored on a regular basis as the chances of heat losses to the surrounding rocks are very high. This technique may not be a good option for a hydrate-bound system in permafrost locations. Long-term thermal injection could lead to heat transfer to the permafrost zone, making it unstable thereby reducing sediment strength and integrity. Wherever desired, such a gas recovery scheme will call for careful economic evaluation and detailed engineering.

#### *2.4.2 Depressurization*

In the depressurization technique, the fluid pressure in contact with hydrates is lowered by production, thus bringing hydrates out of the stability region and causing them to dissociate (Figure 2.12). Heat required for hydrate decomposition is supplied by surrounding rocks. The quality, type, and thermal properties of overburden and underburden rocks could play the role of rate-determining step (Selim and Sloan, 1990; Hong and Darvish, 2005). Hence, reservoirs having a larger surface area for heat transfers and hydrate decomposition would be an attractive target for gas production by depressurization. Hydrate production from depressurization is governed by three important mechanisms (Darvish, 2004), these are fluid flow driven, kinetics driven and heat transfer driven mechanisms (Figure 2.12):

- i. *Fluid Flow-Driven Mechanism* - Gas production reduces reservoir pressure, causing a pressure difference between the reservoir fluid ( $p_o$ ) and fluid/hydrate interface ( $p_g$ ).

- ii. *Kinetics-Driven Mechanism* - At constant temperature ( $T_s$ ), the hydrate dissociation rate is proportional to the difference in hydrate equilibrium pressure ( $p_{se}$ ) and fluid pressure ( $p_g$ ) at the fluid/hydrate interface (Kim et al., 1987).
- iii. *Heat Transfer-Driven Mechanism* - A cooling effect due to hydrate decomposition (endothermic process) causes a temperature difference between the initial hydrate temperature ( $T_i$ ) and the hydrate dissociation temperature ( $T_s$ ). Heat then flows from the surrounding rocks and fluids to the cooler zone. The rate of heat transfer is governed by the temperature gradient.

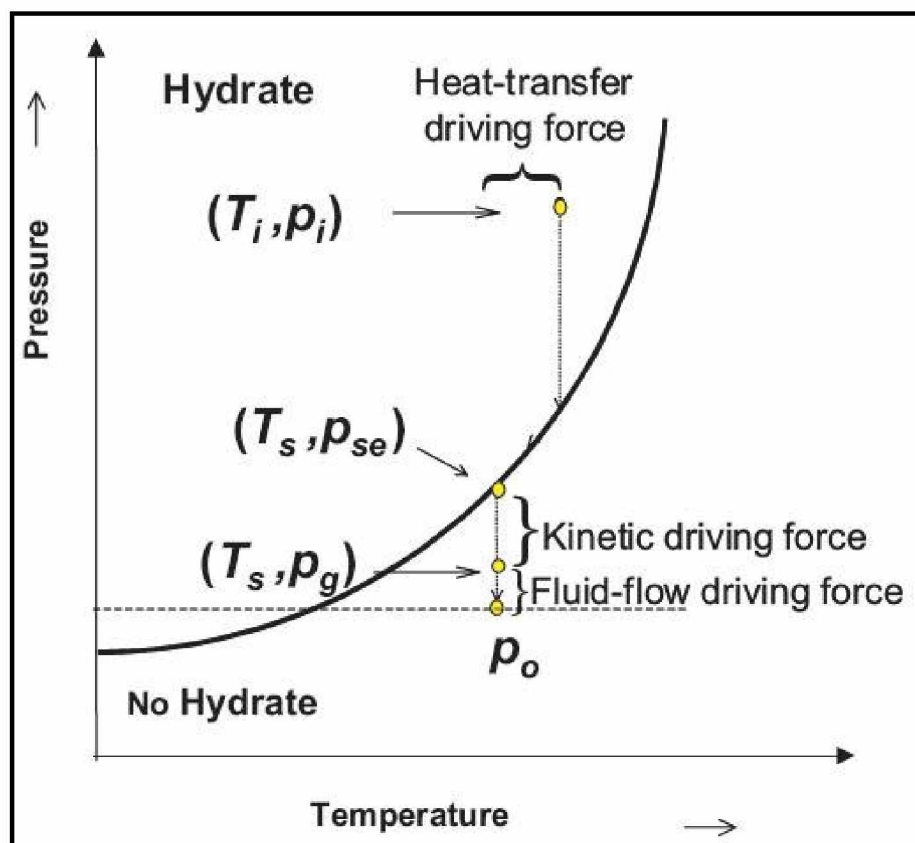


Figure 2.12: Pressure-Temperature Equilibrium Curve Showing Hydrate Production Mechanism for Depressurization Technique (Darvish, 2004)



Studies have proved that the presence of a free gas zone right beneath the hydrate zone is the best-case scenario for gas production from hydrates (Hong, 2003; Darvish, 2004). Free gas production reduces pressure in the hydrate zone at a slower rate, thereby causing controlled dissociation of in-situ hydrates. The dissociating hydrates recharge the reservoir with additional free gas. Similar observations were made in the Messoyakha gas field, where depressurization was considered to be one of the drive mechanisms (Makagon, 1981). Scientists believe that depressurization is the most economical of the three methods (Collett and Kuskra, 1998). However, there are apprehensions that depressurization could lead to ice formation that may affect long-term production. Scientists have argued though, that by designing and controlling production pressures of the reservoir such a phenomenon can be avoided (Darvish, 2004). As with other mechanisms, gas production by depressurization will generate large volumes of mobile water that will be produced along with gas. In case of the Mallik field, where the hydrate layer is said to be associated with a strong aquifer, the magnitude of water production will be even higher. In order to have long-term production from such a reservoir, a water-handling facility will have to be installed (Darvish, 2004). Interestingly, production modeling studies performed by Howe (2004) on MPU type reservoir, where the entire sediment is saturated with hydrates, reveals inherent challenges associated with gas production by depressurization alone.

#### *2.4.3 Inhibitor Injection*

Inhibitors such as methanol and calcium chloride can decompose stable hydrates by shifting the pressure-temperature equilibrium curve (Figure 2.13). This method of gas production by inhibitor injection may not be practical at the field-level due to high cost of inhibitors and transportation of the chemicals to the remote site. However, smaller volumes of methanol and calcium chloride were injected in the Messoyakha field to open the flow path in the vicinity of the wellbore when unwanted plugging occurred due to hydrate formation (Makagon, 1981).

Even though the production mechanisms have been broadly classified, it should be noted that future hydrate production operations will perhaps employ a combination of these mechanisms. This will be done in order to control hydrate dissociation, minimize

ice or hydrate formation, stabilize the wellbore, and maintain long-term gas production through production wells.

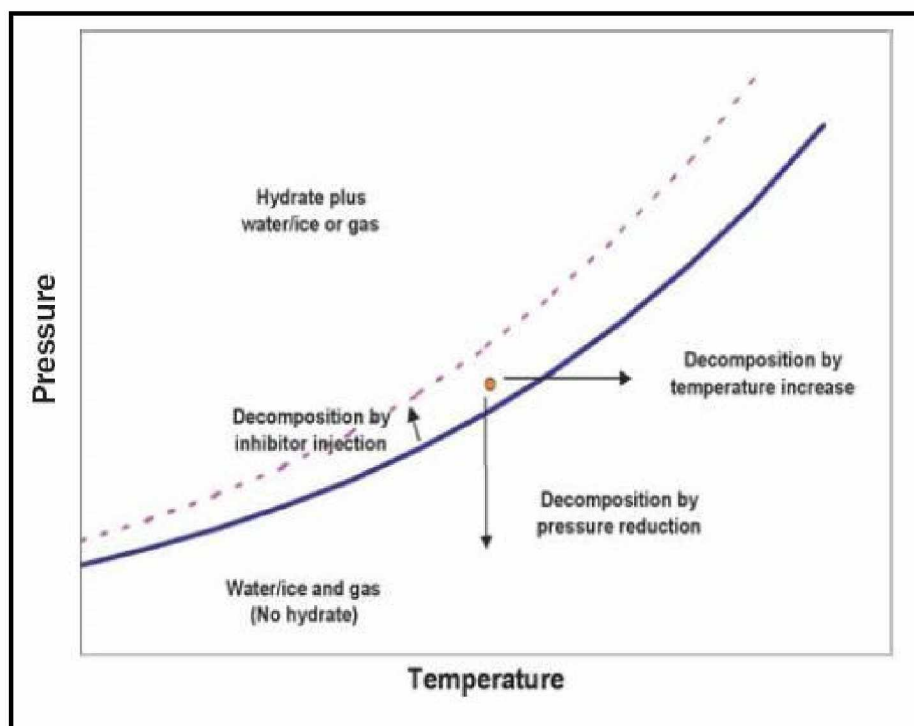


Figure 2.13: Water-Hydrate-Gas Three-Phase Equilibrium Curve and Methods of Hydrate Decomposition (Darvish, 2004)

## 2.5 Modeling Hydrate-Bearing Reservoirs

### 2.5.1 Classification of Gas Hydrate Deposits

Based on reported geologic occurrence to date, natural gas hydrate accumulations have been divided into three main classes, viz. Class 1, Class 2, and Class 3 (Moridis and Collett, 2004). Class 1 accumulations are composed of two layers: a hydrate zone, an underlying two phase fluid zone of free gas and liquid water (Figure 2.14). Class 1 deposits have been subclassified into two kinds: one in which hydrate and free gas exist in a hydrate zone called Class 1 *G* (water-poor system) accumulations and the other one in which hydrate and water exists in a hydrate layer also called Class 1 *W* (gas-poor system) deposits. This class of hydrate exists when the stable hydrate zone envelope

coincides with the bottom of the hydrate layer. These accumulations have been considered the most desirable distribution, as it is easier to destabilize and control hydrate dissociation by producing gas from the free gas layer (Hong, 2003; Darvish, 2004; Moridis et al., 2008a). Wells are completed in gas zone, similar to a conventional gas well. Wellbore stability due to hydrate dissociation may remain a critical issue. The Messoyakha fields in Siberia, Russia and the BGF, Alaska are good examples of Class 1 type hydrate accumulations.

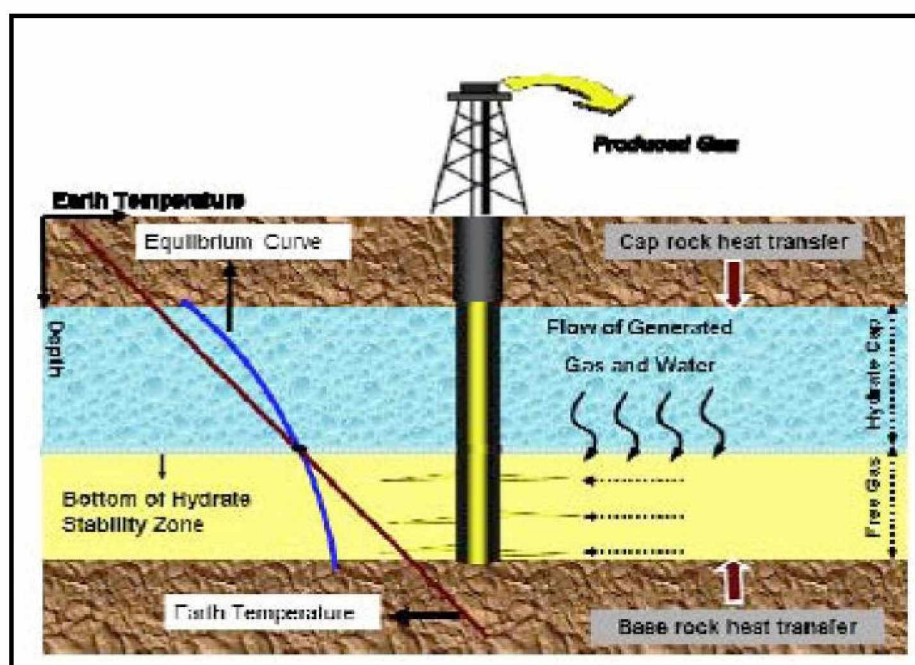


Figure 2.14: Class 1G (Water-Poor System) Accumulations (Moridis et al., 2008a)

The second class of hydrate deposits (Class 2) are comprised of two zones viz. a hydrate-bearing zone and an underlying aquifer (mobile water) zone (Figure 2.15). Mallik deposits are reported to fall under this class of hydrate accumulations (Dallimore and Collett, 2005). For producing gas at an economical rate from such accumulations, these reservoirs will require an initial water production phase followed by a warm water injection process or a combination of both the techniques in order to reduce hydrate zone pressure and increase the temperature (Moridis and Reagan, 2007).

Class 3 hydrate accumulations consist of only a single zone of hydrate layer. No supporting fluid zones lie beneath the hydrate zone. Lower reservoir temperatures and

the absence of a supporting fluid phase limit the gas production from hydrate dissociation. In reality, no single hydrate production mechanism would be able to maintain economic rates of gas production from dissociating hydrates.

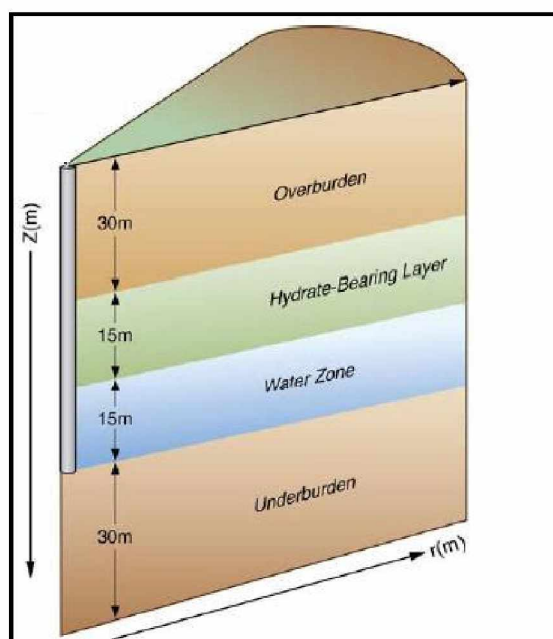


Figure 2.15: Class 2 Hydrate Deposit (Moridis and Reagen, 2007)

New Class 4 deposits are now being proposed, specific to hydrate accumulations found in marine sediments. Oceanic hydrate accumulations are characterized as dispersed hydrate deposits with low hydrate saturations (<10%) that lack confining geological strata (Moridis et al. 2008a).

### 2.5.2 Numerical Simulations

Significant efforts have been made towards modeling hydrate-bearing reservoirs in order to understand and compare their performances under different geologic conditions and production scenarios (Howe, 2004; Moridis et al., 2005; Moridis and Reagen, 2007; Ganti, 2007; Moridis et al., 2008b). Simulation studies provide the cheapest tool to quantify hydrate potential and study the impact of dissociation mechanism on a field-scale. Such studies will govern future reservoir development scenarios and help in optimizing suitable completion techniques and well production patterns. In recent years

several improvements in simulator capabilities and modeling features have taken place. The availability of new codes and revisions in existing codes have improved the analysis techniques and prediction methods (Moridis et al., 2008a). Even with limited knowledge about in-situ hydrates and the physics behind their dissociation, these simulators can determine the technical feasibility of a study area and also assist in quantifying the problem and delivering possible solutions while analyzing the parameter sensitivity.

There are several numerical simulators available that has the capability to simulate the behavior of a geologic hydrate reservoir system. The most commonly used simulators are (Moridis et al., 2008a):

- i. TOUGH+HYDRATE code developed by LBNL
- ii. CMG-STARS developed by Computer Modeling Group, Canada
- iii. The MH-21 code developed by Japan Oil Engineering Company
- iv. The STOMP-HYD code developed by the Pacific Northwest National Laboratory (PNNL)
- v. HYDRSIM simulator developed by the University of Calgary
- vi. University of Houston Hydrate (UH-HYD) code developed by the University of Houston

A code comparison study was recently initiated by the USDOE (USDOE/NETL, 2007) in order to compare and validate the performance of above listed codes. The study showed that all codes are capable of simulating the basic hydrate dissociation mechanism within the porous media. However, in the absence of reliable field data, which is the best comparison tool, the task of code validation remained incomplete (Moridis et al., 2008a).

### *2.5.3 Data Requirements for Gas Hydrate Reservoir Simulation*

Moridis et al. (2008a) have divided the data needs for simulation studies broadly into three major groups. Table 2.1 summarizes the data requirements of individual group as follows:

- i. Data requirements common to all reservoir simulation studies
- ii. Data need related to the presence of hydrates within porous media

- iii. Properties required to initialize gas hydrates, develop phase diagram, and model hydrate formation-dissociation mechanisms

Table 2.1: Summary of Simulator Data Requirements for Performing Hydrate Reservoir Simulation Studies (Moridis et al., 2008a)

<b>Category i. Data common to all reservoir simulation studies</b>
a. Geologic data required to develop static reservoir models
b. Distribution of thermal and hydraulic properties
c. Rock (porous media) properties
d. Gas and aqueous phase properties
e. Numerical computation options
<b>Category ii. Data related to hydrate presence within porous media</b>
a. Effect of hydrates on thermal properties.
b. Wettability related properties
c. Impact of solid phase (hydrates or ice) on permeability of porous media
d. Free gas-water relative permeability data for hydrate-saturated cores and the effect of changing hydrate saturation on effective and relative permeabilities.
e. Hydrate effects on composite geo-mechanical properties such as wellbore stability, adverse effect on flow properties and formation structural integrity.
<b>Category iii. Data needs unique to hydrates</b>
a. Pressure-Temperature relationships and phase behavior diagram
b, Heat of dissociation and temperature relationship
c. Kinetics of hydrate formation and dissociation phenomenon
d. Thermophysical properties of the solid hydrates including density, specific heat, thermal conductivity, and their relationship to pressure and temperature changes.

#### 2.5.4 Gas-Water Relative Permeability Studies

Effective permeability and gas-water relative fluid flow curves are critical data required for performing reservoir simulation studies. Gas recovery strongly depends on the ability of fluids to flow within the porous media (Moridis and Reagen, 2007). Laboratory experiments have been performed to determine the effective and relative flow capacity

of gas and water through the hydrate-saturated porous media under reservoir conditions of pressure and temperature (Jaiswal, 2004; Seol et al., 2006). Generating relative permeability tables for hydrate-bound systems is a challenging task. Hydrate growth and wettability changes are unpredictable phenomena; they make data reproduction difficult on a consistent basis. Thus, empirically obtained permeability data have not been used with much confidence. Currently, analytical models proposed by Moridis et al. (2005) and Hong (2003) are used extensively while defining the two-phase fluid flow behavior within hydrate saturated porous media. The Computer Modeling Group (CMG) reservoir simulator utilizes Stone II model (Stone, 1973) to define the three-phase relative permeability data (hydrate phase is considered as an extremely viscous or immobile phase with near zero mobility).

## **2.6 Global Methane Hydrate Research Activities**

Many nations worldwide have realized the importance of characterizing and quantifying hydrate resources. With increasing awareness about hydrate research, governments of many countries have started investing heavily in hydrate exploration. The U.S. methane hydrate research program currently includes laboratory-based experiments, and reservoir simulation studies (Moridis et al., 2008a). Field-scale pilot studies have already been performed in the ANS (Hunter et al., 2007) and offshore of the Gulf of Mexico. Long-term testing and possible commercial production is expected to happen first in permafrost deposits of the ANS (Moridis et al., 2008a). Japan has developed a detailed hydrate research plan and has already performed exploration programs. Approximately thirty six wells have been drilled in hydrate-bearing zones in the Nankai Trough basin, off Japan's east coast (Takahashi and Tsuji, 2005). The Government of India has developed an ambitious National Methane Hydrate Program to quantify the nation's total hydrate resource and to devise a plan for future gas production in order to meet its growing energy needs. To date, the program has confirmed the occurrence of hydrates in four offshore locations (Moridis et al., 2008a). Similarly, China and Korea have their respective national hydrate programs with a focus towards quantifying hydrate resources. There are many other nations that have either started research on naturally occurring hydrates or are currently preparing research roadmaps (Moridis et al., 2008a).

### 3. METHODOLOGY FOR RESERVOIR ENGINEERING OF HYDRATE SYSTEMS

#### 3.1 Gas Hydrate Stability Modeling

##### *3.1.1 Background and Objectives*

Gas recharge from in-situ hydrate dissociation has been proposed as one of the active drive mechanisms possible in the EB and WAL gas pools (Glenn and Allen, 1991; Stokes et al., 2005; Stokes and Walsh, 2007). To investigate this hypothesis, an engineering approach was adopted to develop methane hydrate stability models for the three gas pools. The following were the objectives of this study:

- i. To validate hydrate phase behavior predictions of CSM-HYD software against experimental results and available empirical models.
- ii. To develop methane hydrate stability models using CSM-HYD for the EB, WAL, and SB gas pools.

##### *3.1.2 Data and Assumptions*

###### *3.1.2.1 Gas Analysis Data*

More than 75 gas composition data were studied, and a corresponding number of hydrate phase behavior diagrams were constructed using CSM-HYD. Recently collected gas sample data from EB Wells #14, #15, and #21, SB Wells #9, #10, and #11, and WAL Wells #5, #8, and #10 were analyzed (Walsh et al., 2007). Other gas analysis data were obtained from literature (Gruy, 1978), NSB files (unpublished), 2005 analysis reports of Petro-Canada Inc. (unpublished), Exxon U.S. gas analysis reports (unpublished), and a paper published by Holba et al. (1994). For a consolidated list of gas composition data, refer to Walsh et al. (2007).



### 3.1.2.2 Formation Water Salinity Data

Formation water salinity data were acquired for EB Wells #14, #15, #17, #19, and #20 from NSB files (unpublished). Salinity data for WAL Well #1 also were obtained from NSB files (unpublished). No such data were available for the SB gas field.

After careful evaluation of the available data from the EB wells, it was concluded that the collected water samples were contaminated during sampling; hence they did not represent actual formation water properties. As a result, the EB well datasets were disregarded during the study.

The unavailability of salinity data in the SB gas fields and limited data in the EB and WAL pools created an element of uncertainty over the actual formation water property. An extensive literature review showed that the formation water salinity could range from an average salt concentration of 0% to 4% w/w. Therefore, the salinity of 0%, 2%, and 4% w/w were also chosen for the study apart from the data available in the reports. For a comprehensive list of formation water salinity datasets used in this study, refer to Walsh et al. (2007).

### 3.1.2.3 Pressure Gradient Data

Pressure gradient data for EB Wells #14, #15, and #19, and SB Wells #6 and #13 were collected from Allen and Crouch (1988). Additionally, Darkwah and Allen (1996) reported pressure gradient data for EB Wells #14 and # 21, SB Wells #6 and #13, and WAL gas Wells #2, #3, #4, #5, #6, #7, #8, #9, and #10.

After carefully evaluating pressure gradient data from the reservoirs, a gradient of 0.5 psi/ft was chosen for the EB and SB gas fields, whereas, a pressure gradient of 0.45 psi/ft was chosen to represent the pressure gradient of the WAL gas pool.

Using pressure gradient data, the depth equivalent of pressure was estimated for all the three fields. These estimations were followed by correcting the reservoir depths with

respect to mean sea level. The datum was changed from Kelly Bushing (KB) elevations to the mean sea level using the well history data. All well files were obtained from the Alaska Oil and Gas Conservation Commission (AOGCC) website (<http://www.state.ak.us/admin/ogc/homeogc.shtml>).

#### *3.1.2.4 Temperature Gradient Data*

Static temperature gradient data were acquired for EB Wells #15 and #21 in March 2007 (Walsh et al., 2007). Temperature gradient data for other BGF wells were obtained from NSB files (unpublished). These data included geothermal gradient data for EB Wells #14, #19, and #21, SB Wells #6 and #13, and WAL Wells #2, #3, #4, #5, #6, #7, #8, #9, and #10 (Stokes et al., 2005). Refer to Walsh et al. (2007) for a detailed list of temperature gradient data.

Technical limitations such as cooling effect, occurring while acquiring the downhole temperature and the inability to measure bottomhole temperature in some wells resulted in poor data quality. Consequently, the gradient data obtained for different wells were not an accurate representation of the subsurface temperature profile. Due to these constraints, hydrate stability models were developed for individual field. Thus, hydrate distribution maps for each gas pool could only be generated based on the field level stability model.

#### *3.1.3 CSM-HYD Results Validation*

During initial evaluation, CSM-HYD was chosen for predicting three-phase (water-hydrate-free gas) equilibrium relationship, based on gas composition and water salinity data. The software was developed by Sloan and his team (Sloan, 1998). The algorithm of the software is based on a statistical thermodynamic model proposed by Van der Waals and Platteeuw (1959). It can predict equilibrium pressure, given any temperature, and vice versa. It also can predict stable hydrate structure that would form, given a set of gas composition and water salinity data.

CSM-HYD phase behavior results were verified by comparing them with the experimental data (Westervelt, 2004). Empirical equations (Kamath and Holder, 1987; Moridis 2003) were simultaneously tested against the experimental data for their validity at higher water salinities. The dataset and models were chosen particularly if they closely represented hydrate phase behavior for ANS gas compositions (Westervelt, 2004; Kamath and Holder, 1987) or if they were derived from numerous experimental work done previously (Moridis, 2003).

Based on experiments, Kamath and Holder (1987) generated two regression equations predicting hydrate equilibrium relationships. Later, Collett (1993) updated the model for ANS hydrate reservoirs. One curve is used for temperatures below the freezing point of water (Equation 3.1) while the other is used for temperatures above freezing (Equation 3.2).

$$P_{se} = \exp \left[ 14.7170 - \frac{1886.79}{T_{se}} \right] \quad \text{for } 248 \leq T_{se} \leq 273 \quad (3.1)$$

$$P_{se} = \exp \left[ 38.9803 - \frac{8533.80}{T_{se}} \right] \quad \text{for } 273 \leq T_{se} \leq 298 \quad (3.2)$$

where  $P_{se}$  - equilibrium pressure, kPa and  $T_{se}$  - equilibrium temperature, °K.

Moridis (2003) developed a general regression expression based on data from several phase behavior studies reported by Sloan (1998). Figure 3.1 shows the two relationships and their respective ranges, where  $I$  - ice,  $L_w$  - water,  $H$  - hydrate, and  $V$  - free gas components. This model is currently being used by the TOUGH+HYDRATE reservoir simulator developed by LBNL.

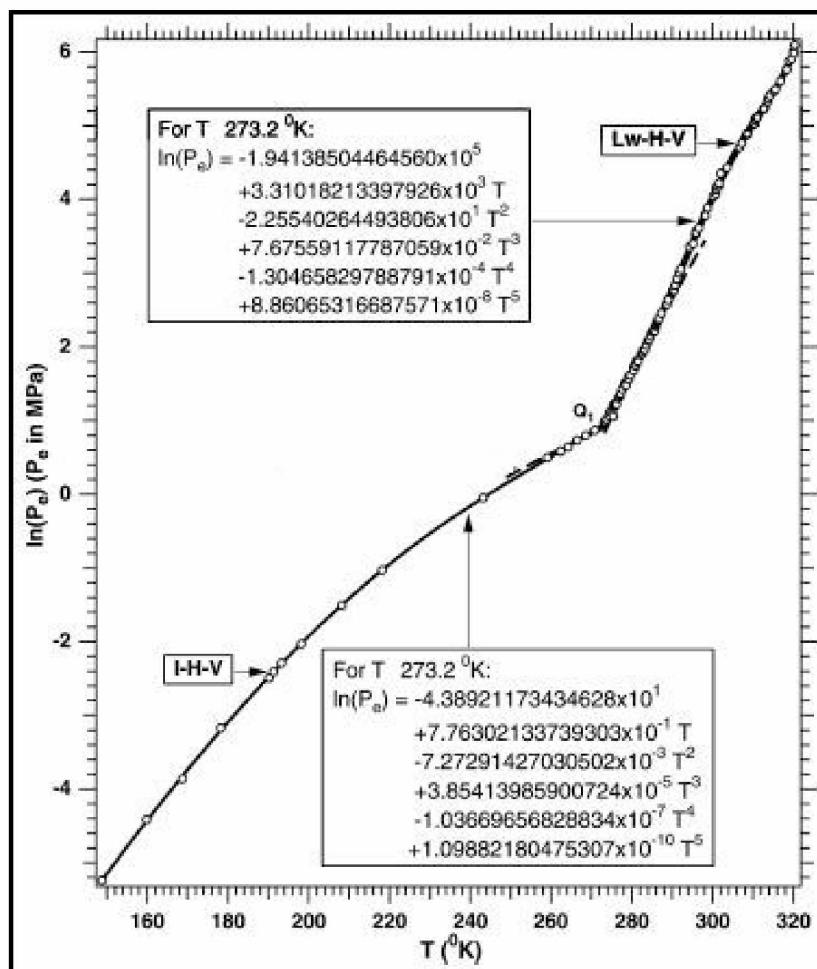


Figure 3.1: Hydrate Equilibrium Pressure-Temperature Relationship (Moridis, 2003)

Westervelt (2004) performed phase behavior experiments in the laboratory. He reported hydrate equilibrium curves by capturing hydrate formation and dissociation phenomenon in bulk phase, inside synthetic porous media and Anadarko sand samples. Pure methane gas (99% purity) was brought in contact with 2% and 4% w/w brine solution at reservoir pressure and temperatures (depicting the ANS conditions). The hydrate formation was observed using a digital camera. Later, the system temperature was gradually increased and hydrate dissociation was captured and equilibrium curve was generated. Similarly, Westervelt (2004) collected hydrate equilibrium pressure-temperature data points for synthetic porous media sample by monitoring the pressure profile of the porous media system (no visual observation possible).

### *3.1.4 Gas Hydrate Stability Model Development*

The algorithm describing the hydrate stability model development is presented below (Refer to Appendix A for flowchart):

Step 1: Start

Step 2: Obtain gas analysis, salinity, pressure and temperature gradient data

Step 3: Load gas analysis and water salinity data in CSM-HYD program

Step 4: Run CSM-HYD program

Step 5: Read hydrate equilibrium pressures for known temperature

Step 6: Get depth equivalent using pressure gradient data

Step 7: Set sea level as datum and correct reservoir depths

Step 8: Repeat STEP 2 to STEP 6 until all temperature ranges are completed

Step 9: Generate depth vs. temperature (hydrates) and geothermal gradient (reservoir condition) plots together.

Estimate hydrate stability envelope

Compare stability envelope with reservoir pay zone thickness.

Step 10: Repeat STEP 1 through 8 for new dataset

Step 11: Stop

## **3.2 Material Balance Study**

### *3.2.1 Background and Objectives*

Stokes and Walsh (2006) reported pressure buildup tests on two EB wells (EB #14 and #21) and later (Stokes and Walsh, 2007) compared the static reservoir pressure data with historical pressure data reported by Allen and Crouch (1988). Figure 3.2 represents the performance plot of the EB gas field. The figure shows an initial drop in static reservoir pressure with gas production, which indicates the conventional response of a volumetric gas reservoir, producing by gas expansion mechanism. Interestingly, long-term production showed gradual pressure stabilization. Such pressure supports are generally considered as the signature response of water influx from a communicating

aquifer (Craft and Hawkins, 1990). However, this argument may not hold true for the EB reservoir. The following observations were made by Stokes and Walsh (2007), suggesting the possible contribution from an unknown drive mechanism:

- i. Negligible (~1,600 bbls) water production observed to date (Sep 01, 2007).
- ii. Reservoir produced ~8 bcf of gas by Sep 01, 2007 much higher than Allen and Crouch (1988) estimate of ~6 bcf.
- iii. None of the EB gas wells have watered out due to possible water encroachment as anticipated (Allen and Crouch, 1988).

Such observations suggested additional pressure support from a different source. Gas recharge from dissociating in-situ hydrates could be one of the mechanisms. However, the possibility of water influx from an aquifer could not be ruled out. Understanding the reservoir drive mechanism holds a key to future reservoir development. Current ambiguity with the EB reservoir performance makes this task more challenging.

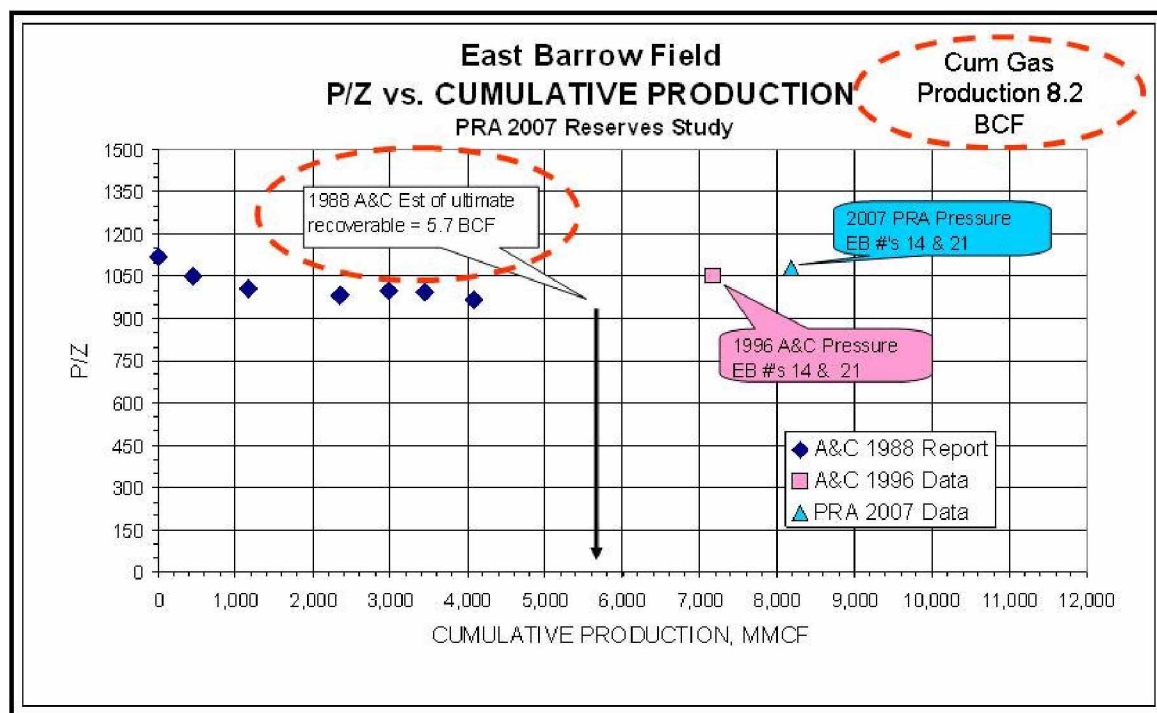


Figure 3.2: EB Gas Reservoir Performance Plot (Stokes and Walsh, 2007)

The objective of this study was to develop a stepwise procedure to understand the impact and possible contribution of different drive mechanisms on the overall performance of a tank-type static reservoir model depicting the EB gas pool (Figure 3.3). First, the response of a volumetric gas tank (Step 1) was compared against the available production data. This was followed by the performance study of a waterdrive mechanism (Step 2). Next, a hydrate tank (Step 3) was attached to the volumetric gas reservoir to study and evaluate the response with the production history data. The combined effect of aquifer- and hydrate-driven mechanisms was studied by bringing them together in contact with the free gas tank (Step 4). Based on this material balance study, attempts were made to match the historic production data. A successful history matching and sensitivity study could further strengthen the conclusions from this study.

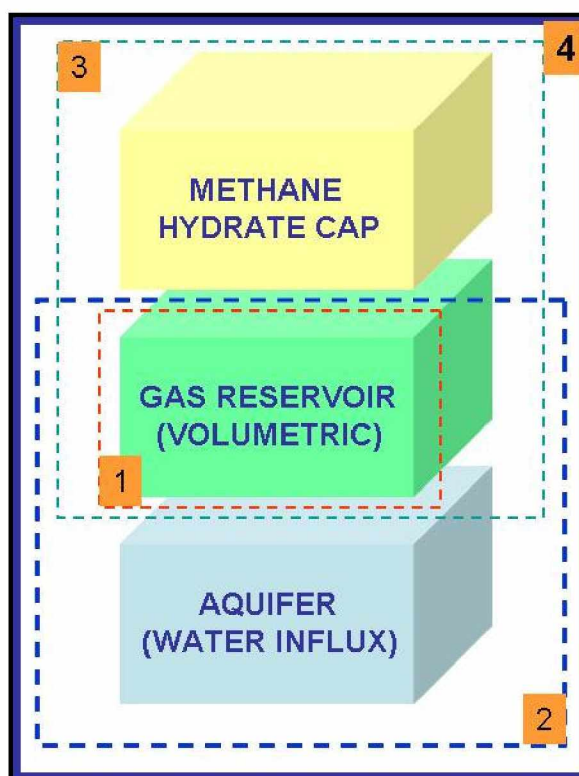


Figure 3.3: Methodology Followed for Material Balance Study

No material balance study was performed for the SB gas field. The reservoir had already produced over 70% of initial gas in-place and has shown conventional free gas depletion mechanism (Stokes and Walsh, 2006). On the other hand, the size of the WAL gas field

is huge with an estimated original gas in-place (OGIP) in the range of 250 bcf. To date, just over 5% of recoverable gas in-place has been produced (Stokes et al., 2005). Even though this field is estimated to have stable in-situ hydrates in updip locations of the reservoir (Glenn and Allen, 1991; Stokes et al., 2005), the response from dissociating hydrates (if any) was difficult to observe with available production history data. Static pressure of the WAL field has not dropped considerably; hence it was too early to draw a conclusion about the reservoir drive mechanism. A material balance study is not sensitive in capturing the response of associated aquifer or dissociating hydrates (if any). Thus, material balance study was not undertaken for the WAL reservoir. Nevertheless, possible drive mechanisms of the reservoir were carefully evaluated by performing dynamic reservoir simulation studies (explained later).

### *3.2.2 Data and Assumptions*

#### *3.2.2.1 Reservoir Thickness*

Gruy (1978) reported that the EB reservoir geology mainly consisted of two hydrocarbon producing zones. One is the Upper Barrow sand and the other is the Lower Barrow sand. The Upper Barrow sand in the EB field is much tighter and less well developed than the Lower Barrow sand. The main producing zone is the Lower Barrow sand. The sand is found in the lower part of the Kingak formation. The thickness of the Lower Barrow sand averages around 20 ft in the EB field. For this study, an average Lower Barrow sand thickness of 22 ft was considered (refer to detailed review work performed by Panda and Morahan, 2008).

The area covered by the Upper Barrow sand is approximately 3,454 acres and contains 68,725 acre-ft of pay zone, whereas the area covered by the Lower Barrow sand is approximately 1,771 acres and contains 32,033 acre-ft of pay (Gruy, 1978). Due to the structural variation in the Lower Barrow sand and unavailability of detailed seismic data, an average reservoir area of 1,000 acres was chosen for the study. Morahan (2008) has recently reported his observations after evaluating available seismic data of the Barrow High area including the EB gas field.



Gruy (1978) observed the existence of a small fault extending across the field from the northwest to southeast direction between EB #17 and the remainder of the field. Significant differences in bottomhole pressures and gas compositions between east and west areas were the basis of his conclusions. It was later argued, however, that this fault may not be of a sealing type due to its small displacement (Allen and Crouch, 1988).

Allen and Crouch (1988) analyzed seven years of production data and conducted well deliverability studies before concluding that the EB gas field exhibited no signs that would indicate the existing fault was effective (sealing), hence they suggested that the existing fault could be ignored during mapping and material balance calculations. Hence, for material balance study, the EB reservoir was considered to be a single homogenous tank system.

### *3.2.2.2 Reservoir Properties*

Gruy (1978) conducted routine core analysis on samples obtained from Lower Barrow sand to obtain reservoir properties such as permeability and porosity. Two wells, EB #12 and #17, were cored, and the results are presented in Table 3.1 below. Further, Gruy (1978) performed well-testing analysis and obtained permeability in the range of 30-40 md. Significant differences were observed between the core analysis and well-testing permeability data.

Hence, with an element of uncertainty over reservoir permeability, an average absolute permeability of 100 md was chosen for the material balance study. The entire reservoir was considered isotropic with uniform permeability in horizontal and vertical directions.

Table 3.1: Core Analysis Results for Wells EB #12 and #17 (Gruy, 1978)

<b>Reservoir</b>	<b>Well, EB #</b>	<b>Thickness, ft</b>	<b>Permeability, md</b>	<b>Porosity, %</b>
West	12	22	857	20
East	17	27	303	22

Log analysis results were reported by Gruy (1978) for Wells EB #12, #14, #17, and #19 to determine the clay content in Lower Barrow sand. Results from log analysis were extended to obtain effective porosity and water saturation (Table 3.2).

Table 3.2: Log Analysis Results for Wells EB #12, #14, #17, and #19 (Gruy, 1978)

<b>Reservoir</b>	<b>Well, EB #</b>	<b>Net Pay, ft</b>	<b>Effective Porosity, %</b>	<b>Water Saturation, %</b>
West	12	19.5	20.95	32.29
West	19	17.5	21.56	41.25
East	14	25.0	23.47	54.54
East	17	12.0	22.33	51.16

A substantially high percentage of water saturation was observed, primarily due to the invasion of salty mud or filtrate. Hence, the water saturation results obtained by this method proved to be incorrect. Therefore, for material balance analysis, an average water saturation of 20% was selected.

### 3.2.2.3 Initial Reservoir Pressure and Temperature

Gruy (1978) performed pressure buildup tests in Wells EB #17 and #19. The original bottomhole pressures corrected to a datum of -2000 ft were found to be 1008 psi in the east block and 994 psi in the west fault block. However, according to Allen and Crouch (1988), the existence of a fault line had no impact on the overall performance of the reservoir. Hence, an average initial reservoir pressure of 1010 psi was considered for the material balance study.

Gruy (1978) gathered downhole temperature data in Well SB #13 and obtained a reservoir temperature of 62 °F. Dynamic temperature gradient plots obtained for Wells EB #14, #19, and #21 (NSB Files, unpublished) suggested that the average bottomhole temperature for the EB well could be in the range of 45 °F. Later, Stokes and Walsh (2006) measured the static reservoir temperature gradients for Wells EB #15 and #21.

They obtained an average static reservoir temperature of 50 °F. Considering possible errors in the case of old data due to cooling effect, a static bottomhole temperature of 50 °F was chosen as initial reservoir temperature.

#### *3.2.2.4 Original Gas In-Place (OGIP)*

Preliminary material balance studies were performed by Gruy (1978). The recovery factor obtained for Lower Barrow sand was estimated to be 77% for an abandonment pressure of 235 psi. The OGIP calculated for Lower Barrow sand was around 15 bcf. In contrast to previous conclusions, Allen and Crouch (1988) reported OGIP to be around 6.5 bcf. They included the impact of strong aquifer support while estimating the initial gas reserves. They estimated that by the end of 1988 about 91% of OGIP would be recovered and the rest could be recovered by mid 1990s.

Recently, Stokes and Walsh (2007) performed static pressure tests and concluded that the current static reservoir pressure was around 935 psi, and gas production continued with negligible water production. Interestingly, the reservoir continued to deliver gas, and still producing, contrary to previous findings (Allen and Crouch, 1988).

Since the possibility of finding in-situ hydrates within Lower Barrow sands could not be ruled out, no attempts were made to estimate initial and current in-place gas for the EB pool. They were later accurately estimated by developing static reservoir models (Panda and Morahan, 2008) and by performing dynamic reservoir simulation studies (explained later).

#### *3.2.2.5 Water Influx*

The presence of free gas-water contact (GWC) within the EB gas reservoir was reported by Gruy (1978). He concluded that the reservoir drive mechanism was primarily gas driven with negligible water influx. However, Allen and Crouch (1988) conducted a detailed water influx study based on seven years of production history data, and claimed that the reservoir was under strong aquifer support. In contrast to previous studies,

currently the reservoir is producing gas with negligible volumes of produced water, and no well has been plugged due to excessive water production. Thus, the impact of an associated aquifer could not be claimed with certainty. Nevertheless, the water influx model was studied as a separate scenario to gauge and compare its impact on overall reservoir performance.

### 3.2.2.6 Production Data

Production data constitute a critical aspect of the material balance study. Stokes and Walsh (2007) collected production history data of the EB wells. Production data for wells are available from Dec 01, 1981 to Sep 01, 2007 (Figure 3.4). Production data were logged on a monthly basis for each well and included information such as well number, well type, gas production rate, water production rate, production days and reporting days. Individual well production data are presented later.

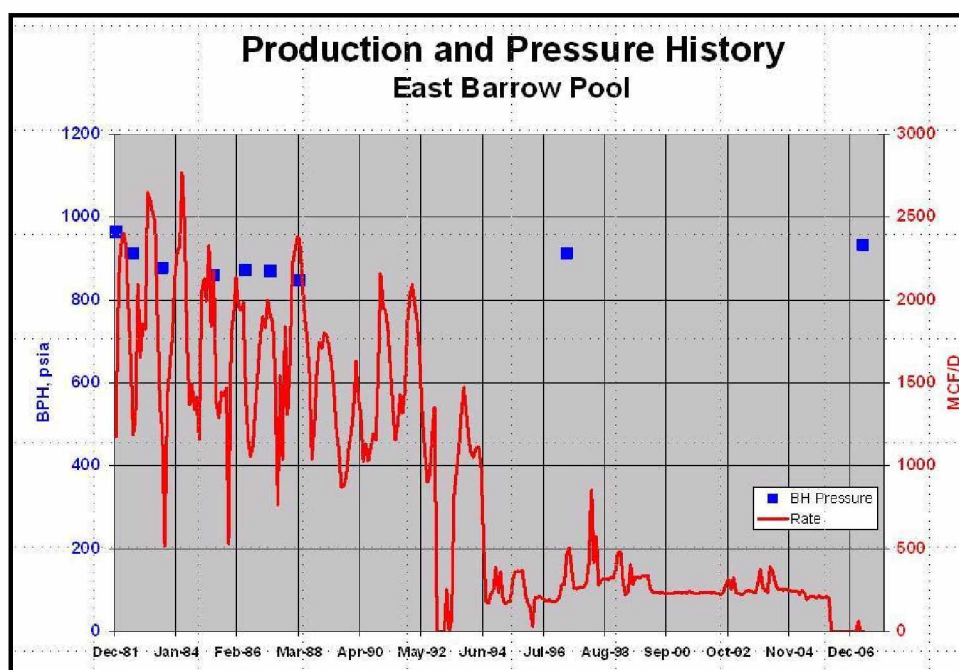


Figure 3.4: Production History Chart for the EB Gas Pool (Stokes and Walsh, 2007)

Unfortunately, flowing bottomhole pressures were not reported on a regular basis. Since, the available shut-in pressures were collected from few EB wells (Figure 3.4), they may not represent the average reservoir pressures. As a result of this, it was assumed that the static reservoir pressure data may deviate from the average reservoir pressure data by a maximum error of  $\pm 10\%$ . This vital piece of information was included as part of the production history data. As expected, monthly gas production rates never remained constant for the reservoir (Figure 3.4) hence, suitable assumptions were made while developing the material balance models.

### 3.2.2.7 Summary

The reservoir data considered for material balance study is summarized in Table 3.3.

Table 3.3: Reservoir Properties Considered for the Material Balance Study

Sr. No.	EB Reservoir Properties	Data Selected
1.	Area	1000 acres
2.	Thickness	22 ft
3.	Permeability	100 md
4.	Porosity	20%
5.	Water Saturation	20%
6.	Initial Reservoir Pressure	1010 psi
7.	Initial Reservoir Temperature	50 °F
8.	Gas Specific Gravity	0.579
9.	Initial Gas In-Place	Not Estimated
10.	Water Influx	Not Estimated

### 3.2.3 Methodology

#### 3.2.3.1 Volumetric Model

To understand the underlying theory behind this model, refer to Appendix B. Methodologies developed for the original Extended Material Balance (EMB) model were modified based on available reservoir and production data. The stepwise procedure followed has been described below:

Step 1: Using gas specific gravity, initial reservoir pressure, and uniform reservoir temperature (considering isothermal conditions), calculate the gas deviation factor,  $z(t)$ , based on the Dranchuk and Abou Kassem equation of state as described in Craft and Hawkins (1990). Obtain the  $z(t)$ -factor as a function of pressure and plot  $P(t)/z(t)$  vs.  $P(t)$  on a Cartesian scale (Figure 3.5).

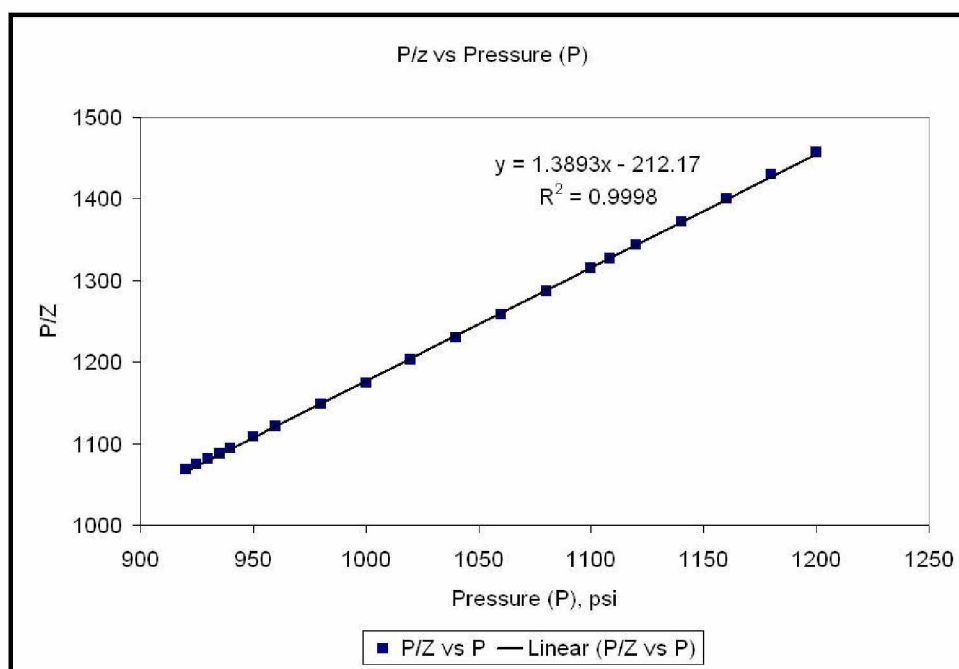


Figure 3.5:  $P(t)/z(t)$  vs. Pressure,  $P(t)$  Relationship

The obtained relationship (Figure 3.5) can be represented as:

$$\frac{P(t)}{z(t)} = 1.3893P(t) - 212.7 \quad (3.3)$$

Step 2: Apply the conventional material balance model (Equation 3.4) for the volumetric gas reservoir (Craft and Hawkins, 1990). Initial estimates of  $P(t)/z(t)$  with  $G_p(t)$  were made by plugging initial reservoir pressure data,  $P_i$ , and guessing OGIP,  $G$ .

$$\frac{P(t)}{z(t)} = \left\{ \frac{P_i}{z_i} - mG_p(t) \right\} \quad (3.4)$$

where slope  $m$  defined by

$$m = \left( \frac{P_i}{z_i G} \right) \quad (3.5)$$

where  $P(t)$  - reservoir pressure, psi;  $z(t)$  - gas deviation factor;  $P_i$  - initial reservoir pressure, psi;  $z_i$  - gas deviation factor at initial reservoir pressure;  $m$  - slope, psi/scf;  $G_p(t)$  - cumulative gas production, scf; and  $G$  - OGIP, scf.

Step 3: Establish  $P(t)/z(t)$  vs. time relationship by substituting known cumulative gas production data,  $G_p(t)$ , in the material balance equation obtained in Step 2. Next, generate reservoir pressure,  $P(t)$ , as a function of time by plugging time-dependent  $P(t)/z(t)$  into Equation (3.3).

Step 4: Since no information was available about flowing bottomhole pressure (FBHP), four-point deliverability test data from the EB gas reservoir were used (Stokes and Walsh, 2007). Pseudosteady state was considered and a correlation was developed to relate reservoir pseudo-reduced pressure and pseudo-reduced

bottomhole pressures with gas production rates. Pseudo-reduced components were converted using gas viscosity,  $\mu_g$ , and  $z(t)$ -factor data. Gas viscosity calculations were performed by using Lee, Gonzalez, and Eakin correlations (Craft and Hawkins, 1990).

Step 5: Knowing gas production rates,  $Q_g(t)$ , reservoir pressure,  $P(t)$  (Step 3), and FBHP,  $P_{wf}(t)$  (Step 4), calculate deliverability constant,  $C$ , on a monthly basis by rearranging Equation (B.3) as:

$$C = \frac{Q_g(t)}{(P(t)^2 - P_{wf}(t)^2)} \quad (3.6)$$

Step 6: Plot  $C$  against time,  $t$ . If  $C$  was not constant (i.e., if the plot was not a horizontal line), guess a new OGIP,  $G$ , and repeat Steps 2, 3, and 5.

Step 7: If constant,  $C$ , was attained, then plot the representative  $P(t)/z(t)$  relationship and compare it with existing pressure history data.

### 3.2.3.2 Water Influx Model

To understand the impact of an aquifer on the EB reservoir, the gas reservoir was assumed to be under the influence of constant water influx from an aquifer. The associated aquifer was considered strong enough to supply required volumes of water in order to maintain the observed pressure response. A graphical technique proposed by Pletcher (2001) and Ahmed and McKinney (2005) was used to analytically test the EB reservoir in the presence of an aquifer support and estimate other unknown parameters such as OGIP, cumulative water influx, and aquifer size. The theory of this model is explained in detail in Appendix C. In order to apply the water influx model, following steps were followed.



Step 1: Use Dranchuk and Abou Kasseem equation of state, as described in Craft and Hawkins (1990) to generate  $z$ -factor for corresponding pressures starting from an initial pressure of 1010 psi. Plot  $z(t)$  vs.  $P(t)$  and develop a linear correlation between the two parameters.

Stage 2: Generate  $z$ -factor and gas formation volume factor,  $B_g(t)$ , for available reservoir shut-in pressure data.

Step 3: Develop  $\frac{(G_p(t)B_g(t) + W_p(t)B_w(t))}{(B_g(t) - B_{gi})}$  term by using the production data. Plot the term,  $\frac{(G_p(t)B_g(t) + W_p(t)B_w(t))}{(B_g(t) - B_{gi})}$ , as a function of  $G_p(t)$  for available reservoir shut-in pressures.

Step 4: Draw the best slope through the dataset.

Step 5: If the slope was zero (horizontal), then the reservoir is volumetric. Stop the calculations.

Step 6: If the slope was not zero, then the reservoir was under waterdrive. Estimate the strength of the aquifer qualitatively by studying the slope.

Step 7: The intercept on the y-axis (at  $G_p(t) = 0$ ) can be considered as the apparent OGIP for this case. Estimate OGIP using this technique. However, it must be noted that this may not be an accurate estimate (refer to Appendix C for details).

Step 8: Use Equation (C.2) to calculate the cumulative water influx,  $W_e(t)$  from known OGIP (obtained above).

Step 9: Estimate aquifer size by assuming water and formation compressibility factors.

### 3.2.3.3 Hydrate Model

A stepwise procedure was developed to study the impact of hydrate zone thickness on reservoir pressure. Refer to Appendix D for an understanding of the concept behind the hydrate model.

Step 1: *Model Validation* - The first step in using the hydrate model was to validate the hydrate model (Gerami and Darvish, 2006) with no hydrate layer (free gas reservoir). The response of such a model must match conventional decline response (Craft and Hawkins, 1990); the new model was called *modified hydrate model*. To carry out model validation, a free gas tank was considered. The areal extent of the reservoir was considered to be 8 acres whereas the thickness of the reservoir was considered very large (a semi-infinite system). All other reservoir properties were assumed the same as considered for the EB reservoir (Table 3.3). The material balance equations were solved assuming a constant production rate of 5 Mscf/Day. The calculations were performed for a small production period in order to keep reservoir pressures fairly high. No temperature and pressure gradients were considered in this case.

Based on these assumptions, conventional material balance calculations were carried out by considering a volumetric (depletion drive) gas reservoir.  $P(t)/z(t)$  was then plotted against  $G_p(t)$ . Reservoir pressures were also calculated by estimating the  $z(t)$ -factor simultaneously.

After several attempts, the hydrate model was modified to account for temperature reduction within the reservoir. A gas reservoir without hydrate was modeled by considering a fictitious hydrate layer. It was further assumed that the initial reservoir pressure was controlled by this hydrate zone. Temperature change in the reservoir was calculated by estimating hydrate-cap temperature parameter,  $b(t)$  (remained constant for a volumetric reservoir model without hydrates), and Equation (D.2). Thus, due to the adiabatic behavior of the

reservoir, the hydrate material balance equation was modified, and temperature terms were retained. The hydrate material balance model modified for this case takes the form

$$G\left(\frac{P_{sc} z(t) T(t)}{T_{sc} P(t)}\right) - G\left(\frac{P_{sc} z_i T_i}{T_{sc} P_i}\right) = G_p\left(\frac{P_{sc} z(t) T(t)}{T_{sc} P(t)}\right) \quad (3.7)$$

where  $P_{sc}$  - standard pressure, psi, and  $T_{sc}$  - standard temperature, °R.

$\frac{P(t)}{z(t)}$  vs.  $G_p(t)$  was plotted against  $G_p(t)$  using the *modified hydrate model*. The performance of the two models was compared. Under present circumstances, *modified hydrate model* must show a close match with the volumetric model. This will validate the *modified hydrate model* (without hydrates). After model validation, use the modified model to compare the performance against the original hydrate model (with hydrates).

Step 2: CMG-STARs simulation was carried out with the previously assumed reservoir model (without hydrates) to obtain reservoir performance (pressure) with time. The obtained results were compared with results obtained from the conventional volumetric material balance and the *modified hydrate model*.

Step 3: The *modified hydrate model* was scaled up to represent the EB reservoir properties and production data (Table 3.3). The production data had variable gas production rates. This violated the application of the *modified hydrate model* (refer to assumptions in Appendix D). To generate similar conditions, an average gas production rate was chosen ( $Q_g = 1600$  Mscf/Day). With this assumption, the *modified hydrate model* was applied to obtain  $\frac{P(t)}{z(t)}$  vs.  $G_p(t)$  and pressure vs. time plots.

Step 4: The CMG-STARS reservoir model was correspondingly scaled up to match the EB reservoir conditions. The simulator response was compared with the results obtained from the *modified hydrate model*, as a second stage of validation.

Step 5: Original hydrate model (Gerami and Darvish, 2006) was then used to obtain pressure response in the presence of a hydrate-cap. An EB type reservoir was produced at a constant rate of 1600 Mscf/Day. In this case, the hydrate-cap temperature parameter,  $b(t)$ , became a function of time as well. The parameter was used to obtain the hydrate-cap temperature, changing continuously with time. Again, the hydrate-cap temperature was considered to be the reservoir temperature. Kamath and Holder (1987) empirical correlation (Equation 3.2) was used to obtain the equilibrium pressures at corresponding temperatures. As assumed previously, hydrate equilibrium pressure was considered as the reservoir pressure (Appendix D). The impact of hydrate zone thickness on the performance of the EB type reservoir model was studied by following the hydrate material balance procedure for different hydrate zone thickness (varying from 0.5 ft to 22 ft).

#### 3.2.3.4 CMG-STARS Simulation Model

##### *a. Background*

The hydrate model does not allow evaluation of reservoir performance due to the combined effect of water and hydrate drive mechanisms. Thus, to understand the impact of these two mechanisms together on a free gas reservoir, the CMG-STARS simulator was used.

##### *b. Methodology*

Step 1: An aquifer tank was added to the existing CMG-STARS model (no hydrates). Edgewater drive was considered, and the size of the aquifer was varied from 30 ft to 100 ft. The performance of the reservoir was then compared. To have a

comparison of waterdrive reservoir with hydrate-bound gas reservoir, results from the hydrate model were also included in the comparison. To keep the comparison simple, only the performances of the reservoir with minimum (0.5 ft) and maximum (22 ft) hydrate zone thicknesses were included.

Step 2: In continuation with the previous step, the CMG-STARS reservoir (gas with aquifer) model was modified by adding a hydrate zone. Care was taken while selecting aquifer size. After evaluating several scenarios, two aquifer sizes were chosen: one was a weak aquifer (33 ft thick) and the other, a strong one (100 ft thick). The performance of the reservoir was evaluated by varying the hydrate thickness (1 ft, 10 ft, and 22 ft).

Step 3: The performance of one of the scenarios closely matched the actual production data. Hence to have a better match, a preliminary production history matching exercise was carried out. It must be noted that, this history matching procedure was based on simple tank model (mechanistic). To obtain the best match, several runs were made by adjusting parameters, such as production rates, permeability, and porosity in aquifer zones.

Step 4: The history matched model was then used to carry out sensitivity analysis. Parameters such as reservoir permeability, gas production rates, and free gas-to-hydrate-zone-thickness ratios were altered to measure their sensitivity.

### **3.3 Gas-Water Relative Permeability Study**

#### *3.3.1 Background and Objectives*

An understanding of gas-water relative flow mechanisms through a hydrate-saturated core is required while developing dynamic simulation models for hydrate production. Saturation changes due to hydrate dissociation continuously alter the relative flowability of mobile gas and water, thus making it difficult to predict the behavior analytically. Hence, there is a need to obtain gas-water relative permeability experimental data at

different hydrate saturations. This is possible by performing laboratory or pilot-level experiments. To determine the same, Jaiswal (2004) designed a state-of-the-art gas-water relative permeability setup at the PDL, UAF. He used core samples from the ANS and performed hydrate formation and dissociation experiments, followed by conducting unsteady-state displacement runs in order to calculate gas-water relative permeability within hydrate-bearing unconsolidated sand samples. Jaiswal (2004) concluded from his study that the gas-water relative permeability behaviors are inherently affected by hydrate growth and distribution within the core sample. Thus, the consistency and accuracy of obtaining the empirical data is considered a challenging task.

Empirical models for relative permeability calculations within hydrate systems have not been published to date. Currently, analytical models are being used to develop the relative permeability tables. Equations developed by Hong (2003) have been previously used while developing reservoir models in CMG-STARs (Howe, 2004). The relative permeability models for hydrate-saturated systems are presented below (Hong, 2003).

#### Water Relative Permeability

$$k_{rw} = k_{rwo} \bar{S}_w^{-0.5} [1 - (1 - \bar{S}_w)^{-1/m}]^2 \quad (3.8)$$

#### Gas Relative Permeability

$$k_{rg} = k_{rgo} \bar{S}_g^{-0.5} (1 - \bar{S}_{wH})^{-2m} \quad (3.9)$$

#### Capillary pressure between gaseous and aqueous phases

$$p_c = p_{co} [(\bar{S}_w)^{-1/m} - 1]^{(1-m)} \quad (3.10)$$

where

$$\text{Normalized Water Saturation} \quad \bar{S}_w = \frac{S_w - S_{wr}}{1 - S_{wr} - S_{gr}} \quad (3.11)$$

$$\text{Normalized Hydrate Saturation} \quad \bar{S}_{wH} = \frac{S_w + S_H - S_{wr}}{1 - S_{wr} - S_{gr}} \quad (3.12)$$

$$\text{Normalized Gas Saturation} \quad \bar{S}_g = \frac{1 - S_w - S_H - S_{gr}}{1 - S_{wr} - S_{gr}} \quad (3.13)$$

where  $S_w$  - water saturation;  $S_{wr}$  - irreducible water saturation;  $S_{gr}$  - residual gas saturation;  $k_{rwo}$  - water relative permeability at residual gas saturation (single-phase flow);  $k_{rgo}$  - gas relative permeability at irreducible water saturation (single-phase flow);  $m$  - 0.45 (rocktype - sandstone);  $p_{co}$  - capillary pressure at 100% water saturation; and  $p_c$  - capillary pressure at given water saturation.

NLREG can be used to tune Equations (3.8) and (3.9) based on the experimental data. NLREG performs statistical regression analysis to estimate the values of parameters for linear, multivariate, polynomial, logistic, exponential, and general nonlinear functions. The regression analysis determines the values of the parameters that cause the function to best fit the experimental data. This process is also called “curve fitting.” NLREG allows us to specify the function whose parameters are being estimated using ordinary algebraic notations. In addition to determining the parameter estimates, NLREG can be directed to generate an output file with predicted values and residuals. It can also plot the data observations and the computed function.

After studying Equations (3.8) and (3.9), it was decided to tune one parameter at a time. Thus, parameter  $a$  (Equations 3.14 and 3.15) was chosen for tuning based on experimental data obtained for this study.

#### Water Relative Permeability

$$k_{rw} = k_{rwo} S_w^{-0.5} [1 - (1 - S_w)^{-1/m}]^{0.45} a \quad (3.14)$$

#### Gas Relative Permeability

$$k_{rg} = k_{rgo} S_g^{-0.5} (1 - S_{wH})^{0.45(a)} \quad (3.15)$$

To characterize the fluid flow behavior within the hydrate zone of the EB reservoir, relative permeability experiments were performed using the existing setup (Jaiswal, 2004). However, core samples from BGF were not available; instead a Berea sandstone (BS) consolidated core sample was used. EB reservoir conditions were maintained while performing the experiments. There was also a need to tune the existing analytical model and develop reservoir specific models that could be used during simulation studies. Based on these requirements, the following objectives were set for this study:

- i. Perform hydrate formation and dissociation experiments within the consolidated core sample by maintaining the EB reservoir conditions.
- ii. Conduct unsteady-state displacement experiments at different hydrate saturations so as to represent initial, current, and depleted EB reservoir condition.
- iii. Generate gas-water relative permeability tables using unsteady-state displacement data by applying Johnson-Bossler-Naumann (JBN) method (Jaiswal, 2004).
- iv. Perform nonlinear regression analysis, using NLREG software and tune existing analytical models (Hong, 2003) to generate empirical equations closely representing the EB reservoir fluid flow behavior.

### *3.3.2 Experimental Setup*

The basic design philosophy of the experimental setup remained the same as developed by Jaiswal (2004). However, a few hardware modifications and procedural changes were made in order to accommodate the consolidated core sample and improve core-flooding experiments in the presence of hydrates. Figure 3.6 presents an image of the gas-water relative permeability experimental setup. The following modifications were done in the setup:

- i. The precision of pressure measuring instruments was increased in order to handle small volumes associated with the consolidated core sample.



- ii. The chilling unit was re-calibrated to maintain an accurate temperature profile.
- iii. The gasflooding procedure to be performed soon after hydrate formation (Jaiswal, 2004) was omitted during this study. This decision was taken to avoid unnecessary hydrate formation and undesired increase in residual gas saturations within the core sample. Gasflooding step would have further restricted the two-phase flow.
- iv. Safety features/locks were incorporated in the setup. These include the addition of valves (valves V6, V9, and V10 in Figure 3.7) to isolate and the clean methane gas tank (PC2) when not in use.

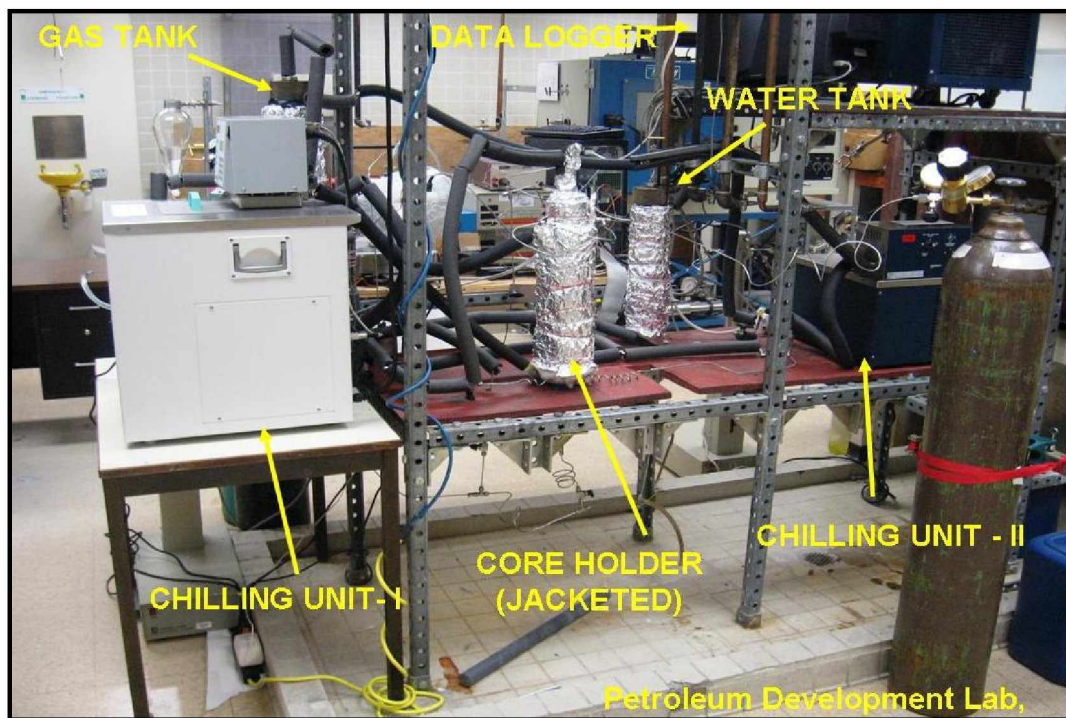


Figure 3.6: Gas-Water Relative Permeability Setup (Jaiswal, 2004)

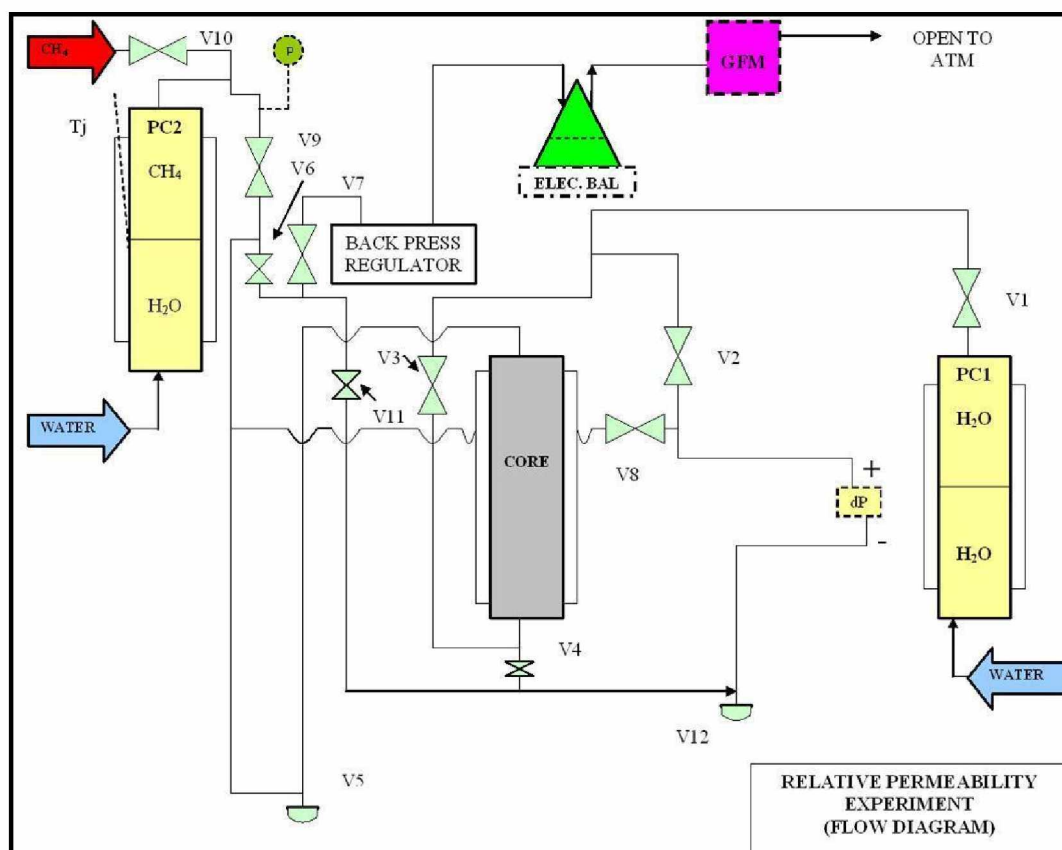


Figure 3.7: Flow Diagram - Gas-Water Relative Permeability Experiment

PC1 - gas tank (accumulator); PC2 - water tank (accumulator); CORE - core holder; ELEC. BAL - electrical balance; GFM - gas flow meter, at STD; PG - pressure gauge; dP - differential pressure transducers; and V# - valves.

### 3.3.3 Procedures

Procedures followed during the experiment are summarized below. For additional details, refer to the experimental work performed by Jaiswal (2004).

#### 3.3.3.1 Porosity and Absolute Permeability Determination

Step 1: BS dimensions were recorded. The core was completely dried in an oven at 80 °F. Dry weight was measured and the sample was then soaked in distilled water for two days.

Step 2: After two days, the wet weight of the sample was measured, and porosity was calculated. This procedure was repeated three times to reduce experimental errors.

Step 3: Later, the sample was placed inside the core holder. Overburden pressure of 500 psi was applied through the annulus space by using a combination of water and helium gas.

Step 4: A waterflooding run was performed at lower flow rates (~1 ml/min). Backpressure was maintained at 300 psi. Approximately 15 times the pore volume of water was flooded through the core to regain water lost during core handling.

Step 5: After steady-state was achieved, the differential pressure across the core was recorded. Darcy's law was applied to obtain absolute permeability of the core sample.

#### 3.3.3.2 Hydrate Formation and Dissociation Experiments

Step 6: After initial waterflooding, the core was isolated from the rest of the system. Overburden pressure was increased to 1500 psi. The pore pressure within the core sample was also raised to 950 psi by allowing high-pressure gas (950 psi), from the gas accumulator, to flow from PC1 to the top of the core.

Step 7: The water pump connected to the bottom of the core through the water accumulator (PC2) was then opened. The pump ran at a refill rate of ~0.1 ml/min to remove water from the core sample, equivalent to the desired hydrate saturations. High-pressure gas entered the core and replaced the void spaces. Care was taken while performing this run, as the chances of gas breakthrough were very high.

Step 8: Once the desired fraction of pore volumes was occupied by the gas, the core sample was isolated from the rest of the system. However, the line connected from the top of the core to the gas reservoir was kept open. The pump connected to the gas accumulator was run at a constant pressure of 950 psi to capture the volume/pressure fluctuation occurring due to hydrate formation/dissociation, respectively.

Step 9: The temperature of the core holder was then gradually decreased by circulating cold antifreeze fluid through the jacket of the core holder. The temperature of the antifreeze was controlled by using a chilling unit. The core holder was allowed to cool gradually from ambient temperature to around 42 to 44 °F in 24 hrs. The temperature of PC1 was kept at ambient conditions. Any change in gas volume/pressure could then be attributed to cooling effect and hydrate formation occurring in the core sample.

Step 10: Meanwhile, the data acquisition system (Jaiswal, 2004) continuously recorded the temperature, including the core holder and cooling jacket. Gas pump data, such as flow rate and pressure, were also recorded simultaneously.

Step 11: The hydrate formation phenomenon was captured when an instant rise in gas flow rate was observed on the gas pump.

Step 12: After stable hydrate formation was observed (after approximately 24 hrs), the cooling system was switched off. The core holder was allowed to attain ambient conditions. The temperature and gas pump pressure data (gas pump stopped) were captured to generate the pressure profile during hydrate dissociation.

Step 13: Hydrate dissociation was characterized by a rise in gas pump pressure.

### 3.3.3.3 Unsteady-State Displacement Experiments

The pressure and temperature data given below were taken from one of the experimental runs.

Step 1: The hydrate formation run was performed again, as explained earlier. Pressure and temperature parameters were kept the same as discussed previously. However, while forming hydrates at different saturations, slight variation in final reservoir pressure could not be avoided.

Step 2: After hydrate formation, the core was isolated. The temperature of the core holder was maintained around 42 to 44 °F. Gas and water tank temperature were now reduced to ~47 °F. This was done by circulating chilled fluid through the jacket of the two reservoirs.

Step 3: Upon achieving the desired temperatures, waterflooding was performed at a constant differential pressure of 29 psi. Nearly 15 times the pore volume of water was flooded. This step was accomplished without performing the gasflooding run prior to waterflooding as proposed by Jaiswal (2004). Volumes of water and gas collected were compared with injection volumes to calculate the un-reacted gas and final hydrate saturation within the core. Care was taken to avoid dissociation of hydrates. GFM was constantly monitored to capture sudden gas flow due to dissociation.

Step 4: Once the system was partially saturated with water, constant water flow rate was recorded. Darcy's law was applied to calculate the effective permeability of water at known hydrate saturation (refer appendix E for hydrate saturation determination). This was chosen as the base permeability for relative permeability table generation. Waterflooding was then stopped.

Step 5: Next, unsteady-state experiments were performed by flooding the core with gas at constant differential pressure. Due to the non-wetting nature of the gas, higher

differential pressure was required to generate significant gas flow through the system (128 psi in this case).

Step 6: The gasflooding run produced water for some time, followed a by gas-water two-phase flow. The water was collected and constantly measured using electronic balance. Gas flow rate was also captured online using the GFM. When no further water flow was observed, gasflooding was continued for 10 times the pore volume, and then constant gas flow rate was recorded.

Step 7: The recorded gas flow rate was used to calculate effective gas permeability at irreducible water saturation. This was the second end-point data. Mobile water collected helped in calculating irreducible water saturations within the core.

Step 8: Based on relative fluid flow data, captured during gasflooding run, the JBN method was applied to generate the gas-water relative permeability table Jaiswal (2004).

#### 3.3.4 Tuning Relative Permeability Model

Relative permeability experimental data were customized to represent the analytical model (Hong, 2003) so that they could be used for tuning. Equations (3.14) and (3.15) were tuned using NLREG software. A small program was written in NLREG (refer to Appendix F) to define the unknown parameter, to specify the algebraic equation to be matched, and to load the dataset required for regression. The NLREG program delivered the tuned value of the parameter and also generated the correlation coefficient,  $R^2$ , thus quantifying the performance of the fit.

### **3.4 Reservoir Simulation Study**

#### *3.4.1 Background and Objectives*

The material balance studies on the EB reservoir concluded that the average reservoir pressure history can be well explained by a combination of water influx and methane hydrate dissociation (refer to Results and Discussion on material balance study). The hydrate stability modeling and material balance studies justified the next step in modeling the EB reservoir using a full-scale 3D dynamic simulation model. The CMG-STARS reservoir simulator was used to perform simulation studies.

Glenn and Allen (1990), Stokes et al. (2005), and hydrate stability modeling studies (refer to Results and Discussion) suggested significant hydrate deposits in an updip locations of the WAL gas field and, hence, required detailed evaluation. To quantify hydrates and history match the production data, full-scale reservoir simulation studies were also performed for the WAL gas field based on the methodology developed for the EB reservoir. The objectives of this study were as follows:

- i. To develop state-of-the-art full-field dynamic reservoir simulation models for the EB and WAL gas fields using CMG-STARS.
- ii. To match reservoir's historical performance by performing field-level and individual well-level matches.
- iii. To perform reservoir sensitivity analysis in support of the history matching studies.
- iv. To develop and compare forecasting runs to propose the best scenario for future production.

#### *3.4.2 CMG-STARS Reservoir Simulator*

STARS, developed by CMG group, was used to model gas production from a hydrate reservoir. STARS can model the flow of three-phase, multi-component fluids using cartesian, cylindrical or mixed coordinates. The input parameters for the model can be in

the forms of field data or they can be generated by correlations built within the model. It also offers a unique discretized wellbore option, which allows improved modeling of horizontal wells. STARS is designed to simulate variety of complex oilfield production and enhancement processes; however, it is primarily used for conventional black oil studies. To simulate gas production by hydrate dissociation in STARS, adjustments are made to accommodate the properties of hydrate. In this study, “hydrate” is considered as the oil phase with very high viscosity and suppressed relative mobility. Explained below are the salient features/options available with CMG-STARS that were utilized to develop the dynamic reservoir model.

#### *3.4.2.1 Reservoir Grid*

CMG-STARS offers two ways to initialize the reservoir grid. The first method is by specifying the dimensions and number of blocks in a grid using the graphic user interface; the second method is by directly importing the grid dimensions from an external data file (a CMG-STARS compatible file).

Based on reservoir geology and well log data, a static reservoir model depicting the EB gas reservoir was built using ROXAR RMS<sup>R</sup> software (Panda and Morahan, 2008). The data file generated using this software was directly imported into CMG-STARS data file by using the \*INCLUDE keyword. The geological description and the geostatistical modeling procedures were described and developed by Panda and Morahan (2008).

#### *3.4.2.2 Reservoir Properties*

The graphic user interface in CMG-STARS allows layer-wise (K direction) initialization of all reservoir properties. This method is an approximate way to develop the dynamic reservoir model and may not give a true picture of the actual reservoir condition. A detailed geostatistical modeling approach was followed by Panda and Morahan (2008) to obtain reservoir properties such as porosity and permeability (all three directions). Advanced features of the STARS simulator (example \*INCLUDE keyword) were then used to import these properties. Reservoir properties such as pressure, temperature,



permeability (I, J and K direction), water, hydrate, and gas saturations were specified by using key information such as reservoir depths, initial reservoir pressure, geothermal gradient, hydrate-free gas contact (HGC), and GWC. A formula was written using CMG's Add/Edit formula feature. The formula was loaded for all the layers (k-direction) using "specify property" and "region/sector" options to initialize the desired property. Similarly, the model was initialized with other reservoir properties.

#### *3.4.2.3 Thermal Properties*

Thermal rock properties, such as volumetric heat capacity and thermal conductivity have been specified under this section. A single rock type was considered for the reservoir model. Provision of initializing overburden temperature has also been provided under this section. Apart from dissociation by depressurization (due to gas production), hydrate dissociation is partially controlled by heat supply from matrix and overburden/underburden rocks (Darvish, 2004). Hence, the option of choosing overburden temperature is critical with respect to hydrate dissociation. In this case, a constant overburden temperature was chosen.

#### *3.4.2.4 Fluid/Component Properties*

For hydrate-gas-water system, properties of three components were initialized. Water was modeled as aqueous phase, and methane, as gaseous phase. The hydrate phase was modeled as an oil phase in STARS, using a very high viscosity of 1000 cp. Component properties such as critical pressure, critical temperature, molecular weight, density, viscosity, enthalpies, etc., were provided under respective sections. Each phase was considered independent and had an initial mole fraction of 1 (i.e., no dissolved gas in oil or water).

When hydrate dissociates, it splits into methane and water. One molecule of hydrate gives off approximately 1 molecule of methane and 5.75 molecules of water. The hydrate dissociation mechanism can be represented by an irreversible first-order chemical reaction, where hydrate (reactant) undergoes physical change into water and

free gas in the presence of additional heat of dissociation. The chemical reaction is given by



where  $\Delta H$  is the heat of dissociation of hydrates, BTU/lbmole. The reaction rate constant,  $k_d$ , is defined by the Arrhenius equation. The value of each component in the Arrhenius equation can be provided through a user interface or by using the keywords \*FREQFAC, \*RENTH, \*EACT. The Arrhenius equation is given by

$$k_d = k_d^o \exp\left(-\frac{E_a}{RT}\right) \quad (3.17)$$

where  $k_d$  - reaction rate constant, lbmole/lb-day;  $k_d^o$  - frequency factor (CMG Keyword \*FRQFAC);  $E_a$  - activation energy (CMG Keyword, \*EACT), BTU/lbmole;  $R$  - universal gas constant (CMG default property), BTU/lbmole-°R; and  $T$  - reservoir temperature, °R. The rate of hydrate decomposition is given by the Kim Bishnoi Model (Kim et al., 1987) as presented in Equation 3.18.

$$\frac{dC_H}{dt} = k_d A_d [P_{se}(t) - P(t)] \quad (3.18)$$

where  $\frac{dC_H}{dt}$  - rate of hydrate decomposition, lbmole/ft<sup>3</sup>-day;  $k_d$  - reaction rate constant, lbmole/lb-day;  $A_d$  - surface area per unit volume, ft<sup>1</sup>;  $P_{se}(t)$  - equilibrium pressure, psi; and  $P(t)$  - average reservoir pressure (time dependent), psi.

As observed above, the rate of reaction is governed by the extent of deviation observed from the equilibrium (Uddin et al., 2006). This deviation from equilibrium is governed by the equilibrium parameter, also called the  $K$  parameter. The model's  $K$  parameter is

initialized using the three-phase pressure-temperature equilibrium correlation proposed by Kamath and Holder (1987). The correlation (Equation 3.2) is a good approximation of the methane hydrate thermodynamic relationship. The following CMG-STARs keywords were used to define  $K$  parameter:  $rxk1$ ,  $rxk2$ ,  $rxk3$ ,  $rxk4$ , and  $rxk5$  (Howe, 2004). The three-phase equilibrium parameter is defined as

$$K(t) = \frac{P_{se}(t)}{P(t)} \quad (3.19)$$

Combining Equations (3.2) and (3.19),  $K$  value is given by the expression

$$K(t) = \left(\frac{1}{P(t)}\right) \exp\left(38.9803 - \frac{8533.80}{T_{se}(t)}\right) \quad (3.20)$$

where  $T_{se}(t)$  - equilibrium reservoir temperature, °K. In CMG-STARs, the above expression is represented by

$$K(t) = \left(\frac{rxk1}{P(t)} + rxk2 \times P(t) + rxk3\right) \exp\left(\frac{rxk4}{T_{se}(t) - rxk5}\right) \quad (3.21)$$

where  $rxk1$ ,  $rxk2$ ,  $rxk3$ ,  $rxk4$ , and  $rxk5$  are the coefficients defining equilibrium parameter,  $K$ .

#### 3.4.2.5 Relative Permeabilities and Capillary Pressure Functions

The relative permeability models proposed by Hong (2003) were used to develop relative permeabilities and capillary pressure functions. For detailed discussion on Hong (2003) model, refer discussion on the experimental study (Equations 3.8, 3.9, 3.10, 3.11, 3.12, and 3.13).

The three-phase (hydrate-gas-water) relative permeability was represented in CMG-STARS using Stone II (Stone, 1973) model (normalized). For the EB and WAL models a single rock type was considered. The rock type was assumed to be completely water-wet. Two relative permeability curves (water-hydrate table and hydrate-gas table) were initialized to define the relative flow of each phase. CMG-STARS allows smoothing of the relative permeability curve by providing the option of end-point rescaling. Based on the known end-point data, the three-phase relative permeability can be easily re-scaled to match reservoir fluid flow conditions.

#### *3.4.2.6 Production Well Modeling*

CMG-STARS provides a powerful tool to initialize a well as a producer or injector. A discretized wellbore option helps in defining the well horizontally, vertically, or in any layer by defining it on a cell-to-cell basis. These wells can be produced or shut-in at any time or time period during the production life of the reservoir, depending on the actual field conditions. Well completions can also be altered at any time during the production.

The wells are produced with the help of constraints. These constraints range from operating at “MIN” flowing bottomhole pressure, to “MAX” gas production rate. Users can monitor other parameters such as free gas-oil ratio (GOR) in order to shut-in the well whenever the set limit is reached. Any number of constraints can be given to the well. The first constraint given to any well is called the primary constraint. Simulator controls the primary constraint first and then attempts to maintain other constraints, if given. These constraints can be altered at any time based on the production data. The well constraints can also be imported from production data file. For the EB and WAL reservoirs, monthly production data were loaded (imported) for each well.

### 3.4.3 Model Initialization

#### 3.4.3.1 East Barrow Gas Field

Several reservoir models were initialized, and the results were matched with the production history data. The history matching criteria and results are explained in subsequent sections. Based on history matching studies a best-case model was selected.

The best-case scenario consisted of a hydrate-cap overlying the free gas zone and underlain with the *model aquifer*. This section discusses the reservoir properties and wellbore initialization procedures followed for the best-case. All parameters were initialized in field units.

##### *a. Reservoir Grid*

Based on reservoir geology and well log data (as explained before), a detailed reservoir model depicting the EB gas reservoir was constructed using ROXAR RMS<sup>R</sup> (Panda and Morahan, 2008). The data file generated using the software was directly imported into CMG-STARs using \*INCLUDE keyword.

The model was generated using a corner point grid system by choosing a grid having 54 blocks in I, 37 blocks in J, and 25 blocks in K directions, using a total of 49,950 gridblocks. Based on geologic information, several gridblocks were rendered inactive by using the \*NULL keyword. These gridblocks were not part of the active reservoir volume. The dimension of each gridblock was 600 ft by 600 ft (IJ plane). The gridblock thickness in K direction was variable and ranges anywhere between 1.09 ft and 3.22 ft. The gridblocks were thinner in the updip section (west direction) and thicker in the downdip locations (east direction). The topmost section of the reservoir was at a depth of 1900 ft below sea level, whereas the deepest section was at a depth of 2330 ft below sea level. However, the pay zone range was between 1901 ft to 2328 ft below sea level. The 3D

reservoir grid is shown in Figure 3.8. Figures 3.9, 3.10, and 3.11 present the IJ view of the reservoir grid at plane 1 (K=1), plane 12 (K=12), and plane 25 (K=25) respectively.

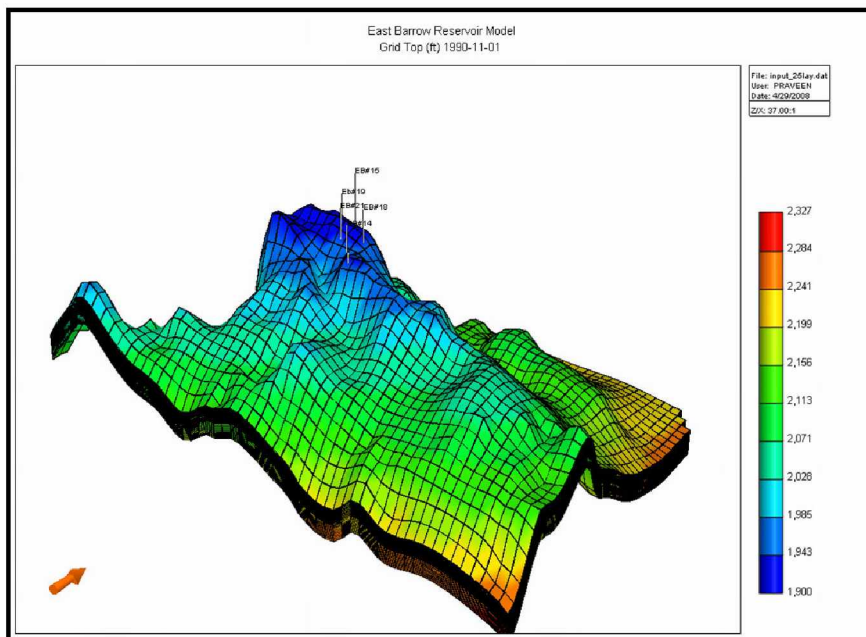


Figure 3.8: Reservoir Grid - 3D View

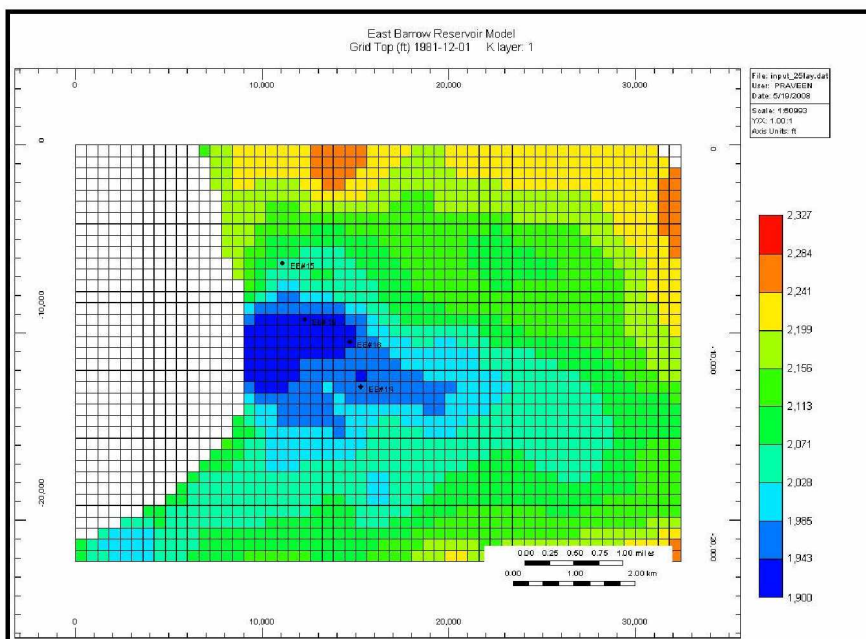


Figure 3.9: Reservoir Grid (K Layer 1) - IJ Plane View

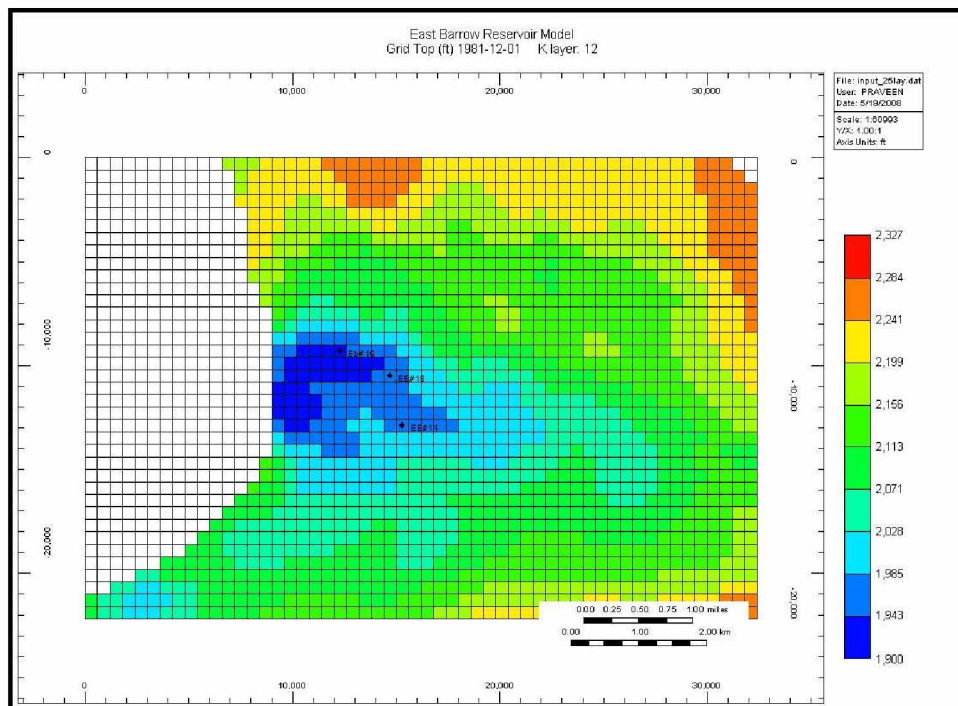


Figure 3.10: Reservoir Grid (K Layer 12) - IJ Plane View

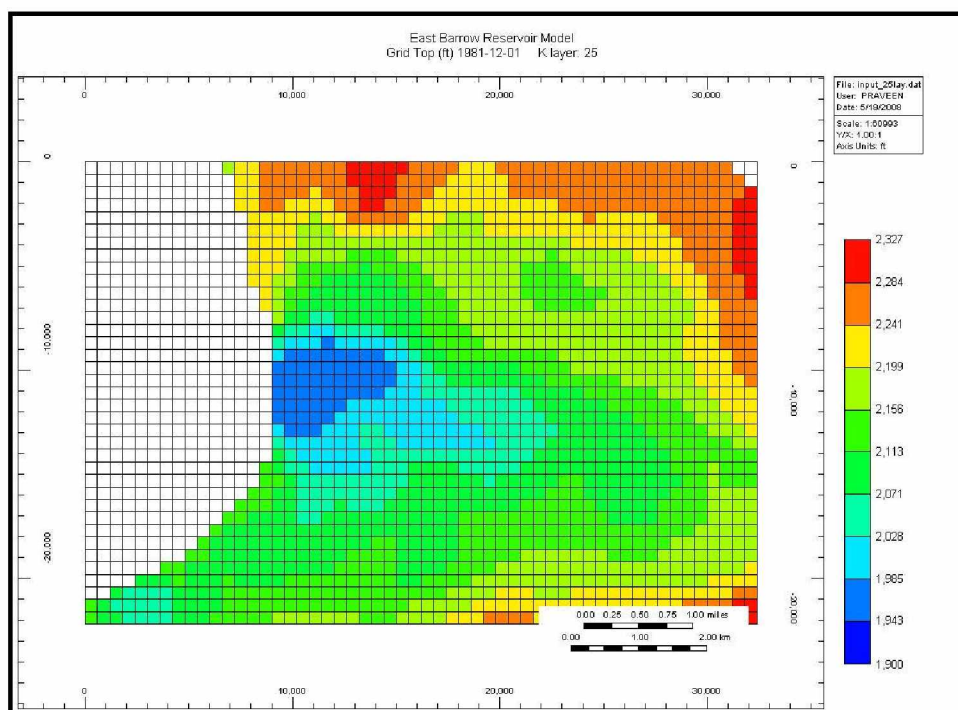


Figure 3.11: Reservoir Grid (K Layer 25) - IJ Plane View

## *b. Reservoir Properties*

### 1. Porosity

For details regarding porosity distribution and estimation procedures refer to work done by Panda and Morahan (2008). The porosity distribution file was loaded into the CMG-STARs data file using the \*INCLUDE keyword. The porosity of the reservoir ranges from 5% (min) to 24% (max). The geological study on the reservoir has identified the existence of semi-permeable barrier (a shaly layer) between Upper and Lower Barrow sand (Panda and Morahan, 2008). To represent a similar condition, layer 16 (K=16) was assigned a lower porosity of 5%. Figure 3.12 shows a 3D view of porosity distribution. Figure 3.13 presents the IJ plane view of the shaly layer (K=16).

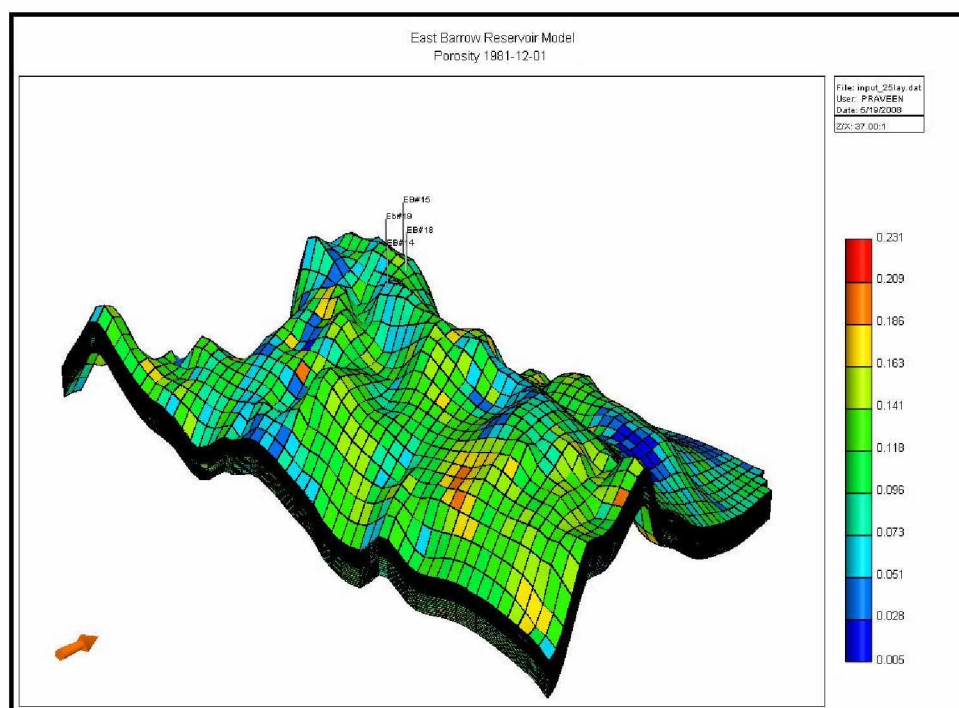


Figure 3.12: Porosity Distribution, % - 3D View



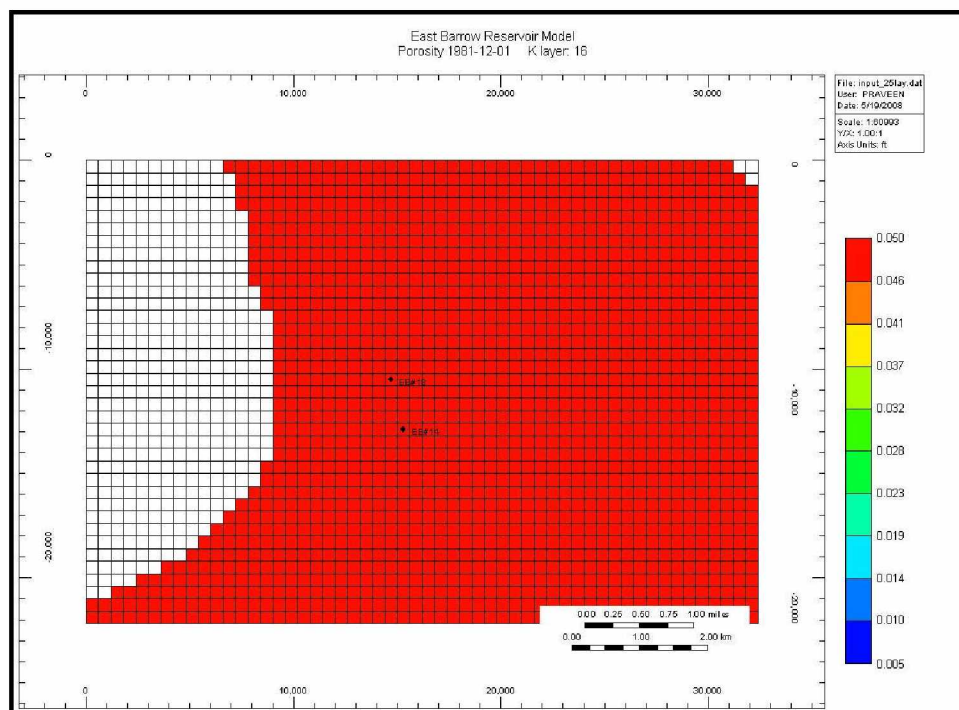


Figure 3.13: Porosity - 5% (K Layer 16) - IJ Plane View

## 2. Permeability

Reservoir permeability was calculated on the basis of well log data. Details regarding reservoir characterization and the geostatistical modeling approach have already been explained by Panda and Morahan (2008). The \*INCLUDE keyword was used to load the permeability data directly into the reservoir model. Reservoir permeability (I, J, and K directions) is predominately low, mostly in the range of 1 to 50 md. As layer 16 (K=16) was identified as a permeability barrier (shaly layer), the entire layer was assigned a constant permeability of 5 md in all directions. Figures 3.14, 3.15, and 3.16 show the 3D view of permeability distribution within the reservoir in I, J, and K directions and Figure 3.17 presents the plan of permeability in I direction (valid for J, and K directions as well) for layer 16 (shaly layer).

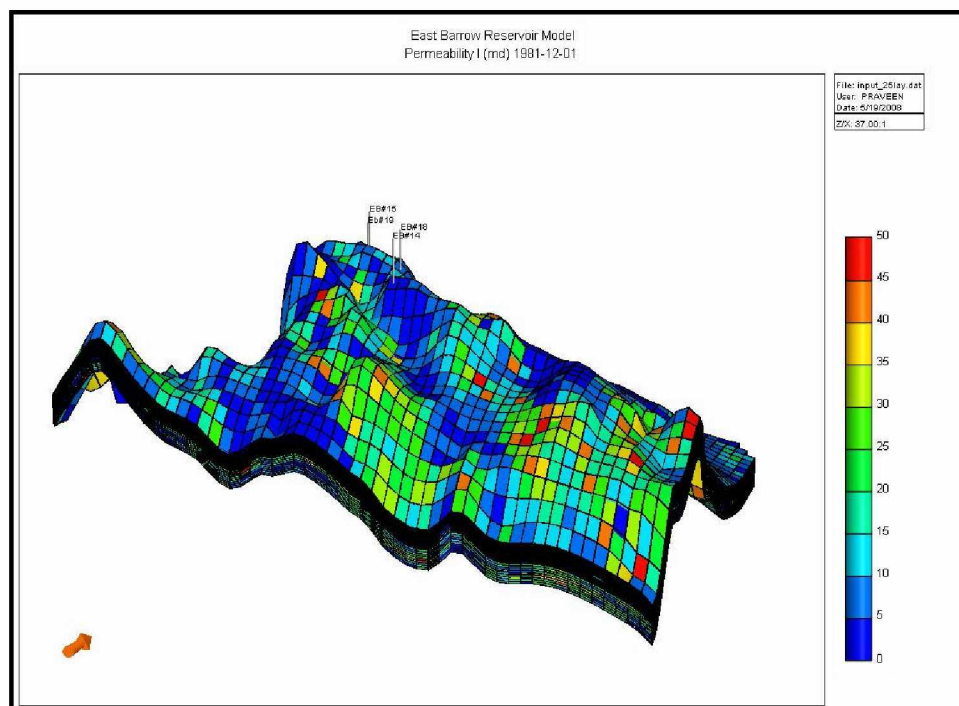


Figure 3.14: Permeability Distribution - I Direction, md - 3D View

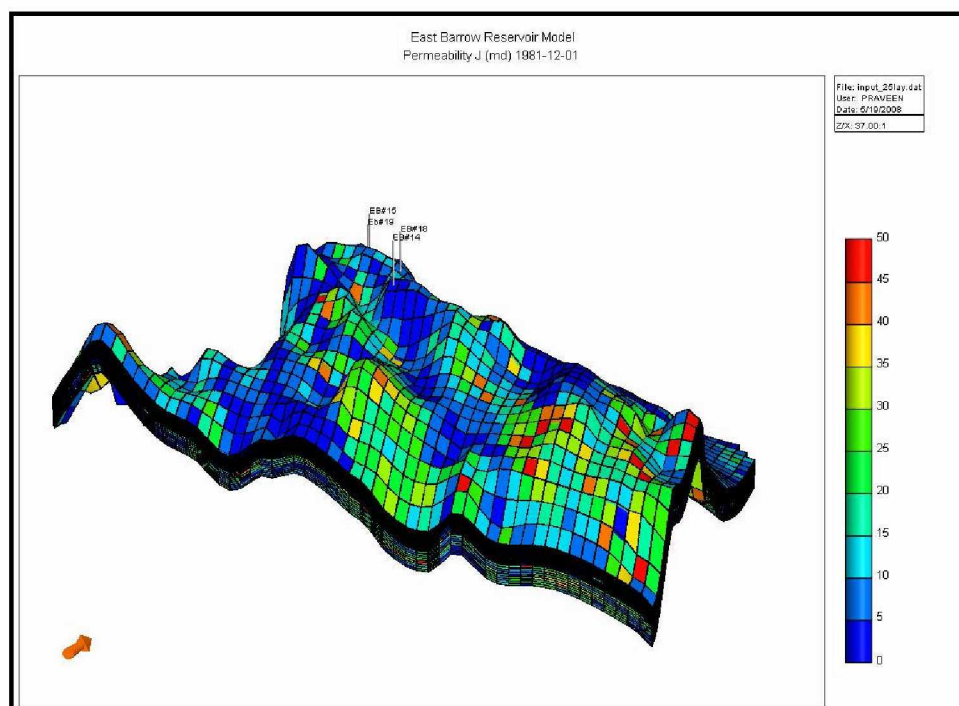


Figure 3.15: Permeability Distribution - J Direction, md - 3D View

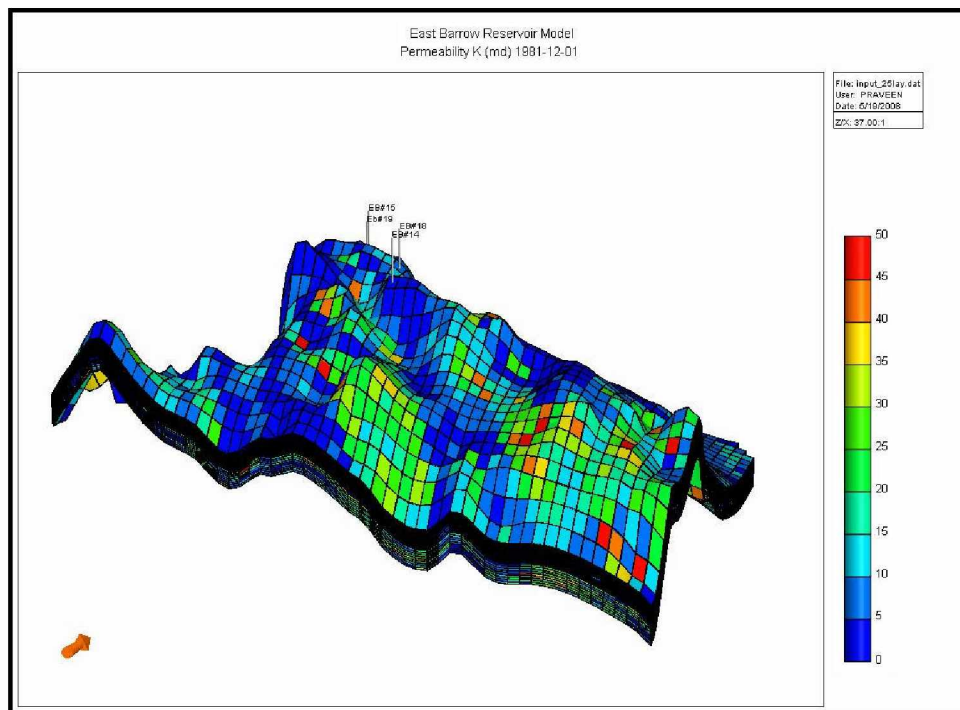


Figure 3.16: Permeability Distribution - K Direction, md - 3D View

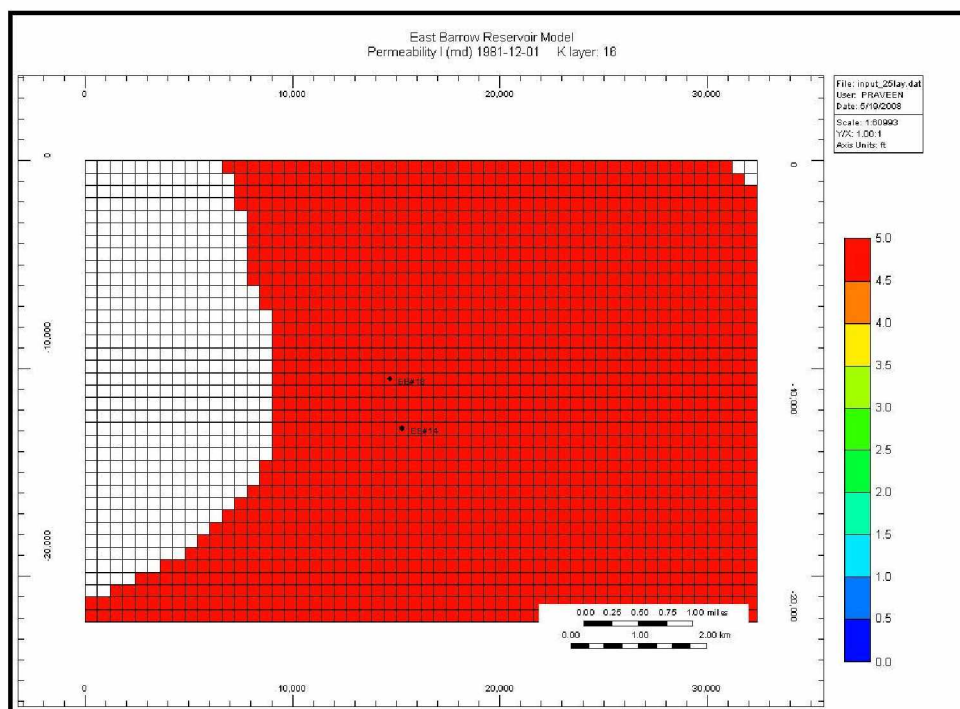


Figure 3.17: Permeability - 5 md (K Layer 16) - IJ Plane View

### 3. Initial Temperature

Geothermal gradient data obtained for the EB reservoir was 1.60 °F/100 ft. The reservoir initial temperature (top) was 41 °F and the bottommost region had a temperature of 47.70 °F. The temperature distribution within the reservoir is initialized on the basis of reservoir depth (Figure 3.18). A formula was written in formula editor and then loaded for the entire model. The formula calculates the initial reservoir temperature at respective depths and initializes each gridblock accordingly (Figure 3.19).

Note that the value 1900 in formula editor (Figure 3.19) is the depth to the top of the reservoir, and 41 is the corresponding temperature, whereas  $X0$  (variable) is the depth of the reservoir at a particular gridblock. The formula is given as

$$X0 \times 0.016 + 41$$

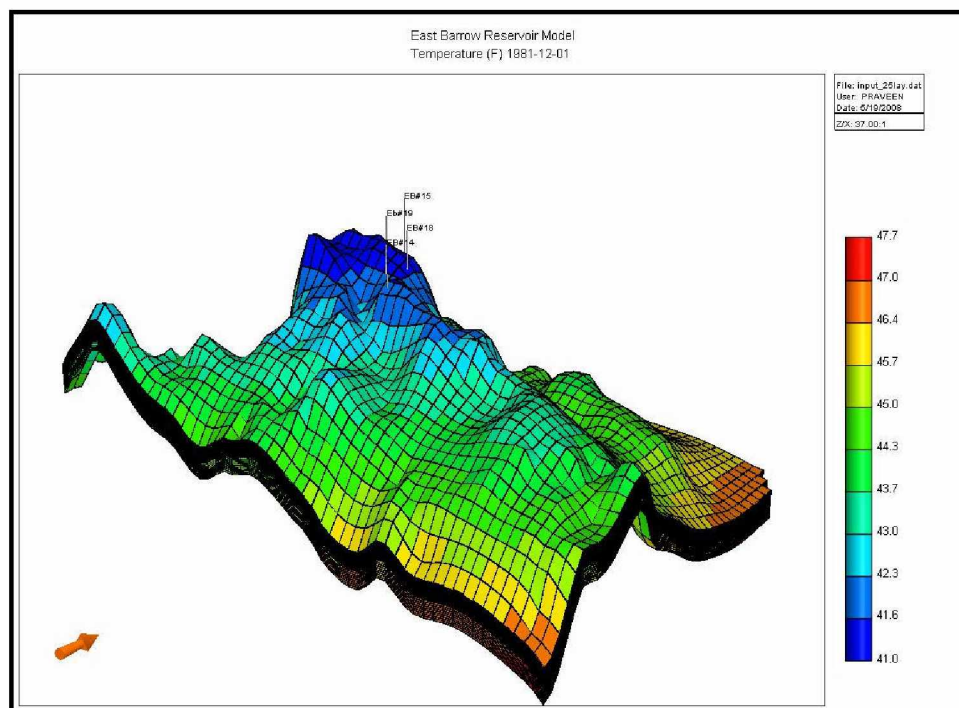


Figure 3.18: Initial Temperature Distribution, °F (on Dec 01, 1981) - 3D View



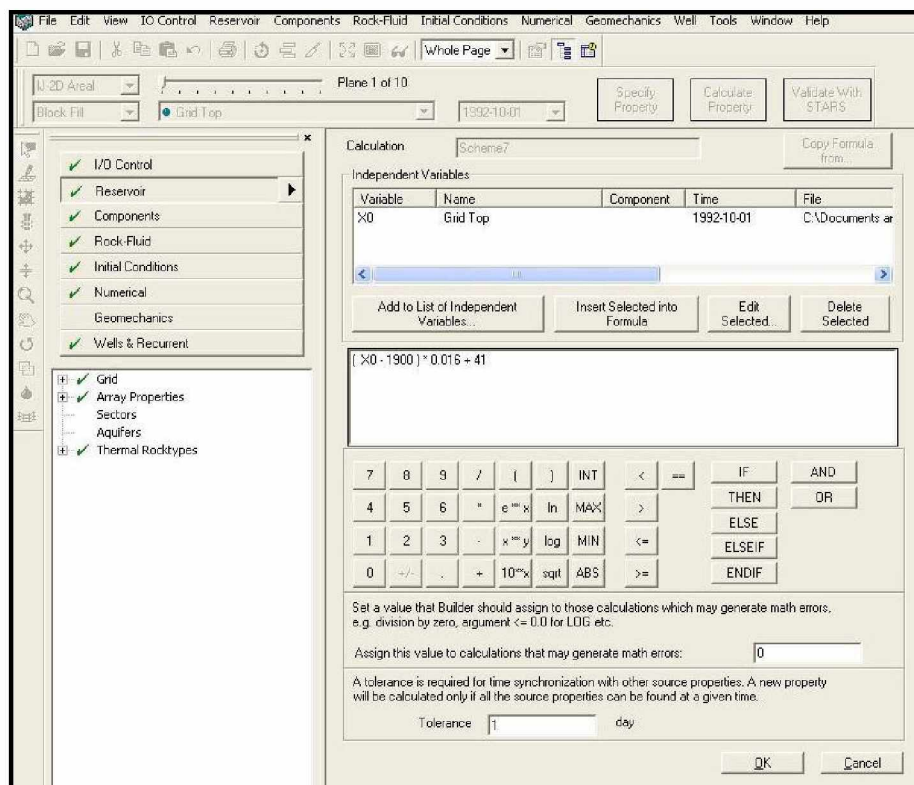


Figure 3.19: Formula Editor - Initializing Temperature Distribution

#### 4. Initial Reservoir Pressure

Well-testing and pressure gradient data reported in previous studies (Gruy, 1978; Panda and Morahan, 2008) conducted for the EB gas pool concluded that the initial reservoir pressure is 975 psi. Since the model is comprised of hydrate-cap and free gas zone underlain with a weak *model aquifer*, the effect of gravity on reservoir pressure within the all three zones were neglected. The entire reservoir was initialized with an average reservoir pressure of 975 psi (Figures 3.20 and 3.21). The effect of gravity segregation can be removed by switching the “vertical equilibrium calculations” to OFF mode.

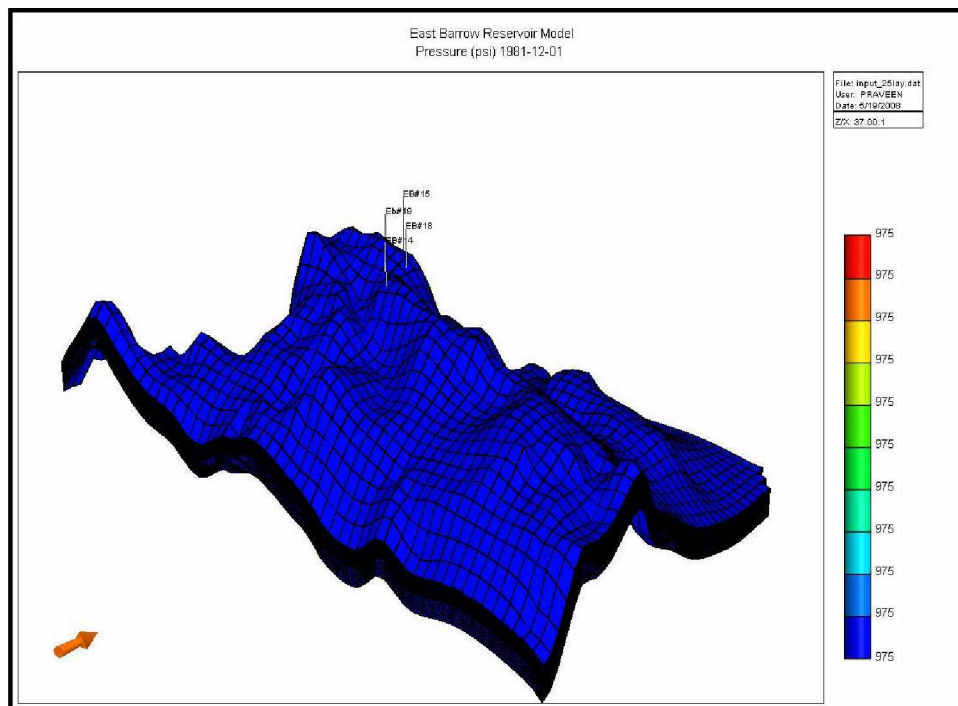


Figure 3.20: Initial Pressure, psi (on Dec 01, 1981) - 3D View

**STARS Initial Conditions**

Vertical Equilibrium Calculation Methods

Depth-Average Capillary-Gravity Method ( VERTICAL\_DEPTH\_AVE )

Do Not Perform Vertical Equilibrium Calculations ( VERTICAL OFF )

Pseudo Time-Step  Not Recommended, may be removed in the future.

Only Pressure Changes ( VERTICAL\_ON\_PSTEP n )

All Properties Change ( VERTICL\_ALLPROP\_PSTEP n )

Initialization Region

Region 1: Initialization Region Specifications  
Initialization Set Number 1 is not defined. Grid depth range: 1899.98 to 2329.76 ft

Reference Pressure ( REFPRES ):

Location For Reference Pressure

Reference Depth ( REFDEPTH )

Reference Block ( REFBLOCK )  
(UBA Format i.e. i1 j1 k1 / i2 j2 k2 ... )

Initial Reservoir Saturation

Water-Oil Contact Depth ( DWOC )

Gas-Oil Contact Depth ( DGOC )

Figure 3.21: Initial Condition - No Vertical Equilibrium Calculation

## 5. Initial Hydrate Saturation

Thermodynamic condition of pressure-temperature (Figure 3.22) for the EB gas field lies very close to the three-phase pressure-temperature equilibrium curve ( $L_w - H - V$ , basis 100% methane). This means that the hydrates are susceptible to dissociation even with a small change in local pressure or temperature. Higher local geothermal gradients could be one of the reasons for possible discontinuity in hydrate distribution within the hydrate zone (at same depth). To initialize this condition in CMG-STARs, the three phases (i.e., hydrates, free gas, and bounded water) were assumed to be existing together in the hydrate zone, uniformly distributed within the pore spaces. The HGC for the EB gas reservoir was estimated to be at 2050 ft (Panda and Morahan, 2008).

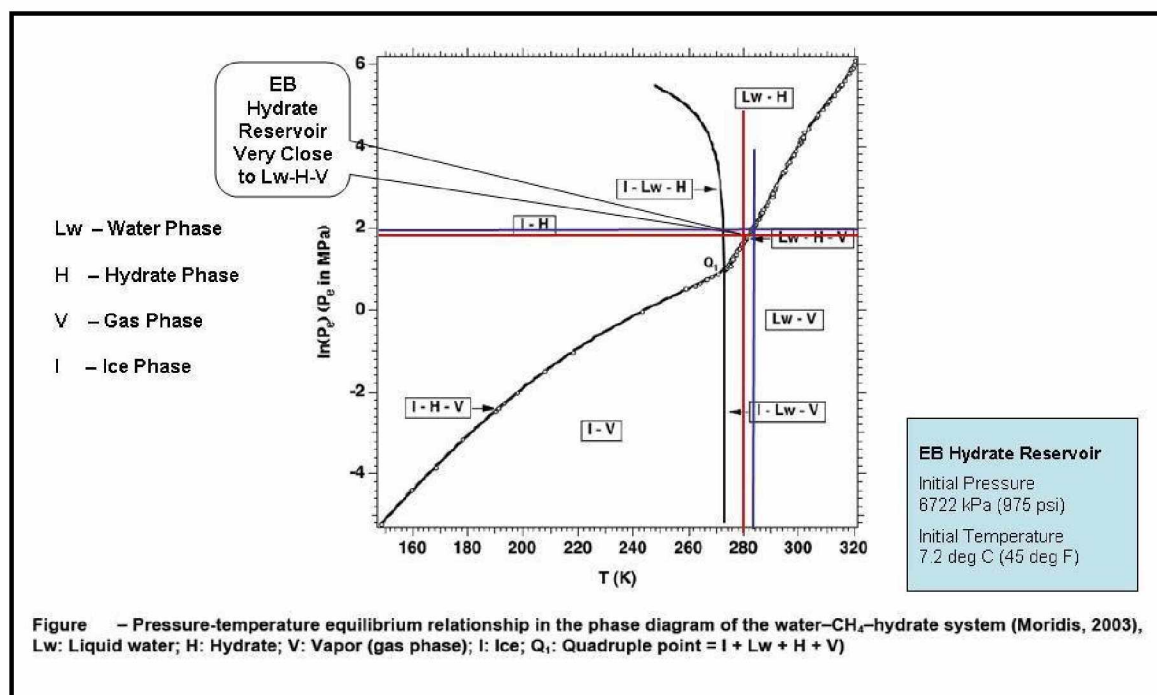


Figure 3.22: Pressure-Temperature Equilibrium Curve Showing Initial Thermodynamic Condition of the EB Reservoir (Modified from Moridis, 2003)

History matching and sensitivity studies confirmed that the EB reservoir is overlain with a thick hydrate-cap. An average hydrate saturation of 31% was able to best match the

production data (explained in later section). Moreover, CMG-STARS was not able to simulate scenarios with hydrate saturation greater than 40% (explained later).

Physical evidence of similar hydrate saturations of 33.9% and 32.6% were reported by Collett (2002) for NWE (ANS) sand units D and E, respectively. These were a vital piece of physical evidence that correlated well with the proposed EB hydrate distribution.

To initialize hydrate saturation, a formula was written using formula editor. The formula was developed using grid bottom depth, hydrate saturation parameter, and HGC data. The formula defines a hydrate saturation of 31% to all gridblocks where the depths were equal or shallower than 2050 ft but deeper than 1900 ft. For all other gridblocks, the formula assigned a hydrate saturation of 0% (Figure 3.23). Figure 3.24 is the 3D view of hydrate distribution. Figure 3.25 is a two-dimensional (2D) IJ plane view of the top layer showing hydrate distribution. Figure 3.26 is a magnified 2D (IK plane) image showing HGC at 2050 ft. The formula is given as

$$IF((X0 > 1900)AND(X0 \leq 2050))THEN((X1 \times 0.31))ELSE((X1 \times 0))$$

where  $X0$  - grid bottom depth, ft and  $X1$  - initial hydrate saturation, %.



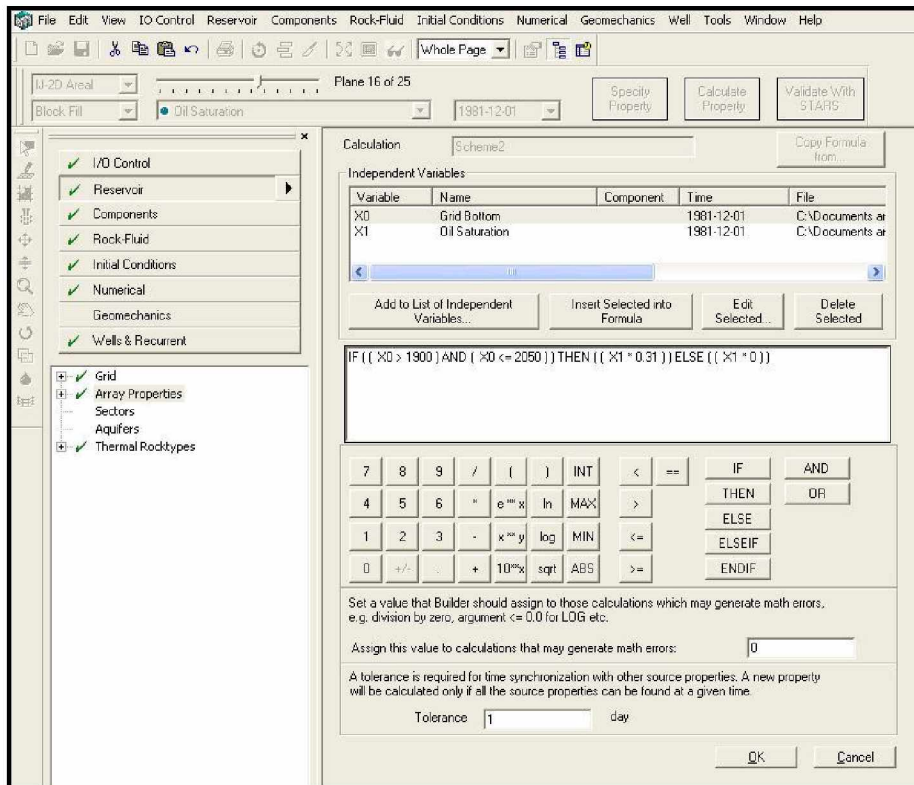


Figure 3.23: Formula Editor - Initializing Hydrate Saturation

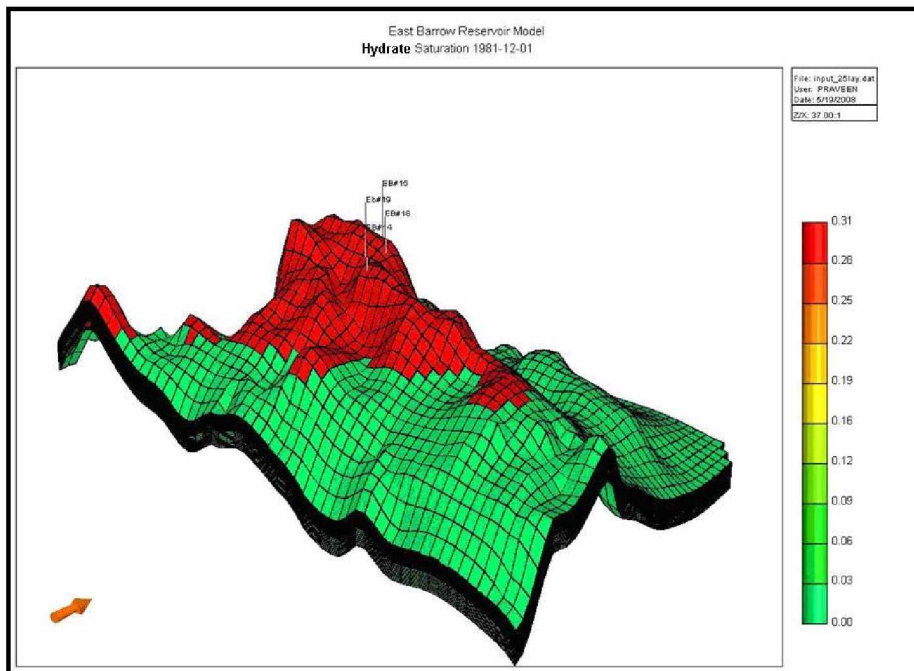


Figure 3.24: Initial Hydrate Saturation, % (on Dec 01, 1981) - 3D View

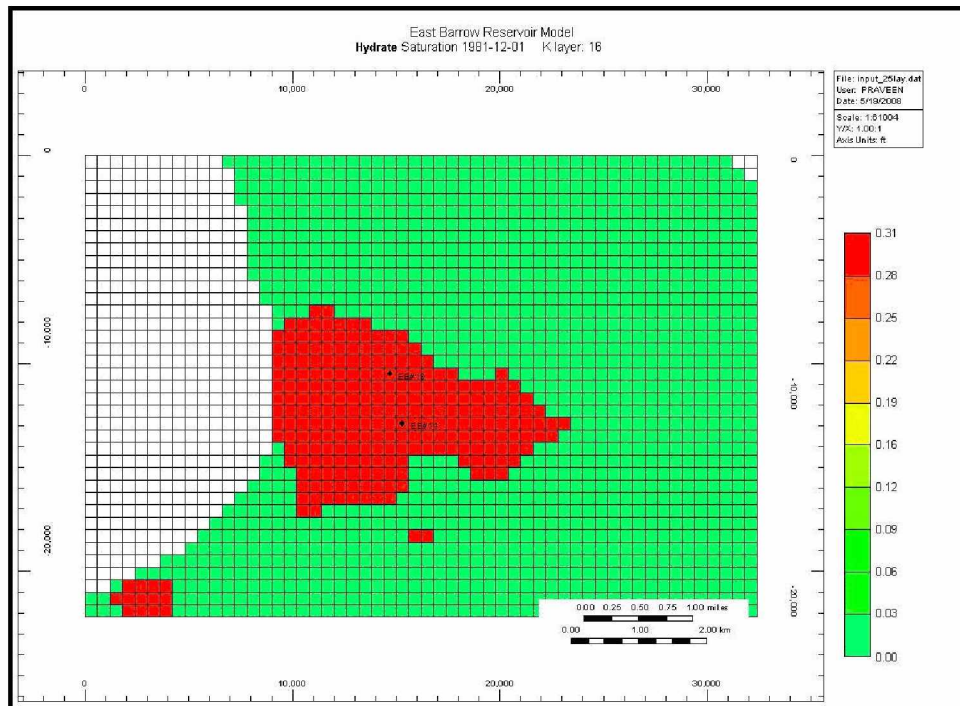


Figure 3.25: Initial Hydrate Saturation, % (K Layer 1) - IJ Plane View

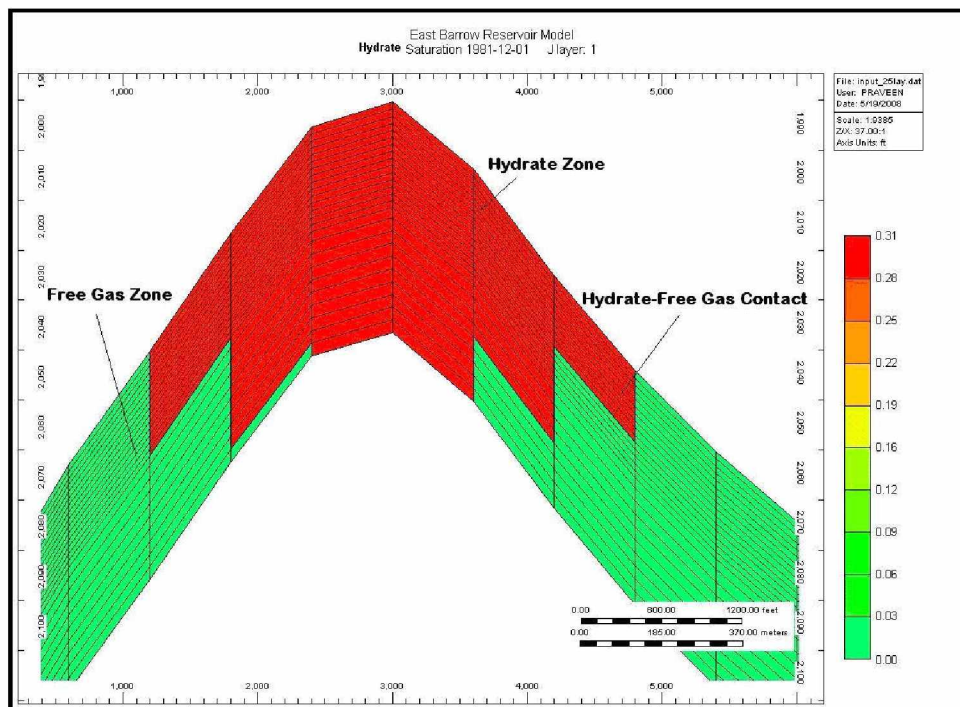


Figure 3.26: Initial HGC (on Dec 01, 1981) - IK Plane View

## 6. Initial Gas Saturation

Just below the hydrate-cap is the free gas zone. However, since the thermodynamic condition of the hydrate zone is such that the hydrate phase and free gas phase exist together in the hydrate zone (pocket of free gas) along with the bounded water phase, the gas phase saturation needs to be defined for both hydrate zone and free gas zone. Well logs have shown that the connate (bounded) water saturation for both the hydrate and free gas zone is 55%, and the GWC was around 2080 ft (Panda and Morahan, 2008). Hence, the initial free gas saturation of 14% was initialized in the hydrate zone and 45% in the free gas zone.

To initialize free gas saturation, a formula was written using formula editor. The formula was developed using grid bottom, gas saturation, HGC, and GWC data. The formula defined an initial gas saturation of 14% to all gridblocks where the depth was equal or shallower than 2050 ft but deeper than 1900 ft. For a depth range of 2050 ft to 2080 ft the initial gas saturation was initialized at 45%. For all other gridblocks (those lying outside the range), the formula assigned a gas saturation of 0% (Figure 3.27). Figure 3.28 shows a 3D view of free gas distribution. Figure 3.29 is a 2D view (IJ plane) showing gas distribution. Figure 3.30 is a 2D (IK plane) image showing HGC and GWC at 2050 ft and 2080 ft, respectively. The formula is given as

$$IF((X0 > 1900) AND (X0 \leq 2050)) THEN ((X1 \times 0.14)) ELSE IF ((X0 > 2050) AND (X0 \leq 2080)) THEN ((X1 \times 0.45)) ELSE ((X1 \times 0))$$

Where  $X0$  - grid bottom depth, ft; and  $X1$  - initial gas saturation, %.

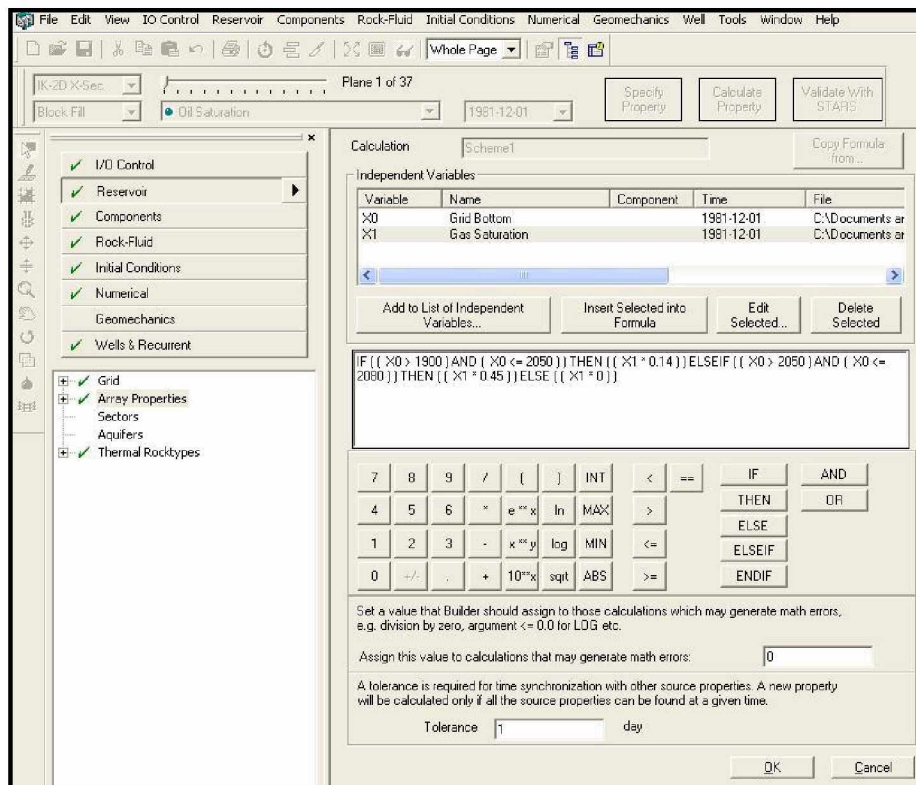


Figure 3.27: Formula Editor - Initializing Gas Saturation

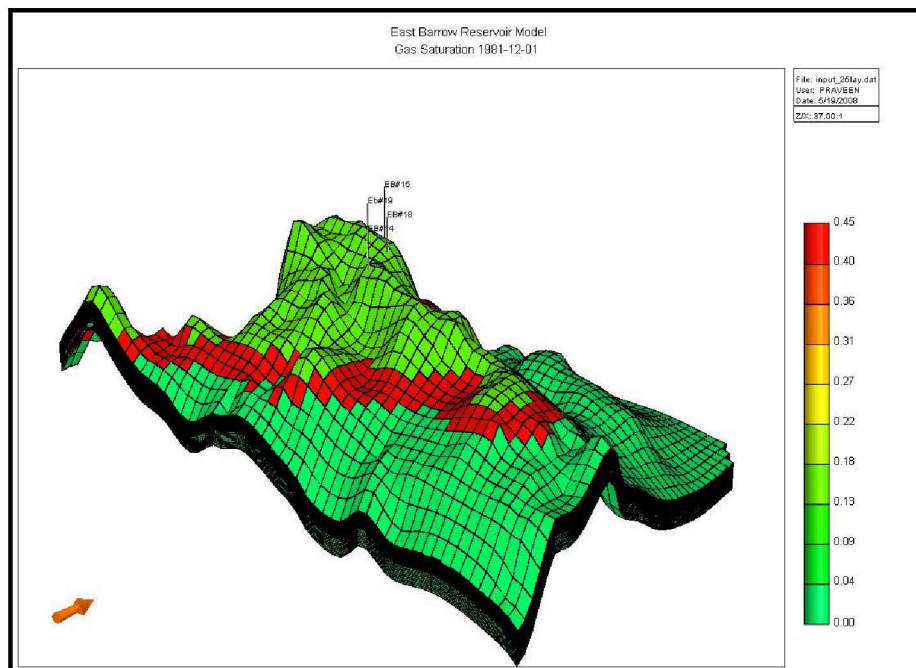


Figure 3.28: Initial Gas Saturation, % (on Dec 01, 1981) - 3D View



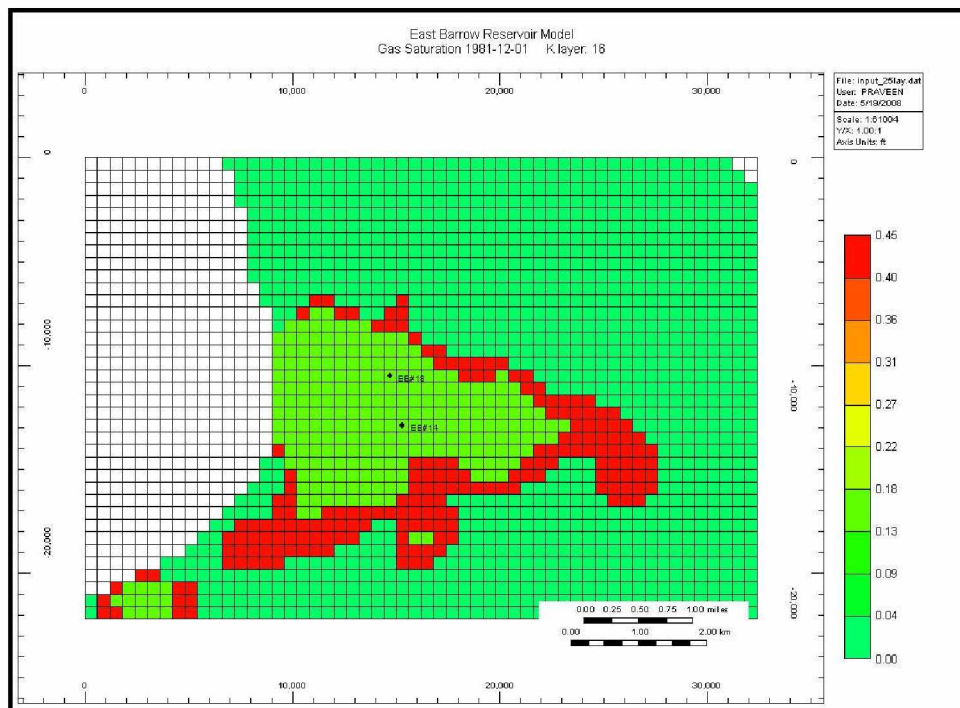


Figure 3.29: Initial Gas Saturation, % (K Layer 1) - IJ Plane View

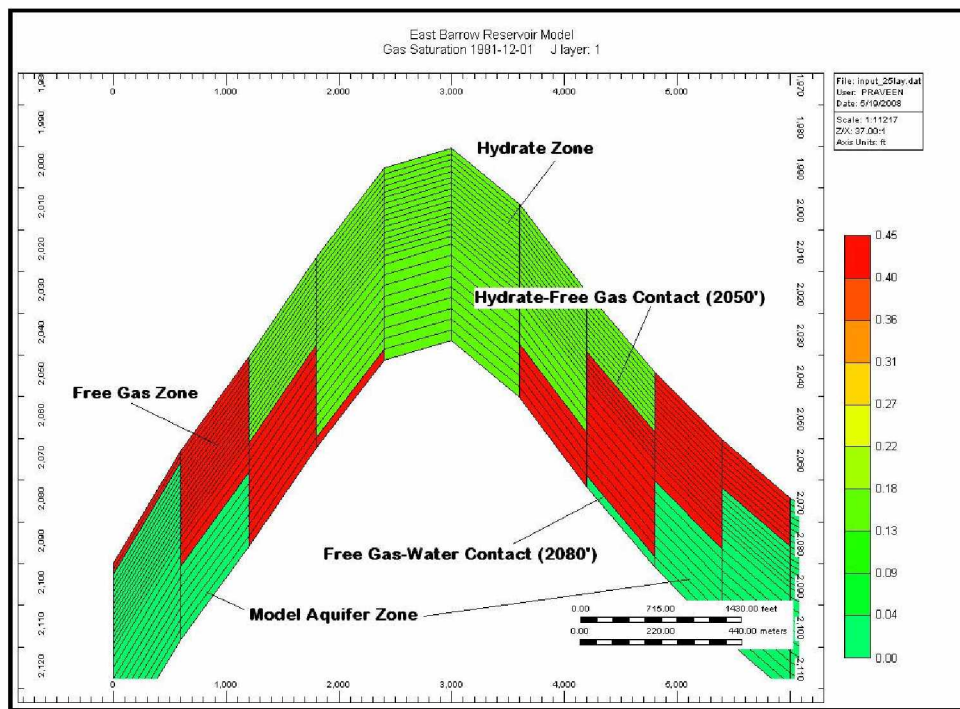


Figure 3.30: Initial HGC and GWC (on Dec 01, 1981) - IK Plane View

## 7. Initial Water Saturation

As stated earlier, well log data suggested that the initial bounded water saturation in hydrate and free gas zones is very high, i.e., 55%. Well log data and the material balance study showed the presence of weak aquifer below the free gas zone. CMG-STARS offers different aquifer models (called *numerical aquifer*) that can be easily attached to a given hydrate-free gas system, but in order to improve the reservoir accuracy, the aquifer was constructed as part of the reservoir model (called *model aquifer*). *Model aquifer* zone is created by initializing the zone with an initial water saturation of 100%.

To initialize water saturation, a formula was written using formula editor. The formula was developed using grid bottom, initial water saturation and GWC data. The formula defines an initial water saturation of 55% to all gridblocks where the grid depth was equal or shallower than 2080 ft but deeper than 1900 ft. For all other gridblocks (those lying outside the range), the formula assigned an initial water saturation of 100% (Figure 3.31). Figure 3.32 shows a 3D view of water distribution. Figure 3.33 is a 2D view (IJ plane) showing water distribution. Figure 3.34 is a 2D (IK plane) image showing free gas-water contact at 2080' ft. The formula is given as

$$IF((X0 > 1900)AND(X0 \leq 2080))THEN((X1 \times 0.55))ELSE((X1 \times 1))$$

where  $X0$  - grid bottom depth, ft and  $X1$  - initial water saturation, %.

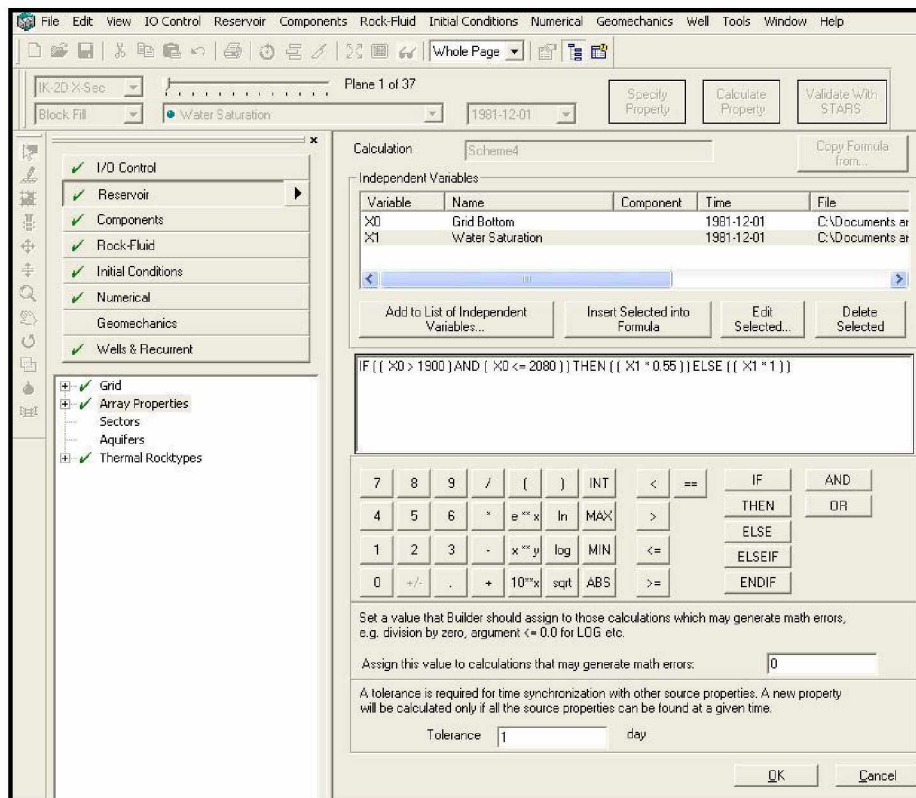


Figure 3.31: Formula Editor - Initializing Water Saturation

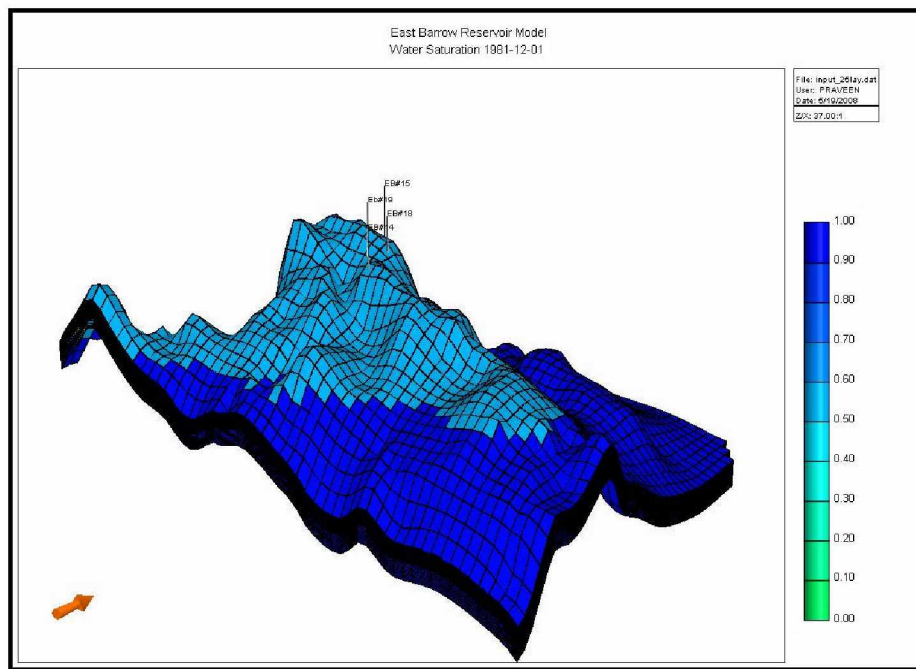


Figure 3.32: Initial Water Saturation, % (on Dec 01, 1981) - 3D View

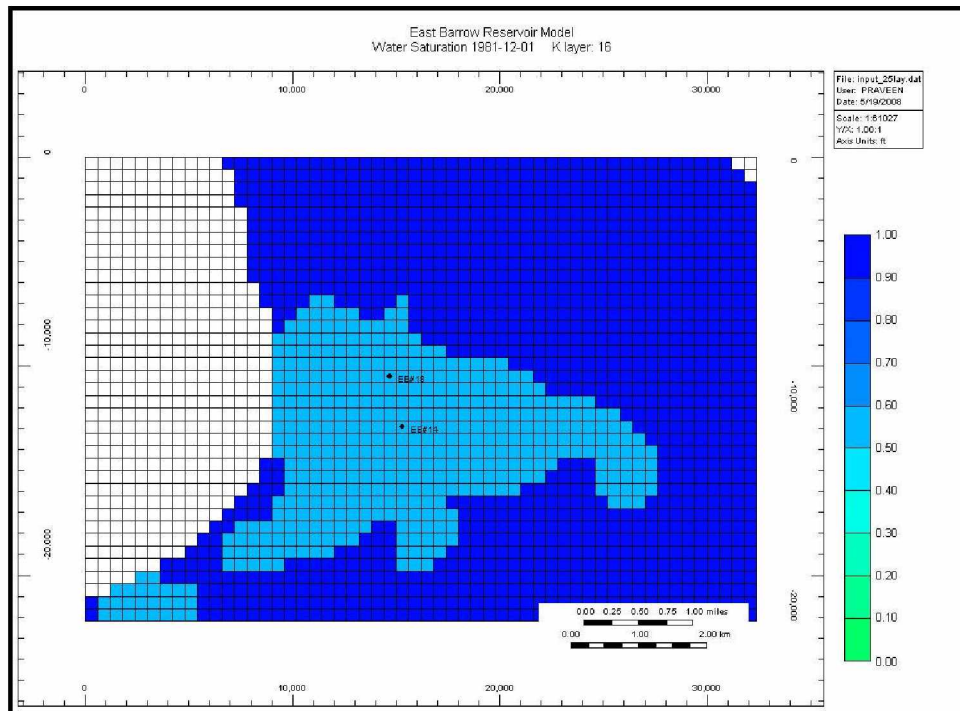


Figure 3.33: Initial Water Saturation, % (K Layer 1) - IJ Plane View

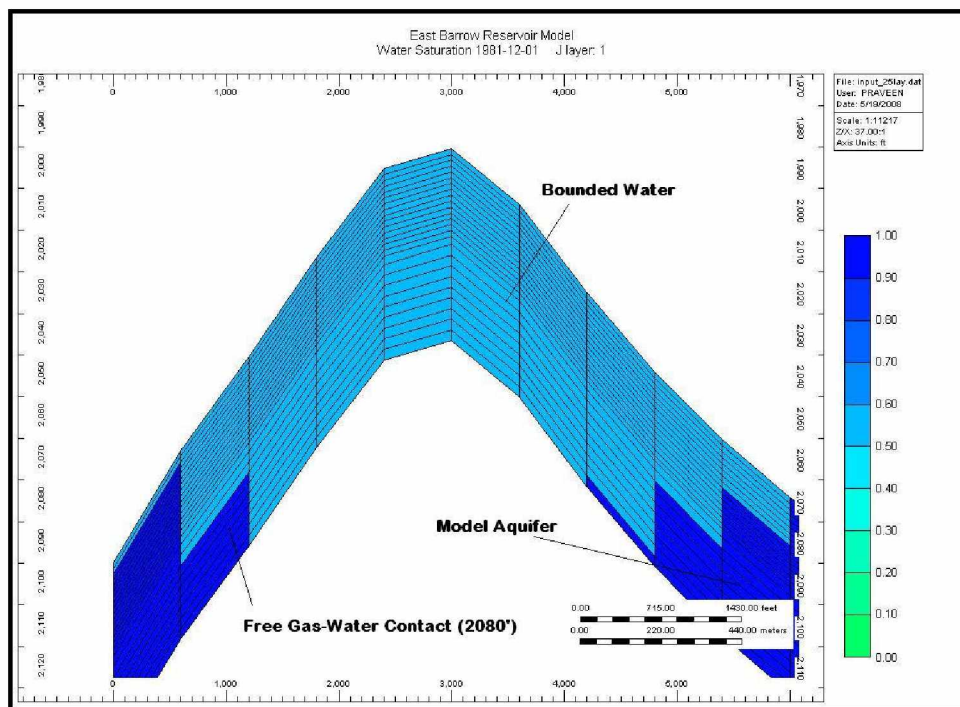


Figure 3.34: Initial GWC (on Dec 01, 1981) - IK Plane View



The initial condition for the best case are summarized in Table 3.4 presented below.

Table 3.4: Summary of Initial Condition for the EB Reservoir Model (Best Case)

Zone	Pressure	Temperature	Saturation	Remarks
Hydrate	975 psi	Temperature Gradient 1.60 °F/100 ft	$S_h = 31\%$ $S_g = 14\%$ $S_w = 55\%$	Lying Close to $L_w - H - V$ (Equilibrium) Curve
Free Gas*		Top Temp 41 °F	$S_g = 45\%$ $S_w = 55\%$	*HGC - 2050 ft
Aquifer**			$S_w = 100\%$	**GWC - 2080 ft

#### c. Thermal Properties

Refer to Appendix G.

#### d. Fluid Component Properties

Refer to Appendix G.

#### e. Relative Permeabilities and Capillary Pressure Functions

The three-phase relative permeability data developed by Howe (2004) had lower initial water saturation of 20%. Since the initial water saturation in case of the EB is very high (55%), the end-point rescaling was performed on the available data to represent the reservoir fluid flow conditions. Figures 3.35 and 3.36 show the hydrate-water two-phase relative permeability curve and water capillary pressure curve, respectively. Figures 3.37 and 3.38 show the free gas-hydrate two-phase relative permeability curve and gas capillary pressure curve, respectively.

Table 3.5 summarizes the end-point saturations and relative permeability data for the hydrate-water (\*SWT) relative permeability curve. Table 3.6 summarizes the end-point

saturations and relative permeability data for the free gas-hydrate (\*SLT) relative permeability curve.

Table 3.5: End-Point Saturation and Relative Permeability for Hydrate-Water System

<b>End-Point Saturations</b>	
Critical Water Saturation ( $S_{wcrit}$ )	0.55
Irreducible Hydrate Saturation ( $S_{oirw}$ )	0.00
Connate Water Saturation ( $S_{wcon}$ )	0.55
Residual Hydrate Saturation ( $S_{orw}$ )	0.40
<b>End-Point Relative Permeability</b>	
Water Relative Permeability (Single-Phase Flow) $k_{rw}$ End-Point (Max $k_{rw}$ )	0.70
Hydrate Relative Permeability (Single-Phase Flow) $k_{row}$ End-Point (Max $k_{row}$ )	0.0001

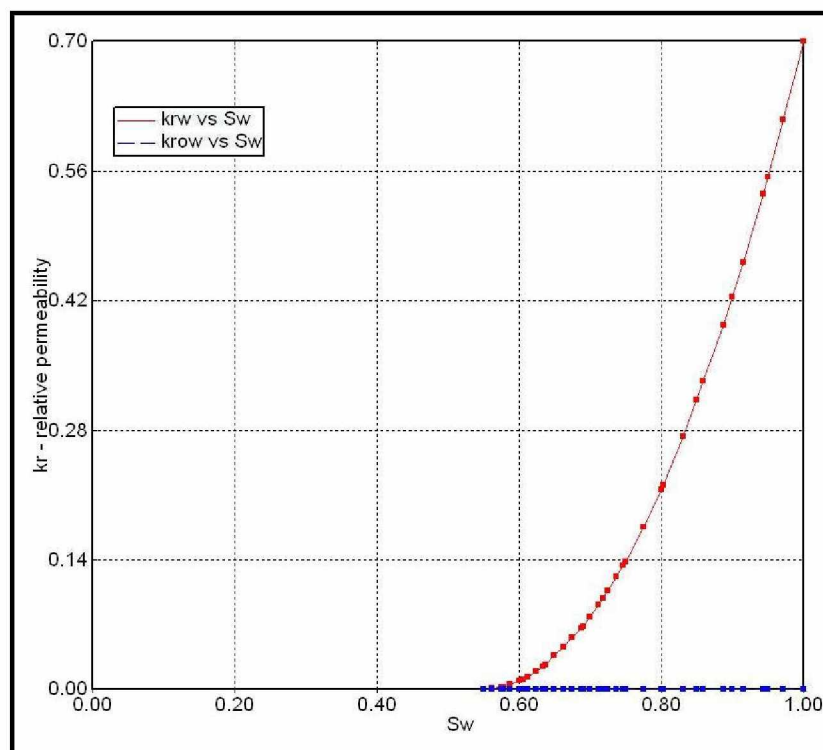


Figure 3.35: Hydrate-Water Relative Permeability Curve (CMG Keyword \*SWT)

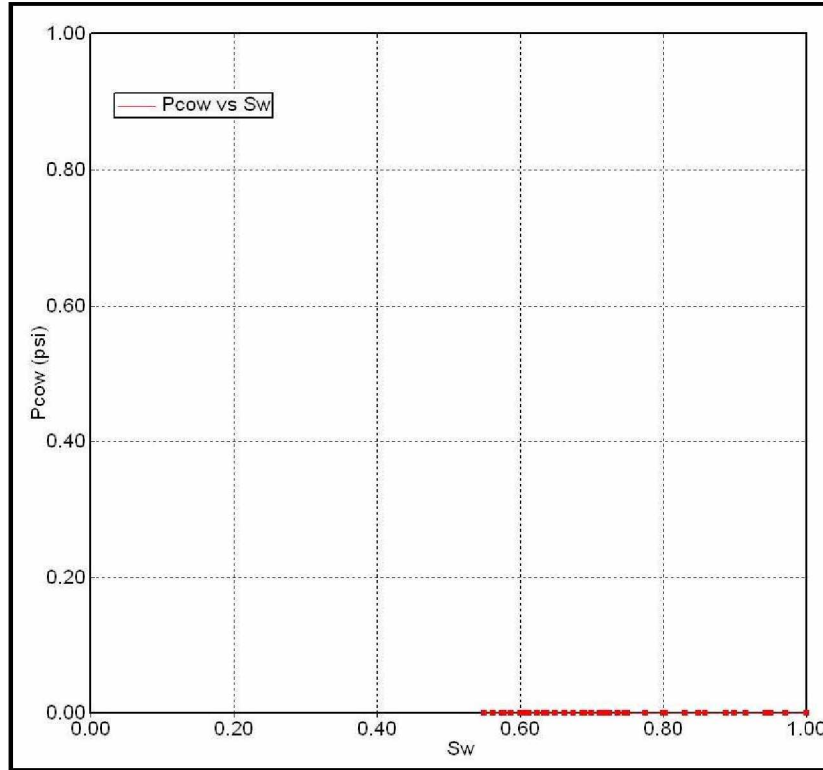


Figure 3.36: Water Capillary Pressure (CMG Keyword \*SWT)

Table 3.6: End-Point Saturation and Relative Permeability for Gas-Hydrate System

<b>End-Point Saturations</b>	
Critical Gas Saturation ( $S_{gcrit}$ )	0.05
Connate Hydrate Saturation ( $S_{lcon}$ )	0.55
Connate Gas Saturation ( $S_{gcon}$ )	0.05
Residual Hydrate Saturation ( $S_{orl}$ )	0.55
<b>End-Point Relative Permeability</b>	
Gas Relative Permeability (Single-Phase Flow) $k_{rg}$ End-Point (Max $k_{rg}$ )	0.90
Hydrate Relative Permeability (Single-Phase Flow) $k_{rog}$ End-Point (Max $k_{rog}$ )	9e-005

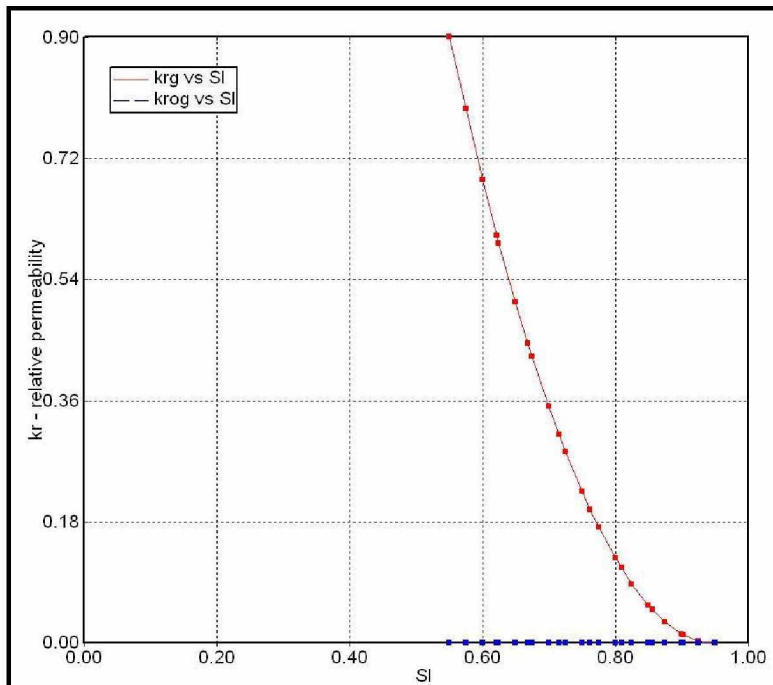


Figure 3.37: Gas-Hydrate Relative Permeability Curve (CMG Keyword \*SLT)

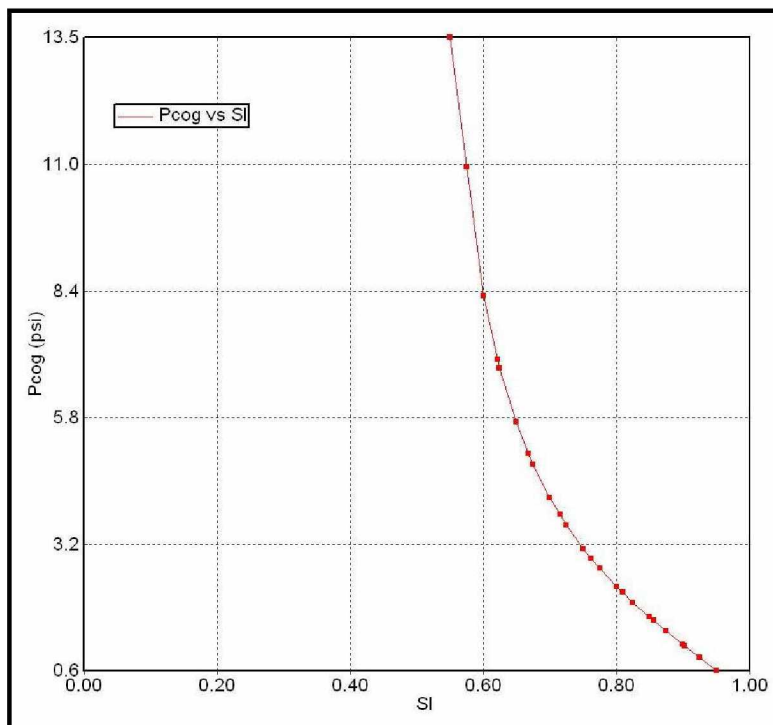


Figure 3.38: Gas Capillary Pressure (CMG Keyword \*SLT)

#### *f. Production Well Modeling*

The EB gas pool was first open to production in Dec 01, 1981. A total of five wells have produced over 8 bcf of methane gas up to Sep 01, 2007. A few of the wells that used to produce initially were later abandoned due to maintenance issues. Currently, EB #14 and #19 are the active wells in the region and contribute substantially to the overall gas production.

##### 1. Production History Data

Production history for the EB gas reservoir was acquired from Stokes and Walsh (2007). The production history data was available from Dec 01, 1981 to Sep 01, 2007. The data included monthly gas and water production rates for individual wells. Flowing bottomhole pressure data was not available. The static reservoir pressure data is limited, but sufficient to perform history matching analysis.

The five wells of the EB gas pool are EB #14, #15, #18, #19, and #21. Gas production started in four wells from Dec 01, 1981; these are EB #14, #15, #18, and #19. Production from EB #21 started in Nov 01, 1990. As on Sep 01, 2007, EB #14 was the only producing well. Refer to Figure 3.4 for production history data of EB reservoir.

##### 2. Well Location and Positioning of Perforations

Well files indicate the location, type, and dimensions of all five wells in the region (Stokes and Walsh, 2006). All wells were drilled vertically in updip locations of the reservoir and completed within the reservoir section. Table 3.7 lists the location of each well based on the model coordinates. The location of each well is shown in Figure 3.39.

Wells were perforated using the CMG-STARS interactive "PERF" module. Initially all wells were perforated based on the well files. Several runs were performed to validate gas and water production rates. An optimum number and position of the perforations were finally obtained. All efforts were made to avoid over-perforating the wells. The

specifications and methodology followed to validate well production rates have been explained later. Wellbore diagrams of each well, showing well orientation, and positioning of the perforations, are presented in Appendix H

Table 3.7: Locations (Coordinates) and Dimensions of the EB Wells

Well Name	Coordinates (I, J, K)	Well Direction	Well Radius	Well Completion Date
EB #14	26, 16, 1	K Direction (All Vertical)	0.4583 ft	Dec 01, 1981
EB #15	19, 27, 1		0.5833 ft	Dec 01, 1981
EB #18	25, 20, 1		0.5833 ft	Dec 01, 1981
EB #19	21, 22, 1		0.5833 ft	Dec 01, 1981
EB #21	23, 19, 1		0.5833 ft	Nov 01, 1990

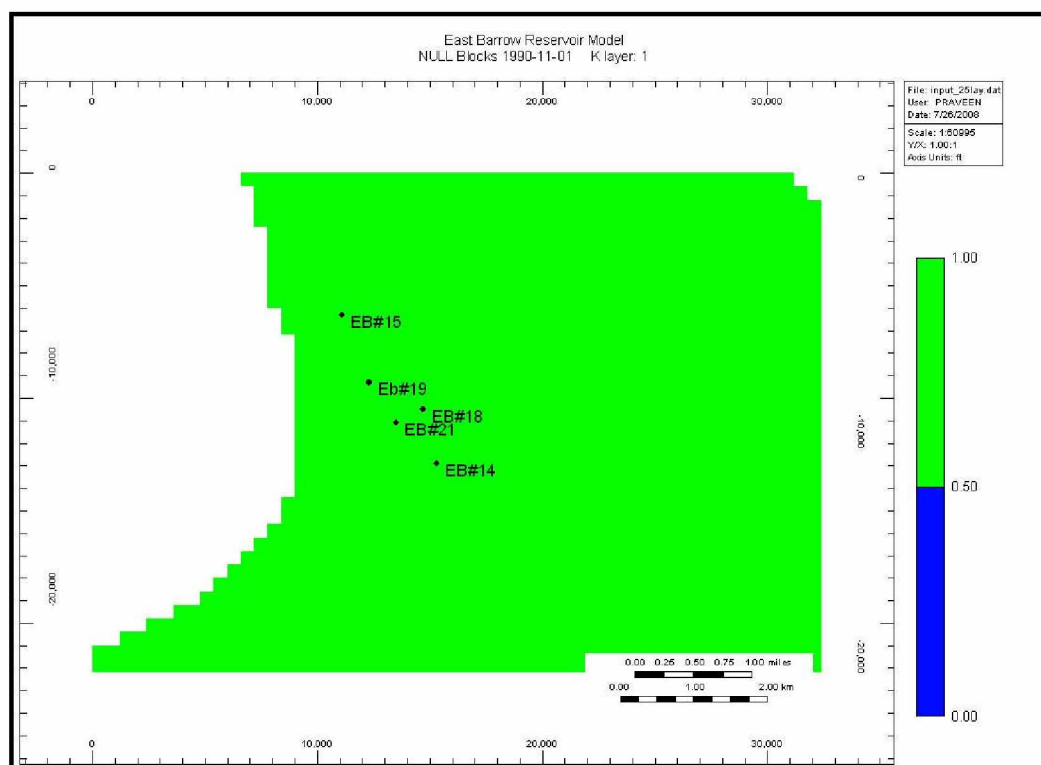


Figure 3.39: Well Locations (IJ Plane View)

### 3. Production Rate Specifications and Data Importing Procedures

Due to unavailability of FBHP data, the only production constraint (primary constraint) that could be used to validate well production model was the monthly gas production. The production data for each well was rewritten in a special format and initialized in CMG-STARS using the "Import Production Data" option. The CMG-STARS keyword \*ALTER can also be used to change the monthly production rate.

The primary operating constraint, considered as the first constraint in CMG-STARS, was entered for the well using \*OPERATE keyword. CMG-STARS keyword \*ALTER modified the primary operating constraint for the specified well. The following steps were followed in order to initialize and alter well production rates.

Step 1: Choose the file containing well production data

Construct gas production data file for each well by following CMG-STARS compatible format. An example case is given below.

```
WELL: EB #14
11717000    12/1/1981
14530000    1/1/1982
```

Upon loading this data file in CMG, a monthly gas production rate of 11,717,000 scf was initialized for the month of Dec 01, 1981 and later CMG-Builder altered the gas production with a new rate of 14,530,000 scf for the month of January 1982 and so on (Figure 3.40).

**Import Production/Injection Data**

Step 1: Choose the file containing well production data

For the Generalized File Reading of production, injection, or pressure data:

1. The data should be organized into columns, with one type of data in each column.
2. The data can be read in free or fixed format mode.
3. A well name must be one of the columns of data, or the well name is identified by unique text (eg. Well: 03-17, in which case the unique text is Well: ).

Please verify that years are 4 digits, since a 2 digit year is not accepted.

Select type of production/injection data file:

General

Name of the file containing the well production/injection data:

C:\Documents and Settings\APRAVEEN\Desktop\WELL\_14.txt

Data field type

Fixed Width - Data is present in columns of fixed width.

Delimited - Characters such as commas, spaces or tabs separate data fields. Columns can vary in width.

How are commas used in the file?

Commas separate data

Commas for thousands (eg: 5,000 = five thousand)

Commas as decimals (eg:5.2 = five + 2/10)

Help View Original File Cancel < Back Next > Finish

Figure 3.40: Step 1 - Choose the File Containing Well Production Data



**Step 2: Choose the file option**

Well name and data were identified by CMG-STARs upon highlighting the same under the respective section (Figure 3.41).

**Import Production/Injection Data**

Step 2: Choose the file options

Please Select(Highlight) the start line of actual data, having valid Date

WELL: EB#14
11717000 12/1/1981
14530000 1/1/1982
13116000 2/1/1982
15520000 3/1/1982
14055000 4/1/1982
14527000 5/1/1982
8734000 6/1/1982
7673000 7/1/1982
6520000 8/1/1982
13786000 9/1/1982
13793000 10/1/1982
19461000 11/1/1982
20105000 12/1/1982

Please Select(Highlight) the line containing first well name

WELL: EB#14
11717000 12/1/1981
14530000 1/1/1982
13116000 2/1/1982
15520000 3/1/1982
14055000 4/1/1982
14527000 5/1/1982
8734000 6/1/1982
7673000 7/1/1982
6520000 8/1/1982
13786000 9/1/1982
13793000 10/1/1982
19461000 11/1/1982
20105000 12/1/1982

Well or group names are in rows

Help View Original File Cancel < Back Next > Finish

Figure 3.41: Step 2 - Choose the File Option



#### Step 4: Choose column details

The first column was identified as follows (Figure 3.43).

- i. Identifier - gas produced
- ii. Related info - volume for period
- iii. Unit - scf
- iv. Expected period - monthly
- v. Missing dates - take zero value

**Import Production/Injection Data**

Step 4: Choose column details

Note: For date formats that span multiple columns (eg. 26 02 1998), please do selection for each column.

	1	2	3
Identifier	Gas Produced	Date/ Time	Ignore Column
Related info	Volume for p...	M D Y (eg. 0...	
Units	SCF		
Expected period	Monthly		
Missing dates	zero(take ze...		
1	WELL:	EB#14	
2	11717000	12/1/1981	
3	14530000	1/1/1982	
4	13116000	2/1/1982	
5	15520000	3/1/1982	
6	14055000	4/1/1982	
7	14527000	5/1/1982	
8	8734000	6/1/1982	
9	7673000	7/1/1982	
10	6520000	8/1/1982	
11	13786000	9/1/1982	
12	13793000	10/1/1982	
13	19461000	11/1/1982	
14	20105000	12/1/1982	
15	27471000	1/1/1983	
16	27986000	2/1/1983	
17	29978000	3/1/1983	
18	30406000	4/1/1983	
19	20104000	5/1/1983	
20	13946000	6/1/1983	
21	12725000	7/1/1983	
22	5495000	8/1/1983	
23	14767000	9/1/1983	
24	17077000	10/1/1983	
25	24678000	11/1/1983	
26	22075000	12/1/1983	
27	28064000	1/1/1984	
28	26890000	2/1/1984	
29	34209000	3/1/1984	

Ignore a column for a well if all data are zero or blanks

Help View Original File Cancel < Back Next > Finish

Figure 3.43: Step 4 - Choose Column Details

The second column was identified as follows (Figure 3.43).

- i. Identifier - date/time
- ii. Related info - MM/DD/YYYY

Step 5: Check Well names and primary constraint

CMG-STARs provides an opportunity to check and modify all initialized parameters (Figure 3.44).

**Import Production/Injection Data**

Step 5: Check well/group names and primary constraints

Injector name suffix: Water injectors:  Gas injectors:  Solvent injectors:

Buttons: Add All, Add Only Producers, Add Only Injectors, Add None, Add Only Matched

For changing primary constraints, please right click on the selected cell(s).

This table lists the existing well/group names that do not match the names in the production file. Select a well/group name by single click and then drag and drop it to the New Name column to the left if you want to use it.

Import Name	Group	Matched	New Name	Add	Primary Constraint	Fraction
1 ● EB#14	<input type="checkbox"/>	<input checked="" type="checkbox"/>		<input checked="" type="checkbox"/>	Gas Produced	1.0

Unmatched Names	
1 ● EB#15	
2 ● EB#18	
3 ● EB#21	
4 ● Eb#19	

Group adjacent periods with rates within  % of each  
(will result in less ALTER keywords)

Import Data Options:

- Import data after this date: 1981-12-01
- For each well/group, apply data after last date of old data (new data append to the end of old data)
- For each well/group, apply data after first date of new data (new data overwrite the old data)

Buttons: Help, View Original File, Cancel, < Back, Next >, Finish

Figure 3.44: Step 5 - Check Well Names and Primary Constraint

#### Step 6: Finish

Pressing the “Finish” button will automatically initialize a new well (example EB #14) and load the gas production data.

#### 4. Well Production Rate Validation

The initialized production wells were tested and validated using the production history data. This step is a necessary quality check required before running full-field simulation.

To validate the well production model, a simple model was developed in CMG. The EB reservoir was assumed to be a free gas reservoir with no associated hydrate-cap or aquifer. A free gas saturation of 45% and bounded water of 55% was considered. All parameters initialized for the best-case model (as previously) were applied to this case. The model was simulated from Dec 01, 1981 to Sep 01, 2007, thus producing gas from all five wells based on respective production history. Well location and perforations were kept the same as initialized previously.

Monthly gas production output for each well was plotted with actual production history data. Any change or deviation in the model results were corrected and simulated again. Upon achieving a close agreement with the production history data, the CMG-STARS well model was considered accurate and ready to be used for performing history matching and sensitivity analysis. Figures 3.45, 3.46, 3.47, 3.48 and 3.49 show the validated monthly gas production rates of EB wells.

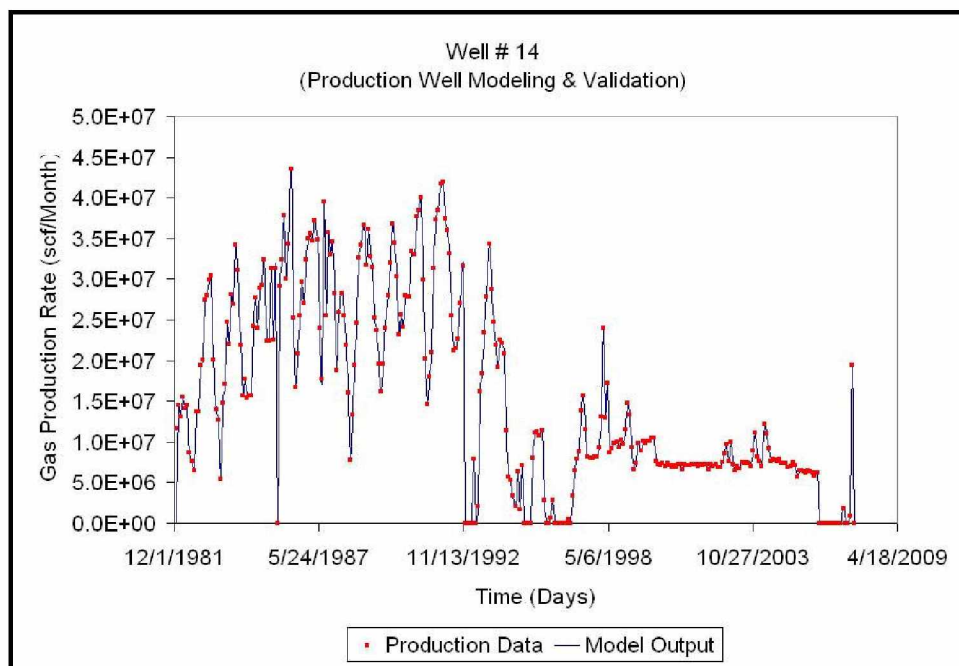


Figure 3.45: Gas Production Rate for EB #14 (Production Data vs. Model Output)

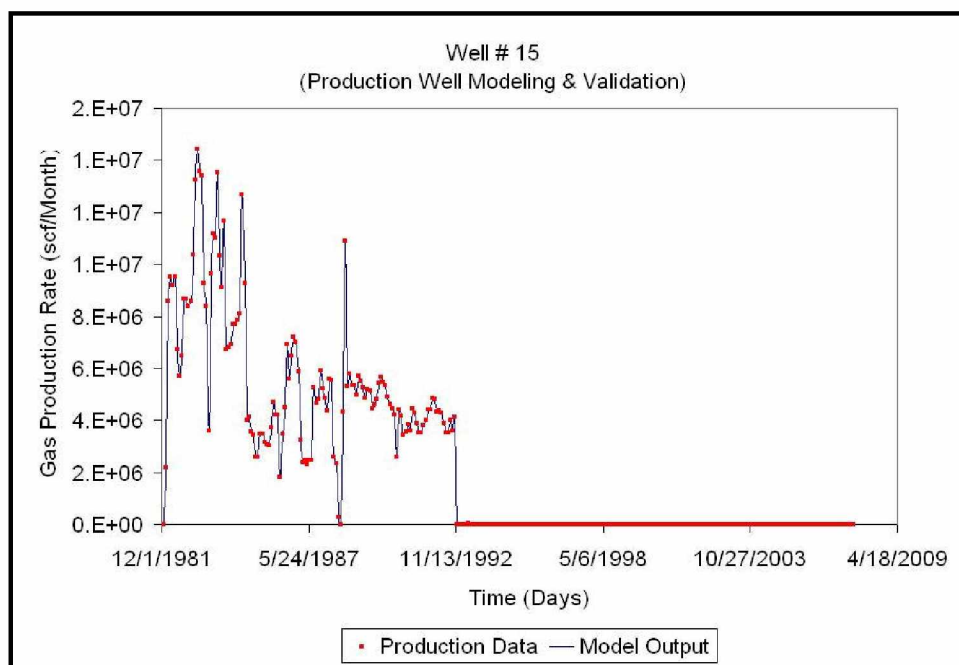


Figure 3.46: Gas Production Rate for EB #15 (Production Data vs. Model Output)

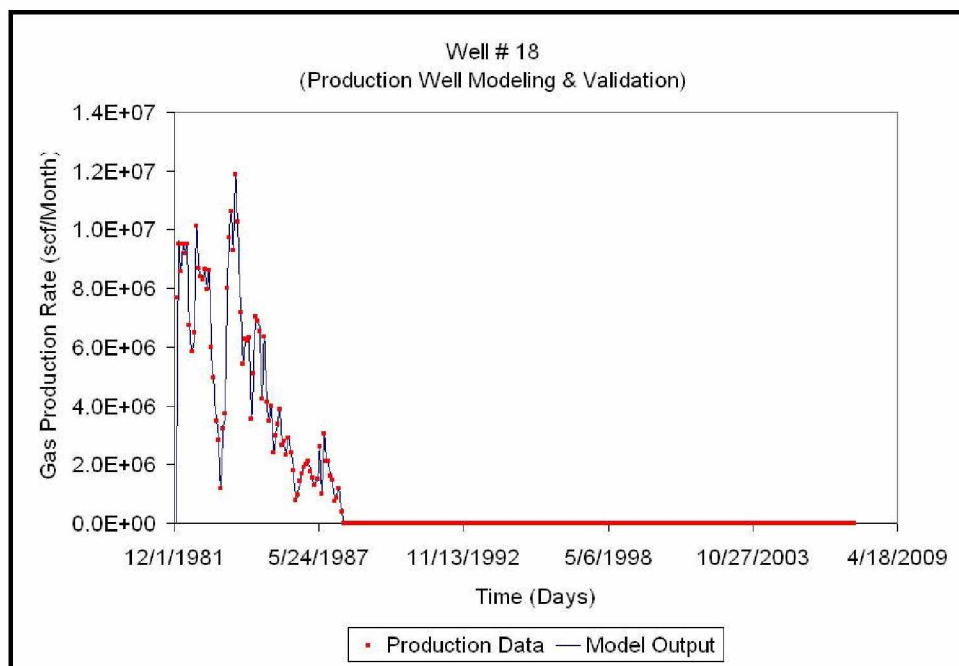


Figure 3.47: Gas Production Rate for EB #18 (Production Data vs. Model Output)

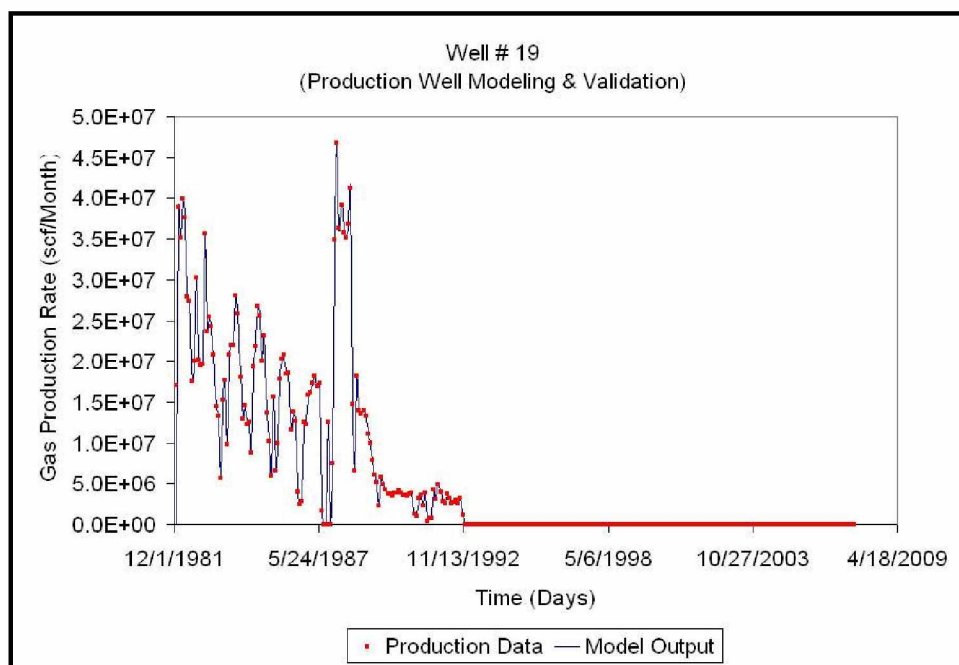


Figure 3.48: Gas Production Rate for EB #19 (Production Data vs. Model Output)

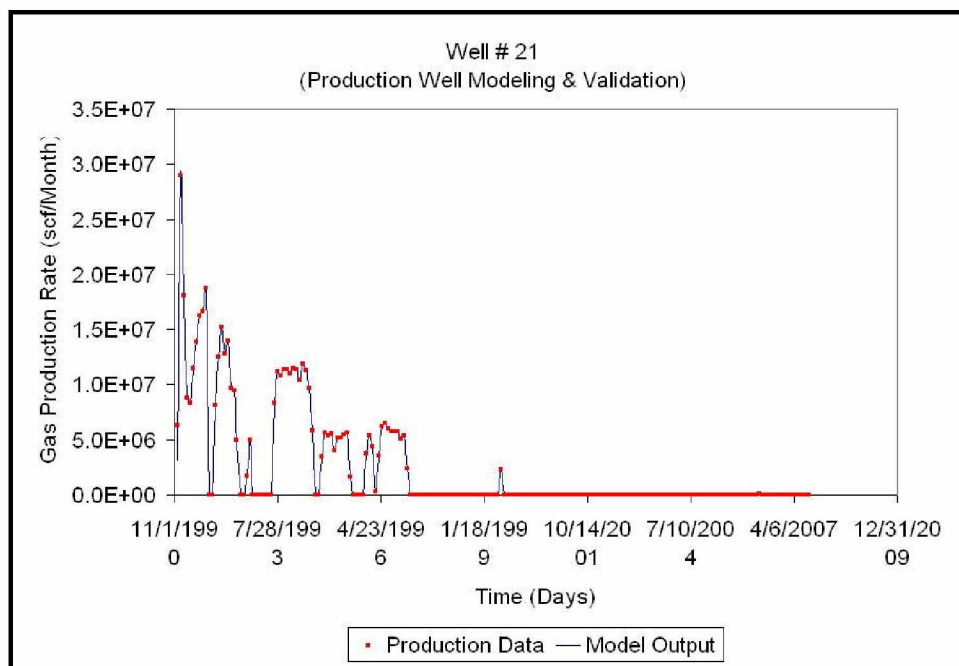


Figure 3.49: Gas Production Rate for EB #21 (Production Data vs. Model Output)

### 3.4.3.2 Walakpa Gas Field

The CMG-STARs simulator was used to build the dynamic reservoir model for the WAL reservoir. The methodology described for the EB was followed while constructing the dynamic WAL reservoir model. Static (LARGE & SMALL) reservoir model was obtained from Panda and Morahan (2008).

- i. Due to processor's computational speed limitation, a SMALL model was extracted from the original WAL model (LARGE model). This SMALL model was utilized to history match the production data. Considerable size of the reservoir was included in the SMALL model (including the section lying within the proposed hydrate stability zone, i.e. the section shallower than than 2000 ft).
- ii. Upon confirming the reservoir drive mechanism, the SMALL model was imported back in the original (LARGE) model. Current reservoir mapping and forecasting run were performed on the LARGE model to quantify in-place hydrate and free gas resources field for future evaluation.



Hydrate stability studies performed for WAL field (refer to results and discussion on hydrate stability modeling) suggested that the stable hydrate zone exists in updip location of the reservoir. Additionally, hydrates were observed in the WAL sandstone in WAL #1 and NSB #6 well logs. The presence of an infinitely strong aquifer was also confirmed after identifying a strong aquifer to the south of the brontosaurus Well #1.

WAL model initialization was performed similar to the EB gas field. In this section, model initialization (in CMG-STARs) for the best-case has been explained briefly. All parameters were initialized in field units. The best-case scenario consisted of a free gas zone overlain with a hydrate-cap and in communication with an infinitely sized *numerical aquifer* (edgewater).

#### a. Reservoir Grid - SMALL Model

The 3D reservoir grid is shown in Figure 3.50.

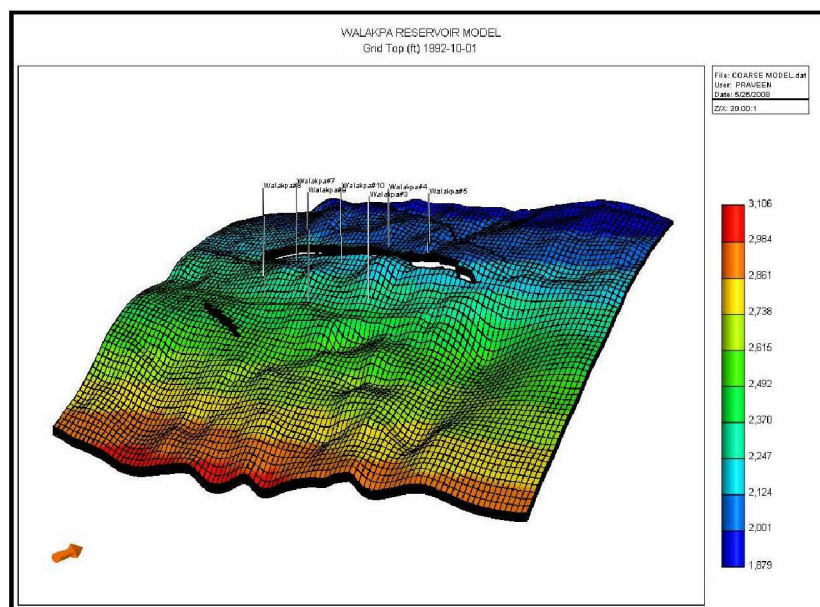


Figure 3.50: Reservoir Grid (SMALL Model) - 3D View

Based on reservoir geology and well log data, a detailed static reservoir model was built using ROXAR RMS<sup>R</sup> software (Panda and Morahan, 2008). The data file generated

using the software was directly imported into CMG-STARs by using the \*INCLUDE keyword. The model was generated using a corner point grid system by choosing a grid having 100 blocks in I, 63 blocks in J, and 10 blocks in K directions, using a total of 63,000 gridblocks. The dimension of each gridblock is 500 ft by 500 ft (IJ plane). The gridblock thickness in K direction is variable and ranges anywhere between 1.6 ft and 4.5 ft. The topmost section of the reservoir is at a depth of 1879 ft below sea level, whereas the deepest section is at a depth of 3111 ft below sea level. However, the pay zone depth ranges between 1879 ft to 3109 ft below sea level.

### *b. Reservoir Properties - SMALL Model*

#### 1. Porosity

Porosity distribution data has been acquired from Panda and Morahan (2008). The porosity data was loaded into a CMG-STARs compatible data file using the \*INCLUDE keyword. The porosity of the reservoir ranges from 8.5% (min) to 24.7% (max). Figure 3.51 shows a 3D view of porosity distribution within the reservoir.

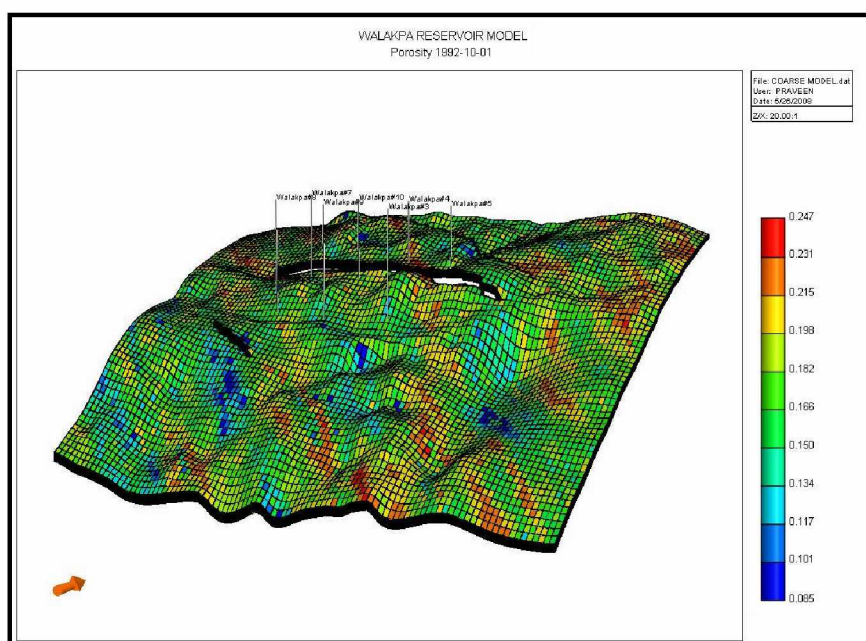


Figure 3.51: Porosity (SMALL Model) - 3D View

## 2. Permeability

Reservoir permeability was obtained on the basis of well log data (Panda and Morahan, 2008). The \*INCLUDE keyword was used to load the permeability data directly into the reservoir model. The reservoir permeability (I, J, and K directions) is mostly in the range of 0.1 to 250 md. Figure 3.52 shows a 3D view of permeability distribution within the reservoir in I direction (similar in J and K directions).

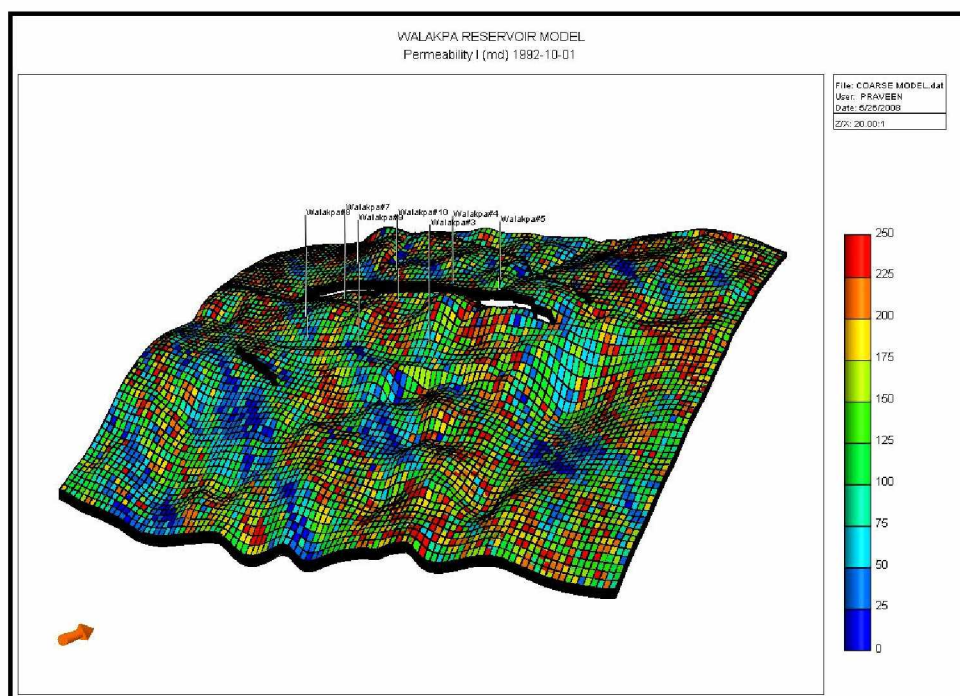


Figure 3.52: Permeability Distribution (SMALL Model) - 3D View

## 3. Initial Temperature

Geothermal gradient data obtained for the WAL reservoir was 1.88 °F/100 ft. The reservoir top temperature was 49.60 °F and the bottommost region had a temperature of 72.40 °F. The temperature distribution within the reservoir was initialized based on reservoir depths (Figure 3.53).

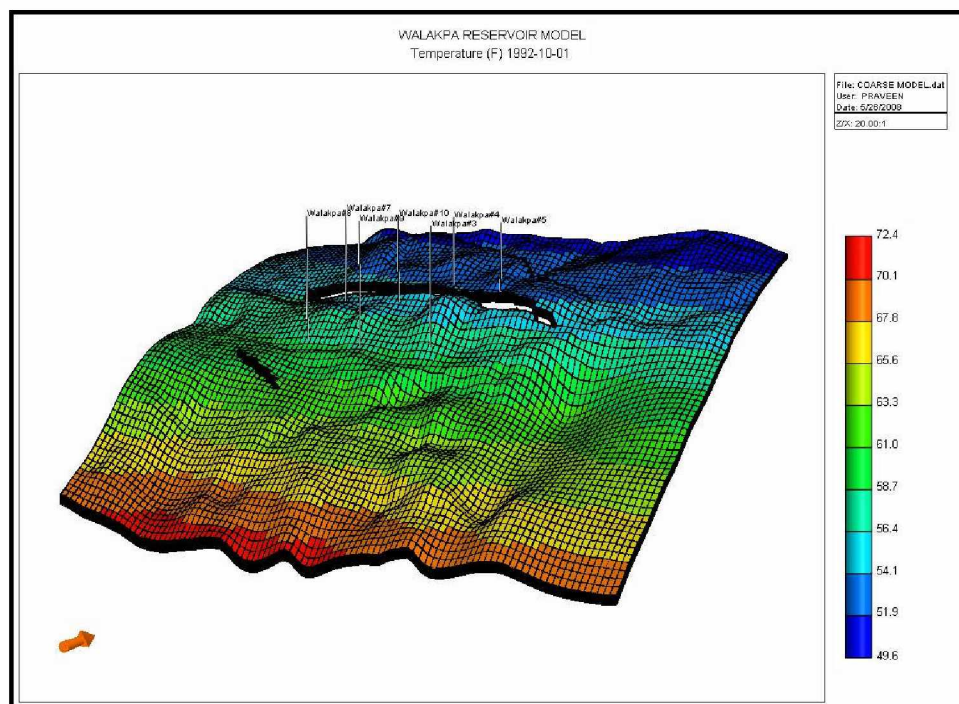


Figure 3.53: Initial Temperature, °F (SMALL Model) - 3D View

#### 4. Initial Reservoir Pressure

Well-testing and pressure gradient data reported in previous studies conducted for the WAL gas pool concluded that the initial pressure of the reservoir was at 1039 psi (Glenn and Allen, 1991; Stokes et al., 2005). The model consisted of a hydrate-cap and free gas zone underlain with *model* and *numerical aquifers*. The effect of gravity on reservoir pressure in the free gas and hydrate zones was neglected. However, the pressure gradient in the aquifer zone was initialized based on a pressure gradient of 0.433 psi/ft. Figure 3.54 shows the initial pressure distribution within the reservoir.



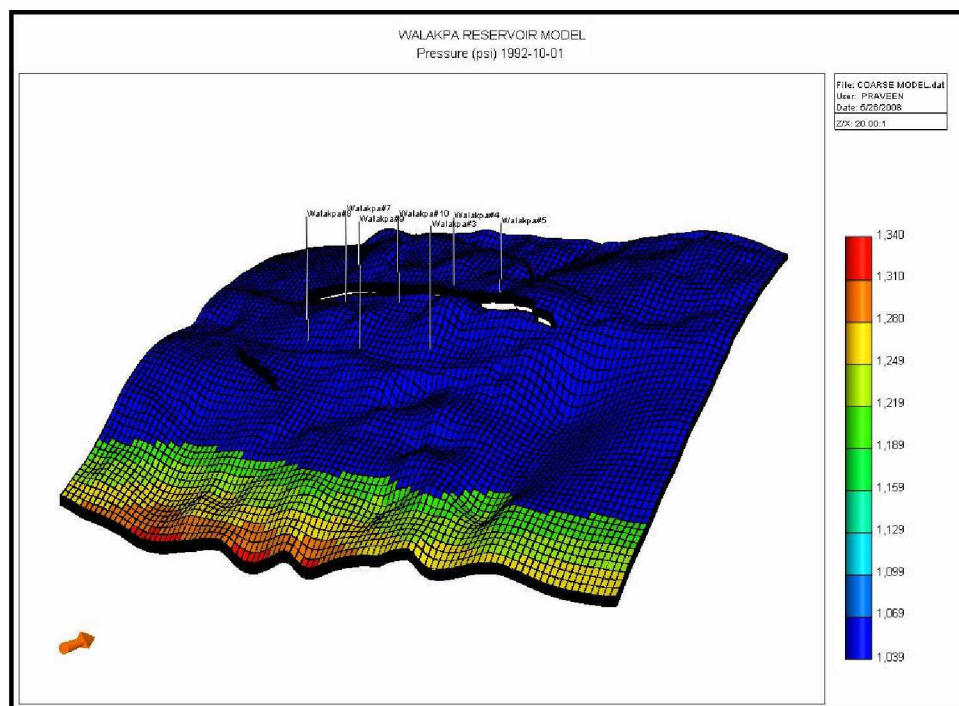


Figure 3.54: Initial Reservoir Pressure, psi (SMALL Model) - 3D View

## 5. Initial Hydrate Saturation

The HGC for the WAL gas reservoir was found to be 2000 ft (Panda and Morahan, 2008). The pressure-temperature condition (Figure 3.55) for the WAL gas field lies on the three-phase pressure-temperature equilibrium curve ( $L_w - H - V$ , basis 100% methane). This implies that the hydrate zone could be partially saturated with free gas as well (occurrence of free gas pocket due to higher local geothermal gradient at the same depth). In the absence of physical evidence (well log data) and with similarity to the EB reservoir conditions, an initial hydrate saturation of 30% was taken for the WAL gas fields. To initialize this condition in CMG-STARs, the three phases (i.e., hydrates, free gas, and bounded water) were considered existing together within hydrate zone. An initial hydrate saturation of 0% was initialized in free gas and aquifer zones.

Figure 3.56 shows a 3D view of hydrate distribution. Figure 3.57 is a magnified 2D (JK plane) image showing hydrate saturation in hydrate zone up to HGC (at 2000 ft).

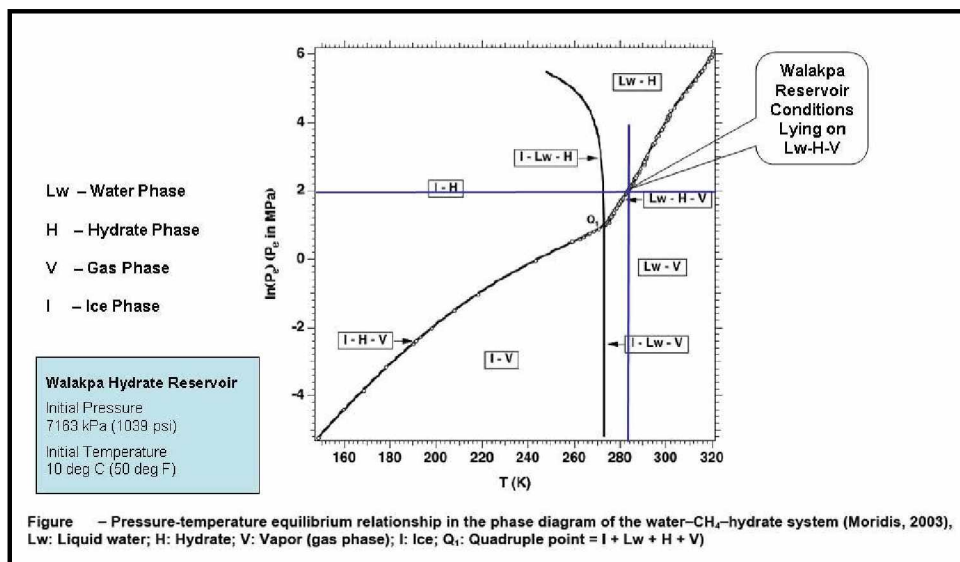


Figure 3.55: Pressure-Temperature Equilibrium Curve Showing Initial Thermodynamic Condition of the WAL Reservoir (Modified from Moridis, 2003)

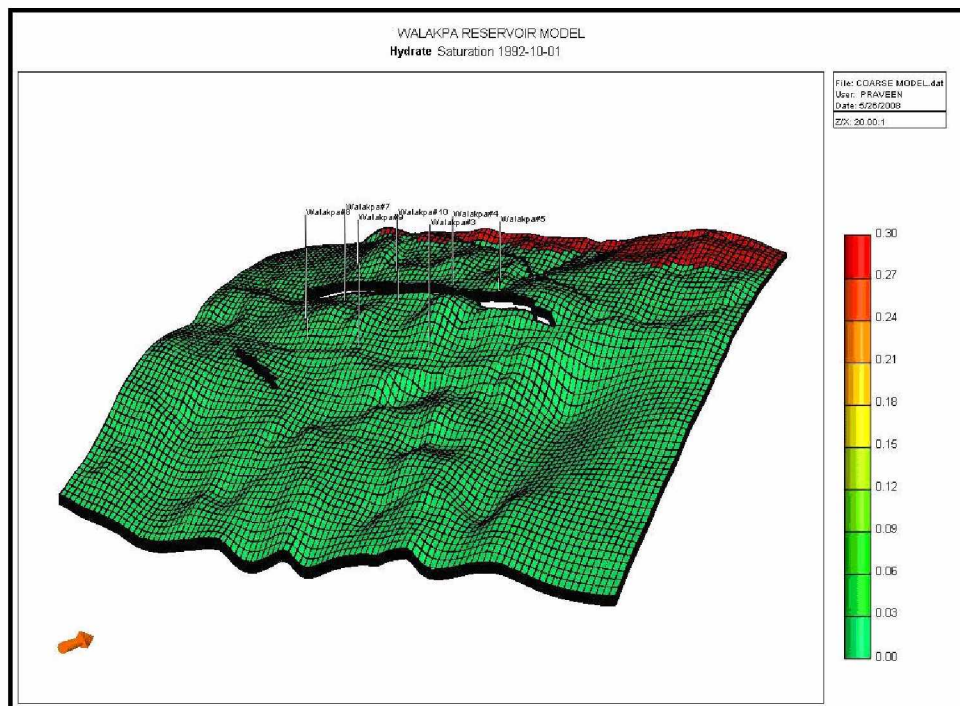


Figure 3.56: Initial Hydrate Saturation, % (SMALL Model) - 3D View

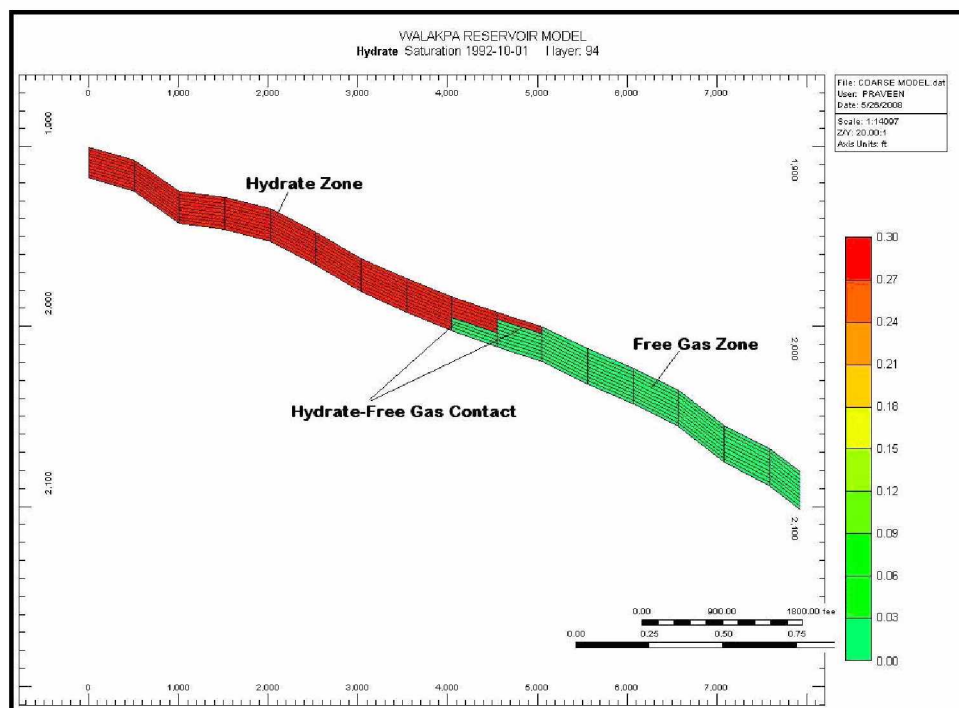


Figure 3.57: Initial HGC (SMALL Model) - JK Plane View

## 6. Initial Gas Saturation

Right below the hydrate-cap is the free gas zone. However, since the thermodynamic condition of a hydrate zone is such that the hydrate phase and free gas phase exist together in the hydrate zone (pocket of free gas) along with the bounded water phase, the initial gas phase saturation was needed to be defined for both the hydrate zone and the free gas zone. The well logs for the EB showed that the bounded water saturation for both the zones was 55%; in the absence of well log data from the WAL reservoir, the EB data was chosen. The GWC was found to be at 2750 ft (Panda & Morahan, 2008). Free gas saturation was initialized as 15% and 45% in the hydrate and free gas zones respectively. Initial gas saturation of 0% was initialized in the *model aquifer* zone. Figure 3.58 presents a 3D view of free gas distribution. Figure 3.59 is a 2D (JK plane) image showing HGC and GWC at 2000 ft and 2750 ft below sea level, respectively.

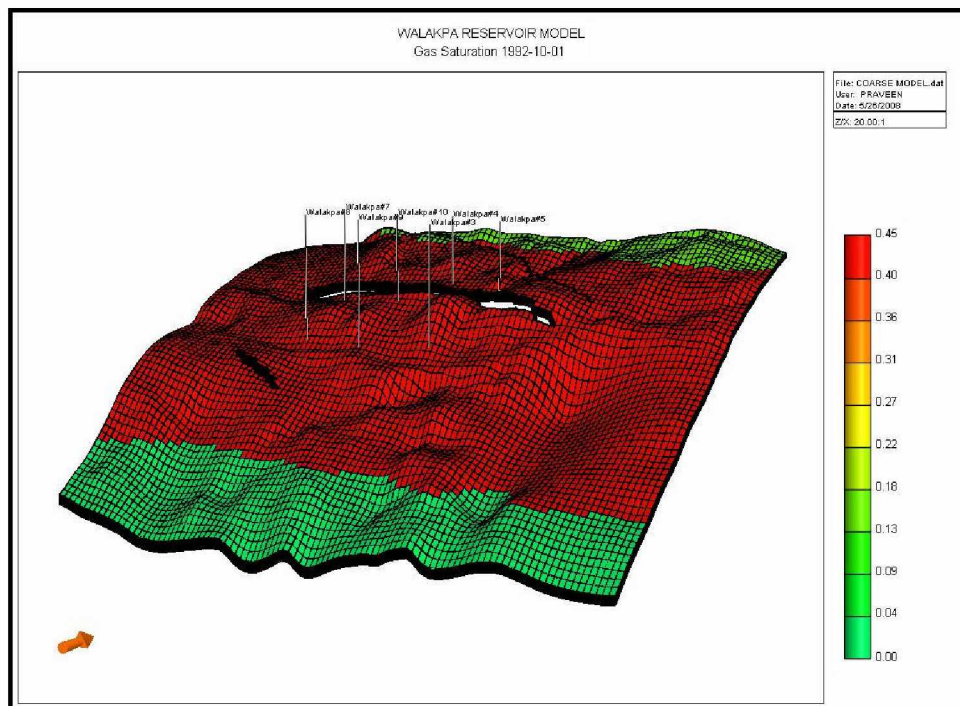


Figure 3.58: Initial Gas Saturation, % (SMALL Model) - 3D View

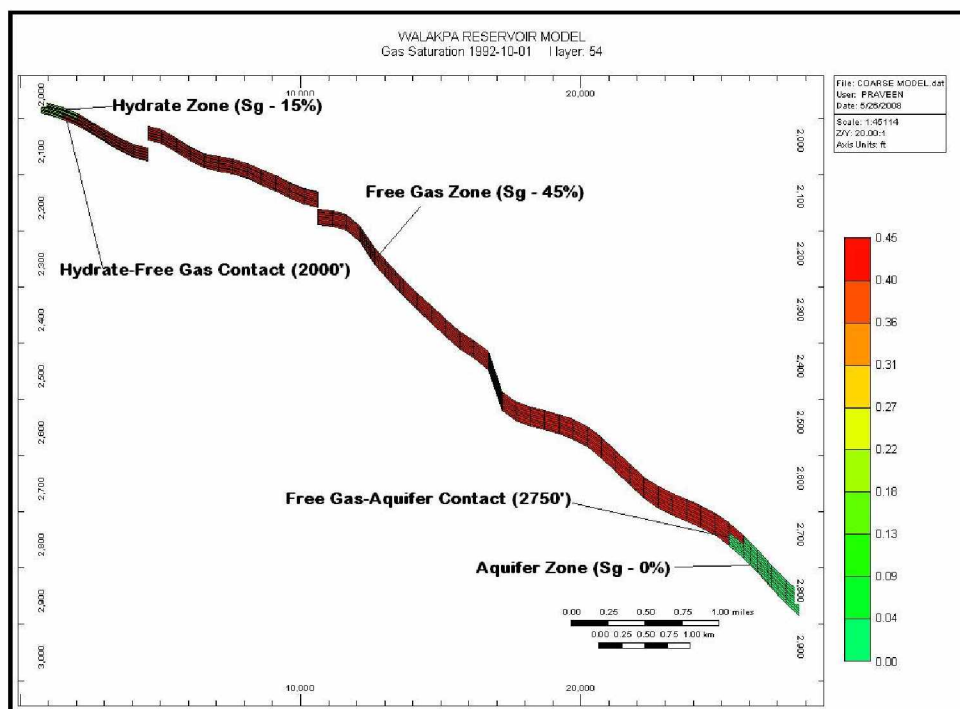


Figure 3.59: Initial HGC and GWC (SMALL Model) - JK Plane View



## 7. Initial Water Saturation

In the absence of initial water saturation data, EB reservoir data was used. An initial water saturation of 100% was initialized in the *model aquifer* zone. Additionally, an infinitely sized *numerical aquifer* was also initialized on the south side of the reservoir. Figure 3.60 shows a 3D view of water distribution. Figure 3.61 is a 2D (JK plane) image showing GWC at 2750 ft. The initial condition for WAL is summarized in Table 3.8 presented below.

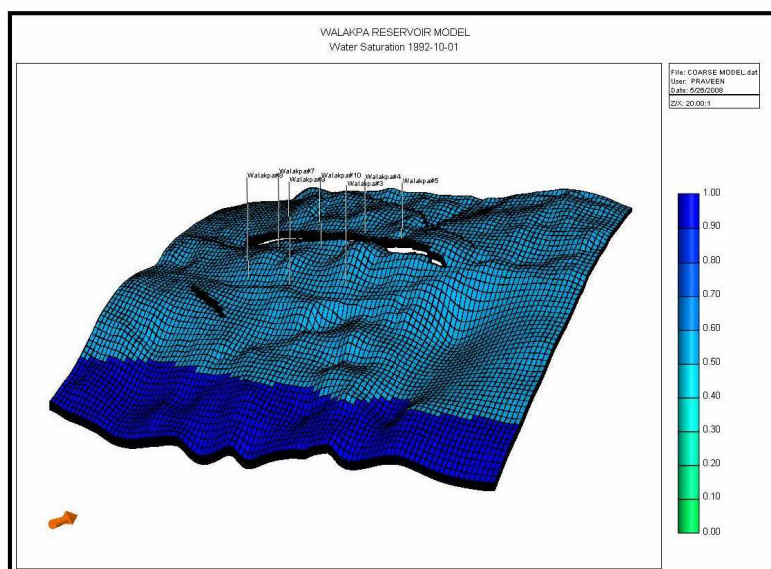


Figure 3.60: Initial Water Saturation, % (SMALL Model) - 3D View

Table 3.8: Summary of Initial Reservoir Condition (WAL Reservoir Model)

Zone	Pressure	Temperature	Saturation	Remarks
Hydrate	1039 psi	Temperature Gradient 1.88 °F/100 ft	$S_h = 30\%$ $S_g = 15\%$ $S_w = 55\%$	Lying on $L_w - H - V$ (Equilibrium) Curve
Free Gas*	**Press Grad 0.433		$S_g = 45\%$ $S_w = 55\%$	*HGC - 2000 ft
Aquifer**	psi/ft	Top Temp 49.6 °F	$S_w = 100\%$	**GWC - 2750 ft **Model+Numerical Aq

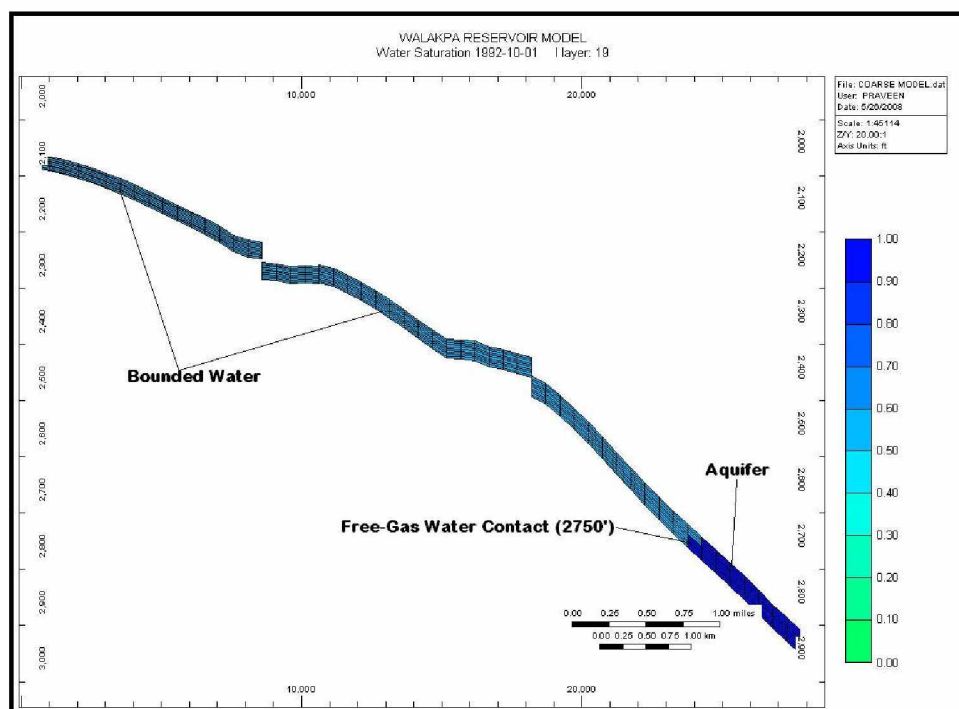


Figure 3.61: Initial GWC (SMALL Model) - JK Plane View

*c. Thermal Properties*

Refer to Appendix G.

*d. Fluid/Component Properties*

Refer to Appendix G

*e. Relative Permeabilities and Capillary Pressure Functions*

Refer to previous section for details.

*f. Production Well Modeling*

The production history data and well details for WAL gas field are presented in Table 3.9. Table 3.10 presents location and completion date of each well. Figure 3.62 is a 2D image showing locations of wells in WAL gas field.

Table 3.9: Production History Data for the WAL Gas Field (Stokes et al., 2005)

<b>Production Data (WAL Gas Field)</b>	
Number of Wells	WAL #2, #3, #4, #5, #6, #7, #8, #9, and #10 (Total 9 Producing Wells)
Completion	All in Gas Zone
Production Period	Oct 01, 1992 to Sept 01, 2007
Cumulative Gas Production	17.11 bcf
Cumulative Water Production	Not Reported

Table 3.10: Locations (Coordinates) and Dimension of WAL Wells

<b>Well Name</b>	<b>Coordinate (I, J, K)</b>	<b>Well Direction</b>	<b>Well Radius</b>	<b>Well Completion Date</b>
WAL #2	54, 22, 1	K Direction (Vertical Well)	0.4933 ft	Apr 01, 2000
WAL #3	51, 34, 1		0.5305 ft	Oct 01, 1992
WAL #4	49, 45, 1		0.5305 ft	Oct 01, 1992
WAL #5	59, 43, 1		0.5305 ft	Oct 01, 1992
WAL #6	66, 31, 1		0.5305 ft	Apr 01, 1997
WAL #7	29, 43, 1		0.5305 ft	Oct 01, 1992
WAL #8	27, 34, 1		0.5305 ft	Oct 01, 1992
WAL #9	38, 33, 1		0.5305 ft	Oct 01, 1992
WAL #10	40, 42, 1		0.5305 ft	Oct 01, 1992

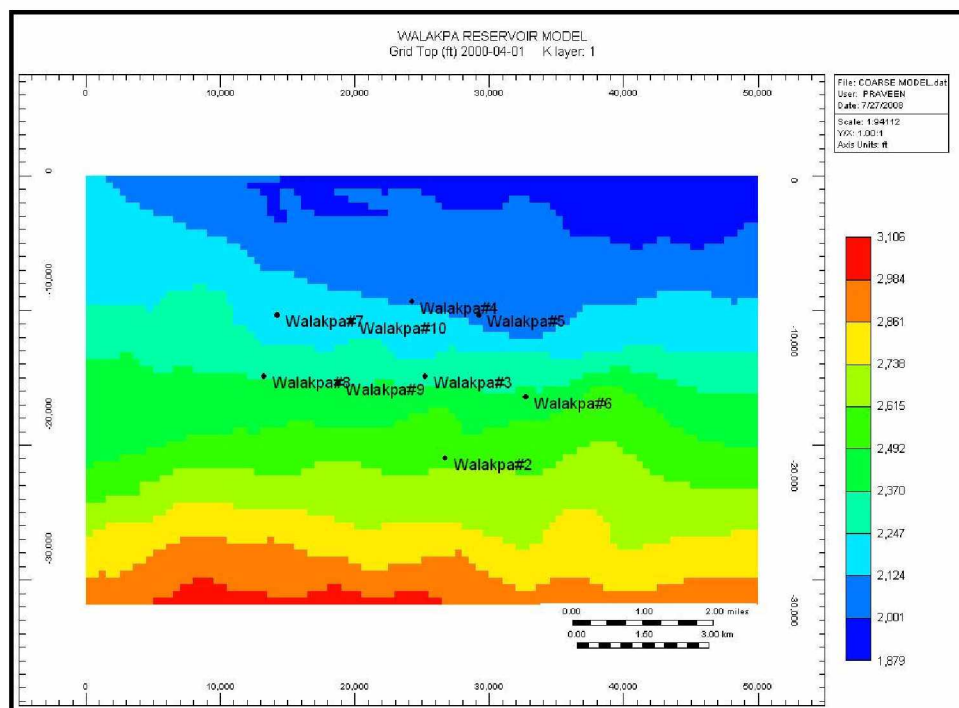


Figure 3.62: Well Locations (SMALL Model) - IJ Plane View

### 3.4.4 History Matching Study

#### 3.4.4.1 East Barrow Gas Field

The objective of the history matching analysis was to build a reservoir model that closely matches the performance of the EB gas field and represents current reservoir conditions. The quality and accuracy of predicting future reservoir behavior lie in developing the best-suited model. Hence, the criteria followed while performing history matching plays a crucial role. Availability and quality of production history, geologic, and well log data are the governing parameters.

The EB gas reservoir is data limited. Hence, an attempt was made to develop a dynamic reservoir model that could best describe the historical performance of the reservoir. A topdown approach was followed while performing the history matching study. The reservoir level match was performed followed by individual well-level match. The history match criteria and the approach chosen for this study are given below.

### *a. Field-Level Match Criteria*

#### 1. Cumulative Gas Production

The cumulative gas production obtained from model output was compared with production history data. While evaluating several scenarios, this became a crucial parameter.

#### 2. Cumulative Water Production

There was no control on water production in any well. Negligible water production has been observed to date. Hence, the cumulative water production comparison could provide vital information about the mobile water distribution near the wellbore region.

#### 3. Average Reservoir Pressure

Pressure is a gridblock property, and CMG-STARS performs material balance calculations on each gridblock. However, due to pressure variation within the reservoir, there was no provision to directly obtain average reservoir pressure for the reservoir. Blockwise pressure data can be used to generate average reservoir pressure, but the task was cumbersome and time-consuming. To approximate similar results, several gridblocks were chosen, and their pressure profiles were compared with reservoir pressure distribution.

The pressure profile in the downdip location (far away from the producing well) remained unaffected most of the time due to the presence of an aquifer. Moreover, since the production history data were collected from active wells, they represented average drainage pressure for nearby locations. Based on these observations, a gridblock in an updip location (block number 19, 19, 1) was chosen to represent average reservoir pressure. Figure 3.63 shows the location of the gridblock.

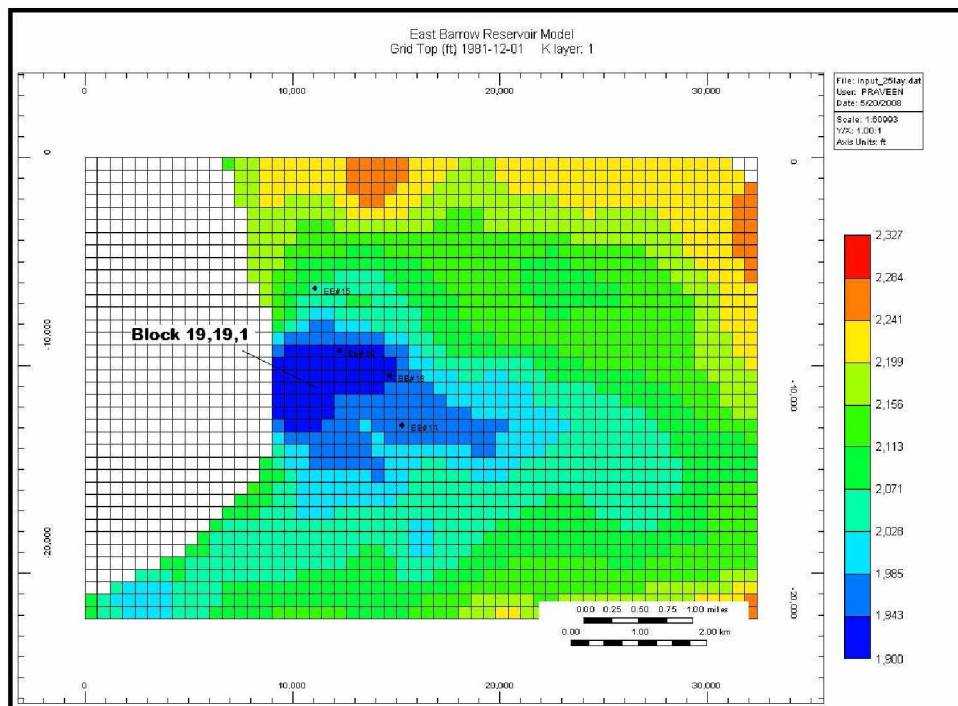


Figure 3.63: Block 19,19,1 Representing Average Reservoir Pressure

### *b. Well-Level Match Criteria*

#### 1. Gas Production Rate

The model results were obtained for individual wells and compared with historic production data.

#### 2. Water Production Rate

Water production rates were also performed on individual wells to compare the water production data. As negligible quantities of water have been produced to date, well-level match may not be a good parameter to rely on. However, comparing the water production rate for each well with the simulated result will strengthen the basis on which the history matching exercise was performed.

*c. Approach*

The material balance study followed a simple step-by-step approach in analyzing reservoir drive mechanism. A similar approach was adopted while evaluating the reservoir response using a field-scale reservoir model. Six reservoir models were developed and initialized in CMG-STARs. The model outputs were evaluated by comparing the field-level and well-level data. The model initialization procedure was the same as explained previously. The cases studied are tabulated in Table 3.11.

Table 3.11: History Matching Cases

<b>Cases</b>	<b>Reservoir Model</b>	<b>Description</b>
<i>A</i>	Free Gas Reservoir (Only Gas Model)	A simple free gas reservoir model with no hydrate-cap and no aquifer support
<i>B</i>	Free Gas Reservoir with Associated Aquifer (Gas + Aquifer Model)	Free gas reservoir model associated with aquifer support ( <i>model aquifer</i> )
<i>C</i>	Free Gas Reservoir with Associated Hydrate-Cap and Aquifer Supports (HYD + Gas + Aquifer Model)	Free gas reservoir model associated with thick hydrate-cap on the top and <i>model aquifer</i> support at the bottom.
<i>D</i>	Hydrate Reservoir (Only HYD Model)	A reservoir model saturated with methane hydrates, bounded water and free gas (respecting thermodynamic equilibrium)
<i>E</i>	Hydrate-Cap Associated with Free Gas (HYD + Gas Model)	Free gas reservoir model associated with thick hydrate zone
<i>F</i>	Hydrate-Associated with Model Aquifer (HYD + Aquifer Model)	A hydrate rich reservoir model associated <i>model aquifer</i> support. (No free gas)

The parameters initialized for different cases are listed in Tables 3.12, 3.13, 3.14, 3.15, 3.16, and 3.17; all other parameters remained the same as explained for the best-case model.

Table 3.12: Initial Condition for Case *A* (Only Gas Model)

Zone	Pressure	Temperature	Saturation	Remarks
Hydrate	975 psi	Temperature	No Hydrate Zone ( $S_h = 0\%$ )	
Free Gas		Gradient 1.60 °F/100 ft	$S_g = 45\%$ $S_w = 55\%$	Covers Entire Reservoir
Aquifer		Top Temp 41 °F	No Aquifer Zone	

Table 3.13: Initial Condition for Case *B* (Gas + Aquifer Model)

Zone	Pressure	Temperature	Saturation	Remarks
Hydrate	975 psi	Temperature	No Hydrate Zone ( $S_h = 0\%$ )	
Free Gas		Gradient 1.60 °F/100 ft	$S_g = 45\%$ $S_w = 55\%$	GWC - 2080 ft
Aquifer		Top Temp 41 °F	$S_w = 100\%$	

Table 3.14: Initial Condition for Case *C* (HYD + Gas + Aquifer Model)

Zone	Pressure	Temperature	Saturation	Remarks
Hydrate	975 psi	Temperature Gradient 1.60 °F/100 ft	$S_h = 31\%$ $S_g = 14\%$ $S_w = 55\%$	Lying Close to $L_w - H - V$ (Equilibrium) Curve
Free Gas		Top Temp 41 °F	$S_g = 45\%$ $S_w = 55\%$	HGC - 2050 ft
Aquifer			$S_w = 100\%$	GWC - 2080 ft



Table 3.15: Initial Condition for Case *D* (Only HYD Model)

Zone	Pressure	Temperature	Saturation	Remarks
Hydrate	975 psi	Temperature Gradient 1.60 °F/100 ft	$S_h = 31\%$ $S_g = 14\%$ $S_w = 55\%$	Lying Close to $L_w$ - $H - V$ (Equilibrium) Curve Hydrate Covers Entire Reservoir
Free Gas		Top Temp 41 °F	No Free Gas Zone ( $S_g = 0\%$ )	
Aquifer		No Aquifer Zone		

Table 3.16: Initial Condition for Case *E* (HYD + Gas Model)

Zone	Pressure	Temperature	Saturation	Remarks
Hydrate	975 psi	Temperature Gradient 1.60 °F/100 ft	$S_h = 31\%$ $S_g = 14\%$ $S_w = 55\%$	Lying Close to $L_w$ - $H - V$ (Equilibrium) Curve
Free Gas		Top Temp 41 °F	$S_g = 45\%$ $S_w = 55\%$	HGC - 2050 ft
Aquifer		No Aquifer Zone ( $S_w = 0\%$ )		

Table 3.17: Initial Condition for Case *F* (HYD + Aquifer Model)

Zone	Pressure	Temperature	Saturation	Remarks
Hydrate	975 psi	Temperature Gradient 1.60 °F/100 ft	$S_h = 31\%$ $S_g = 14\%$ $S_w = 55\%$	Lying Close to $L_w$ - $H - V$ (Equilibrium) Curve
Free Gas		Top Temp 41 °F	No Free Gas Zone ( $S_g = 0\%$ )	
Aquifer			$S_w = 100\%$	HWC - 2080 ft

### 3.4.4.2 Walakpa Gas Field

#### a. Approach

A methodology similar to EB was followed for the WAL gas fields. The following two cases were studied (Tables 3.18 and 3.19).

Table 3.18: Initial Condition for Case A (Gas + Aquifer Model)

Zone	Pressure	Temperature	Saturation	Remarks
Hydrate	1039 psi	Temperature	No Hydrate Zone	
Free Gas	0.433 psi/ft	Gradient	$S_g = 45\%$	GWC - 2750 ft
	(in Aquifer)	1.88 °F/100 ft	$S_w = 55\%$	
Aquifer		Top Temp 49.60 °F	$S_w = 100\%$	

Table 3.19: Initial Condition for Case B (HYD + Gas + Aquifer Model)

Zone	Pressure	Temperature	Saturation	Remarks
Hydrate	1039 psi	Temperature	$S_h = 30\%$	Lying Close to $L_w - H - V$ (Equilibrium) Curve
	0.433 psi/ft	Gradient	$S_g = 15\%$	
Free Gas	(in Aquifer)	1.88 °F/100 ft	$S_w = 55\%$	HGC - 2000 ft
		Top Temp 49.60 °F	$S_g = 45\%$	GWC - 2750 ft
Aquifer			$S_w = 55\%$	
			$S_w = 100\%$	

### 3.4.5 Sensitivity Study

#### 3.4.5.1 East Barrow Gas Field

The best-case (history matched) was subjected to a sensitivity study. The goal of performing the sensitivity study was to quantify the effect of each parameter on overall reservoir performance. Additionally, the sensitivity study shall support the argument of

choosing the best-case model (history matched case). The parameter sensitivity was categorized into four major groups. These categories were identified based on their importance in quantifying the methane hydrate resource potential of the EB gas field. These are:

- i. Free Gas Zone Size
- ii. Hydrate Saturation
- iii. Hydrate Zone Size
- iv. Aquifer Strength and Size

#### i. Free Gas Zone Size

The free gas zone size was altered by changing GWC. The CMG-STARS formula editor was used to edit GWC for different case studies. The size of the hydrate zone was kept the same. The effect of changing the free gas zone size was observed by plotting average reservoir pressure, cumulative gas, and water production. Five different free gas zone sizes were studied. These are:

- a. Free Gas-Water Contact - 2060 ft
- b. Free Gas-Water Contact - 2070 ft
- c. Free Gas-Water Contact - 2080 ft (Best-Case)
- d. Free Gas-Water Contact - 2090 ft
- e. No Free Gas-Water Contact (HYD + Free Gas Model)

#### ii. Hydrate Saturation

A hydrate saturation of 31% was used to match pressure history (best-case model). The effect of hydrate saturation on reservoir performance was studied as part of the parameter sensitivity. Five different cases were studied. These are :

- a. Hydrate Saturation = 0% (Gas + Aquifer Model)
- b. Hydrate Saturation = 5%

- c. Hydrate Saturaton = 15%
- d. Hydrate Saturation = 31% (Best-Case Model)
- e. Hydrate Saturation = 40%

### iii. Hydrate Zone Size

The hydrate zone size was changed by altering the HGC. Changing the hydrate zone size altered the cumulative water production and average reservoir pressure. Six different cases were studied These are :

- a. No Hydrate Zone (Gas + Aquifer model)
- b. Hydrate-Free Gas Contact at 2030 ft
- c. Hydrate-Free Gas Contact at 2040 ft
- d. Hydrate-Free Gas Contact at 2050 ft (Best-Case Model)
- e. Hydrate-Free Gas Contact at 2060 ft
- f. Hydrate-Water Contact at 2080 ft (HYD + Aquifer model)

### iv. Aquifer Strength and Size

The material balance study indicated that the reservoir is not volumetric (refer to Results and Discussion on the material balance study). Reservoir was under the effect of external pressure support. This support was either from dissociating hydrates or a strong aquifer. Detailed analysis showed that it was due to the combined effect of the two sources. This became the basis of developing the best-case model during the history matching study. However, it was equally important to investigate the effect of aquifer support on the free gas reservoir. The aquifer sensitivity was studied by attaching the *numerical aquifer* available in CMG-STARS. The size and strength of the *numerical aquifer* was changed, performance recorded, and compared with production data. It should be noted that the aquifer study was performed on a free gas-*model aquifer* reservoir system; no hydrate-cap was considered for this case.

The *numerical aquifer* was initialized in CMG-STARs by using the graphic user interface “aquifers.” The interface provide three options: BOTTOM aquifer model, BOUNDARY aquifer model, and REGION aquifer model. The *numerical aquifer* was initalized using the \*AQUIFER keyword followed by the desired aquifer model. Definitions are:

\*AQUIFER: Specifies the aquifer location, via one of three methods

\*BOTTOM: Connects the aquifer to the bottom of the reservoir

\*BOUNDARY: Connects to all boundary blocks in the sides of the reservoir

\*REGION: Connects aquifer to an arbitrary list of fundamental gridblocks via I, J, and K address ranges I1(:I2) J1(:J2) K1(:K2)

Figure 3.64 presents the aquifer options available with CMG-STARs

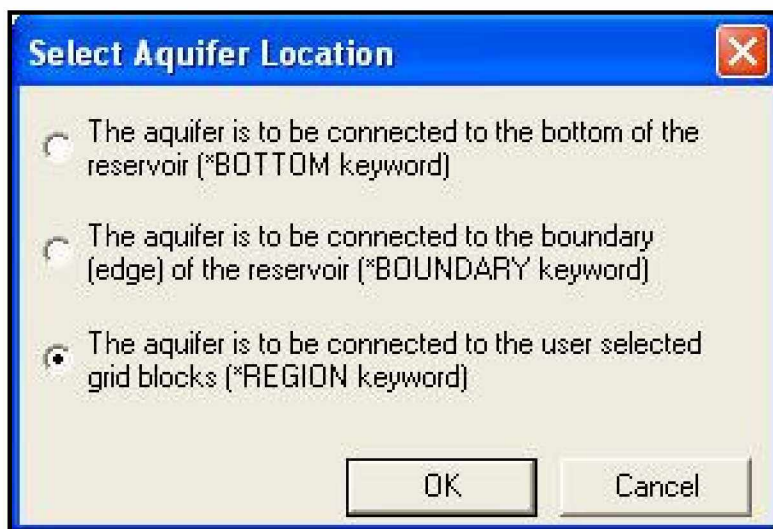


Figure 3.64: Aquifer Options (CMG-STARs)

### 1. Initializing Bottom Aquifer

Figure 3.65 shows the parameters initialized in order to define the bottom *numerical aquifer* to the free gas-*model aquifer* system. The aquifer was kept infinitely strong in this case. This can be easily made finite by changing the limits of the *numerical aquifer* size. Figure 3.66 shows an example of a finite bottom aquifer.

The screenshot shows the 'Aquifer Properties' dialog box with the following settings:

- Name: Aquifer 1
- Location: Bottom
- Thickness: (empty)
- Porosity: 0.2
- Permeability: 5 md
- Radius: (empty)
- Angle (fraction of a circle): (empty)
- R-Ratio: (empty)
- Modelling Method: Carter-Tracy (infinite extent)
- Geometry: Rectangular, Infinite
- Viscosity: 1 cp
- Heat Capacity: 34 Btu/(ft<sup>3</sup>\*F)
- Thermal Conductivity: 24.0104 Btu/(ft\*day\*F)
- Compressibility: 4e-006 1/psi
- Leak: Leakage is allowed

At the bottom, the 'Define dimensionless pressure influence function' section has 'Table' selected and 'Steady State' unselected. The 'Edit/View' button is visible next to the 'Table' option.

Figure 3.65: Initializing Bottom Aquifer (Infinite Size)

The screenshot shows the 'Aquifer Properties' dialog box with the following settings:

- Name: Aquifer 1
- Location: Bottom
- Thickness: (empty)
- Porosity: 0.2
- Permeability: 5 md
- Radius: (empty)
- Angle (fraction of a circle): (empty)
- R-Ratio: (empty)
- Modelling Method: Carter-Tracy (limited extent)
- Geometry: Rectangular, Finite
- Viscosity: 1 cp
- Heat Capacity: 34 Btu/(ft<sup>3</sup>\*F)
- Thermal Conductivity: 24.0104 Btu/(ft\*day\*F)
- Compressibility: 4e-006 1/psi
- Leak: Leakage is allowed

At the bottom, the 'Define dimensionless pressure influence function' section has 'Table' selected and 'Steady State' unselected. The 'Edit/View' button is visible next to the 'Table' option.

Figure 3.66: Initializing Bottom Aquifer (Finite Size)

## 2. Initializing Edge Aquifer

The \*REGION keyword was used to attach the *numerical aquifer* to the north, east, and south directions of the reservoir. The strength of the reservoir was made finite and infinite to test the sensitivity. Figures 3.67 and 3.68 show parameters initialized to define the infinite and finite edge aquifer to the reservoir model, respectively.

Property	Value
Name	Aquifer 1
Location	Regions
Thickness	
Porosity	0.2
Permeability	5 md
Radius	
Angle (fraction of a circle)	
R-Ratio	
Modelling Method	Carter-Tracy (infinite extent)
Geometry	Rectangular   Infinite
Viscosity	1 cp
Heat Capacity	34 Btu/(ft³°F)
Thermal Conductivity	24.0104 Btu/(ft·day°F)
Compressibility	4e-006 1/psi
Leak	Leakage is allowed

Figure 3.67: Initializing Region Aquifer (Infinite Size)

The following were the scenarios studied as part of the *numerical aquifer* sensitivity study:

- a. All Aquifer Sensitivity
- b. Bottom Aquifer Sensitivity
- c. Edge Aquifer Sensitivity
- d. Infinite Aquifer Sensitivity
- e. Finite Aquifer Sensitivity
- f. Aquifer Sensitivity at Gas-Water Contact at 2080 ft

- g. Aquifer Sensitivity at Gas-Water Contact at 2070 ft
- h. Aquifer Sensitivity at Gas-Water Contact at 2045 ft

Figure 3.68: Initializing Region Aquifer (Finite Size)

### 3.4.5.2 Walakpa Gas Field

Sensitivity studies were performed on the WAL gas pool as part of the history matching studies. Production data was limited, and the reservoir free gas reserves were huge; hence it was difficult to capture and conclude the impact of parameters on overall reservoir performance.

### 3.4.6 Forecasting Study

#### 3.4.6.1 East Barrow Gas Field

The best-case model provides a useful tool to locate the current location of “sweet” spots (high gas and hydrate concentration zones) within the reservoir. Based on reservoir



mapping studies, locations for drilling future infill wells were proposed. Horizontal and vertical infill wells were drilled to predict the reservoir performance for the next 30 years. Several models were simulated to compare the technical feasibility of adding a horizontal or vertical test well, or completing existing wells laterally. However, these forecasting runs were not supported by economic modeling.

The CMG-STARs keyword \*RESTART offers an easy way to start a new simulation run from the last simulation date. For the EB gas reservoir, the last simulation date was Sep 01, 2007. On activating the \*RESTART keyword, the existing model loaded the previous simulation run obtained for the best-case model and started the simulation run from Sep 01, 2007 to Sep 01, 2037. EB #14 and #19 were the two active wells in the region. Hence scenarios were developed taking these active wells only. Eight forecasting runs were simulated in this study:

- i. Producing EB #14 (Only)
- ii. Producing EB #19 (Only)
- iii. Producing EB #14 and #19 (Together)
- iv. Completing and Producing EB #14 in Horizontal Plane (~1000 ft Long)
- v. Completing and Producing EB #19 in Horizontal Plane (~1000 ft Long)
- vi. Completing and Producing EB #14 and #19 in Horizontal Plane (~1000 ft Long, Each)
- vii. Producing EB #14 and #19 with New Vertical Test Well
- viii. Producing EB #14 and #19 with New Horizontal Test Well (~1000 ft Long)

The wellbore diagram for EB #14 and #19, completed in horizontal plane (both vertical and horizontal sections are open to flow), and new vertical and horizontal infill wells are shown in Appendix I.

#### *3.4.6.2 Walakpa Gas Field*

Forecasting study on the WAL gas field was performed similar to EB study. All wells in the region were active, and with limited production data, it was difficult to compare

reservoir performance with new wells. Thus, single forecasting run was made where all the existing wells were made to produce at equal rates for next 30 years. Table 3.20 summarizes the forecasting study for the WAL reservoir.

Table 3.20: Summary of Forecasting Runs

Simulation Period	30 Years (Sep 01, 2007 to Sep 01, 2037)
Well Produced	All Existing Wells
Production Rate	500 Mscf/Day/Well (Constant) (Cumulative Rate - 4.5 MMscf/Day)
New Test Well	Not Added
Model Studied	WAL Original (LARGE) Model

Forecasting study was performed on the original (LARGE) model that was developed based on geologic study performed by Panda and Morahan (2008). The LARGE model extended in updip locations of the reservoir and was based on predictions of limited geologic and seismic data. The history matched SMALL model was imported in the LARGE model and forecasting run was performed.

## 4. RESULTS AND DISCUSSION

### 4.1 Gas Hydrate Stability Modeling

#### 4.1.1 CSM-HYD Results Validation

Reservoir depths vs. temperature plots were prepared for a gas composition having 99% methane in contact with formation water salinity of 2% and 4% w/w, respectively. Figures 4.1 and 4.2 present the comparative plot. CSM-HYD results (Figure 4.1) show good agreement with the experimental data (Westervelt, 2004). On the other hand, a higher degree of deviation was observed between the empirical models and the experimental data.

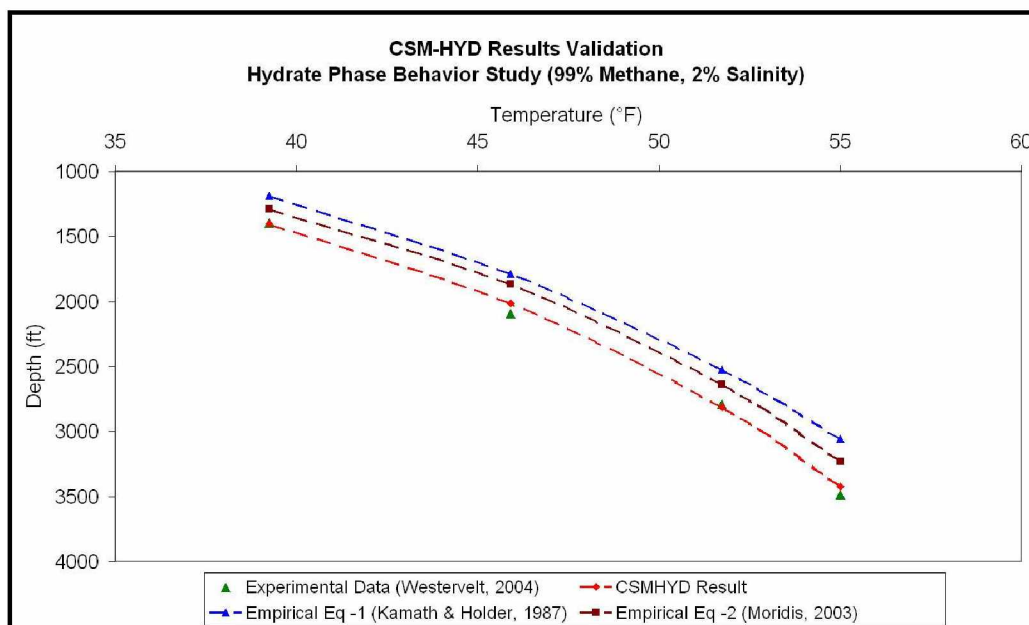


Figure 4.1: CSM-HYD Results Validation Study (99% Methane, 2% w/w Salinity)

With 4% w/w formation water salinity, some deviation was observed for CSM-HYD results at higher reservoir temperatures (Figure 4.2). However, the magnitude of error was much higher when empirical models were compared.

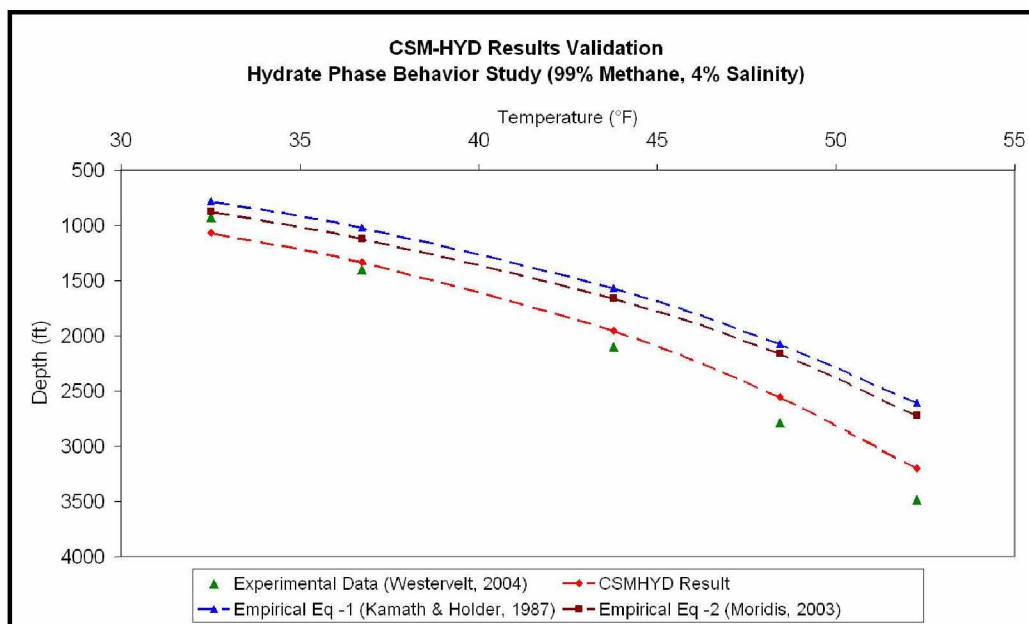


Figure 4.2: CSM-HYD Results Validation Study (99% Methane, 4% w/w Salinity)

Table 4.1 quantifies the degree of deviation observed between the experimental data and the model outputs. Interestingly, the Kamath and Holder (1987) empirical model showed a larger degree of separation in comparison with Moridis (2003) model for both the scenarios (Tables 4.1 and 4.2).

Table 4.1: Root Mean Square Error Analysis

<b>Models (Compared Against Westervelt, (2004) Data)</b>	<b>99% Methane and 2% w/w Salinity</b>	<b>99% Methane and 4% w/w Salinity</b>
	<b>Root Mean Square Error (%)</b>	
CSM-HYD	2.07%	9.21%
Moridis, 2003	7.95%	19.34%
Kamath and Holder, 1987	12.97%	24.23%

#### *4.1.2 Gas Hydrate Stability Models*

Based on the previously explained methodology, methane hydrate stability models were developed for the SB, EB and WAL gas fields using CSM-HYD software (Figures 4.3, 4.4, and 4.5). The CSM-HYD equilibrium predictions were plotted considering 0%, 2%, and 4% w/w salt concentrations. Available temperature gradient data were also plotted, and the range of hydrate stability was estimated. Findings from this study are explained below.

##### *4.1.2.1 South Barrow Gas Field*

From the SB hydrate stability model (Figure 4.3), it was concluded that the temperature gradient of the reservoir was much higher than required for having stable hydrates within reservoir depths. Hence, stable hydrate zones were not found within reservoir pay zone depths (2200 ft to 2400 ft) for formation water salinity range of 0%, 2%, and 4% w/w.

##### *4.1.2.2 East Barrow Gas Field*

Results from the EB were encouraging as hydrate stability zone existed for the range of salt concentration studied (Figure 4.4). Even though the temperature gradient data were scarce and may not be a true representation of reservoir conditions, the plot gave a good picture of the hydrate stability within the pay zone (2000 ft to 2150 ft). The base of hydrate zone stability crossed the geothermal gradient within the Middle Barrow sand (Figure 4.4). This phenomenon suggested that the in-situ hydrates were possibly associated with a free gas reservoir (Figure 4.5), an example of Class 1 type reservoir.

##### *4.1.2.3 Walakpa Gas Field*

The hydrate stability model for the WAL gas field showed promising results (Figure 4.6 and 4.7). As was expected, the stable hydrate zone was not found within deeper zones of the WAL sand, where existing wells were completed (2000 ft to 2600 ft). However, a stable hydrate phase, existing in updip locations (1700 ft to 2000 ft), was predicted.

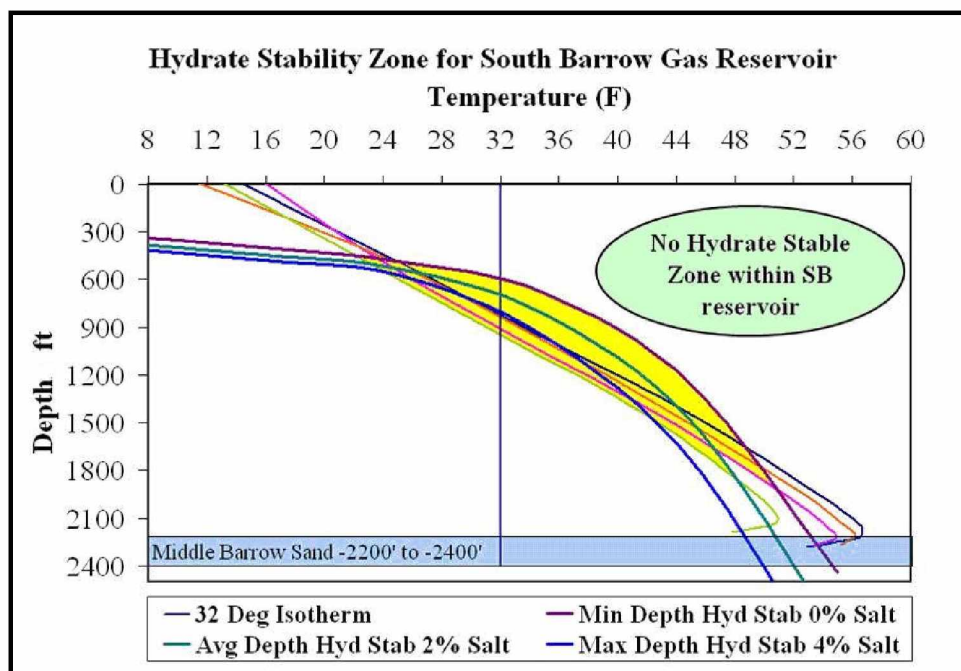


Figure 4.3: Hydrate Stability Model for the SB Gas Field

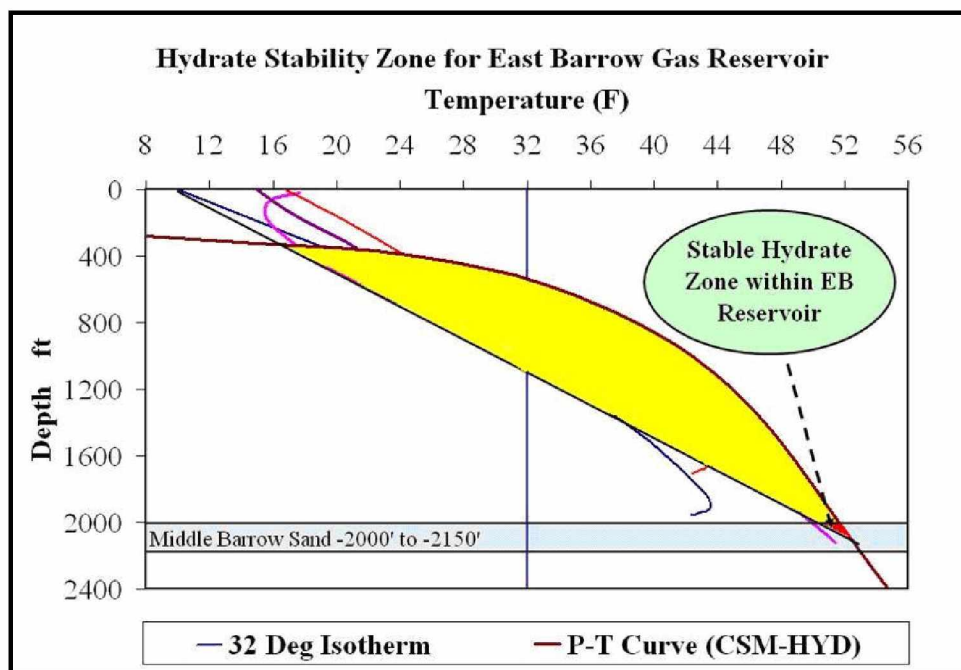


Figure 4.4: Hydrate Stability Model for the EB Gas Field

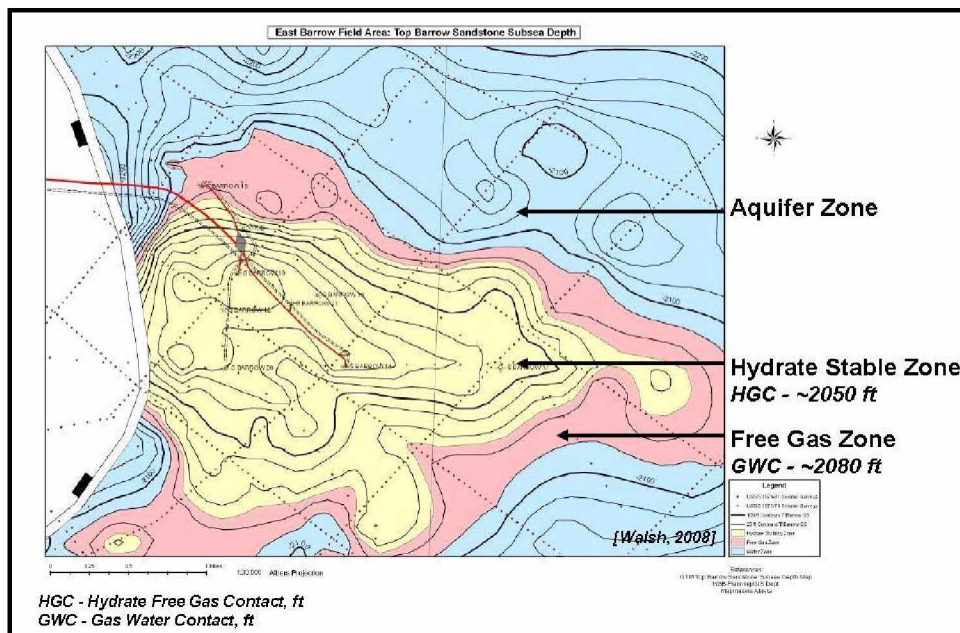


Figure 4.5: Structural Diagram Showing Hydrate Stability Zone (Walsh, 2008)

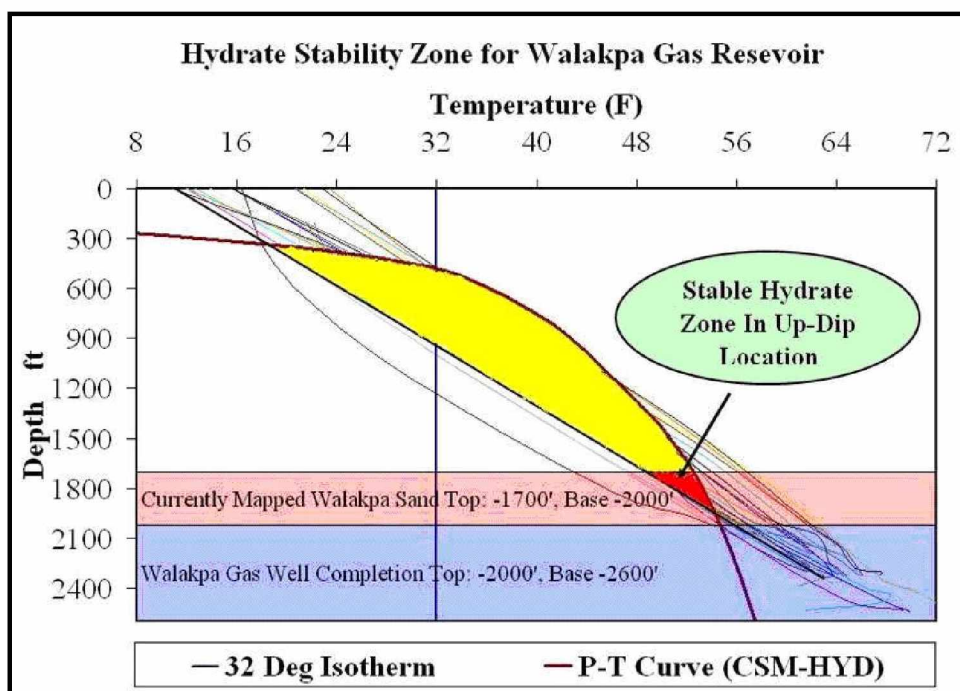


Figure 4.6: Hydrate Stability Model for the WAL Gas Field







#### 4.2.1 Volumetric Model

The methodology presented previously was applied to the EB gas reservoir. Several iterations were carried out to obtain a constant value of  $C$ . The  $z$ -factor and gas viscosity calculations also were performed to supply the accurate gas property. The best-case (constant  $C$ ) scenario was obtained by assuming an OGIP,  $G$ , of 90 bcf. Initial fluctuation in production data was neglected while selecting the constant  $C$  (Figure 4.8). The initial reserve obtained using this model was exceptionally high compared to previous volumetric estimates of 15 bcf (Gruy, 1978). The possible reason for higher estimates with the volumetric method is that this model assumes a tight gas reservoir system, and the iterations are aimed at providing a fixed value of deliverability constant (gas property assumed constant), which was possible only when the average pressure remained closer to the initial pressure. This is physically achievable only if the gas production is low (tight gas) and the reservoir have exceptionally large volumes of OGIP.

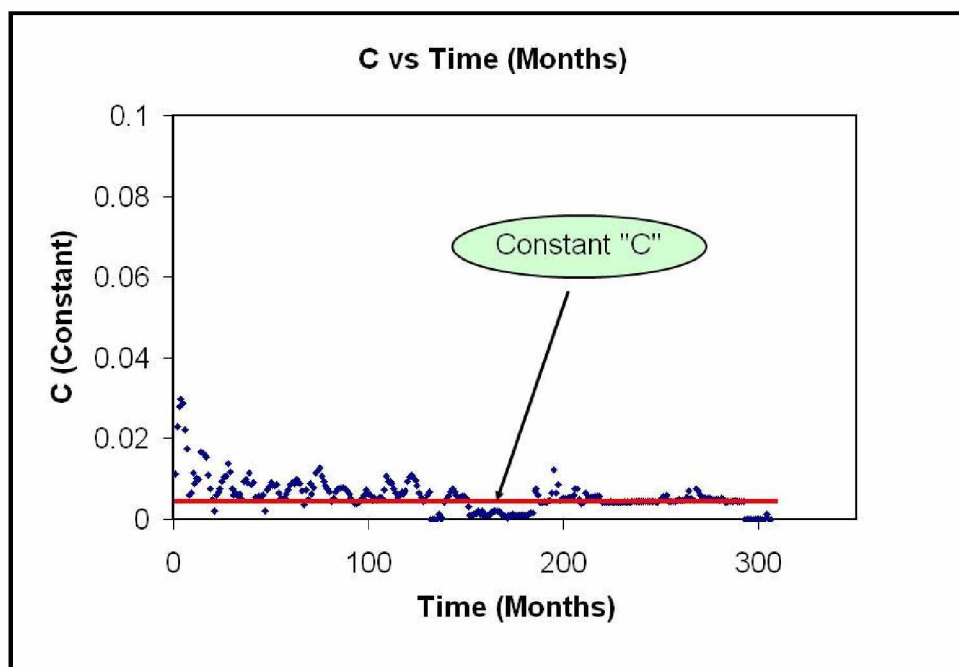


Figure 4.8: Volumetric Model - Constant (Horizontal)  $C$  vs. Time (Months)

The  $\frac{P(t)}{z(t)}$  vs.  $G_p(t)$  relationship obtained for the best-case was compared with production data in Figure 4.9. As is clearly evident, the profile obtained from the model followed a typical volumetric gas reservoir response. Subsequently, the  $\frac{P(t)}{z(t)}$  vs.  $G_p(t)$  relationship obtained for the best-case was used to obtain average reservoir pressure,  $P(t)$  vs. monthly production period,  $t$ , (Figure 4.10). The plot was again compared with the production profile. Extremely low (near zero) production rates kept the bottomhole pressures essentially equal to the reservoir pressures, and hence the volumetric model managed to match the production history data in later times.

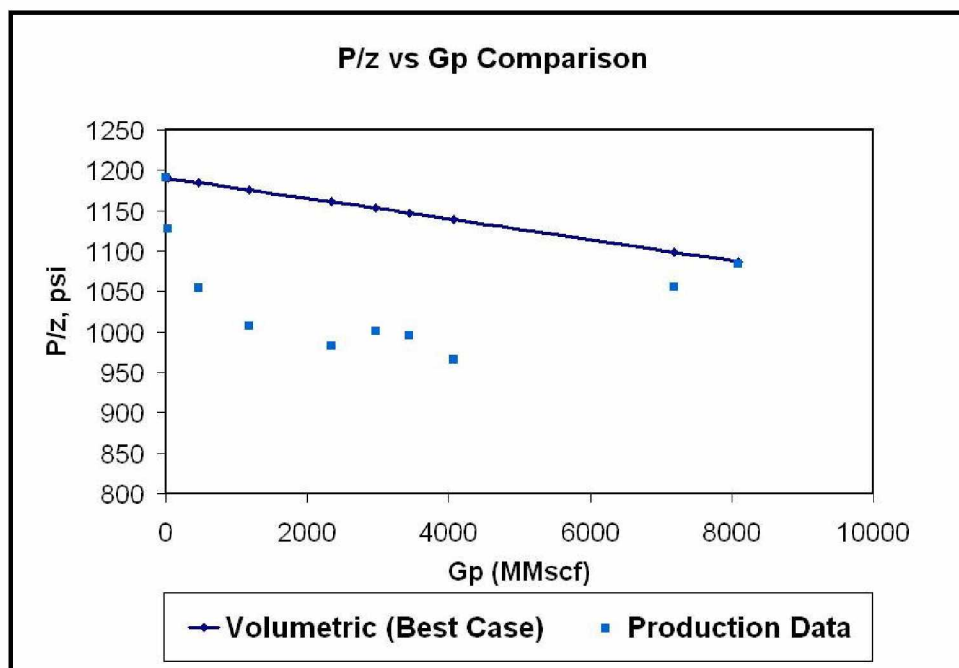


Figure 4.9: Volumetric Model -  $\frac{P(t)}{z(t)}$  vs.  $G_p(t)$  Plot for the EB Reservoir

A maximum error of 20% was observed between the volumetric model results and the production data. Figures 4.9 and 4.10 show that the production history data taken from the EB gas reservoir never followed the response of a volumetric model. This considerable deviation confirmed that the EB gas reservoir was not volumetric.

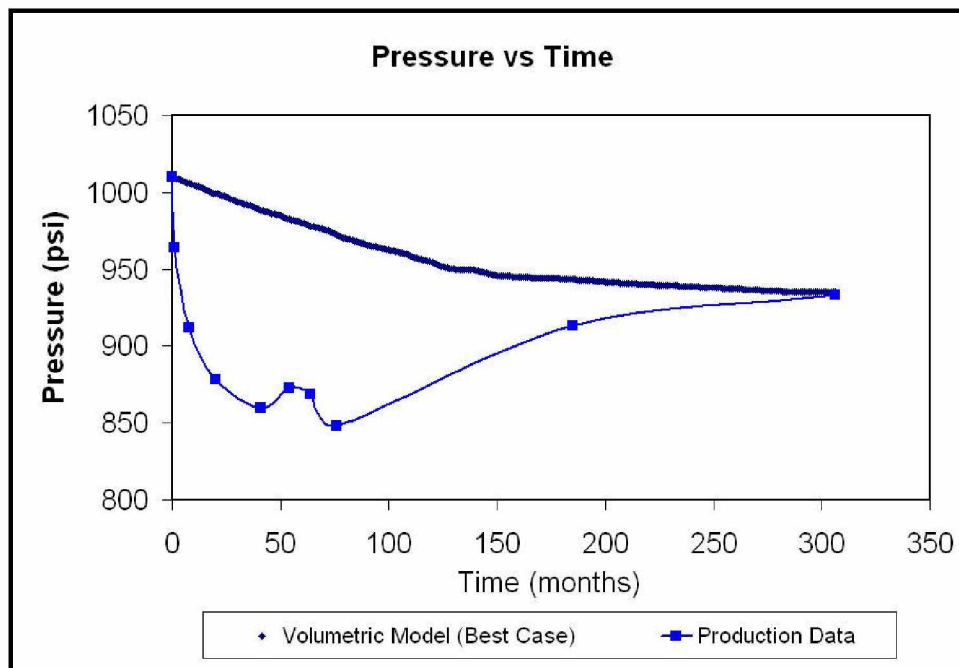


Figure 4.10: Volumetric Model - Pressure vs. Time Plot for the EB Reservoir

#### 4.2.2 Water Influx Model

The EB production data were utilized to develop material balance model considering a waterdrive mechanism. Figure 4.11 shows a plot between  $\frac{G_p(t)B_g(t) + W_p(t)B_w(t)}{(B_g(t) - B_{gi})}$  and

$G_p(t)$ . Two unique slopes were constructed passing through the data points (Figure 4.11). The following observations and inferences were drawn from the plot:

- i. The data points clearly showed a positive buildup of slope initially, thereby confirming the hypothesis that the reservoir was not volumetric. The gentle slope observed in the early part of gas production strengthens the fact that the reservoir was dominated by initial gas expansion accompanied with small rate of water influx.
- ii. However, later on the impact of gas production showed a jump in the slope (Figure 4.11). This unexpected and drastic change in the slope suggested there was a possibility of having additional pressure support from a new

source. This could be either due to water influx from a new communicating aquifer or dissociating hydrates. Unfortunately, such behaviors could not be explained with the water influx model.

- iii. Due to this limitation, the study was restricted to the early production period only. The first slope developed through the data points crossed the y-axis at an OGIP of 9 bcf. Based on this information, cumulative water influx,  $W_e(t)$ , was estimated. At the end of 4.07 bcf of gas production about 7.0e6 bbls (MMbbls) of water influx had taken place.
- iv. Interestingly, while estimating the aquifer size, it was observed that the aquifer size tended to increase with time and never remained constant. This observation confirmed that the size of the associated aquifer may not be large enough to support observed reservoir pressures. It was also estimated that about 6 MMMbbls of aquifer size was needed to supply 7 MMbbls of water to the reservoir in order to achieve the observed reservoir pressure after 4.07 bcf of gas production.

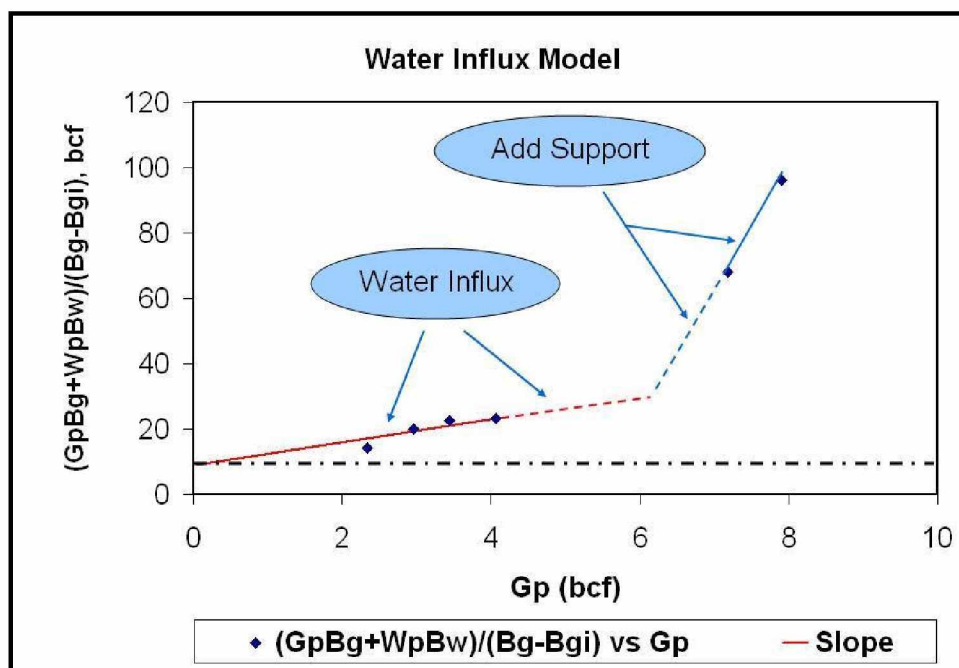


Figure 4.11: Water Influx Model for the EB Reservoir

To summarize, the water influx study confirmed the existence of an aquifer in contact with the gas reservoir. During the early production period, the reservoir was producing under moderate to active waterdrive. However, the model failed to explain the observed shift in the slope (Figure 4.11).

#### 4.2.3 Hydrate Model

Hydrate model and a modified version were developed during this study providing a powerful tool to compare the performance of the EB reservoir in the presence of a hydrate zone and without hydrates respectively.

- i. Modifications to the hydrate model were made to handle a gas reservoir (with no associated hydrates). The result obtained from the *modified hydrate model* was validated by comparing its performance with a volumetric gas reservoir.  $\frac{P(t)}{z(t)}$  vs.  $G_p(t)$  and  $P(t)$  vs. time plots were constructed, and responses were compared (Figure 4.12). The plots showed a close agreement (max error of 1%) between the results obtained using the two different models. The exercise validated the effectiveness of the *modified hydrate model* in representing a free gas reservoir with no hydrates.
- ii. CMG-STARS simulation was carried out considering similar reservoir dimensions and restrictions as in the previous step. A plot comparing the pressure profile of the volumetric reservoir, the *modified hydrate model*, and the CMG-STARS simulation is presented in Figure 4.13. The plot shows a close match between all the three models. This again validated the response of *modified hydrate model*, and hence this model was now used to represent volumetric reservoir conditions while matching the reservoir performance with the hydrate model.

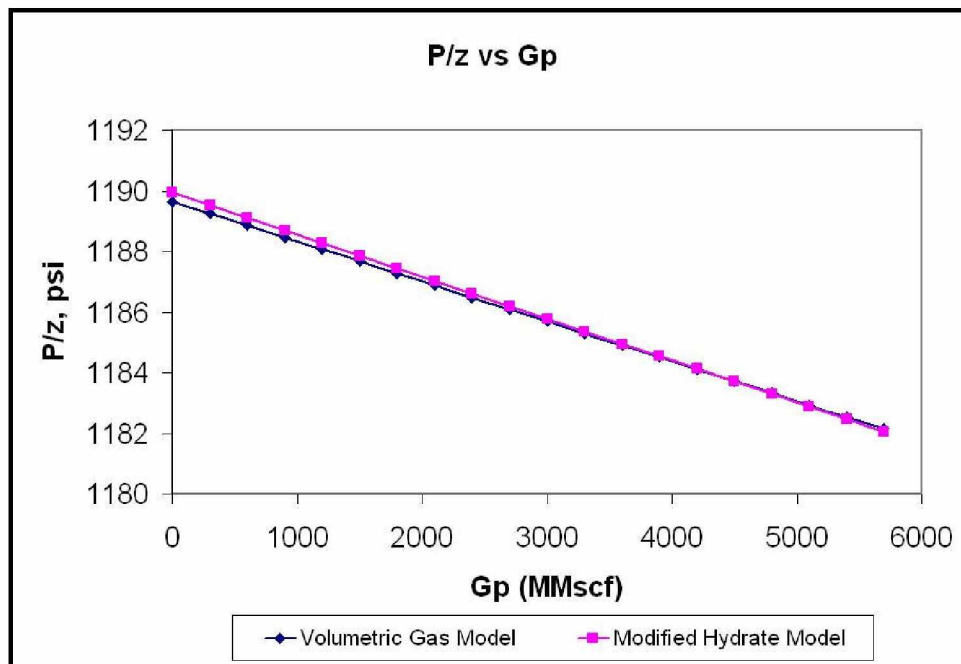


Figure 4.12: Volumetric Gas Reservoir Performance Plot for Mechanistic Model

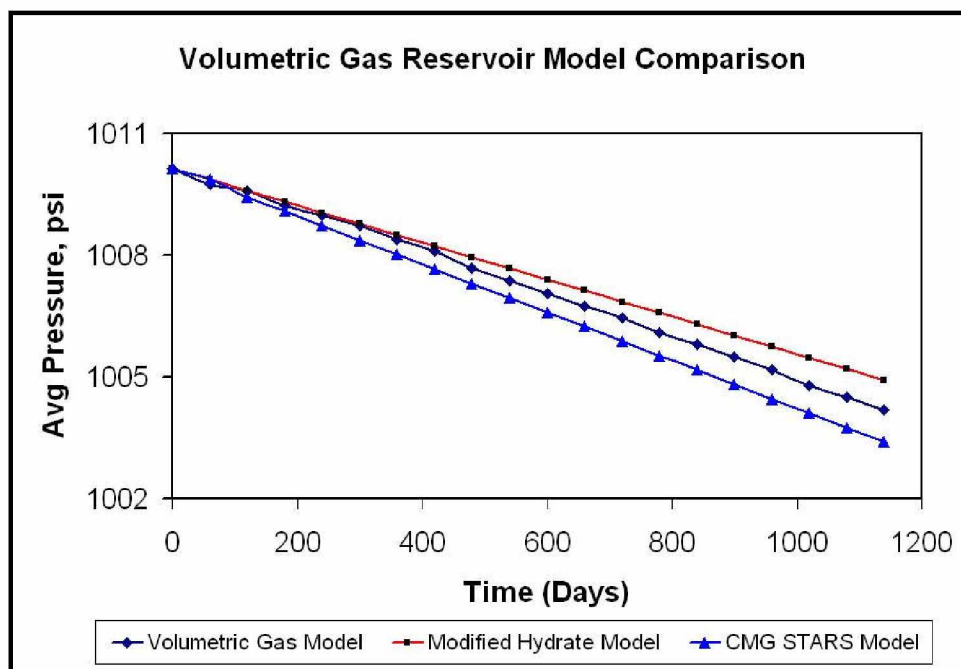


Figure 4.13: Pressure vs. Time Plot for Mechanistic (Gas Reservoir) Model

- iii. The *modified hydrate model* was then applied to the actual EB type reservoir. The reservoir was produced at a constant production rate of 1600 Mscf/Day. Figure 4.14 compares the historical production data with the performance of the *modified hydrate model*. As expected, the model would never match the production data. Thus it can be concluded that the reservoir was under constant external pressure support either from aquifer and/or associated hydrates.

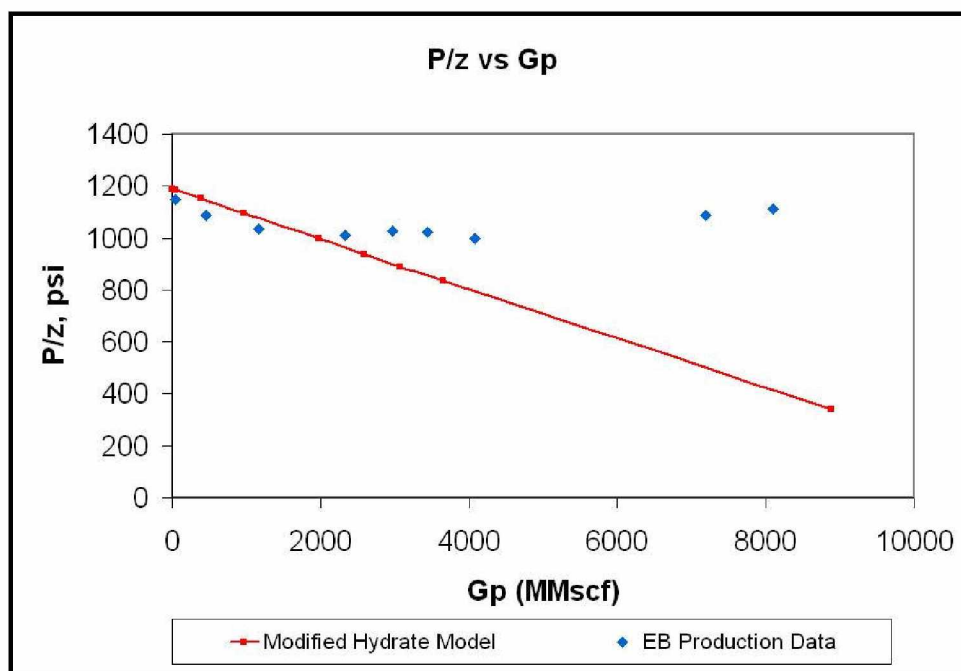


Figure 4.14: Volumetric Gas Reservoir Performance Plot for *Modified Hydrate Model* and the EB Production Data

- iv. The CMG-STARS reservoir model was correspondingly scaled up to represent the EB reservoir dimensions. Reservoir properties were kept the same. Simulation studies were conducted again in the absence of a hydrate layer, and the results were compared with the *modified hydrate model* and the EB production data (Figure 4.15). The plot showed an excellent match between the *modified hydrate model* and CMG-STARS results. However, both the results never matched the production data.



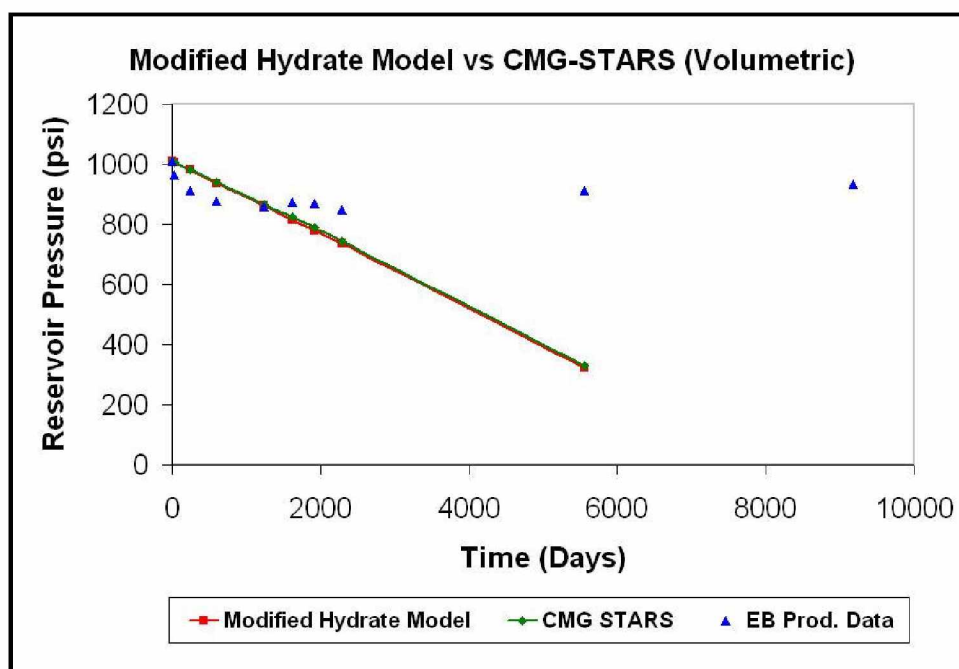


Figure 4.15: Pressure vs. Time Comparison Plot for *Modified Hydrate Model*, *CMG-STARS Model*, and the *EB Production Data*.

- v. To study the impact of hydrate zone thickness on reservoir performance, original hydrate model was used and performance of the EB type reservoir was evaluated. The reservoir sensitivity was compared for different hydrate thickness (Figure 4.16). The plot showed that as the hydrate zone thickness was increased, the reservoir pressure support increased proportionally. Reservoir with hydrate zone (Figure 4.16) showed a better pressure match as compared to free gas volumetric reservoir response (zero hydrate zone thickness modeled using *modified hydrate model*) as shown in the figure.



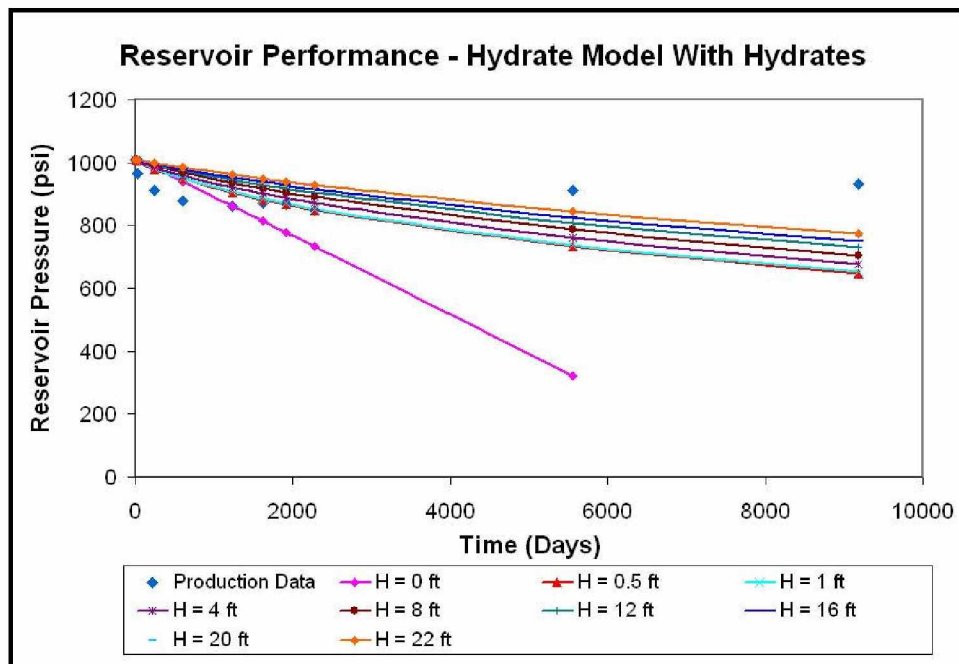


Figure 4.16: Pressure vs. Time Plot for Hydrate Model (Changing Hydrate Zone Size)

#### 4.2.4 CMG-STARS Simulation Model

Hydrate model does not have a provision to include the effect of water influx into the overall material balance. Hence, the CMG-STARS reservoir model was used to develop reservoir models with water influx (with or without hydrate-cap).

- i. A plot was generated to compare the reservoir pressure response for an aquifer-driven system (Figure 4.17). The effect of hydrate layer (using hydrate model) obtained previously was also included in this comparison. The impact of aquifer size on reservoir performance was compared. Figure 4.17 shows that with an increase in aquifer strength, the reservoir pressure tended to stabilize. The plot compared the impact due to hydrate zone thickness against aquifer support. Clearly, the pressure response in the case of a hydrate mechanism was higher than aquifer-driven mechanism. However, both the mechanisms failed to match the production profile independently. Perhaps, a combined effect of hydrate and water influx would bring the reservoir performance much closer to that observed for the EB reservoir.

- ii. Finally, the CMG-STARs reservoir model was modified to include aquifer support and an overlying hydrate-cap. Interestingly, one of the scenarios (Figure 4.18) showed a close match with the production data. This scenario (marked in the figure by red dotted circles) had a free gas reservoir in communication with a weak aquifer (33 ft thick), and was associated with a thick hydrate layer (22 ft).
- iii. Based on encouraging results (Figure 4.18), a preliminary history matching study was initiated to match the reservoir performance and confirm the reservoir drive mechanism. This was performed by tuning parameters such as gas production rates, hydrate zone size, aquifer zone permeability, and porosity. The hydrate-cap thickness was reduced to 18 ft, whereas the aquifer size remained unchanged. An important parameter altered was the gas production rate. It was observed that the EB reservoir initially produced at a very high rate, averaging 1675 Mscf/Day. After a short period of negligible to no production, the reservoir started producing at an average rate of 265 Mscf/Day for the rest of the time. Considering these important aspects, simulator's well production data was altered to produce at a constant rate of 1675 Mscf/Day for first 10 years followed by a short shut-in period of 5 to 6 months. Later, the well was again opened to production at a reduced rate (265 scf/Day). Figure 4.19 shows the reservoir performance matching the EB production data with a root mean square error of 5.5%. It should be noted, however, that the history matching was done to confirm the drive mechanisms active in the reservoir. Detailed field- and well-level history matching studies have been performed during reservoir simulation studies (explained later).

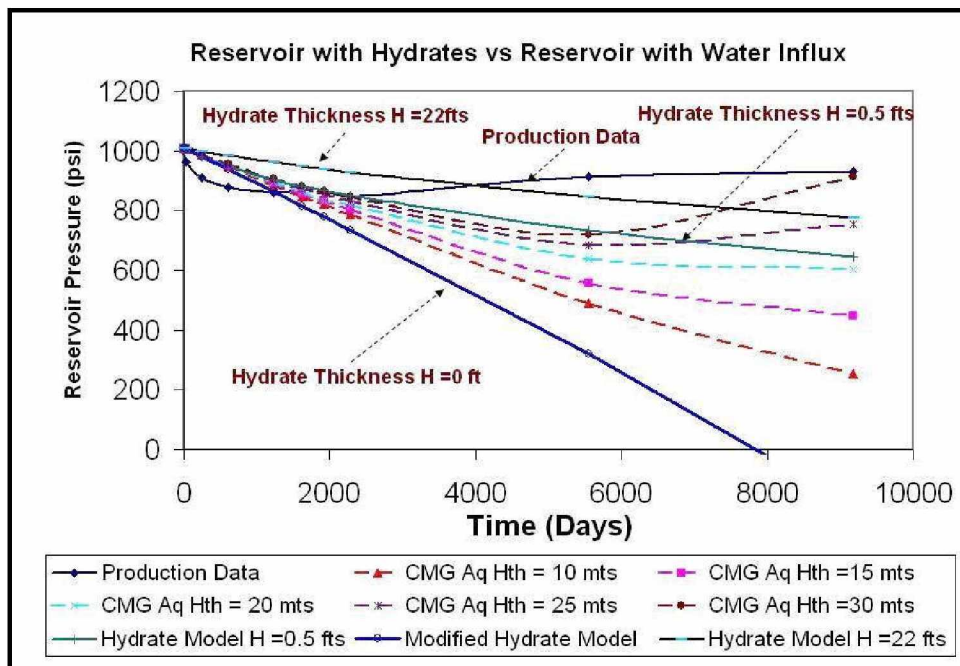


Figure 4.17: Pressure vs. Time Comparison Plot for Hydrate and CMG-STARs Models (Hydrate vs. Aquifer Support)

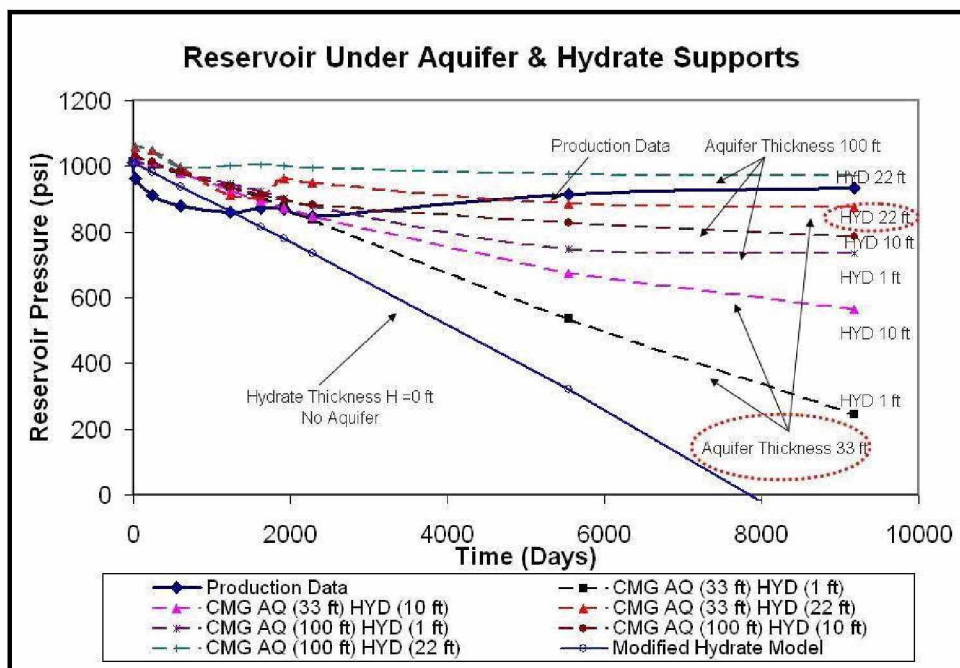


Figure 4.18: Hydrate and Aquifer Supported Gas Reservoir Performance Plot (CMG-STARs Model)

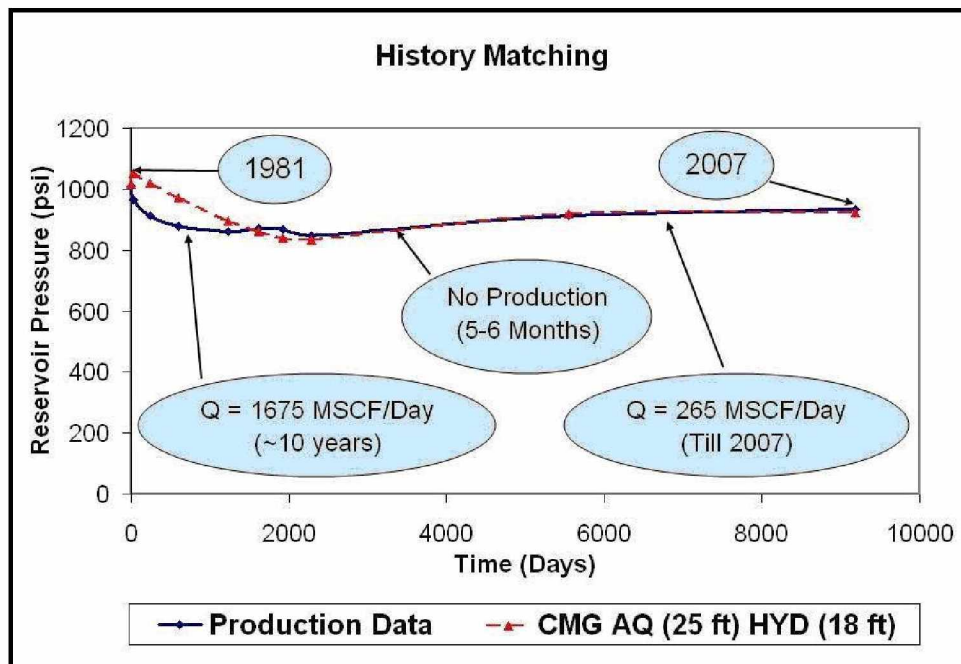


Figure 4.19: The EB Production Data History Matching Plot

- iv. The history matched model was used to conduct sensitivity analysis. The results are explained below:

*Reservoir Permeability:* As is evident, tight gas reservoirs restricted gas production at higher rates, whereas reservoirs with higher permeability sands (100 md to 500 md) drained the reservoir quickly (Figure 4.20). However, with higher permeability reservoir, the pressure in the reservoir started increasing after initial decline. This could be attributed to the combined effect of dissociating hydrates and support from the aquifer.

*Gas Production Rates:* CMG-STARs simulation runs were performed by varying gas production rates. A wide range of production rates were chosen. The plot was generated and is presented in Figure 4.21. A best-case run was also performed by using a single flow rate of 1675 Mscf/Day throughout the production life of the reservoir. This provided a common platform for comparison (all models producing at constant production rates). Lowering gas production rates reduced the rate of pressure decline, but later the

pressure stabilized due to the combined effect of water influx and hydrate dissociation. However, when production rates were extremely high, the reservoir pressure declined at a substantial rate, causing a higher rate of hydrate dissociation. Again, gas production proceeded at a higher rate than the rate of gas recharge from hydrates. In the absence of substantial gas recharge, reservoir pressure continued to decline. Finally, the waterdrive mechanism dominated, and a higher rate of water influx occurred.

*Hydrate Zone/Free Gas Zone Ratio:* Figure 4.22 shows a pressure plot prepared to obtain the performance of the reservoir by varying hydrate and free gas zone thickness. It was evident from the figure that the reservoir performance remained essentially the same with higher hydrate thickness. However, with a thinner hydrate layer, the reservoir pressure declined at a faster rate as the weak aquifer failed to provide sufficient support to the reservoir.

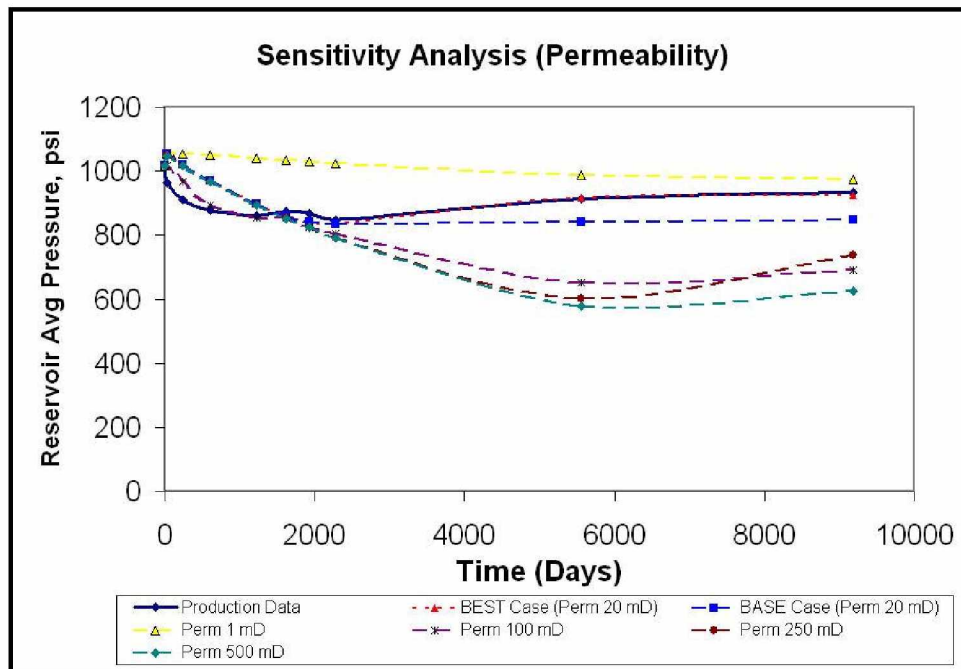


Figure 4.20: Sensitivity Analysis (Permeability)



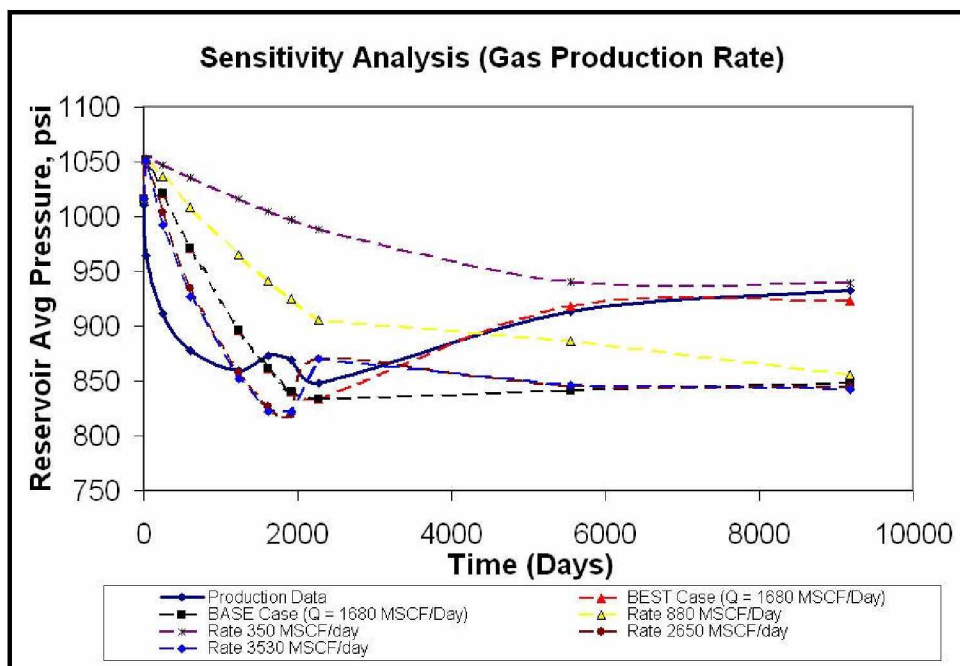


Figure 4.21: Sensitivity Analysis (Gas Production Rates)

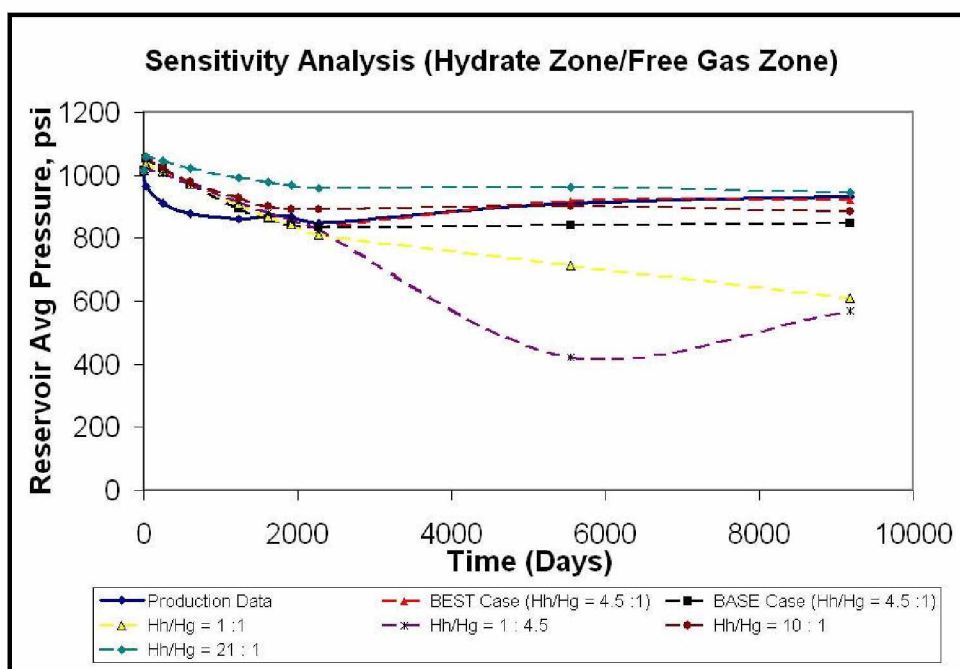


Figure 4.22: Sensitivity Analysis (Hydrate Zone/Free Gas Zone Ratio)

### 4.3 Gas-Water Relative Permeability Study

Gas-water relative permeability experiments were performed on a single BS sample. A Vernier's caliper was used to measure the dimensions of the core sample. Bulk volume was calculated by considering the sample to be perfectly cylindrical in shape. Table 4.2 presents the dimensions and bulk volume of the core sample recorded before the experiments. Results and observations are explained under respective subsections.

Table 4.2: BS Sample Dimensions

<b>BS Sample</b>	
Core Diameter	1.50 in.
Core Length	5.50 in.
Sample Bulk Volume	159.27 ml

#### 4.3.1 Porosity and Absolute Permeability Determination

Experimental runs were repeated three times in order to reduce experimental error. Table 4.3 summarizes the porosity determined for the BS sample. The average porosity calculated for the core sample was 12.98%.

Table 4.3: Results: Sample Porosity

<b>BS Sample</b>	<b>Run I</b>	<b>Run II</b>	<b>Run III</b>	<b>Average</b>
Dry Weight	327.20 gm	327.87 gm	327.53 gm	
Wet Weight	347.44 gm	348.37 gm	348.53 gm	
Water Weight	20.24 gm	20.50 gm	21.00 gm	
Density	1 gm/ml	1 gm/ml	1 gm/ml	
Pore Volume	20.24 ml	20.50 ml	21.00 ml	
Bulk Volume	159.27 ml	159.27 ml	159.27 ml	
Porosity	12.88%	12.87%	13.19%	12.98%

A waterflooding procedure was performed to measure the absolute permeability of the core sample with respect to water (single-phase) flow. Again, three runs were performed to obtain average absolute permeability data for the BS core sample. Table 4.4 presents the recorded data and absolute permeability, as calculated by applying Darcy's law.

Table 4.4: Results: Absolute Permeability

<b>BS Sample</b>	<b>Run I</b>	<b>Run II</b>	<b>Run III</b>	<b>Average</b>
Waterflooding Rate	1 ml/min	1 ml/min	1 ml/min	
Upstream Pressure	309.90 psi	310.20 psi	310 psi	
Downstream Pressure	300 psi	300 psi	300 psi	
Differential Pressure	9.90 psi	10.20 psi	10 psi	
Fluid Viscosity	1 cp	1 cp	1 cp	
Absolute Permeability	33.08 md	32.11 md	32.75 md	32.65 md

Permeability measurements were also made during hydrate formation-dissociation and displacement experiments. The average permeability of ~32 md was observed for BS sample. It should be noted, however, that the core holder was kept vertical while performing core-flooding experiments but, the effect of gravity was not included during permeability determination.

Controlling downstream pressure, using a backpressure regulator, proved to be the biggest challenge. Tubing connected to the backpressure regulator was cleaned each time prior to performing the experiments. Once water starts flowing through the sample the pressure got stabilized and the backpressure regulator became insensitive to disturbance and performed efficiently. Nitrogen gas was used to supply constant backpressure. Use of an incompressible fluid, such as, water could have provided better control on the downstream pressure.



### 4.3.2 Hydrate Formation and Dissociation Experiments

Forming hydrates within a consolidated core sample was a difficult task. Higher capillary pressure and poor temperature control were the primary reasons for several unsuccessful runs. Small pore volume of the core sample affected data acquisition. Pressure or volume change could not be captured due to smaller volumes of hydrate formed or dissociated within available pore space. Several runs were performed in order to achieve optimum process conditions for stable hydrate formation followed by controlled dissociation. The experiments were performed at higher pore pressures to provide a higher degree of precision in capturing the pressure or volume change.

Figure 4.23 shows the volume change profile for the hydrate formation experiment. The data was acquired while forming hydrate within the sediments with average hydrate saturations of 38% (actual). The gas-water two phase flow through BS sample, having a hydrate saturation of 38%, represented a situation similar to initial condition of EB reservoir (an initial hydrate saturation of 31% was estimated for the EB pool after performing detailed reservoir simulation studies explained in the next section).

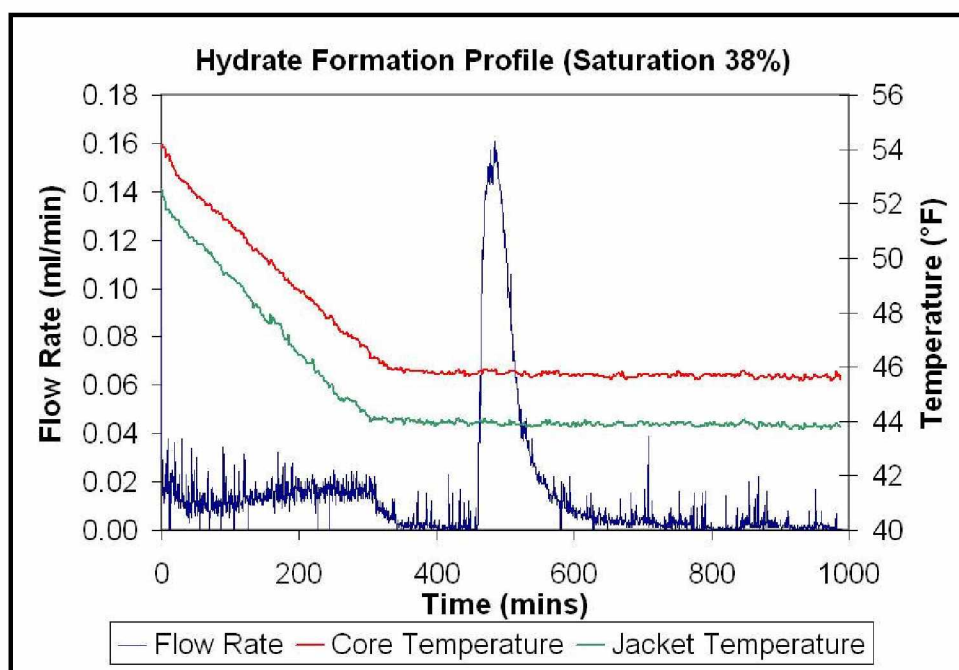


Figure 4.23: Hydrate Formation Profile (Hydrate Saturation 38%)

For this run, the hydrate formation experiment was performed at a pressure of 950 psi by running the pump at constant pressure. The temperature of the core was brought down from ambient conditions to around 42 to 44 °F. Hydrate formation caused a rapid reduction in reservoir pressure as most of the gas was consumed in forming hydrates. To maintain pore pressure, the pump recharged the system with additional gas by increasing the flow rate instantly. All efforts were taken to maintain the EB reservoir conditions. Table 4.5 presents the parameters maintained while forming hydrates at three saturations.

Table 4.5: System Parameters for Hydrate Formation

BS Sample		HYD Sat. 38%	HYD Sat. 14%	HYD Sat. 5%
Core Pressure (Constant)	psig	950 psig	975 psig	925 psig
Core Initial Temperature	°F	83 °F	80 °F	77 °F
Core Final Temperature	°F	44 °F	45 °F	45 °F

Hydrate saturation was quantified and recorded for three different runs. Several hydrate formation runs were successfully performed but later abandoned due to poor hydrate stability during displacement experiments. Three hydrate saturation data were chosen to show the gas-water fluid flow behavior during initial - (38%), current - (14%), and final - (5%) stages of hydrate dissociation within the reservoir, something similar to the hydrate dissociation pattern observed in the EB reservoir (refer to the EB gas reservoir simulation studies).

In case of hydrate dissociation, the gas pump, maintaining system pressure previously, was stopped. The cooling system was also switched off, and the sample was allowed to achieve ambient conditions. During this process, as soon as the core temperature exceeded the hydrate stability temperature, in-situ hydrates started dissociating, thus increasing the volume of gas in the closed system (causing a rise in pressure). A total increase of 28 psi was recorded after complete hydrate dissociation (Figure 4.24). A sharp change in pressure was not observed during the hydrate dissociation. This

observation was attributed to slow gas buildup within the porous media and gas accumulator system. Pore blockage due to undissociated hydrates and produced water (due to hydrate dissociation) could be one of the possible reasons for poor gas permeability through the porous media.

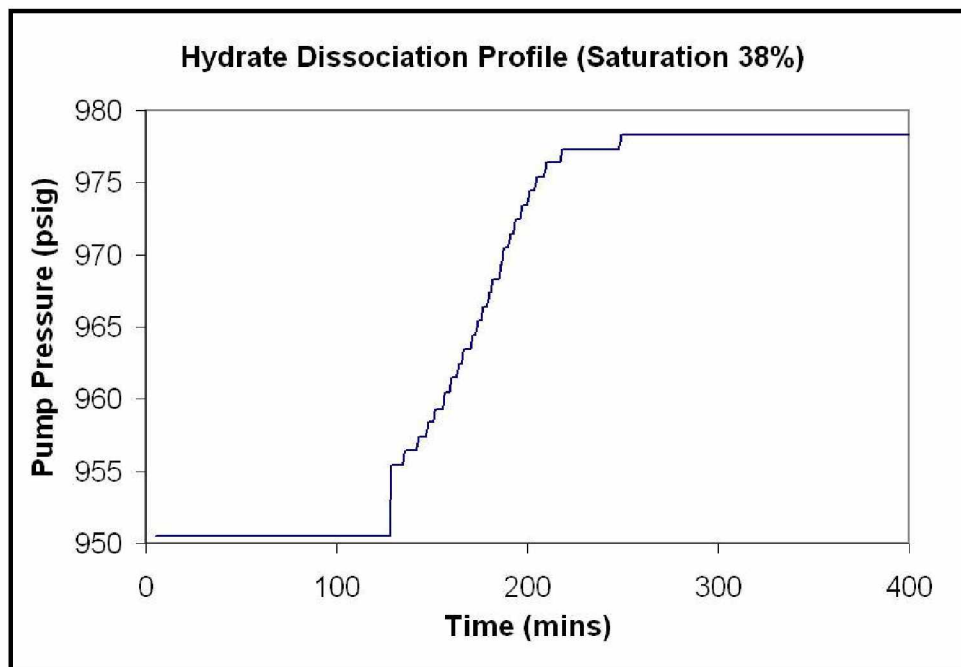


Figure 4.24: Hydrate Dissociation Profile (Hydrate Saturation 38%)

#### 4.3.3 Unsteady-State Displacement Experiments

Appendix E summarizes the results obtained after performing waterflooding and gasflooding procedures through hydrate-saturated cores. Results include the initial hydrate estimates, actual hydrate saturation, effective permeability to water flow (base permeability), and effective permeability to gas flow at irreducible water saturations. Relative permeability plots developed for corresponding hydrate saturations are presented in Figures 4.25, 4.26, and 4.27.

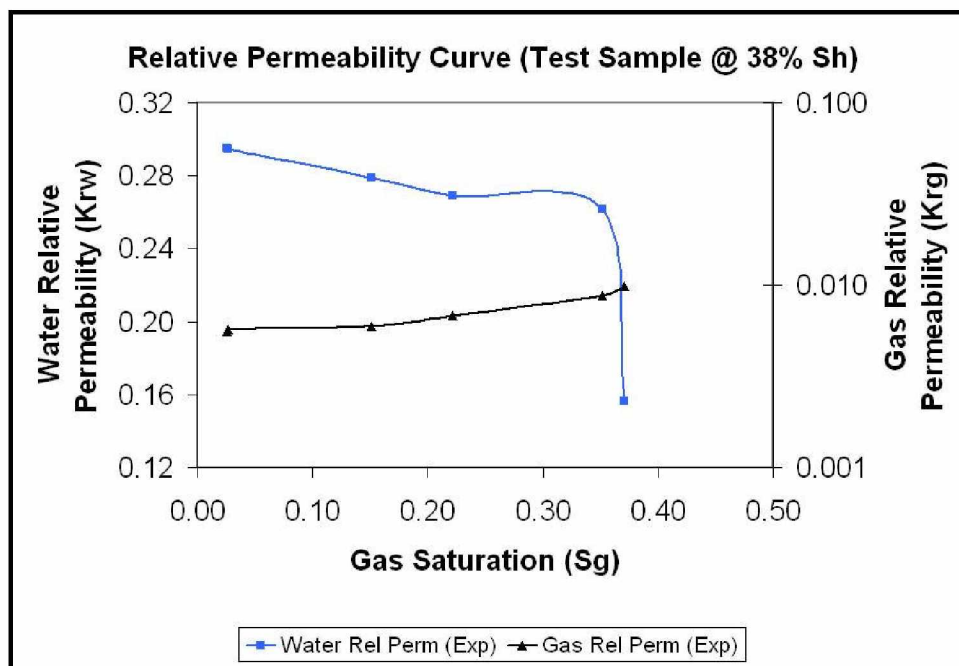


Figure 4.25: Gas-Water Relative Permeability Curve (Hydrate Saturation 38%)

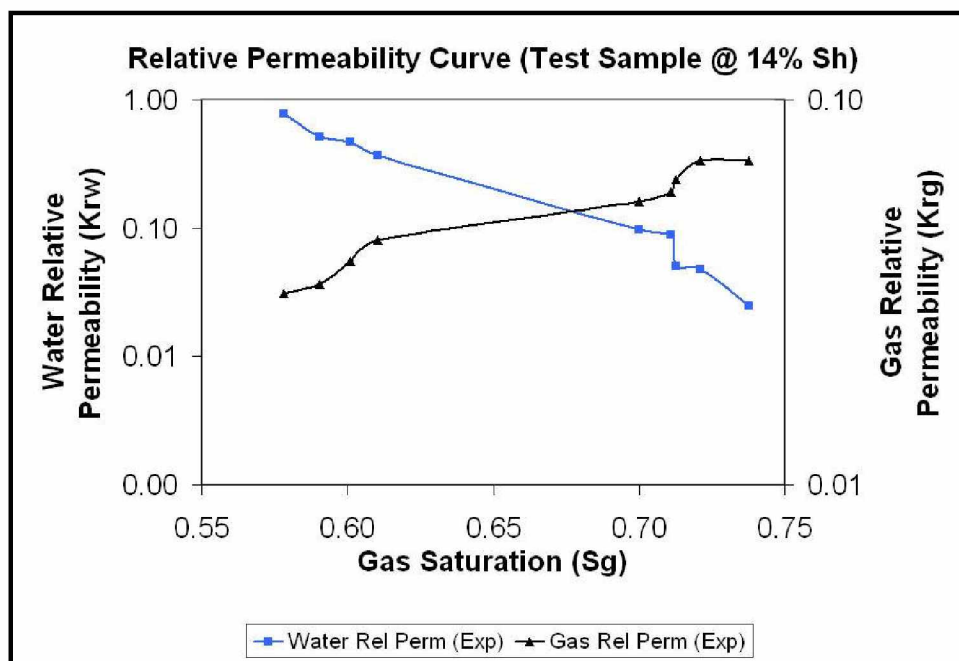


Figure 4.26: Gas-Water Relative Permeability Curve (Hydrate Saturation 14%)

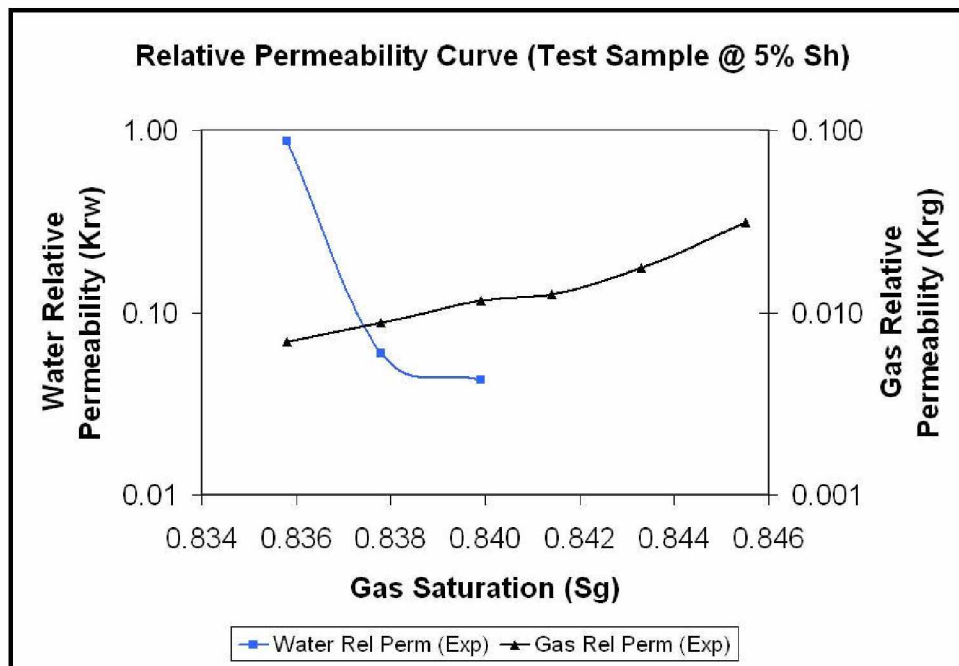


Figure 4.27: Gas-Water Relative Permeability Curve (Hydrate Saturation 5%)

While forming hydrates within the core sample, it was concluded that, in all the cases, 100% conversion of available gas (limiting component) into hydrate was not recorded. On further investigation of this issue, it was found that the operating pressure and temperature conditions of the core were close to the three-phase pressure and temperature equilibrium curve similar to EB conditions (Figure 3.22); hence the hydrate conversion process was slower than expected. For 100% conversion (at faster rate), rapid stirring of the fluid (free gas and water) was required which was not possible to perform inside the porous media.

The second important observation was that the two-phase fluid flow (free gas and water flow) was obtained for a short duration of time; hence the relative permeability table could not be extended for a wider range of saturations. In-situ hydrates had reduced the effective permeability of water and gas by a magnitude of ten and thousand, respectively, making gas flow extremely difficult. Furthermore, higher capillary pressures and related end effects prevented gas injection at smaller differential pressure. At higher differential pressure, gas flowed through the sample, but it was inconsistent.

Table 4.6 presents the effect of changing hydrate saturation on irreducible water saturation and effective permeability to water and gas flows. The data showed that with increasing hydrate saturation, the water displacing capacity of the injected gas reduced substantially. Figure 4.28 shows the effect of hydrate saturation on water and gas flows (effective permeability).

Table 4.6: Effect of Hydrate Saturation on Irreducible Water Saturation and Gas-Water Effective Permeabilities

Hydrate Saturation	38%	14%	5%
Irreducible Water Saturation (%) (Based on Total Pore Volume)	~38%	~14.70%	~13.95%
Effective Permeability to Water Flow (md)	1.97 md	8.50 md	26 md
Effective Permeability to Gas Flow (md) (At Irreducible Water Saturation, %)	0.02 md	0.80 md	0.84 md

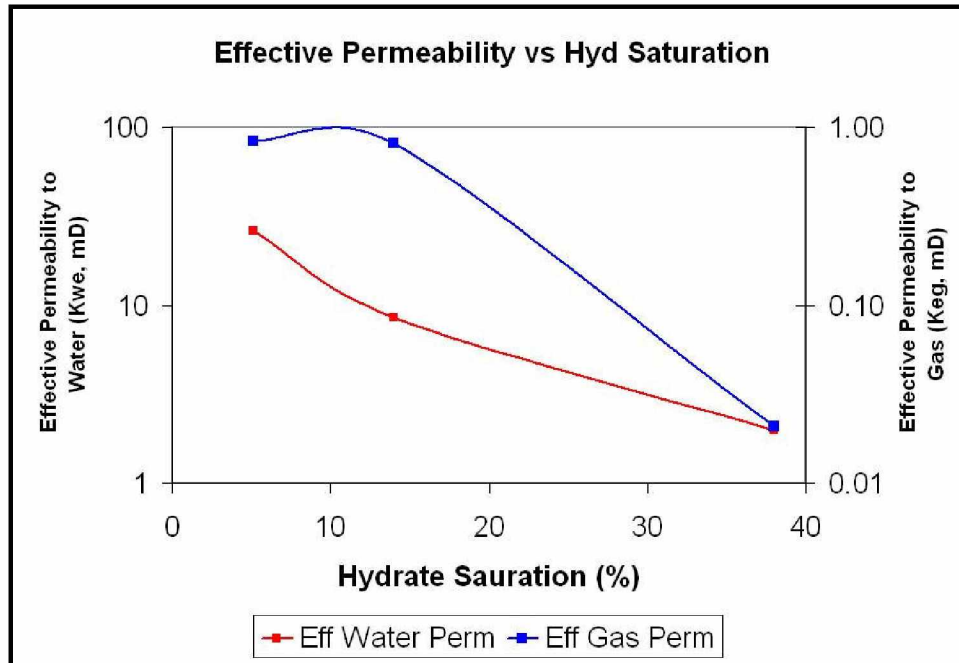


Figure 4.28: Effective Permeability vs. Hydrate Saturation

#### 4.3.4 Tuning the Relative Permeability Model

The Hong (2003) model was tuned based on relative permeability data obtained from the experiments (Equations 3.14 and 3.15). The regression coefficient,  $a$ , obtained after performing nonlinear regression analysis is presented in Table 4.7. The goodness of the fit was quantified by recording the correlation coefficient,  $R^2$ . Table 4.7 also presents the  $R^2$  value for each analysis.

Table 4.7: Tuned Parameters of Relative Permeability Model

Hydrate Saturation	$a$ (Water)	$R^2$ (%)	$a$ (Gas)	$R^2$ (%)
38%	0.15	83.20%	-0.89	67.97%
14%	0.07	49.42%	10.80	82.39%
5%	-0.08	15.39%	738	28.63%

A poor match showed inconsistency in the relative permeability data (Refer Appendix J for relative permeability tables). More datasets are needed to derive a convincing relative permeability model representing the fluid flow behavior of the EB type reservoir.

### 4.4 Reservoir Simulation Study

#### 4.4.1 History Matching

##### 4.4.1.1 East Barrow Gas Field

As explained previously, six different cases were simulated, and the reservoir performance was compared with historical data. The history matching was performed both at the reservoir level and the well-level. The field-level match was initiated for all cases. After achieving a close match, individual well-level matches were performed for the best-case scenario only. The initial estimates of free gas, hydrates, and associated (bounded) water were estimated for each case (Table 4.8).

Table 4.8: Initial Estimates of Free Gas, Hydrate, and Water

Case	Reservoir Model	Hydrate	Free Gas		Water
		billion ft <sup>3</sup> (res)	billion ft <sup>3</sup> (res)	bcf	billion ft <sup>3</sup> (res)
<i>A</i>	Only Gas	0.00 billion ft <sup>3</sup>	1.23 billion ft <sup>3</sup>	94.21 bcf	1.51 billion ft <sup>3</sup>
<i>B</i>	Gas + Aquifer	0.00 billion ft <sup>3</sup>	0.36 billion ft <sup>3</sup>	27.32 bcf	2.38 billion ft <sup>3</sup>
<i>C</i>	HYD + Gas + Aquifer (Best-Case)	0.15 billion ft <sup>3</sup>	0.21 billion ft <sup>3</sup>	15.83 bcf	2.38 billion ft <sup>3</sup>
<i>D</i>	Only HYD	0.85 billion ft <sup>3</sup>	0.38 billion ft <sup>3</sup>	29.31 bcf	1.51 billion ft <sup>3</sup>
<i>E</i>	HYD + Gas	0.15 billion ft <sup>3</sup>	1.08 billion ft <sup>3</sup>	82.62 bcf	1.51 billion ft <sup>3</sup>
<i>F</i>	HYD + Aquifer	0.25 billion ft <sup>3</sup>	0.11 billion ft <sup>3</sup>	08.49 bcf	2.38 billion ft <sup>3</sup>

Table 4.9 presents initial free gas estimates (at STD); these estimates include gas associated with hydrates. The basis for calculating hydrate-associated gas is as follows: one reservoir volume of hydrate (ft<sup>3</sup>, res) is equivalent to 174 scf of free gas.

Table 4.9: Initial Gas In-Place (Free Gas + Hydrate-Associated Gas)

Case	Reservoir Model	Hydrate-Associated Gas (bcf)	Free Gas (bcf)	Total Initial Gas In-Place (Free + Hydrate-Associated) (bcf)
<i>A</i>	Only Gas	00.00 bcf	94.21 bcf	94.21 bcf
<i>B</i>	Gas + Aquifer	00.00 bcf	27.32 bcf	27.32 bcf
<i>C</i>	HYD + Gas + Aquifer (Best-Case)	26.13 bcf	15.83 bcf	41.96 bcf
<i>D</i>	Only HYD	147.62 bcf	29.31 bcf	176.93 bcf
<i>E</i>	HYD + Gas	26.10 bcf	82.62 bcf	108.72 bcf
<i>F</i>	HYD + Aquifer	42.80 bcf	08.49 bcf	51.30 bcf



## a. Field-Level Match

## 1. Cumulative Gas Production

Figure 4.29 is a plot showing cumulative gas production obtained for several scenarios. The cumulative gas production profile for all cases matched perfectly with the production data. However, Case *F* (HYD+Aquifer) produced slightly lesser gas than the production data. Table 4.10 shows the cumulative gas production for each case.

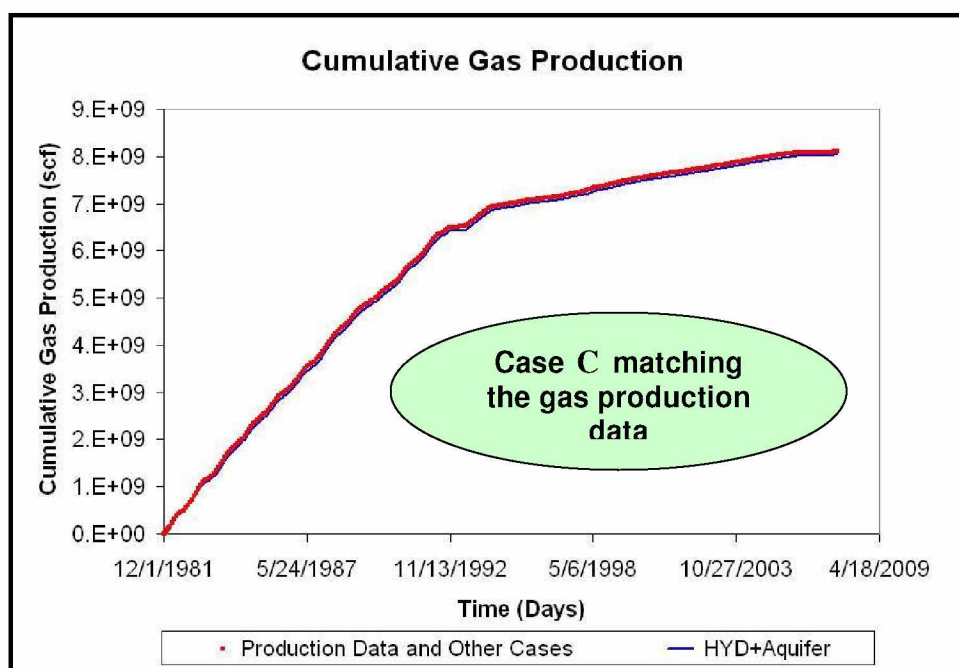


Figure 4.29: Cumulative Gas Production (History Matching)

Table 4.10: Cumulative Gas Production (on Sep 01, 2007)

Case	Cumulative Gas Production (bcf)
Production History Data	8.11 bcf
Cases <i>A</i> to <i>E</i>	8.11 bcf
Case <i>F</i>	8.04 bcf

## 2. Cumulative Water Production

The cumulative water production plot is shown in Figure 4.30. As seen from the plot, the cumulative water production for different scenarios ranged from 20 bbls of water in Case *A* to 9,000 bbls of water in Case *B*. Table 4.11 presents the cumulative water production obtained at the end of the simulation run. Results suggested that Case *C* (Hydrate + Free Gas + Aquifer) closely matched the water production profile at the end of the simulation.

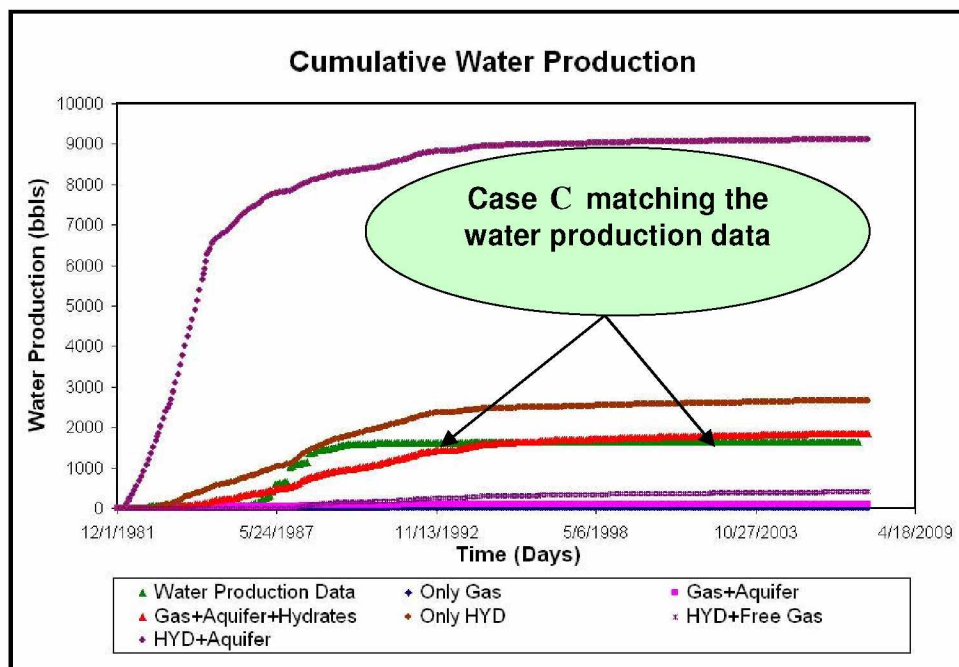


Figure 4.30: Cumulative Water Production (History Matching)

Another similarity observed between Case *C* and the production data was the initial and final slope of the cumulative water production profile. Initial water production profile was lower than later production times; however, the gas production profile was completely opposite (Figure 4.29). This phenomenon was a typical signature of hydrate dissociation. With GWC far away from the producing well (completed in hydrate zone), the only source of water near to the wellbore were the dissociating hydrates. Higher gas production rates reduced the reservoir pressure initially, causing hydrate dissociation.

The produced water got trapped within the pore spaces and remained immobile. With continued hydrate dissociation, critical water saturation was achieved, after which the water became mobile. Being heavier than gas, mobile water fell by gravity segregation and got produced along with the gas.

Table 4.11: Cumulative Water Production (on Sep 01, 2007)

Case	Reservoir Model	Cumulative Water Production (on Sep 01, 2007)
Production History Data	Not Applicable	1,631 bbls
<i>A</i>	Gas Only	19 bbls
<i>B</i>	Gas + Aquifer	106 bbls
<i>C</i>	HYD + Gas + Aquifer	1,850 bbls
<i>D</i>	HYD Only	2,660 bbls
<i>E</i>	HYD + Free Gas	406 bbls
<i>F</i>	HYD + Aquifer	9,110 bbls

Water production in other cases was a strong function of free water availability. However, water production limits were exceeded in the case of the hydrate-aquifer system (Case *F*), combined effect of rising aquifer, scarcity of free gas, and dissociating hydrates caused large volumes of water production in this case.

### 3. Average Reservoir Pressure

Figure 4.31 shows average reservoir pressure response for all cases. Table 4.12 presents the root mean square error between reservoir pressure and history data. The plot (Figure 4.31) showed a close match between pressure data and model response for Cases *C* and *F*. Error check for the two cases show a better match with Case *F*, but, Case *C* successfully matched the production data during the field-level match (refer to the cumulative gas and water production match explained above). Also, the absence of HGC in Case *F* violates the observation from the well log data (Panda and Morahan,

2008). To summarize, Case *C* (i.e., reservoir model with HGC at 2050 ft and GWC at 2080 ft) closely matched (less than 2% error) the field-level response. Based on this conclusion, Case *C* was chosen for further fine tuning to match individual well responses.

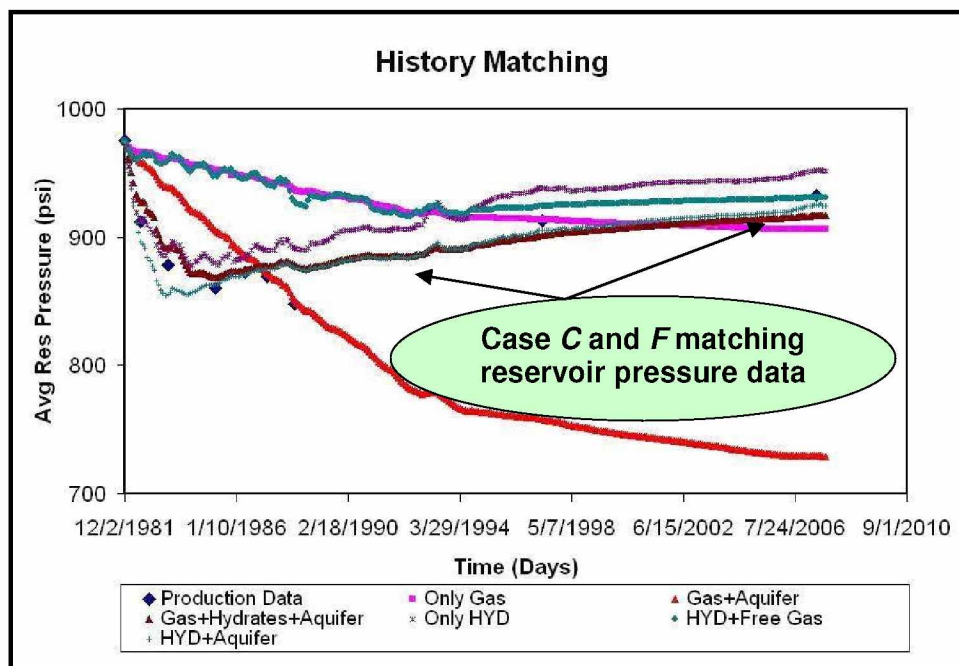


Figure 4.31: Average Reservoir Pressure (History Matching)

Table 4.12: Root Mean Square Error Analysis (Reservoir Pressure vs. Model Output)

Case	Reservoir Model	Root Mean Square Error (%)
Production History Data	Not Applicable	Not Applicable
<i>A</i>	Gas Only	7.10%
<i>B</i>	Gas + Aquifer	9.30%
<i>C</i>	HYD + Gas + Aquifer	1.56%
<i>D</i>	HYD Only	2.28%
<i>E</i>	HYD + Free Gas	6.69%
<i>F</i>	HYD + Aquifer	1.50%

## b. Well-Level Match

### 1. Gas Production Rate

The best-case model (Case C) was selected to match individual well-level match. The first attempt was made to obtain a match between the gas production data (results were similar to that obtained during well production validation procedure, Figures 3.45, 3.46, 3.47, 3.48, and 3.49). Model Case C showed a precise match between individual well production and gas production history data.

### 2. Water Production Rate

The water production data for each well was matched individually (Figures 4.32, 4.33, 4.34, 4.35, and 4.36). The other objective of this exercise was to further tune the number and location of well perforations so as to match the volumes of water produced with minimum number of well perforations.

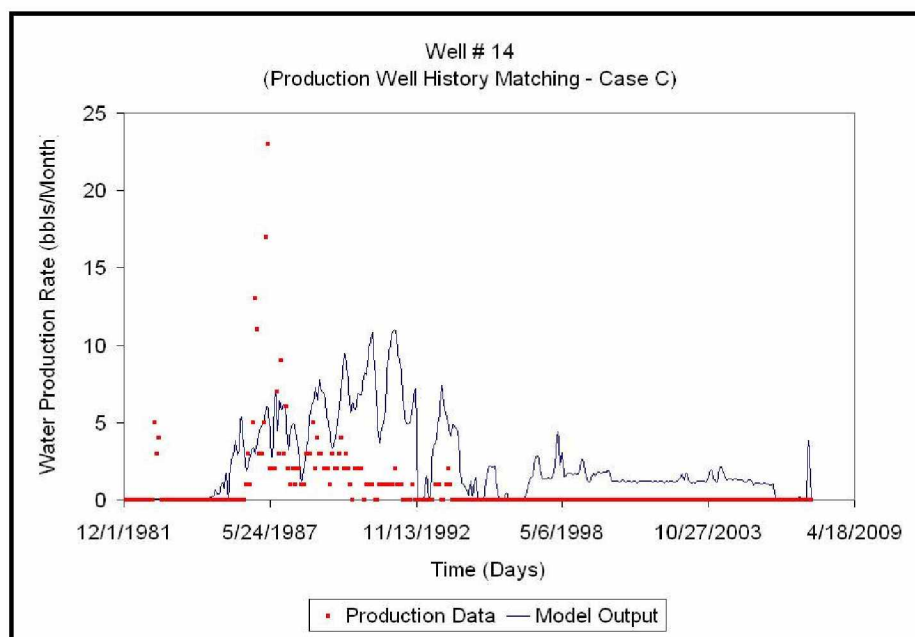


Figure 4.32: Water Production Rate (History Matching) - Well EB #14

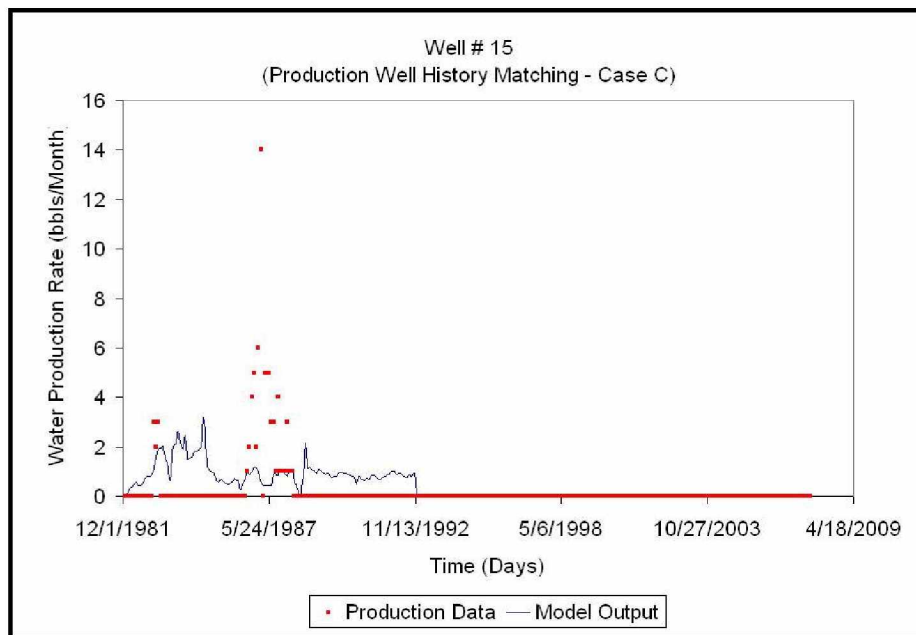


Figure 4.33: Water Production Rate (History Matching) - Well EB #15

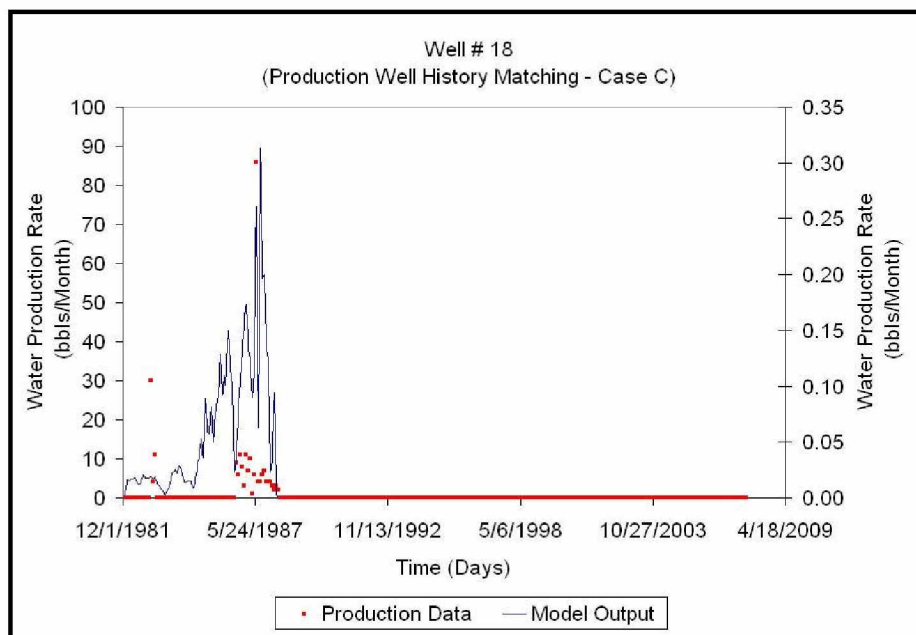


Figure 4.34: Water Production Rate (History Matching) - Well EB #18

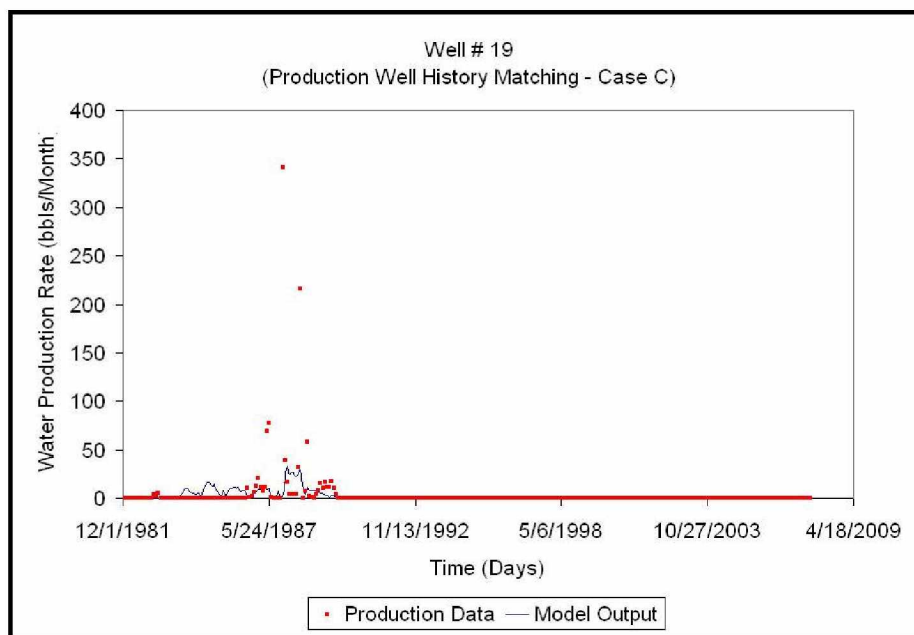


Figure 4.35: Water Production Rate (History Matching) - Well EB #19

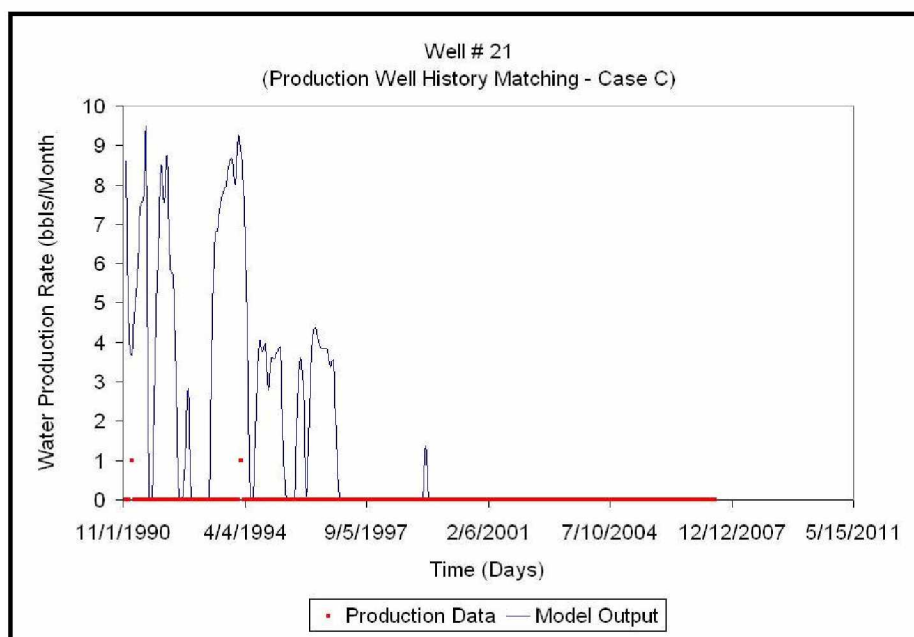


Figure 4.36: Water Production Rate (History Matching) - Well EB #21



### c. Data Analysis

#### 1. Fluid Saturation Profile (All Layers Within Hydrate Zone)

The best-case model (Case *C*) was used to study the current reservoir conditions. To understand the flow dynamics of three fluid phases, gridblocks 19, 19, and ( $K = 1$  to 25) were chosen (Figure 3.63). All gridblocks in the K direction lie within the hydrate zone. Figures 4.37, 4.38, and 4.39 present hydrate, gas, and water phase variation within a hydrate zone during the production life of the reservoir.

Figure 4.37 shows a rapid reduction in hydrate saturation at and near the top and bottom of the reservoir. Faster rate of hydrate depletion suggested that for locations, where all layers ( $K = 1$  to 25) lie within the hydrate zone, dissociation rates were governed primarily by heat transfer from overburden and underburden rocks.

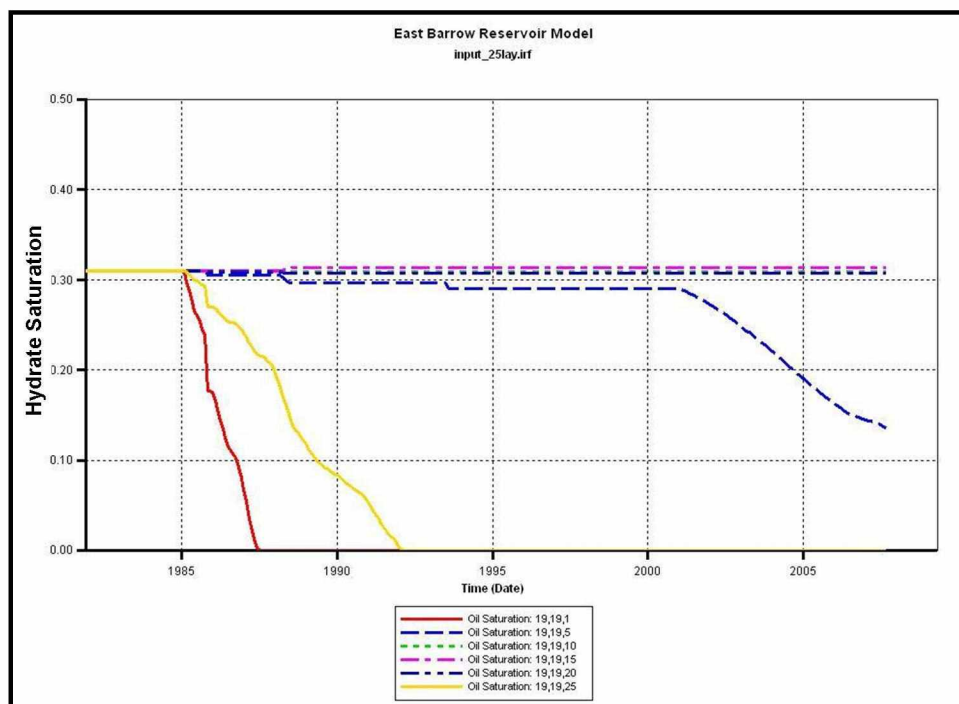


Figure 4.37: Hydrate Saturation Profile (Location 19, 19, and [K = 1 to 25])



Figure 4.38 displays the gas saturation profile within a hydrate zone for gridblocks 19, 19, and (K = 1 to 25). The area of decreased hydrate saturation at and near the top section of the reservoir was partially occupied by produced gas and partially by water. However, at the bottommost section of the reservoir (at and near K = 25), initial hydrate dissociation increased the gas saturation. Later, due to gravity segregation mobile water drained to the bottom of the reservoir, thus decreasing the gas saturation and correspondingly increasing the water saturation (Figure 4.39). Water saturation followed the similar trend; saturation increased in the top few layers of the model due to hydrate dissociation followed by a decrease due to falling water. Similarly, saturation increased by many folds at the bottom of the reservoir due to gravity segregation.

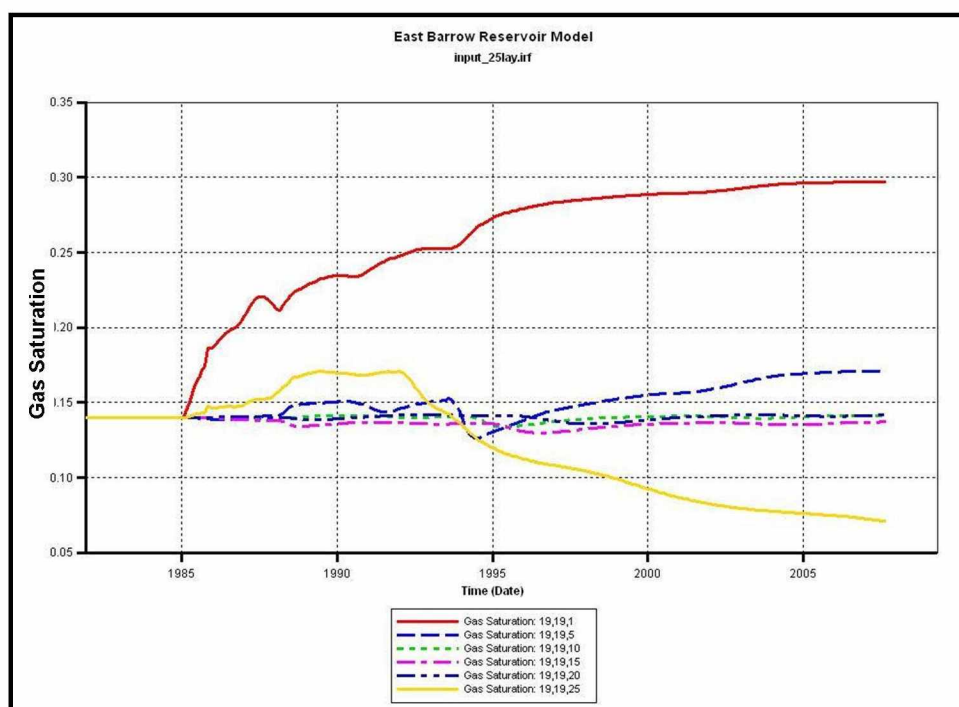


Figure 4.38: Gas Saturation Profile (Location 19, 19, and [K = 1 to 25])

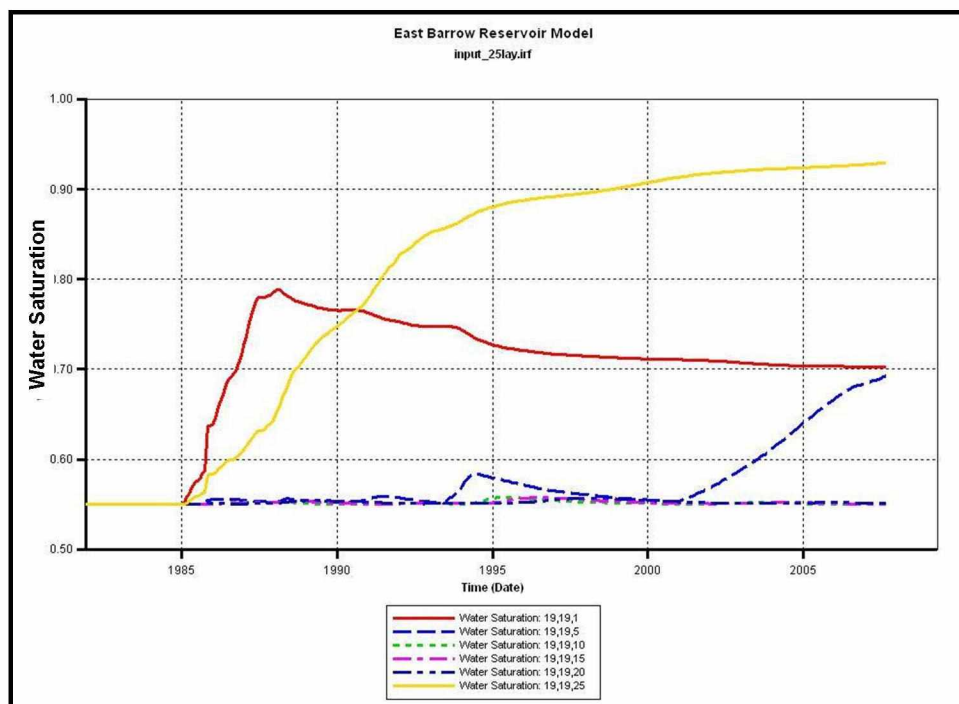


Figure 4.39: Water Saturation Profile (Location 19, 19, and [K = 1 to 25])

## 2. Fluid Saturation Profile (Hydrate-Free Gas-Aquifer Zone)

Gridblocks 29, 8, and (K = 1 to 25) were chosen to understand the reservoir dynamics during gas production (Figure 4.40). The gridblocks in the K direction included all three zones (hydrate-free gas-aquifer). The HGC was at K = 8, whereas GWC was at K = 22. Three plots were generated to study the impact of free gas production on hydrate dissociation and the effect of gravity on water saturation.

Figure 4.41 shows the variation in hydrate saturation within the hydrate zone. It can be seen that the effect of gas production and overburden temperature had increased the rate of hydrate dissociation at and near the top of the reservoir. However, near the hydrate-free gas interface, the rate of hydrate dissociation was predominantly controlled by depressurization.

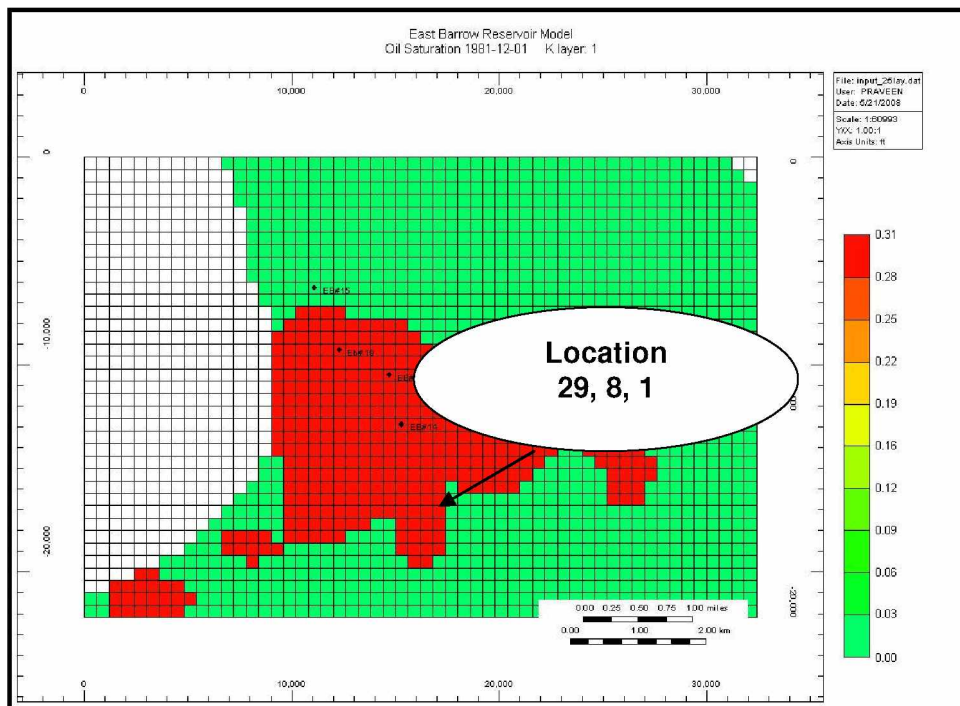


Figure 4.40: Hydrate-Free Gas-Aquifer Zone (Location 29, 8, and [K = 1 to 25])

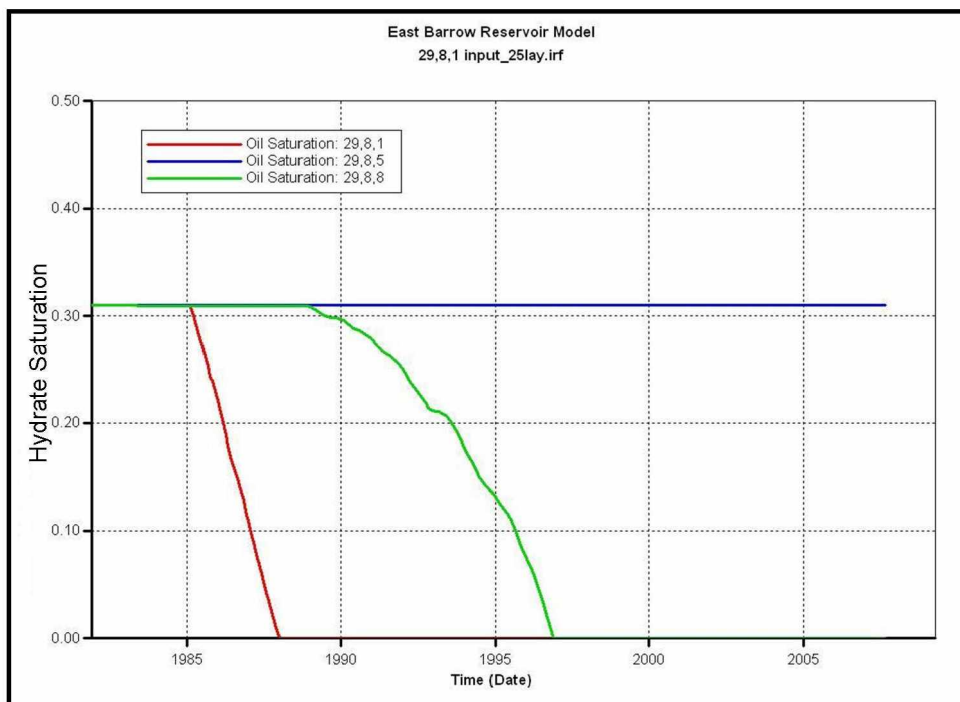


Figure 4.41: Hydrate Saturation Profile (Location 29, 8, and [K = 1 to 8])

The gas saturation profile has been presented in Figure 4.42. The gas saturation at the top of the reservoir increased due to hydrate dissociation. However, the increase was limited to 30% as the rest of the pore space had been occupied by produced water. The gas saturation at  $K = 5$  was unchanged as hydrates remained undissociated so far. Near the HGC ( $K = 8$ ), the gas saturation increased slowly with hydrate dissociation and reached a maximum of 45% upon complete dissociation, showing that the free water has reached the bottom of the reservoir. As expected, the gas saturation in free gas zone ( $K = 15$ ) remained unchanged. Near GWC ( $K = 22$ ), the gas saturation dropped from the initial saturation of 45% to 20%. The primary reason for this reduction was the water influx from the underlying aquifer zone. The mobile water draining from the hydrate zone collected in aquifer zone causing a reduction in the gas saturation. It should be noted that the effect of gas dissolution in water was not considered while initializing these models.

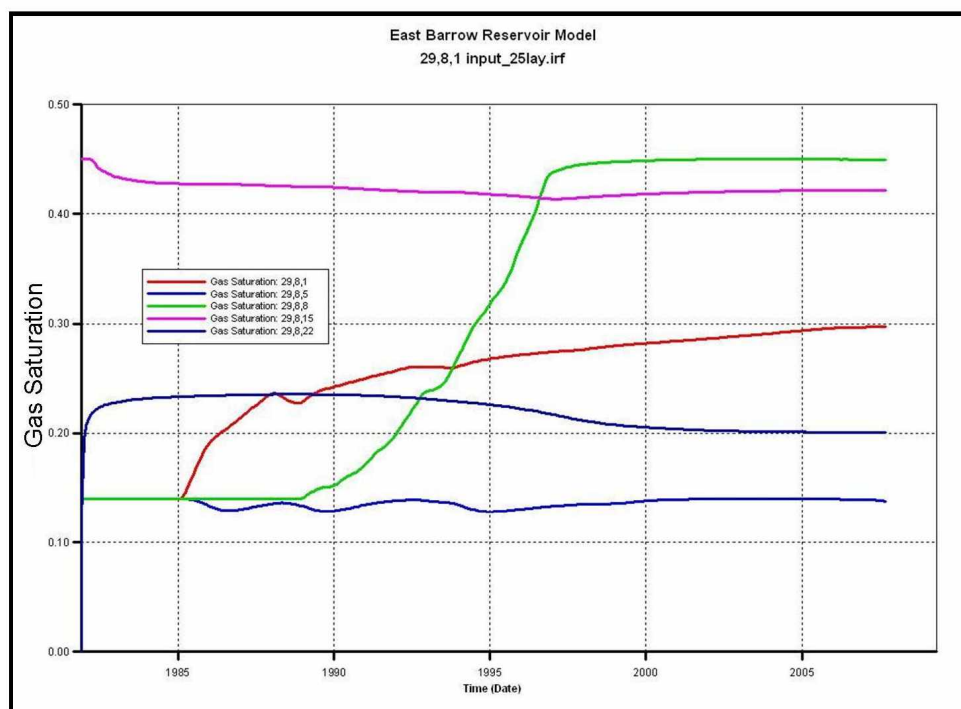


Figure 4.42: Gas Saturation Profile (Location 29, 8 and [K = 1 to 22])

As explained previously, hydrate dissociation caused an increase in water saturation at the top of the reservoir ( $K = 1$ ), but with draining water and rising gas, the trend got

reversed (Figure 4.43). No change in hydrate saturation near the  $K = 5$  zone resulted in no change in water saturation. Again, the water saturation remained the same in the gas zone. Near GWC, the water saturation increased from 55% to 70%. This increase was attributed to water influx from the aquifer zone (during gas production) and hydrate-dissociated free water that occupied pore spaces at the bottom of the reservoir.

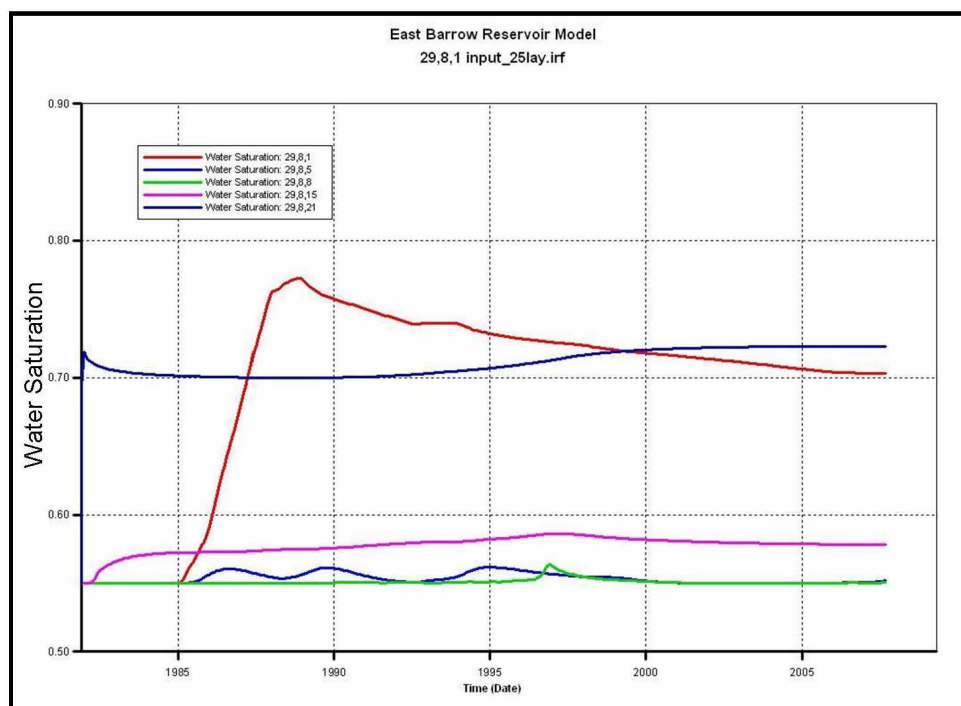


Figure 4.43: Water Saturation Profile (Location 29, 8, and [K = 1 to 22])

### 3. Current Reservoir Properties

Figures 4.44, 4.45, 4.46, 4.47, and 4.48 are the 3D views of the EB reservoir model, showing current distribution of reservoir properties such as pressure, temperature, hydrate phase, gas phase, and water phase saturations, respectively.



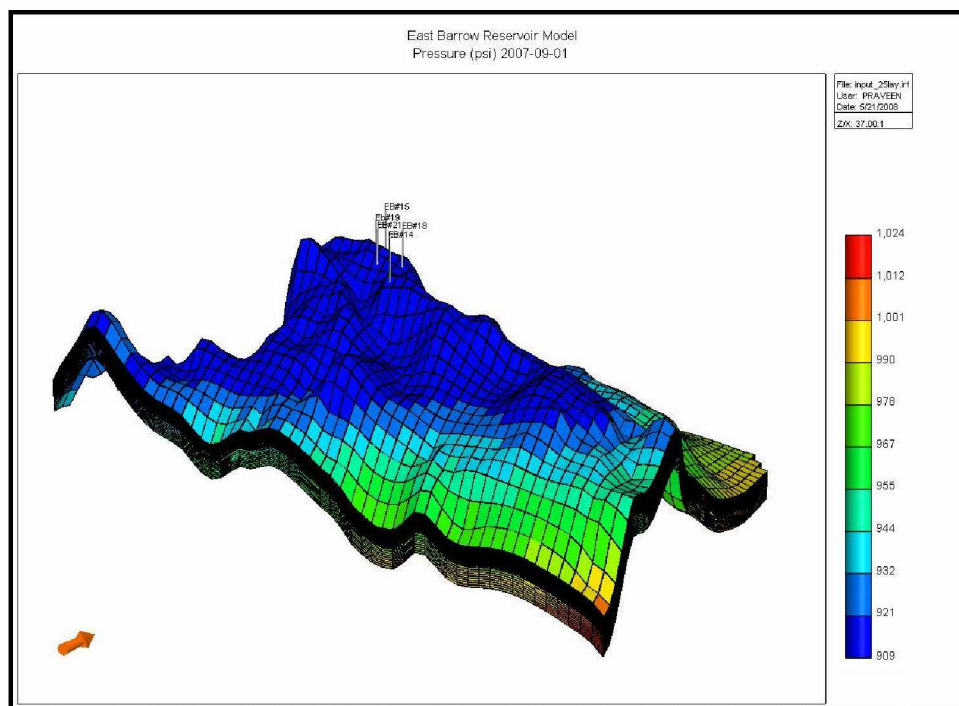


Figure 4.44: Current Reservoir Pressure, psi (on Sep 01, 2007) - 3D View

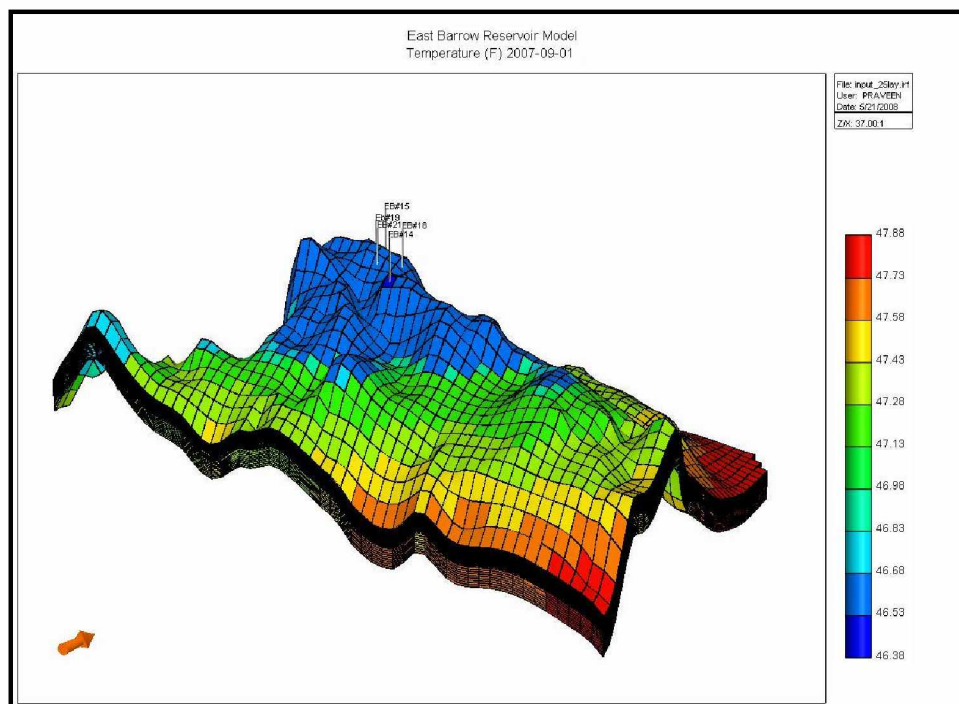


Figure 4.45: Current Reservoir Temperature, °F (on Sep 01, 2007) - 3D View

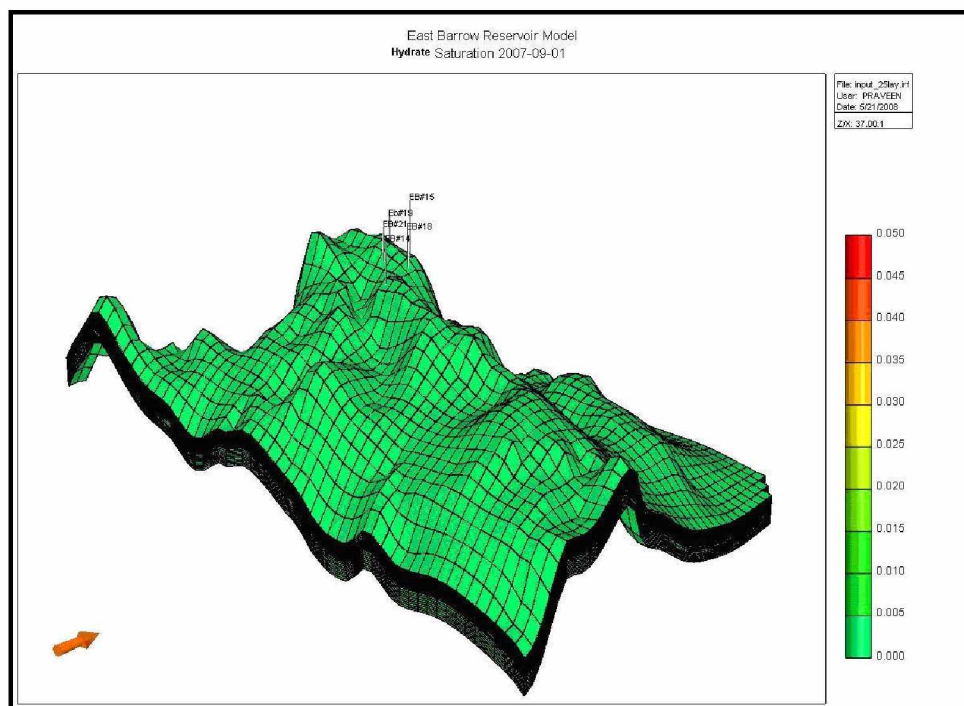


Figure 4.46: Current Hydrate Saturation, % (on Sep 01, 2007) - 3D View

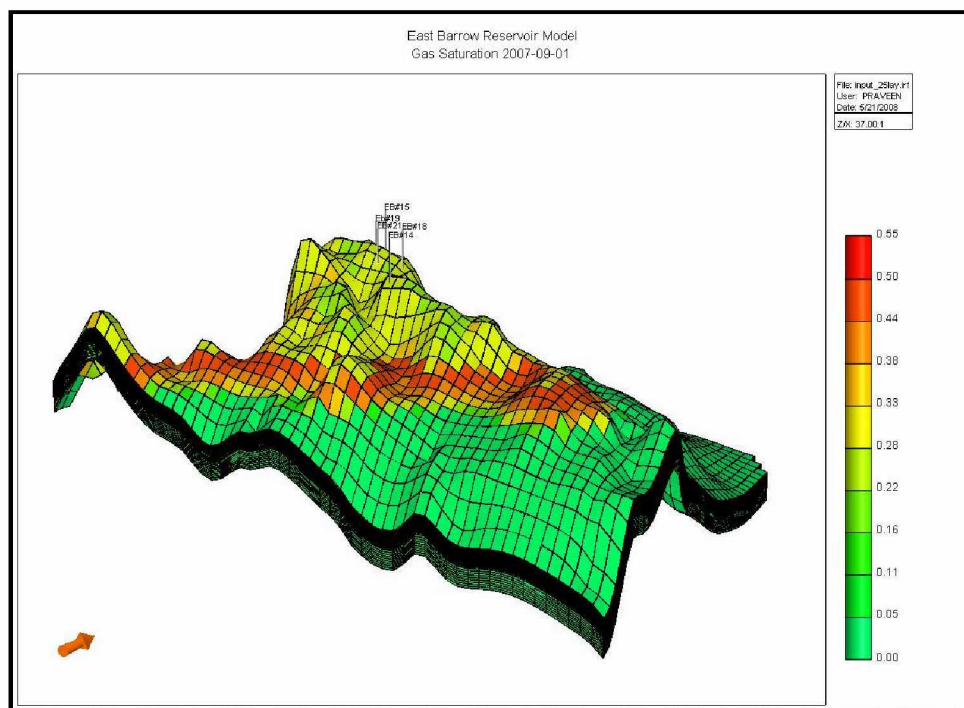


Figure 4.47: Current Gas Saturation, % (on Sep 01, 2007) - 3D View

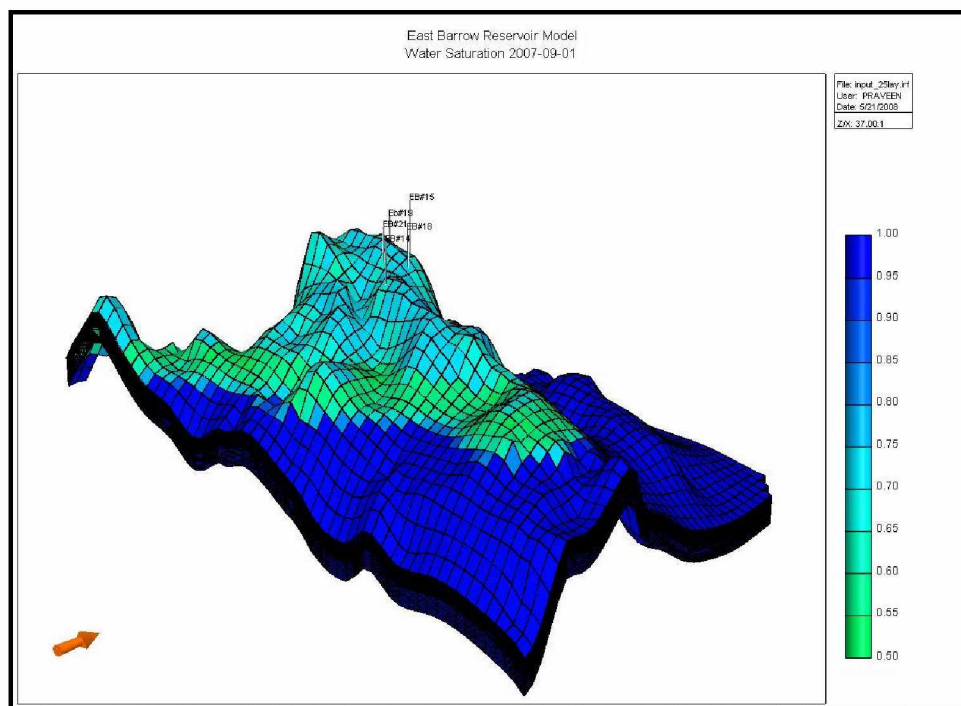


Figure 4.48: Current Water Saturation, % (on Sep 01, 2007) - 3D View

#### 4. HGC and GWC

Figures 4.49 and 4.50 show the changes in HGC. As explained previously, the HGC was initialized at 2050 ft. With hydrate dissociation, the contact shifted upwards to 2045 ft. Figures 4.51 and 4.52 present the change in GWC in the reservoir. The contact shifted upwards from an initial contact at 2080 ft (on Dec 01, 1981) to 2070 ft (on Sep 01, 2007).





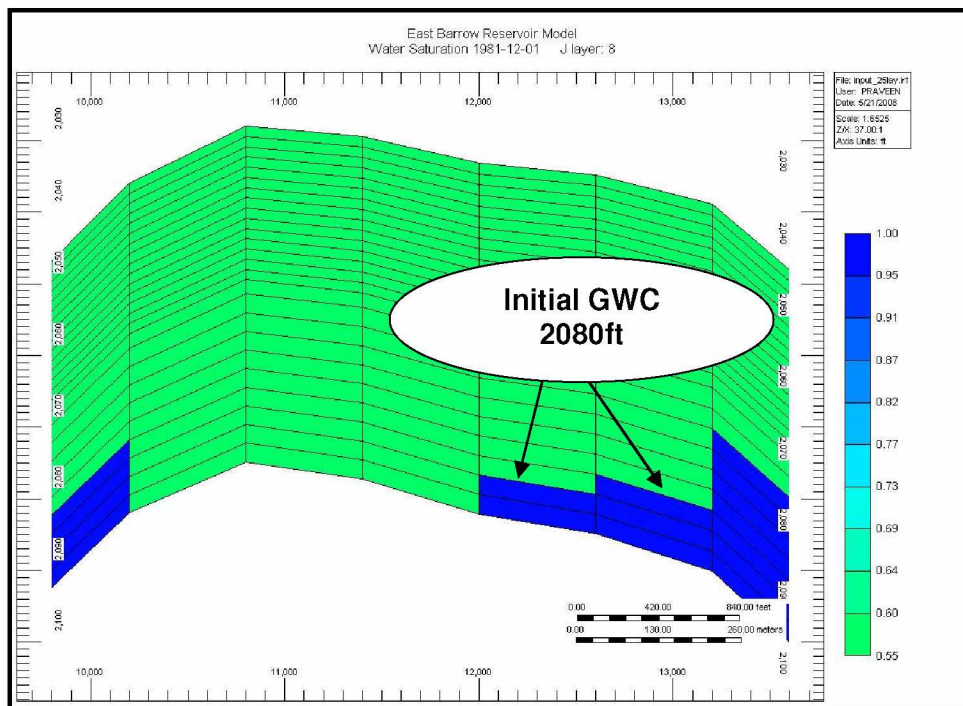


Figure 4.51: Initial GWC at 2080 ft (on Dec 01, 1981)

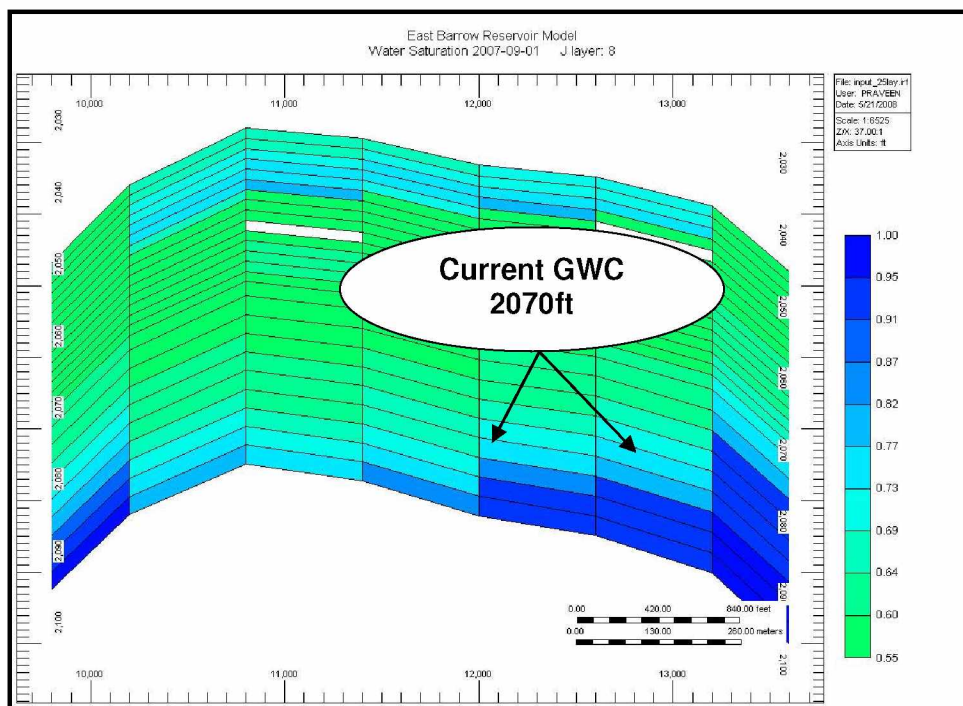


Figure 4.52: Current GWC at 2070 ft (on Sep 01, 2007)

## 5. Hydrate-Free Gas Contribution

To calculate the gas contribution from in-situ hydrates, detailed reservoir mapping was performed. The difference in hydrate resource between the two time periods assisted in estimating the quantity of hydrate dissociated. CMG-STARS estimated “Hydrate per Unit Area” for each IJ block. The area of each gridblock is 600 ft by 600 ft. This information was used to determine the initial and final hydrate in-place and eventually was used to calculate the total volume of gas produced from hydrate dissociation, percentage of hydrate dissociation, and the contribution of hydrate as a percentage of gas produced. The total gas produced from hydrate dissociation and percentage of hydrate dissociation for the best-case model (Case C) have been presented in the Table 4.13 below.

Table 4.13: Hydrate Contribution in Recharging Gas Reservoir

Description	Result
Initial Volume of In-Place Hydrates	26.13 bcf
Volume of Hydrate Dissociated	0.04 billion ft <sup>3</sup> (res)
Gas Produced by Hydrate Dissociation	7.04 bcf
Percentage of Hydrate Dissociation (on Sep 01, 2007)	26.94%
Cumulative Gas Produced (on Sep 01, 2007)	8.11 bcf
Hydrate Contribution as Percentage of Gas Produced	86.81%

Similarly, free gas reserves were estimated by using “Total Free Gas per Unit Area” data obtained from CMG-STARS results. The initial free gas in-place calculated for the EB reservoir was 15.83 bcf (Table 4.9), whereas the current free gas in-place is approximately 14.77 bcf. A total of 8.11 bcf of gas has been produced to date; hence, additional free gas available was supplied by dissociating hydrates (contributing 86.81% of produced gas).

### d. Selecting Locations for Drilling Future Infill Well/s

The approach behind selecting optimum locations for drilling future wells was to target gridblocks with high concentration of free gas in-place. Reservoir mapping was done to

obtain current concentrations of free gas throughout the reservoir. Figure 4.53 shows six locations best-suited for drilling infill wells. The coordinates of these locations are presented in Table 4.14. Out of all the available options, the gridblock that was located structurally higher than other locations was selected for forecasting purposes. The coordinate of the selected gridblock is 25 in I and 10 in J directions (IJ Plane).

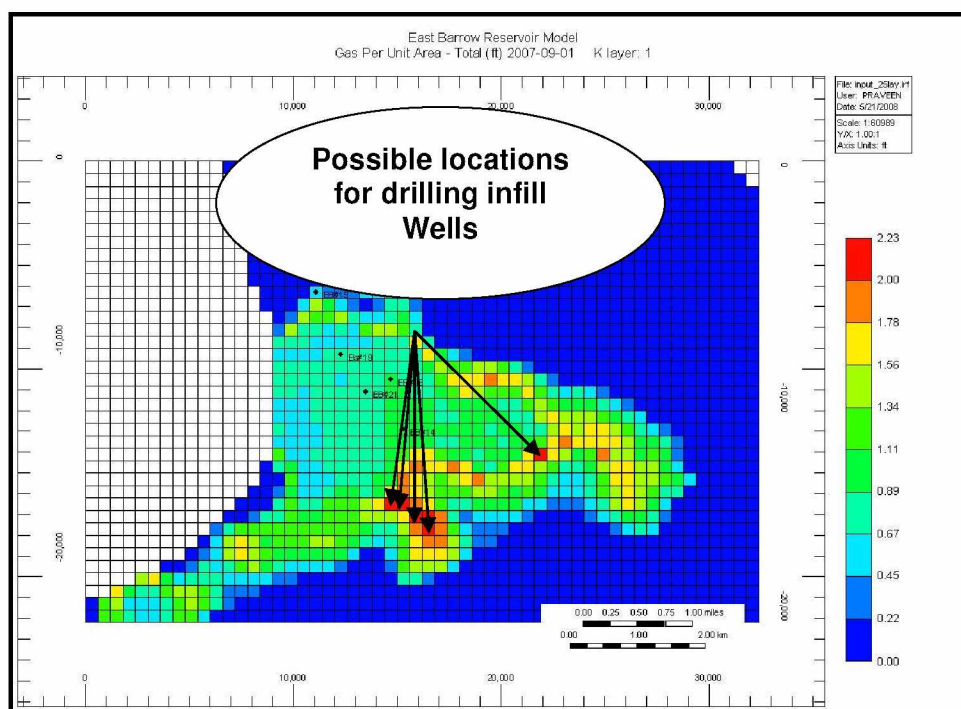


Figure 4.53: Possible Locations for Drilling Infill Wells

Table 4.14: Possible Locations (Gridblock Coordinates) for Drilling Future Wells

Gridblock Coordinates (IJ Plane)	Free Gas Per Unit Area $\text{ft}^3/\text{ft}^2$ (res)
25, 10 (Selected for Drilling Infill Well)	2.15 $\text{ft}^3/\text{ft}^2$ (res)
26, 10	2.14 $\text{ft}^3/\text{ft}^2$ (res)
27, 9	2.04 $\text{ft}^3/\text{ft}^2$ (res)
28, 9	2.02 $\text{ft}^3/\text{ft}^2$ (res)
28, 8	2.22 $\text{ft}^3/\text{ft}^2$ (res)
37, 14	2.02 $\text{ft}^3/\text{ft}^2$ (res)

#### 4.4.1.2 Walakpa Gas Fields

The SMALL model was used to perform history matching studies. It was assumed that the effect of a producing well will be seen by the region included in the SMALL model. Two scenarios were developed to study reservoir performance and match the same with reservoir history data. The history matching was performed both at the reservoir level and the well-level. The reservoir level match was initiated for both the cases. Upon achieving a close match, individual well-level matches were performed for the best-case scenario. Initial estimates of free gas, hydrates, and associated (bounded) water were made for the best-case scenario (Basis: LARGE model). Tables 4.15 and 4.16 present the initial free gas and hydrate estimates (reservoir volumes) and initial free gas estimates (total) respectively for the best-case. These estimates include gas associated with hydrates. The basis for calculating hydrate-associated gas is as follows: one reservoir volume of hydrate (ft<sup>3</sup>, res) is equal to 174 scf of free gas.

Table 4.15: Initial Estimates of Free Gas, Hydrates, and Water (LARGE Model)

Case	Reservoir Model (LARGE Model)	Hydrate	Free Gas		Water
		billion ft <sup>3</sup> (res)	billion ft <sup>3</sup> (res)	bcf	billion ft <sup>3</sup> (res)
<i>B</i>	HYD + Gas + Aquifer (Best-Case)	1.63 billion ft <sup>3</sup>	3.71 billion ft <sup>3</sup>	298 bcf	13.4 billion ft <sup>3</sup>

Table 4.16: Initial Gas In-Place (Free Gas + Hydrate-Associated) (LARGE Model)

Case	Reservoir Model (LARGE Model)	Hydrate Associated Gas (bcf)	Free Gas (bcf)	Total Initial Gas In-Place (bcf)
<i>B</i>	HYD + Gas + Aquifer (Best-Case)	284 bcf	298 bcf	582 bcf



a. Field-Level Match

1. Cumulative Gas Production

Figure 4.54 is a plot showing cumulative gas production obtained for the Cases *A* and *B*. The cumulative gas production profile for both cases matched perfectly with the production data.

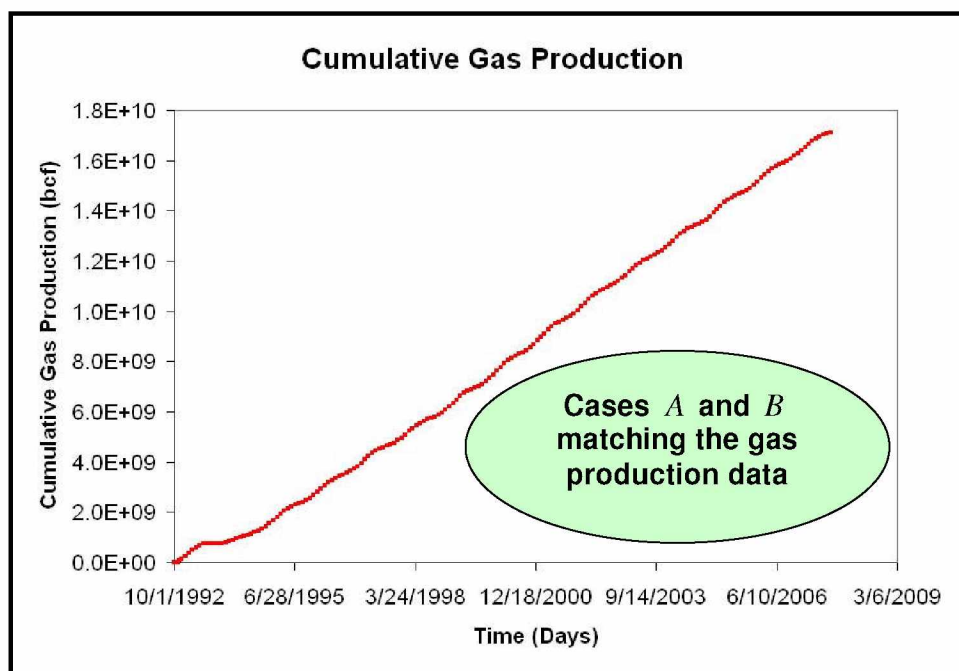


Figure 4.54: Cumulative Gas Production (History Matching Case *A* and *B*) - SMALL Model

2. Reservoir Pressure

Horner pressures and pressure history data were matched for each case individually. Figures 4.55 and 4.56 present the pressure profile of Cases *A* and *B* respectively. The pressure coordinates representing reservoir pressure distribution are presented in Figure 4.57.

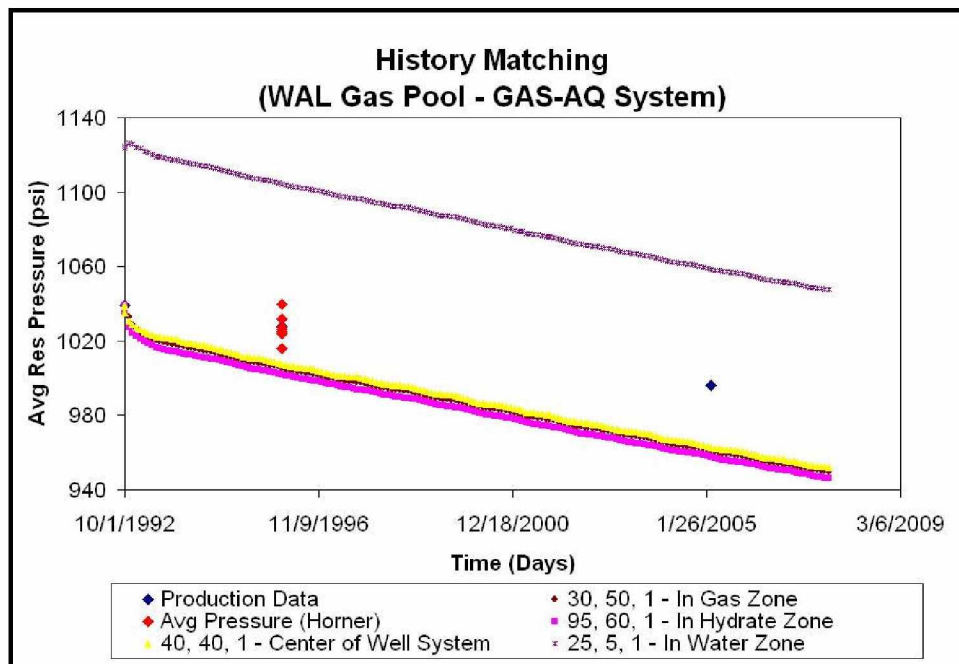


Figure 4.55: Average Reservoir Pressure (History Matching Case A) - SMALL Model

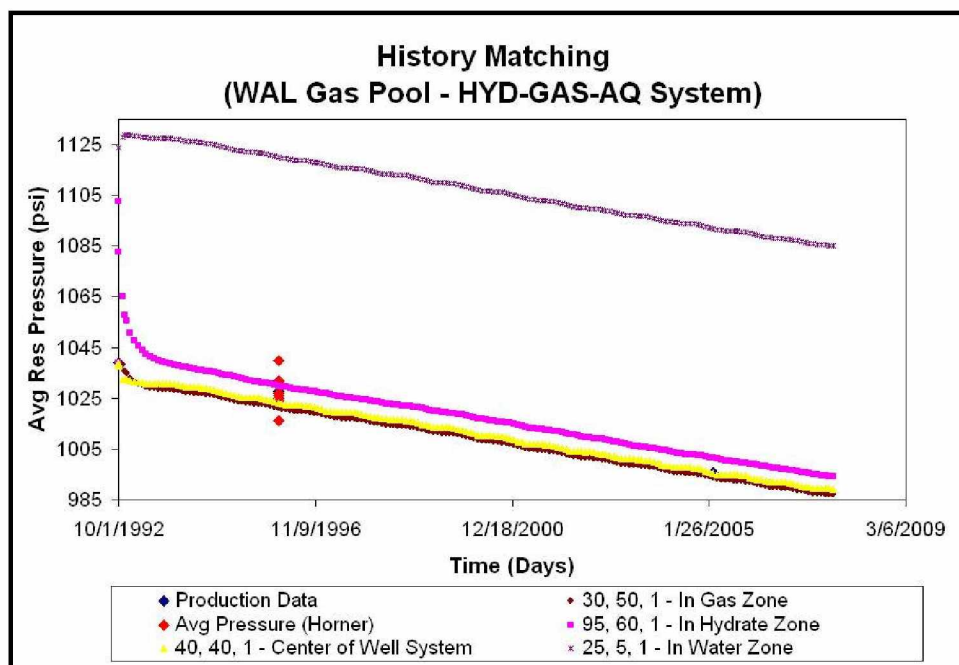


Figure 4.56: Average Reservoir Pressure (History Matching Case B) - SMALL Model

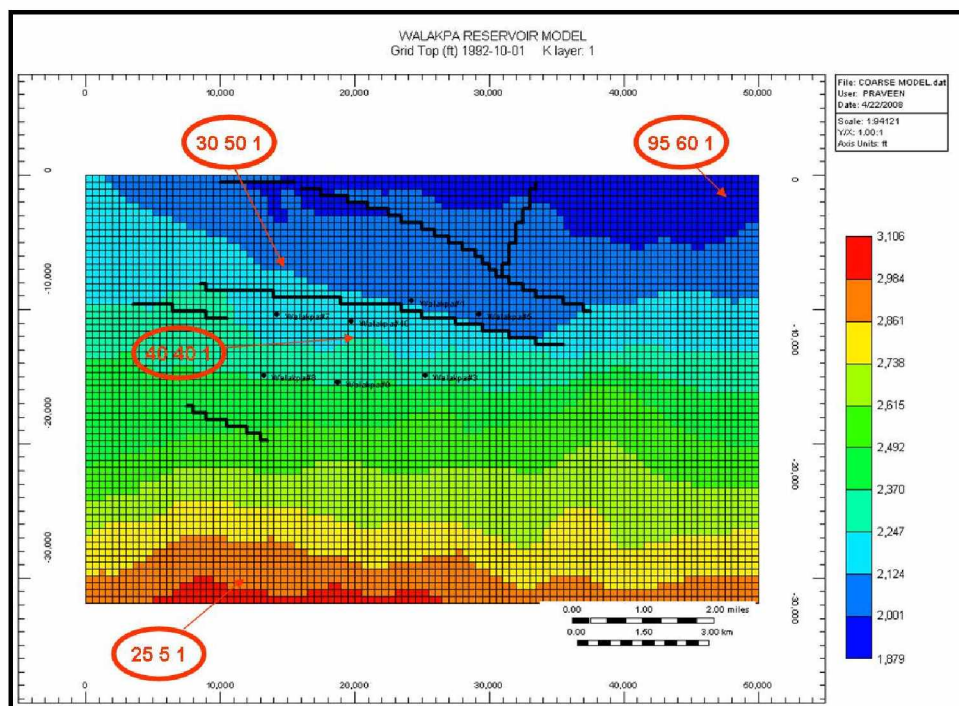


Figure 4.57: IJ Coordinates Representing Reservoir Pressure - SMALL Model

Case *B* matched the reservoir pressure better than Case *A* with a root mean square error less than 0.5% (in the free gas zone). Thus, the WAL gas reservoir was associated with hydrates and strong aquifers with HGC at 2000 ft and GWC at 2750 ft. Root mean square errors for pressure coordinates in Cases *A* and *B* are given in Tables 4.17 and 4.18 respectively.

Table 4.17: Root Mean Square Error Analysis (Case *A*) - SMALL Model

Case <i>A</i> (Reservoir Pressure Coordinates)	Root Mean Square Error (%)
Free Gas Zone (30, 50, 1)	2.40%
Free Gas Zone (95, 60, 1)	2.67%
Center of Well System (40, 40, 1)	2.26%
Aquifer Zone (25, 5, 1)	7.32%



Table 4.18: Root Mean Square Error Analysis (Case B) - SMALL Model

<b>Case B (Reservoir Pressure Coordinates)</b>	<b>Root Mean Square Error (%)</b>
Gas Zone (30, 50, 1)	0.40%
Hydrate Zone (95, 60, 1)	2.45%
Center of Well System (40, 40, 1)	0.27%
Aquifer Zone (25, 5, 1)	8.94%

## b. Well-Level Match

## 1. Gas Production Rate

The best-case model (Case B) was chosen to perform the individual well-level match. A perfect match between individual well production history and model (output) was observed.

## c. Data Analysis

## 1. Hydrate-Free Gas Contribution

The total gas produced from hydrate dissociation and the percentage of hydrate dissociation for the best-case model is presented in Table 4.19 (Basis: LARGE model).

Table 4.19: Hydrate Contribution in Recharging Gas Reservoir (LARGE Model)

<b>Description</b>	<b>Result</b>
Initial Volume of Hydrates	284 bcf
Volume of Hydrate Dissociated	0.17 billion ft <sup>3</sup> (res)
Gas Produced by Hydrate Dissociation	29.54 bcf
Percentage of Hydrate Dissociation (on Sep 01, 2007)	10.40%
Cumulative gas produced (on Sep 01, 2007)	17.11 bcf
Hydrate contribution as Percentage of gas produced	100%

The initial free gas in-place calculated for the WAL reservoir (LARGE) model is 298 bcf, whereas the current free gas in-place is approximately 310 bcf. A total of 17.11 bcf of gas has been produced to date.

#### *4.4.2 Sensitivity Study*

##### *4.4.2.1 East Barrow Gas Field*

The sensitivity parameters have been categorized into five major groups. These categories were identified based on their importance in quantifying the methane hydrate resource potential of the EB gas field. These are

- i. Free Gas Zone Size
- ii. Hydrate Saturation
- iii. Hydrate Zone Size
- iv. Aquifer Strength and Size

#### *i. Free Gas Zone Size*

From Figure 4.58, it was observed that for GWC of 2060 ft, the cumulative gas production was slightly lesser than the production history data. For other cases, sufficient free gas was available; hence, model results matched the production history data. In the case of Figure 4.59, the GWC at 2090 ft and 2080 ft (best-case) closely matched the water production profile. The amount of water produced in the case of GWC at 2090 ft was slightly lesser than the best-case (GWC at 2080 ft), possibly because larger free gas zone kept the aquifer away from the producing wells. Secondly, a thicker gas zone supplied free gas for production and hence, reduced the hydrate dissociation rates. This in turn reduced mobile water build up in hydrate zone. GWC at 2060 ft and 2070 ft produced tremendous volumes of water, mainly attributed to the fact that closer the gas-aquifer contact was to the wellbore, the higher would have been the water production rate. In the case of no aquifer the only mobile water available for production was the water produced during hydrate dissociation.

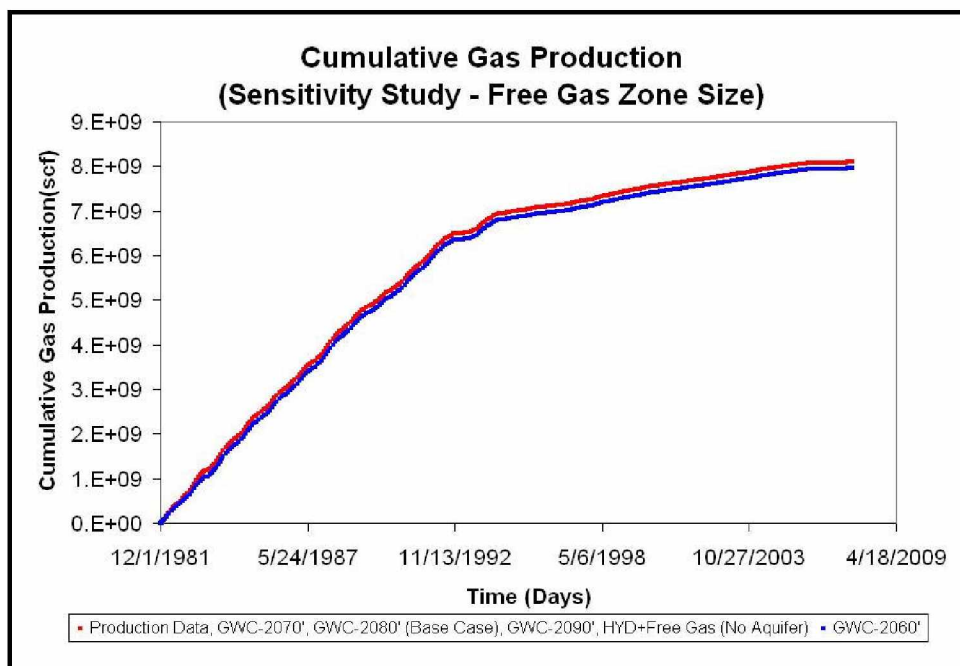


Figure 4.58: Cumulative Gas Production (Sensitivity - Free Gas Zone Size)

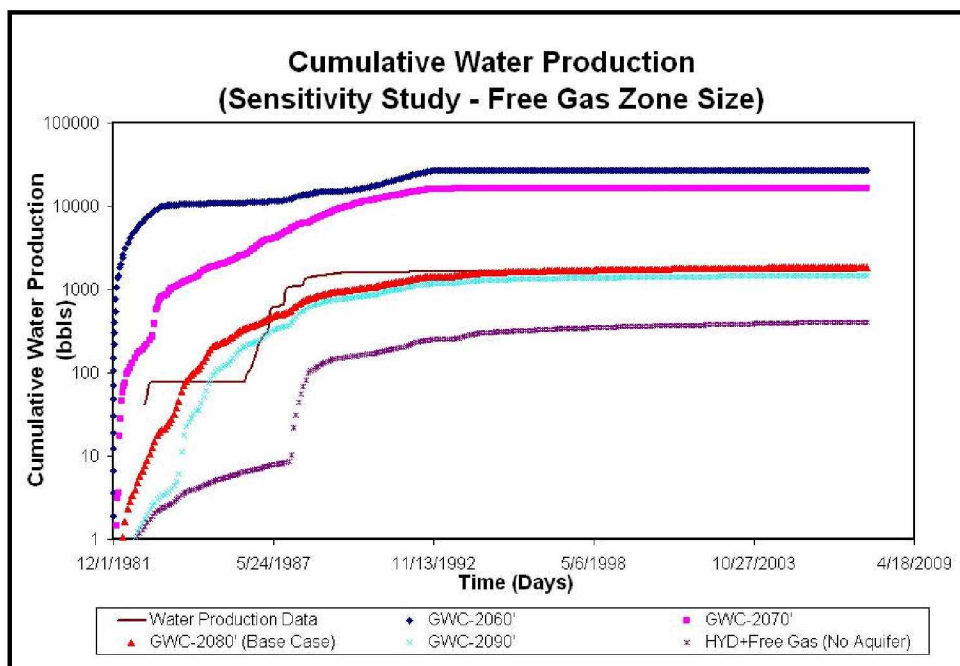


Figure 4.59: Cumulative Water Production (Sensitivity - Free Gas Zone Size)

The average reservoir pressure response was recorded and compared in Figure 4.60. The scenario of GWC at 2090 ft closely followed the best-case model, however, due to the large free gas volumes, it failed to match the pressure during the initial gas production period. GWC at 2060 ft and 2070 ft managed to achieve a better match during initial production, but failed to catch up later, primarily because the rising GWC charged the reservoir with more water, and the reducing the rate of hydrate dissociation.

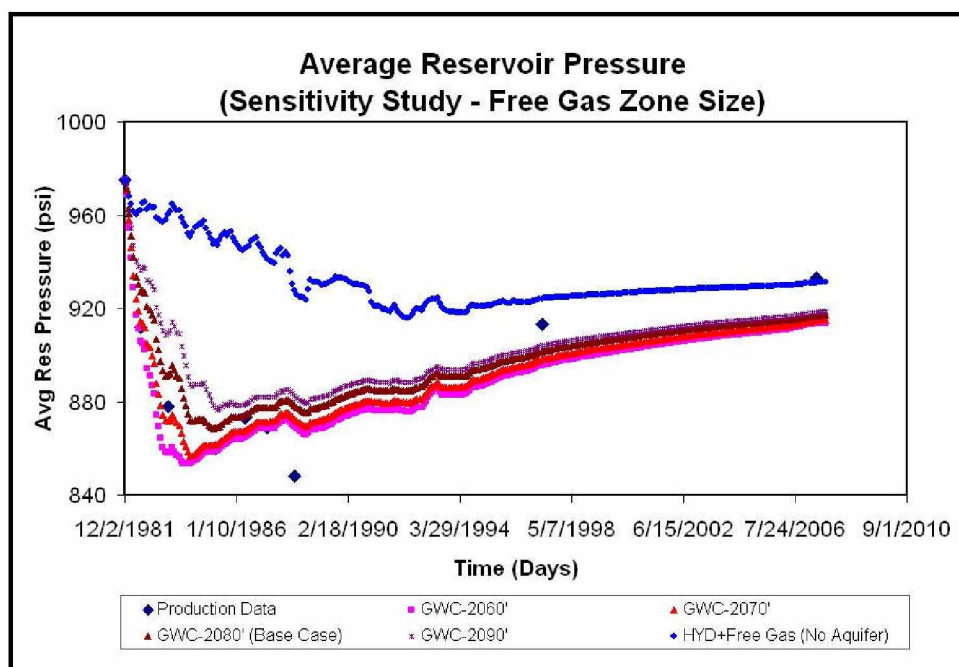


Figure 4.60: Average Reservoir Pressure (Sensitivity - Free Gas Zone Size)

## ii. Hydrate Saturation

Five hydrate saturations were studied to estimate parameter sensitivity. A simulation run was performed also with a hydrate zone completely saturated with hydrates (45%) and bounded water (55%). Numerical difficulties (iterations not converging, higher percentage of material balance error) were observed during the simulation run, and thus, it was aborted.

Cumulative gas production (Figure 4.61) remains unchanged in all but one case, where hydrate saturation was at 40%. A deficiency of free gas in the hydrate zone resulted in a reduction in gas production.

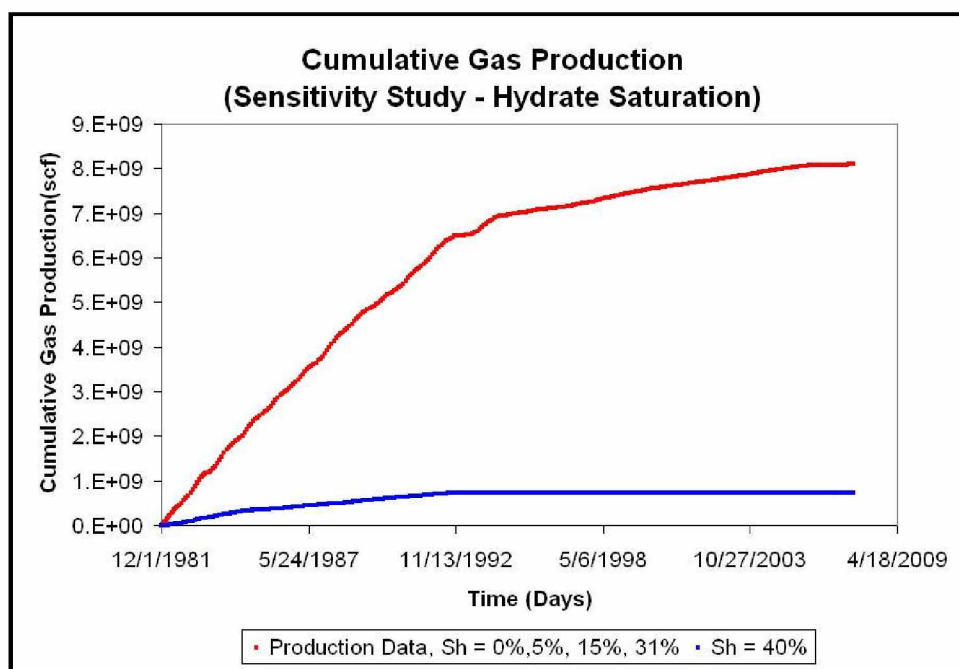


Figure 4.61: Cumulative Gas Production (Sensitivity - Hydrate Saturation)

The water production plot was an interesting comparison (Figure 4.62). Negligible water production was observed for hydrate saturations of 0%, 5%, and 15%, but with a hydrate saturation of 31%, a sudden jump in water production was observed. Again, with 40% hydrate saturation, the water production declined substantially. A possible explanation for this observation was that, at lower hydrate saturation, larger volumes of free gas were available for production. Hence, mobile water generation due to hydrate dissociation was negligible. Hydrate saturation of 31% scenario provided optimum volume of free gas (within the hydrate zone) for initial production, and later dissociating hydrates recharged the reservoir. Eventually, hydrate dissociation caused the immobile produced water to flow towards the wellbore. But for hydrate saturation of 40%, free gas production was restricted, and hence the associated produced water was also proportionally lower. With time, some hydrate dissociation was observed, and this caused a slight jump in the water production rate for this case.

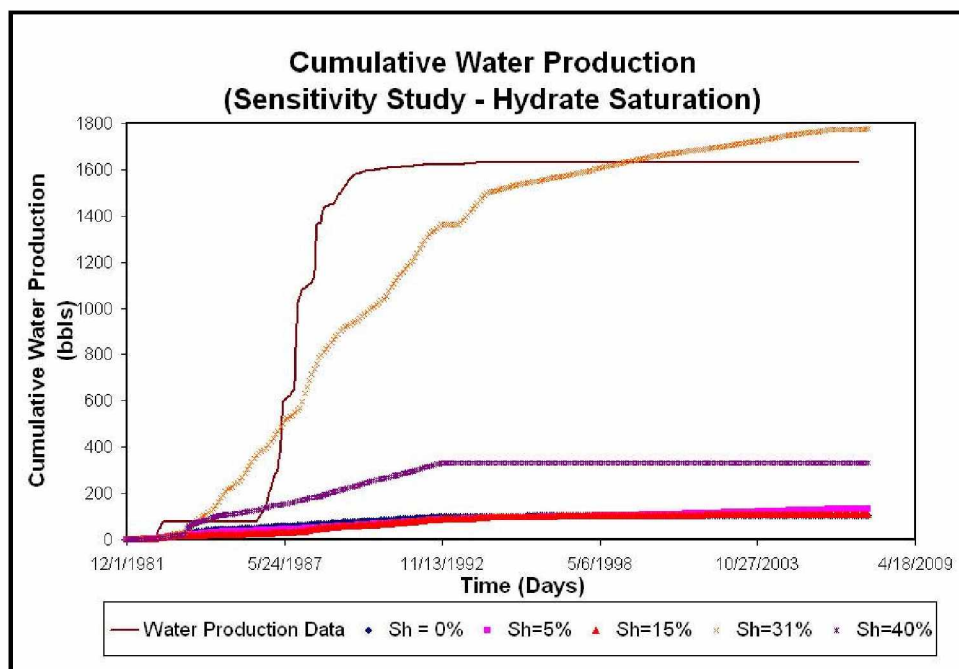


Figure 4.62: Cumulative Water Production (Sensitivity - Hydrate Saturation)

Figure 4.63 is the average reservoir pressure response for different hydrate saturations. Lower hydrate saturations (0% and 5%) were unable to maintain the observed reservoir pressure for a longer time. For a 5% case, dissociating hydrates maintained the reservoir pressure initially. After complete dissociation, the reservoir depleted by gas expansion, which was characterized by rapid pressure decline. On the other hand, hydrate saturation of 15% matched the pressure history in later times. However, during the initial production period, the availability of free gas did not allow the pressure in the reservoir to drop, as was observed in the field. The best-case model (hydrate saturation 31%) managed to support the reservoir pressure and match the production history. The scenario with a hydrate saturation of 40% failed to produce gas at desired rates and, hence, did not match the reservoir pressure response.



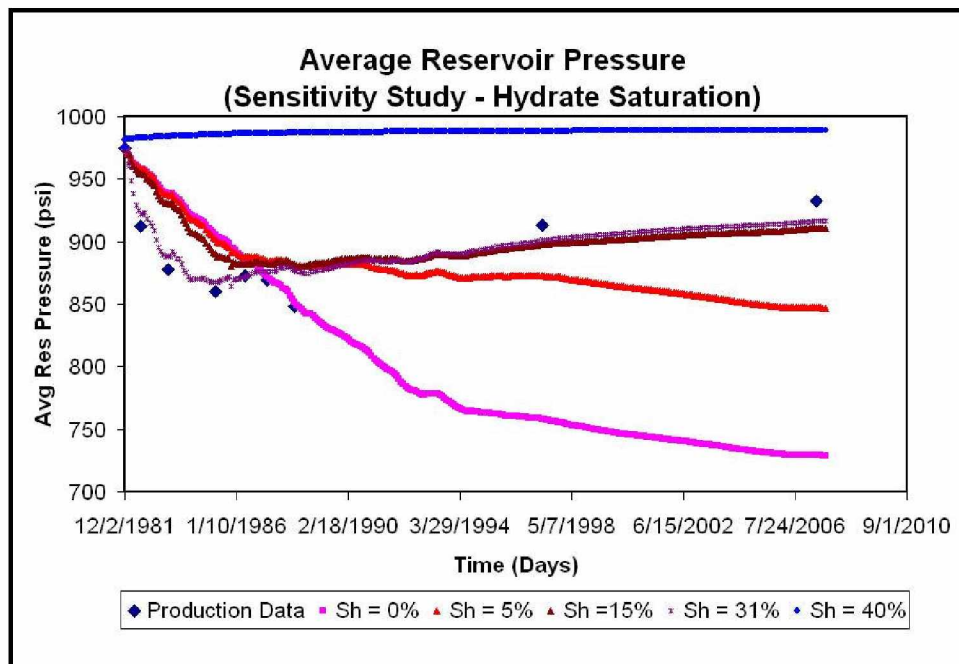


Figure 4.63: Average Reservoir Pressure (Sensitivity - Hydrate Saturation)

### iii. Hydrate Zone Size

Figures 4.64, 4.65, and 4.66 compare the reservoir performance by changing hydrate zone thickness. The cumulative gas production profile presented in Figure 4.64 showed a case where gas production failed to match the production history data. This scenario had hydrate-water contact (HWC) at 2080 ft (no free gas zone), the absence of free gas zone restricted the gas production.

Figure 4.65 shows water production for all the scenarios. Initially, the hydrate-aquifer system, (i.e., a hydrate zone overlying the aquifer zone) produced tremendous volumes of water, because of the unavailability of sufficient gas in the system. Gas production reduced the reservoir pressure; this reduction in reservoir pressure resulted in water coning and hydrates dissociation. The combined effect of the two mechanisms caused high rate of water production. The cumulative water produced in this case reached ~9,000 bbls. The impact of lowering hydrate zone thickness in the case of HGC at 2030 ft, 2040 ft, 2050 ft, and 2060 ft slightly changed the water production profile. The impact of an encroaching aquifer in these cases was minimal (as the rate of water influx was not

very high). Water production was also depended on the rate of hydrate dissociation. With no hydrate zone case (free gas-aquifer), water production is found to be negligible.

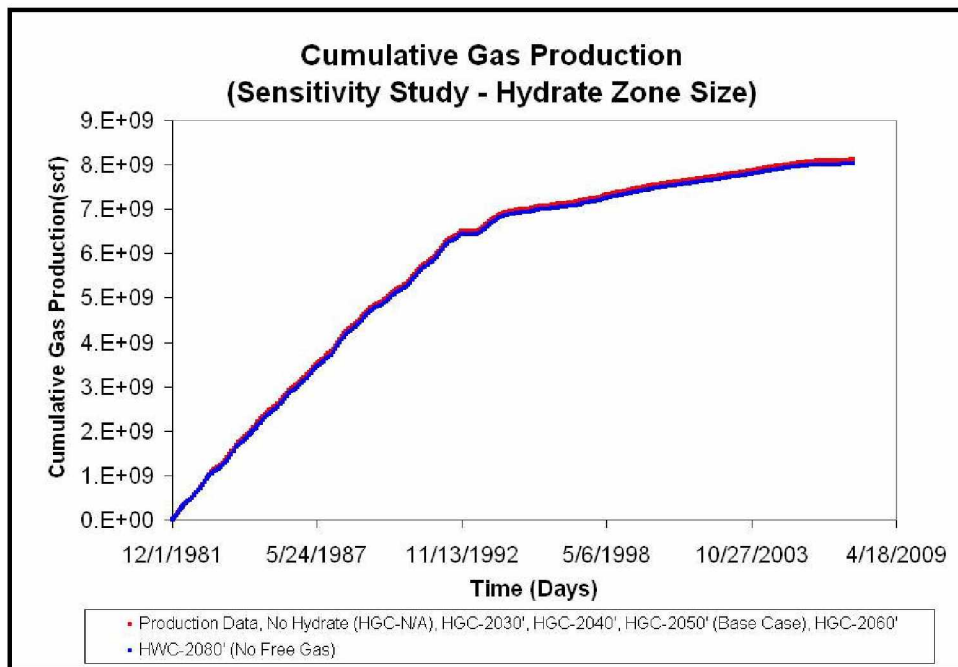


Figure 4.64: Cumulative Gas Production (Sensitivity - Hydrate Zone Size)

Figure 4.66 shows that the change in hydrate zone size had a small impact on reservoir pressure. The primary reason for such an observation was that, with reducing hydrate zone thickness, the gas zone thickness increased, and it compensated for the loss of hydrates to some extent. However, when observed closely, the plot revealed that for thinner hydrate zone size, initial reduction in reservoir pressure overpredicted the reservoir response. Again in later times, due to unavailability of sufficient hydrates, the reservoir underpredicted as compared to observed pressure response. The case with no hydrate zone showed a free gas type expansion pattern even in the presence of an aquifer.



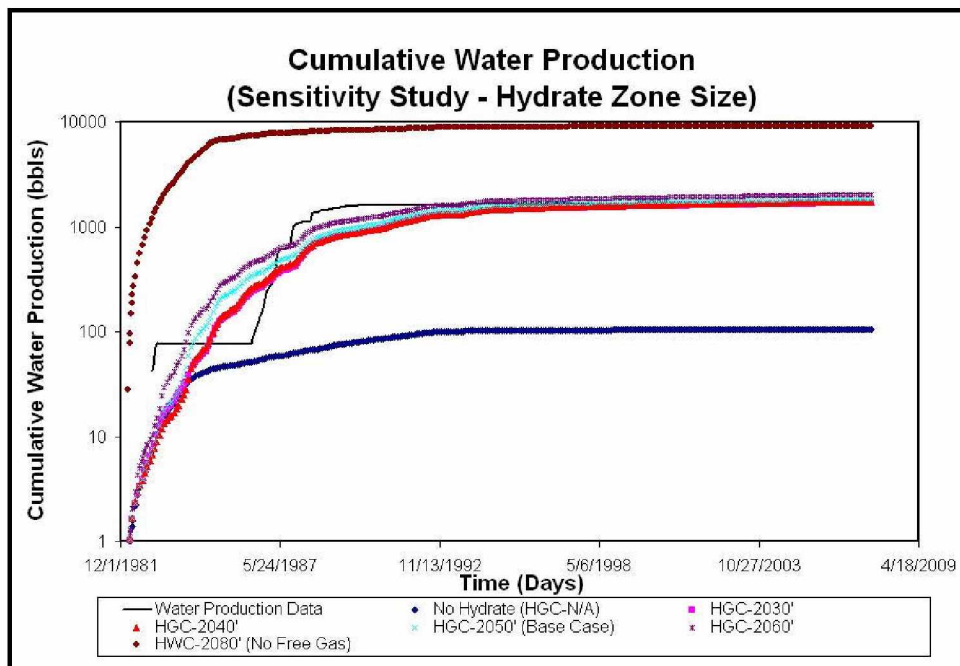


Figure 4.65: Cumulative Water Production (Sensitivity - Hydrate Zone Size)

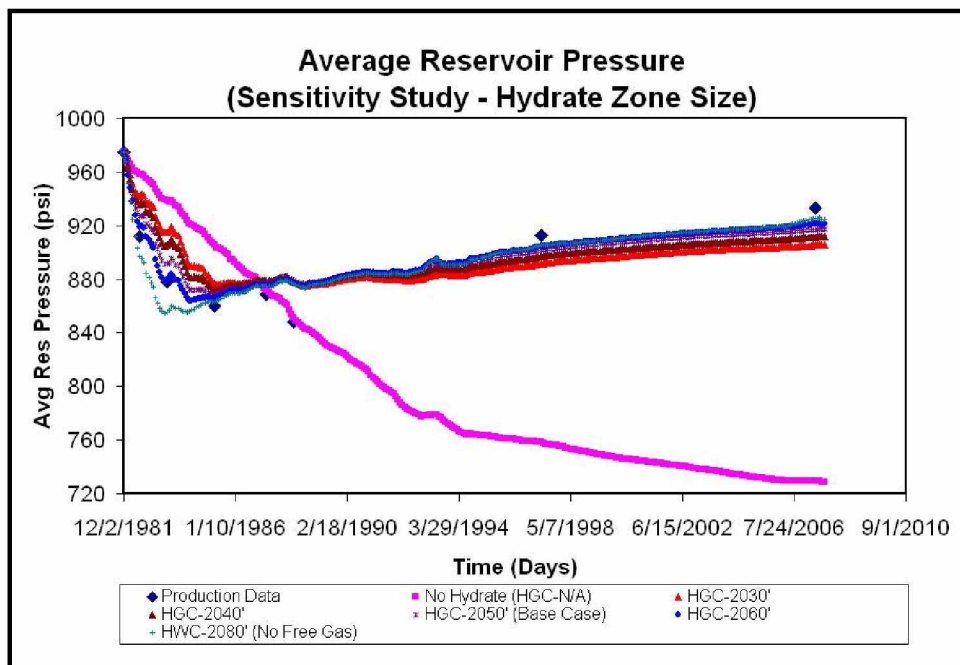


Figure 4.66: Average Reservoir Pressure (Sensitivity - Hydrate Zone Size)

#### iv. Aquifer Strength and Size

To summarize the results from the aquifer study, all sensitivities (free gas-aquifer models) have been explained together.

The aquifer study was performed to understand the impact of aquifer strength and size on reservoir pressure response in the absence of a hydrate-cap. This exercise was initiated also to further evaluate the possibility of matching reservoir performance by changing aquifer strength. Figures 4.67, 4.68, and 4.69 present the summary of all the cases studied as part of the aquifer study. Figure 4.67 shows cumulative gas production with time. It was observed that the effect of *numerical aquifer* strength had no major impact on gas production. However, increasing the *model aquifer* size or decreasing gas saturation (i.e., increasing bounded water saturation) substantially decreased the gas production.

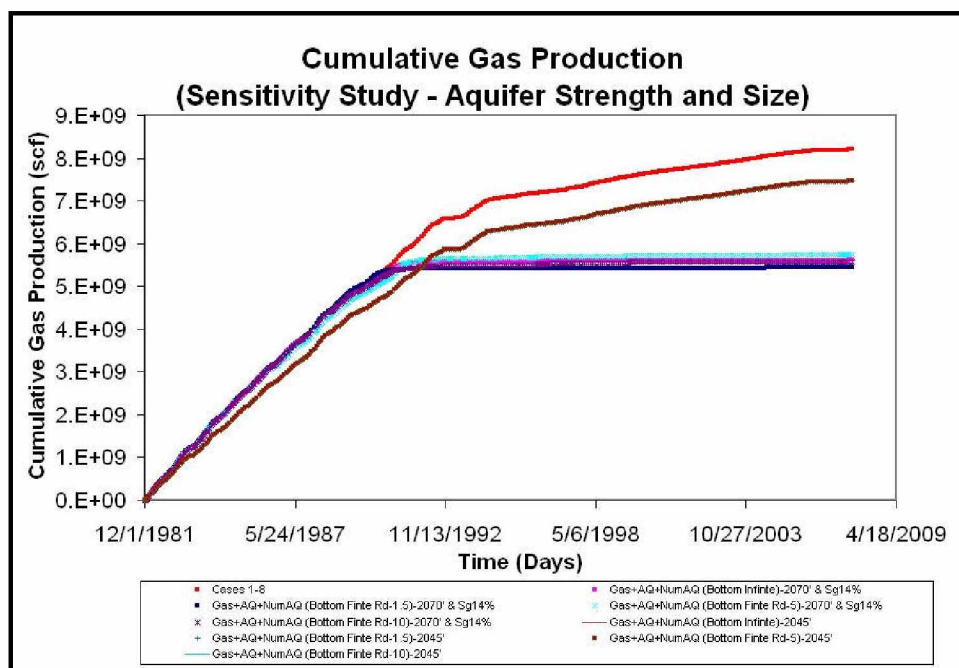


Figure 4.67: Cumulative Gas Production (Sensitivity - Aquifer Strength and Size)

Infinitely sized bottom aquifer systems (Figure 4.68) dominated the reservoir drive mechanism and caused large volumes of water production through the existing wells. Edge aquifer of different sizes had lesser impact on water influx rates.

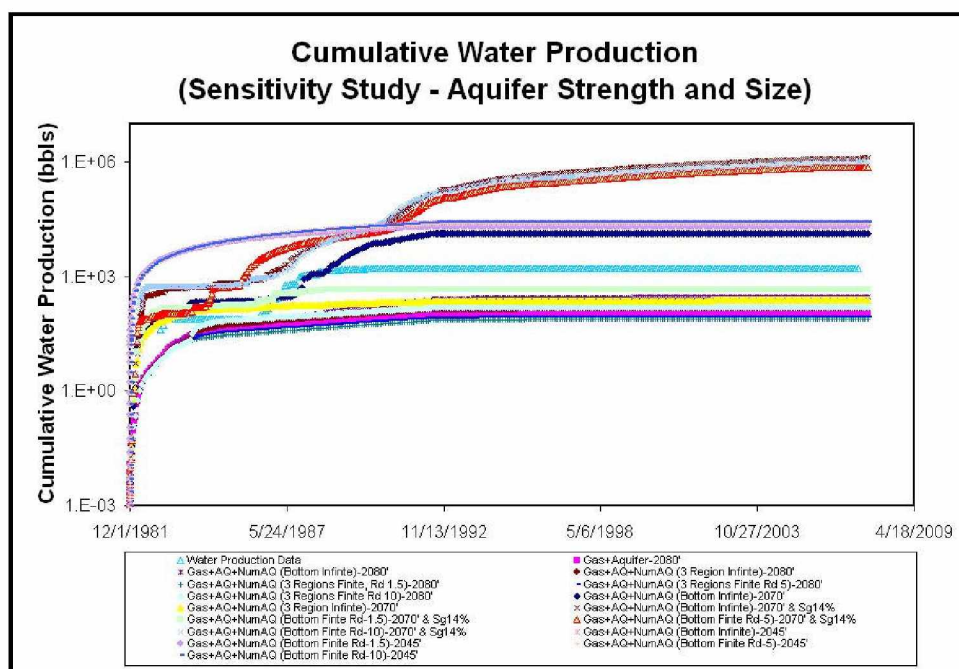


Figure 4.68: Cumulative Water Production (Sensitivity - Aquifer Strength and Size)

Figure 4.69 compares the pressure response in the presence of additional *numerical aquifer*. Again, strong bottom aquifer models stabilized the pressures early in the production life of the reservoir. No such pressure stabilization was observed for an edgewater system during the initial production life of the reservoir. Later, with rapid pressure depletion, water influx rates started rising; and hence, a jump in pressure support was observed.

None of the *numerical aquifer* cases studied was able to match the reservoir history. Hence, it was concluded that the EB reservoir was associated with hydrate and weak aquifer support.

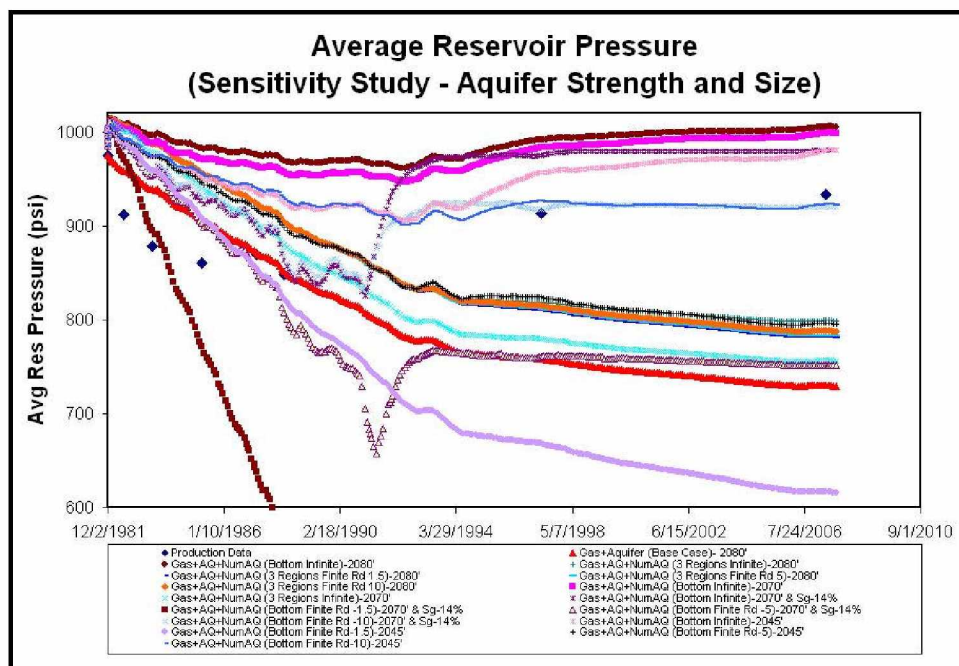


Figure 4.69: Average Reservoir Pressure (Sensitivity - Aquifer Strength and Size)

#### 4.4.3 Forecasting Study

##### 4.4.3.1 East Barrow Gas Field

Average reservoir pressures predicted for 30 years for all forecasting cases have been compared in Figure 4.70. The reservoir performance showed that for the scenario where both EB #14 and #19 (both completed horizontally) were producing, the reservoir pressure depleted at the maximum rate. This was not observed for cases where both existing wells were either produced with a new horizontal or vertical test well. In all these cases, the average reservoir pressure indicated a slight change in slope after 20 to 25 years of production. This showed that the gas production by expansion dominated over the hydrate dissociation mechanism after approximately 20 to 25 years of additional production.



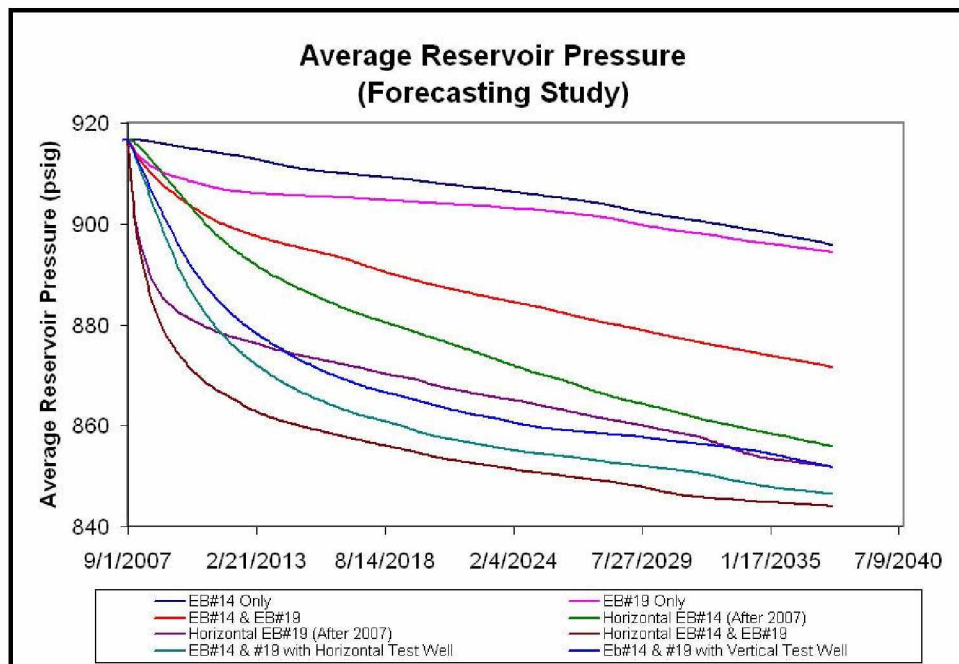


Figure 4.70: Average Reservoir Pressure (Forecasting Study)

The wells were open to flow with a minimum bottomhole pressure constraint of 400 psi (assumed to be the abandonment pressure). EB #14 and #19, producing independently, showed an increase in gas production rates (Figure 4.71). These rates were much higher when both the wells were producing simultaneously. The unavailability of gas slowly decreased the overall gas rate. In the case of horizontal completions performed for EB #14 and #19, higher throughput was observed initially. Later, with the unavailability of free gas, the production rates dropped substantially. Interestingly, a shift in the gas production rates was observed in the case of EB #14 with horizontal completions around the year 2020. This could be due to the hydrate dissociation. However, the behavior could not be explained by water influx as no major shift or change in the water production was observed during that period. Cases where both EB #14 and #19 produced simultaneously along with a new horizontal section, the production rates were observed to be the highest. A combination of existing wells and a new test well (vertical or horizontal) produced gas with fairly higher rates.

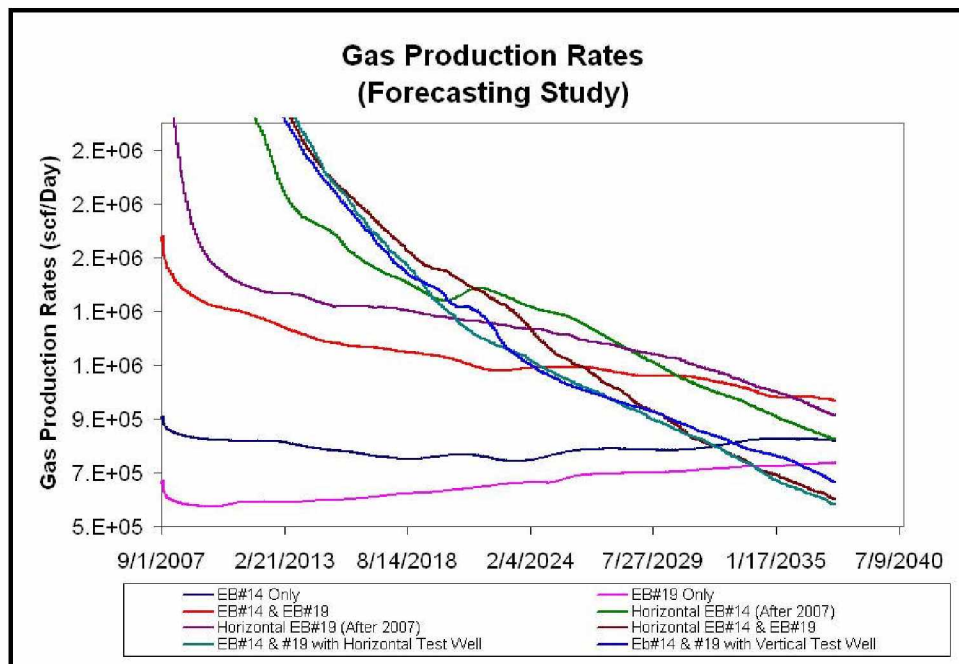


Figure 4.71: Gas Production Rates (Forecasting Study)

Figure 4.72 compares water production of all the scenarios. In this case when both the wells (completed horizontally) were produced, the water production was observed to be extremely high. The lateral was completed at the base of the existing well. This opened the entire surface area of the horizontal section to water flow. Higher gas flow rates attracted produced water and water from the aquifer, drastically increasing the water production rate. Contrary to this, the use of a new horizontal well along with two existing Wells (EB #14 and #19) produced less water.

The total gas recovered from the reservoir has been studied and presented in Figure 4.73. Plot showed that the gas recovery obtained with EB #14 and #19 completed and produced horizontally was very similar to recoveries from existing wells (EB #14 and #19) produced along with a new horizontal well. This was primarily due to the fact that the higher water production observed in the former case reduced gas recovery. The case where, EB #14 and #19 were producing along with new horizontal test well offered the best combination of lower water production and higher recovery; and hence, the economic feasibility of this option could be further explored for future infill drilling.

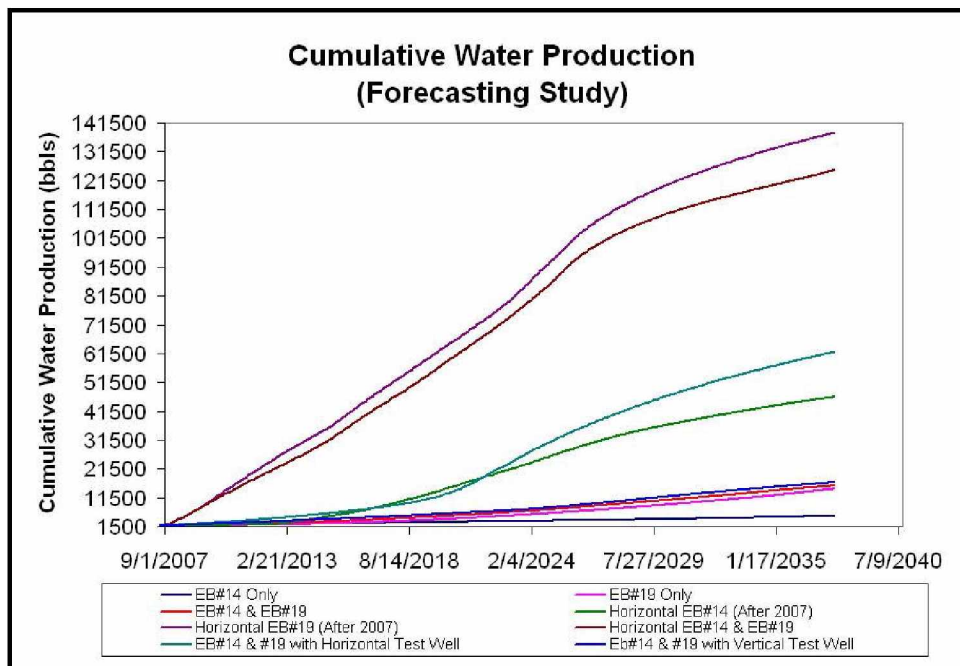


Figure 4.72: Cumulative Water Production (Forecasting Study)

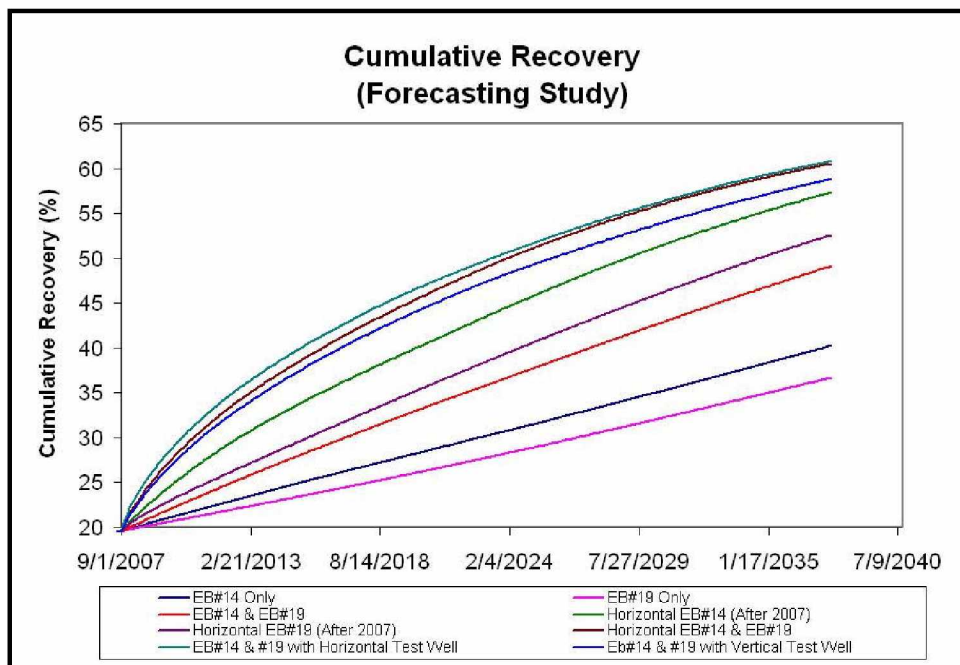


Figure 4.73: Percentage of Gas Recovery (Forecasting Study)

Gas production, recovery, and corresponding water production are listed in Table 4.20 for all the cases.

Table 4.20: Cumulative Gas Production, Recovery, and Water Production from Dec 01, 1981 to Sep 01, 2037 (Forecasting Study)

<b>Cases (From Dec 01, 1981 to Sep 01, 2037)</b>	<b>Cumulative Gas Production (bcf)</b>	<b>Gas Recovery (%)</b>	<b>Cumulative Water Production (bbls)</b>
Producing EB #14 (Only)	16.90 bcf	40.20%	52,70 bbls
Producing EB #19 (Only)	15.40 bcf	36.65%	14,610 bbls
Producing EB #14 and #19 Together	20.60 bcf	49.10%	15,730 bbls
Completing and Producing EB #14 in Horizontal Plane (~1000 ft Long)	24.00 bcf	57.30%	46,450 bbls
Completing and Producing EB #19 in Horizontal Plane (~1000 ft Long)	22.00 bcf	52.50%	137,990 bbls
Completing and Producing EB #14 and #19 in Horizontal Plane (~1000 ft Long)	25.40 bcf	60.50%	125,060 bbls
Producing EB #14 and #19 with Vertical Test Well	25.50 bcf	60.75%	62,040 bbls
Producing EB #14 and #19 with Horizontal Test Well (~1000 ft Long) (Best-Case)	24.70 bcf	58.77%	16,825 bbls



The forecasting and history matched results for the best-case are summarized in Table 4.21. The table also compares the percentage of hydrate dissociation, and quantifies the hydrate contribution.

Table 4.21: Summary of History Matching and Forecasting Results for the Best-Case

<b>EB Results (Best-Case)</b>	<b>Dec 01, 1981 to Sep 01, 2007</b>	<b>Dec 01, 1981 to Sep 01, 2037</b>
	<b>History Matching</b>	<b>Forecasting</b>
Original Gas In-Place (Total - Free Gas+Hyd-Associated)	41.96 bcf	41.96 bcf
Cumulative Gas Production	08.11 bcf	24.70 bcf
Percentage of Gas Recovery	19.33%	58.77%
Gas Produced by Hydrate Dissociation	07.04 bcf	23.50 bcf
Contribution of Hydrate as Percentage of Gas Produced	86.81%	95.14%
Percentage of Hydrate Dissociated	26.94%	89.93%
Cumulative Water Production	1,631 bbls	16,825 bbls

#### 4.4.3.2 Walakpa Gas Field

The forecasting runs were performed on WAL original (LARGE) model that was based on geologic study performed by Panda and Morahan (2008). Table 4.22 summarizes the results from history matching and forecasting studies for the best-case. Figures 4.74, 4.75, and 4.76 present the gas production rate, cumulative gas production, and reservoir pressure, respectively, for the WAL reservoir from Oct 01, 1992 to Sep 01, 2037 (Basis: LARGE model).

Table 4.22: Summary of History Matching and Forecasting Study for the Best-Case

WAL Results (Best-Case)	Cumulative Gas Production (bcf)	Gas Recovery (%)	Cumulative Water Production (bbls)	Percentage of Hydrate Dissociation
LARGE Model (All Existing Wells Producing)				
<i>History Matching</i> Oct 01, 1992 to Sep 01, 2007	17.11 bcf	2.94%	NIL	10.40%
<i>Forecasting</i> Oct 01, 1992 to Sep 01, 2037	65.00 bcf	11.17%	450 bbls	20.10%

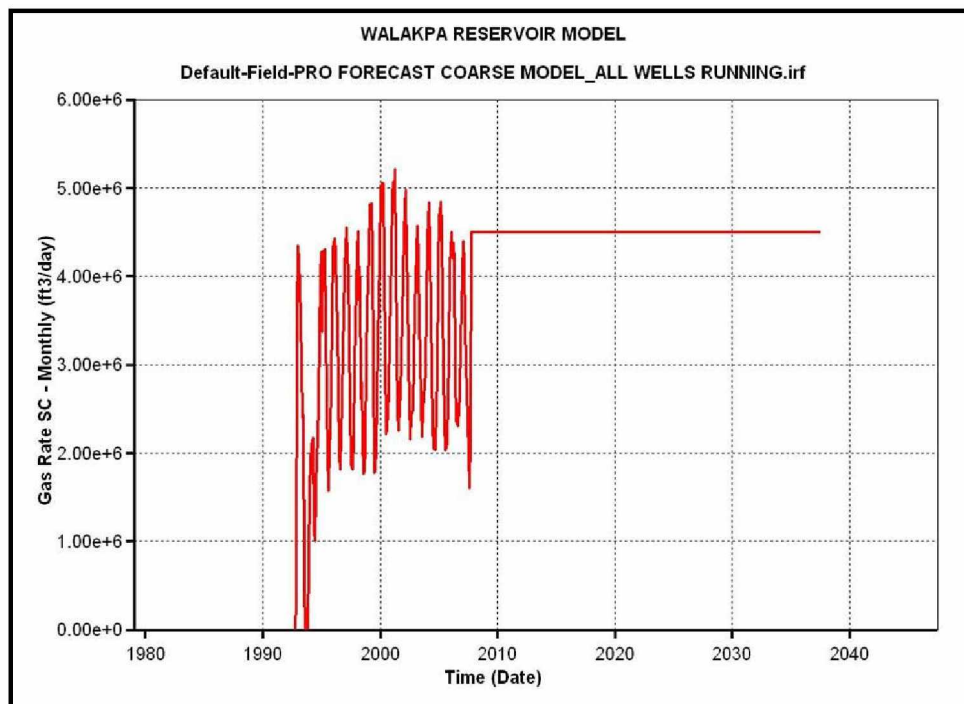


Figure 4.74: Cumulative Gas Production (Forecasting Study) - LARGE Model

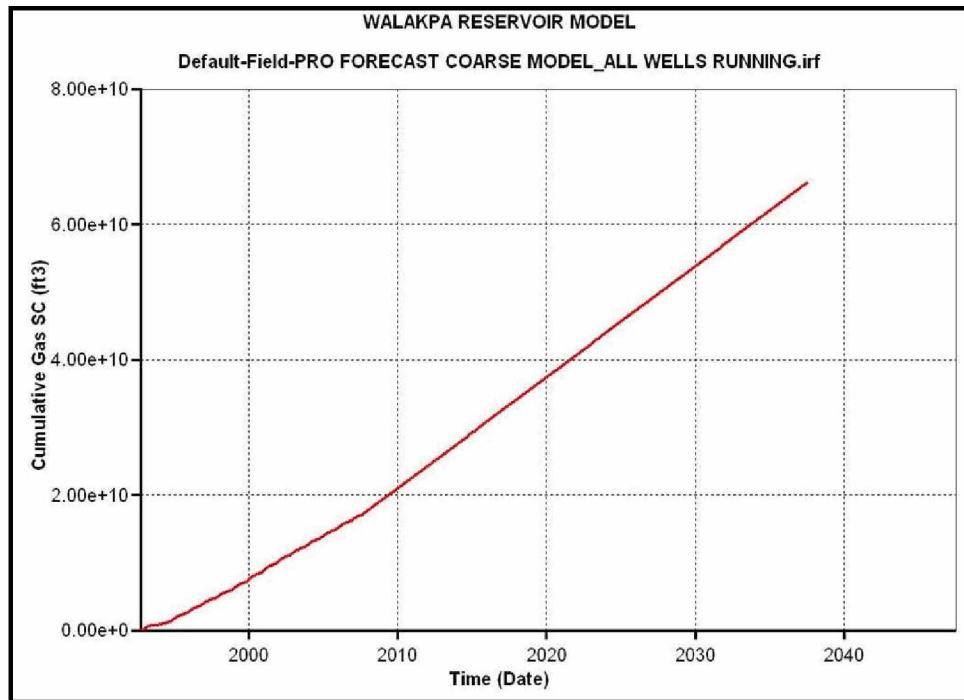


Figure 4.75: Cumulative Gas Production Rate (Forecasting Study) - LARGE Model

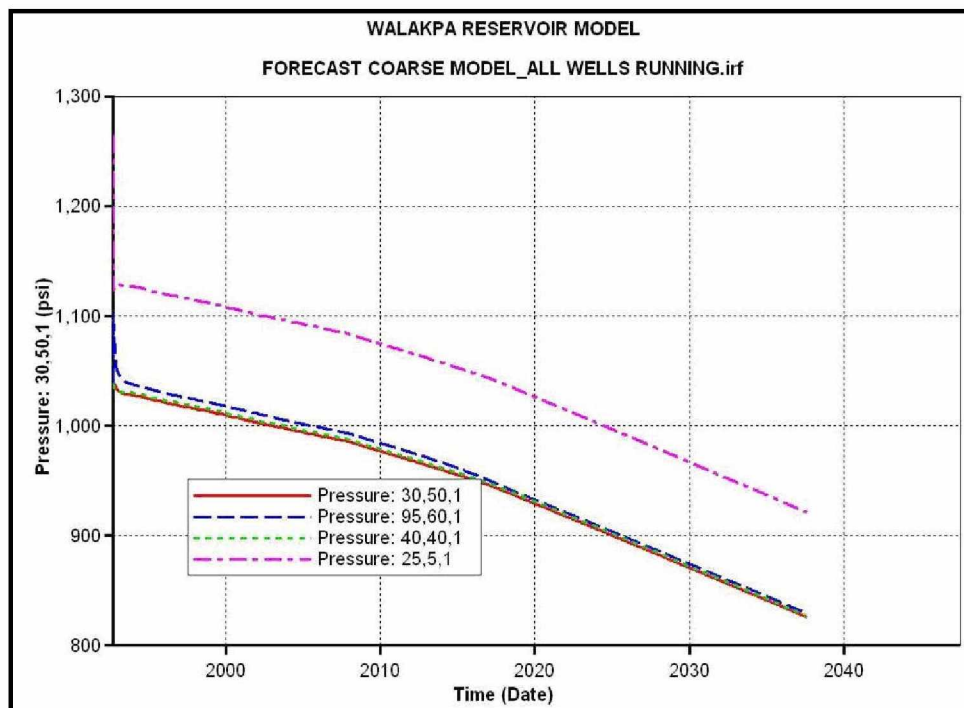


Figure 4.76: Average Reservoir Pressure (Forecasting Study) - LARGE Model

Table 4.23 shows the original gas in-place volumes for WAL reservoir (LARGE model).

Table 4.23: Initial Gas In-Place Estimates for WAL (LARGE Model)

<b>Initial Gas In-Place</b>	<b>LARGE Model</b>
Initial Free Gas In-Place	298.00 bcf
Hydrate-Associated Gas In-Place	284.00 bcf
Total Initial Gas In-Place	582.00 bcf

## 5. CONCLUSIONS AND RECOMMENDATIONS

### 5.1 Conclusions

A comprehensive study was undertaken to investigate the methane hydrate resource potential associated with the BGF. Diagnostic methodologies were developed to test the three fields for the possible hydrate accumulations. An engineering approach was followed to construct hydrate stability models and material balance procedures for identifying the reservoir drive mechanisms. Based on these results, state-of-the-art dynamic reservoir simulation models were developed using advanced features of the CMG-STARS simulator to unlock several possibilities associated with hydrate reservoir development. Reservoir modeling confirmed the key findings of previous study and projected the future performance of the reservoir under different scenarios. Future well locations were proposed, and completion strategies (vertical vs. horizontal well) were thoroughly investigated. Moreover, an optimal plan for future reservoir development was also suggested. Attempts were made also to understand and model the fluid flow behavior through hydrate-saturated porous media by performing relative permeability experiments in the laboratory. This work integrates the basic reservoir engineering philosophy, experimental results, and simulation studies in order to deliver solutions as per the set objectives. The procedures developed in this study could be extended easily to investigate the hydrate resource potential of similar fields.

#### *5.1.1 Gas Hydrate Stability Modeling*

- i. Hydrate phase behavior studies and the construction of stability models proved to be a good elimination criteria. They provided a quick and easy way to evaluate hydrate resource potential of individual gas pools. The selection of an appropriate tool for phase behavior predictions, extensive data gathering, and data analysis turned out to be the key factors responsible for models' accurate response.

- ii. Phase behavior predictions of CSM-HYD software closely matched the empirical results (average error of 5%) and, hence, proved to be the best tool for pressure-temperature predictions.
- iii. The inherent limitation of the Kamath and Holder (1987) model was found when model's predictions deviated considerably from the experimental data at higher water salinities of 2% and 4% w/w (average error of 18%). On the other hand, the Moridis (2003) model proved to be quite effective even with higher water salinity (average error of 12%).
- iv. The EB and WAL gas fields showed the presence of a stable hydrate zone in updip locations of the respective reservoir sands. However, there was a lack of hydrate stability zone within the SB gas pool.

#### *5.1.2 Material Balance Study*

- i. Material balance models were successful in determining reservoir drive mechanisms of the EB gas field. From the study it was concluded that the reservoir was not volumetric. It was under the influence of two external pressure sources i.e. water influx from underlying aquifer and gas recharge from dissociating hydrates. Interestingly, when treated individually, these mechanisms failed to explain the observed pressure response.
- ii. Use of the Kamath and Holder (1987) model for hydrate phase behavior predictions made the response of hydrate model approximate and uncertain.
- iii. The use of CMG-STARS model for predicting unconventional reservoir (hydrate and aquifer supports) behaviors during material balance studies was the special feature of this work. The simulation studies proved to be useful and showed a unique blend of conventional reservoir engineering and modern day reservoir simulation studies.

### *5.1.3 Gas-Water Relative Permeability Study*

- i. The experiments were successful in generating gas-water relative permeability tables for hydrate-saturated core samples. All care was taken to maintain the EB reservoir conditions.
- ii. Capillary pressure effects dominated the two-phase flow through the porous media. The effect of capillary pressure increased with hydrate saturations. Capillary pressure restricted the gas flow and increased irreducible water saturations within the core sample with a rise in hydrate saturations.
- iii. Relative fluid flow data were captured when hydrate saturation within the core sample was maintained at 38%, 14%, and 5%. The data gained physical importance, as they represented three stages (initial, current, and final) of hydrate depletion during the production life of an EB type reservoir.
- iv. An attempt to tune the existing analytical model using the relative permeability data was unsuccessful, as the experimental dataset was limited and represented a small range of gas saturation.
- v. A stable two-phase flow through the core sample was difficult to maintain for a wider range of gas saturation due to the incapability of the setup to maintain higher inlet pressures.

### *5.1.4 Reservoir Simulation Study*

The hydrate resource potential of the EB and WAL reservoirs is promising. Both reservoirs have considerable hydrate potential that can supply large volumes of gas for several years to come.

#### *5.1.4.1 East Barrow Reservoir Model*

- i. Unlike ANS hydrate reservoirs, the EB gas pool is associated with higher geothermal gradients and shallower (lower pressure) reservoir depths. The reservoir's pressure and temperature condition lies very close to the three-phase equilibrium curve. However, this situation cannot be generalized for



the entire reservoir as thermal variation (higher local geothermal gradient) could generate natural pockets of free gas within the hydrate zones. These physical situations are difficult to initialize in the reservoir simulator. However, for simplicity, the hydrate zones in CMG-STARS were initialized with uniform hydrate saturations. For the EB model, a uniform hydrate saturation of 31% matched the reservoir's performance. This shows that the volume (equivalent to 31% saturation) occupied by hydrates are able to provide necessary pressure support to the gas pool.

- ii. The dynamic reservoir simulation model, constructed and initialized in CMG-STARS, was matched successfully with the production data (max error of 1.5%). It was found that the gas reservoir was in communication with a thick layer of hydrates and supported by a weak aquifer from the bottom. The total initial gas (total = free + associated) in-place was found to be 42 bcf. The rise in HGC from 2050 ft to 2045 ft confirmed the dissociation of hydrates at the free gas-hydrate interface. On the other hand, a shift in GWC from an initial depth of 2080 ft to 2070 ft, confirmed partial support from encroaching water.
- iii. Hydrate dissociation was controlled by depressurization and constant heat influx from the surrounding rocks. Higher rates of dissociation were observed at the hydrate-free gas interface and near the top section of the reservoir. By Sep 01, 2007, about 27% of initial hydrates have been dissociated. Dissociating hydrates have charged the free gas reservoir by supplying more than 86% of total produced gas. Total gas recovery was estimated to be around 20%.
- iv. The free gas reservoir with aquifer sensitivity scenarios failed to match the observed reservoir performance, thus confirming the presence of hydrate driven mechanism.
- v. Forecasting runs were performed for the next 30 years of production life of the reservoir. It was predicted that nearly 90% of in-place hydrates would dissociate by the end of Sep 01, 2037 (Basis: best-case).
- vi. The forecasting study showed that the optimum reservoir performance, of maximum gas recovery and minimum water production, could be achieved by producing the existing Wells EB #14 and #19 along with a new horizontal test

well (~1000 ft long). This case produced a cumulative gas of 25 bcf (from Dec 01, 1981 to Sep 01, 2037) which was equivalent to a recovery of ~60% of total initial gas in-place. The cumulative water production for this scenario was predicted to be around 16,825 bbls. This was the lowest cumulative produced water recorded as compared to another scenario having similar gas recoveries. Hence, this scenario has been proposed as the best-case scenario for future reservoir development.

#### 5.1.4.2 Walakpa Reservoir Model

- i. Fluid phase behavior conditions in the WAL gas reservoir were found similar to those at the EB reservoir. Hence, similar treatment was given to the WAL reservoir model.
- ii. The WAL reservoir model, constructed and initialized in CMG-STARs, was successfully matched with the reservoir production and pressure history data with the SMALL model, that only included an updip band of hydrates of 4000 ft in length and associated with infinite aquifer (edgewater) support from the bottom. A LARGE model was initialized also that included hydrates updip to the extent mapped by the reservoir characterization study.
- iii. The WAL simulation study concluded that the reservoir was associated with tremendous volumes of free and hydrate-associated gas i.e. ~580 bcf (Basis LARGE model). The reservoir was fairly young, thus it was difficult to accurately estimate reservoir drive mechanisms with current data. However, history matching showed that the free gas reservoir was overlain with the hydrate zone and was also in communication with an edge aquifer, extending infinitely in south direction.

## **5.2 Recommendations**

- i. Attempts could be made to populate the relative permeability table with more datasets. A large number of data points will reduce disturbance and shall generate a better match between the selected model and the experimental

data. One way to achieve this is by overcoming the current limitations of the setup to minimize the capillary pressure effects. Modifications in the existing setup should be made in order to have good hydrate distribution within the core sample. Larger surface area of the core sample must be opened for gasflooding that, could substantially reduce capillary pressure related issues.

- ii. Well-testing data available in the literature (for EB wells) were used to estimate initial reservoir pressures. This was done by considering the drainage volume of the well to be a free gas tank. However, this condition may not be true for many existing wells that were completed in both hydrate and free gas zones. It is thus highly recommended to modify the existing fluid flow equations (diffusivity) to incorporate the effect of additional gas recharge from hydrate dissociation. The available well-testing data could then be treated with the modified flow equations to accurately determine the initial reservoir pressure.
- iii. Reservoir simulation studies should be performed using a different reservoir simulator, e.g., TOUGH+HYDRATE reservoir simulator. This would validate CMG-STARs capabilities and would also confirm the current findings.
- iv. The proposed plan for future reservoir development was made based on the technical evaluation of different scenarios. However, a detailed economic study, backed by technical feasibility work could have provided more realistic options. Thus, efforts could be made to perform the economic feasibility studies of different production scenarios under investigation.

## REFERENCES

- Ahmed, T. and McKinney, P. D. *Advanced Reservoir Engineering*. Gulf Professional Publishing, 2005, 407p.
- Allen, W. W. and Crouch, W. J. *Engineering Study of South and East Barrow Fields, North Slope Alaska, Alaska*. Technical report prepared for the NSB Gas Development Project, Barrow, Alaska, October 1988, 56p.
- Collett, T. S., Bird, K. J., Kvenvolden, K. A., Magoon, L. B. *Geologic Interrelations Relative to Gas Hydrates within the North Slope of Alaska*. USGS Open-File Report, 1988, pp.150.
- Collett, T. S. *Natural Gas Hydrates of the Prudhoe Bay and Kuparuk River Area, North Slope, Alaska*. AAPG Bulletin, Vol. 77, No. 5, 1993, pp. 793-812.
- Collett, T. S. and Kuskra, V. A. *Hydrates Contain Vast Store of World Gas Resources*. Oil and Gas Journal, Vol. 96, No. 19, May 1998, pp. 90-95.
- Collett, T. S. *Energy Resource Potential of Natural Gas Hydrates*. AAPG Bulletin, Vol. 86, No. 11, November 2002, pp. 1971-1992.
- Collett, T. S. *Alaska North Slope Gas Hydrate Energy Resources*. USGS, Open-File Report, No. 1454, 2004, 4p.
- Craft, B. C. and Hawkins, M. *Applied Petroleum Reservoir Engineering*. (Revised by Terry, R. E.) Second Edition, Prentice Hall Inc., 1990, 419p.
- Dallimore, S. R. and Collett, T. S. *Scientific Results from the Mallik 2002 Gas Hydrate Production Research Well Program, Mackenzie Delta, Northwest Territories, Canada*. Geological Survey of Canada Bulletin, No. 585, 2005 140p.
- Darkwah, S. A. and Allen, W. W. *Engineering Study of the South, East and Walakpa Fields, North Slope Borough, Alaska*. Technical Report Submitted to the NSB, Barrow, Alaska, June 1996, 32p.

Darvish, M. P. *Gas Production from Hydrate Reservoirs and Its Modeling*. Journal of Petroleum Technology (JPT), June 2004, pp. 65-71.

Dvorkin, J., Helgerud, M. B., Waite, W. F., Kirby, S. H., Nur, A. *Introduction to Physical Properties and Elasticity Models*. Natural Gas Hydrates in Oceanic and Permafrost Environments (Max, M. D., ed.), Kluwer Academic Publishers, 2000, 245p.

Ganti, G. *The Effects of Permeability and Well Completion on Methane Gas Production from Hydrate-Bearing Reservoir*. M.S. Thesis, The University of West Virginia, Morgantown, West Virginia, 2007, 76p.

Gerami, S. and Darvish, P. M. *Material Balance and Boundary Dominated Flow Models for Hydrate Capped Gas Reservoirs*. SPE Paper No. 102234, www.spe.org, 2006, pp. 1-16.

Glenn, R. K. and Allen, W. W. *Geology, Reservoir Engineering and Methane Hydrate Resource Potential of the Walakpa Gas Field, North Slope Alaska*. Final Technical Report (Under Grant DE-FG21-91MC28131) Submitted to the USDOE, Morgantown Energy Technology Center, Morgantown, WV, 1991, 26p.

Gruy, H. J.. *Reservoir Engineering and Geologic Study of the East Barrow Field, National Petroleum Reserve in Alaska*. Technical Report Submitted to Husky Oil NPR Operations Inc., Anchorage, Alaska, December 1978, 62p.

Hammerschmidt, E. G. *Formation of Gas Hydrates in Natural Gas Transmission Lines*. Industrial and Engineering Chemistry Journal, August 1934, pp. 851-855.

Holba, A. G., Lundell, L. L., Dzou, I. L., Bone, R. L., Cooley, M. W., Kriel, W. A. *Geochemistry of Natural Gases and Hydrocarbon Liquids from Walakpa Gas Field, North Slope, Alaska*. Walakpa Gas Field Geochemistry Report, AEPT, TX, May 1994, pp. 4-13.

Hong, H. *Modeling of Gas Production from Hydrates in Porous Media*. M.S. Thesis, University of Calgary, Alberta, July 2003, pp. 85-86.

Hong, H. and Darvish, M. P. *Numerical Study of Constant-Rate Gas Production from In Situ Gas Hydrates by Depressurization*. Geological Survey of Canada Bulletin, No. 585, 2005, pp. 1-11.

Howe, S. *Production Modeling and Economic Evaluation of a Potential Gas Hydrate Pilot Production Program on the North Slope of Alaska*. M.S. Thesis, The University of Alaska Fairbanks, Fairbanks, Alaska, May 2004, 160p.

Hunter, R. B., Digert S. A., Boswell, R., Collett, T. S. *Alaska Gas Hydrate Research and Stratigraphic Test Preliminary Results*. The Arctic Energy Summit, Anchorage, Alaska, October 2007, pp.1-12.

Ioannis, N. T. and Lichtner, P. C. *Role of Critical Gas Saturation in Methane Production from Hydrate Dissociation at the Pore Network Scale*. SPE Paper No. 90743, www.spe.org, September 2004, pp. 1-10.

Jaiswal, N. *Measurement of Gas-Water Relative Permeabilities in Hydrate Systems*. M.S. Thesis, University of Alaska Fairbanks, Fairbanks, Alaska, August 2004, 100p.

Kamath, V. A. and Holder, G. D. *Dissociation Heat Transfer Characteristics of Methane Hydrates*. AIChE Journal, Vol.33, No. 2, February 1987, pp. 347-350.

Katz, D. L. *Prediction of Conditions for Hydrate Formation in Natural Gases*. Trans. AIME, 1945, pp.140-160.

Kim, H. C., Bishnoi, P. R., Heidemann, R. A., Rizvi, S. S. H. *Kinetics of Methane Hydrate Decomposition*. Chemical Engineering Science, Vol. 42, No. 7, 1987, pp. 1645-1653.

Kleinberg, R. L. *Hydrates*. Topic Paper No. 24, Working Document of National Petroleum Council (NPC) Global Oil and Gas Study. July 2007, 12p.

Kvenvolden, K. A. *Gas Hydrates - Geological Perspective and Global Change*. Reviews of Geophysics, Vol. 31, 1993, pp. 173-187.

Kvenvolden, K. A. and Roger, B. W. *Gaia's Breath - Global Methane Exhalations*. Marine and Petroleum Geology. Vol 22, 2005, pp. 579-590.

Lachenbruch, A. H., Galanis Jr., S. P., Moses Jr., T. H. *A Thermal Cross Section for the Permafrost and Hydrate Stability Zones in the Kuparuk and Prudhoe Bay Oil Fields*. Geologic Studies in Alaska by the USGS during 1987, 1988, pp. 48-51.

Morahan G. T. *Seismic Evaluation of the Barrow High Area, Including the Walakpa and Barrow Gas Fields*. Topical Report prepared under DoE Project No. DE-FC26-06NT42962 submitted to the USDOE, Morgantown, WV, [www.netl.doe.gov](http://www.netl.doe.gov), March 2008, 29p.

Makagon, Y. F. *Hydrates of Natural Gas*. Penn Well Publishing Company, Tulsa, OK, 1981 237p.

Moridis, G. J. *Numerical Studies of Gas Production from Methane Hydrate*. SPE Paper No. 87330, SPE Journal, December 2003, pp. 359-370.

Moridis, G. J. and Collett, T. S. *Gas Production from Class 1 Hydrate Accumulations*. in *Recent Advances in the Study of Gas Hydrates*. Taylor C. and Qwan, J., Eds, Kluwer Academic, New York, 2004, pp. 75-88.

Moridis, G. J., Kowalsky, M. B., Pruess, K. *Depressurization-Induced Gas Production From Class-1 Hydrate Deposits*. SPE Paper No. 97266, [www.spe.org](http://www.spe.org), October 2005, pp.1-30.

Moridis, G. J. and Reagen, M. T. *Gas Production From Class 2 Hydrate Accumulations in the Permafrost*. SPE Paper No. 110858, [www.spe.org](http://www.spe.org), November 2007, pp. 1-27.

Moridis, G. J., Collett, T. S., Boswell, R., Kurihara, M., Reagen, M. T., Koh, C., Sloan, E. D. *Toward Production from Gas Hydrates: Current Status, Assessment of Resources and Simulation-Based Evaluation of Technology and Potential*. SPE Paper No. 114163, [www.spe.org](http://www.spe.org), February 2008a, pp. 1-43.

Moridis, G. J., Reagen, M. T., Zhang, K. *The Use of Horizontal Wells in Gas Production From Hydrate Accumulations*. Proceedings of the 6<sup>th</sup> International Conference on Gas Hydrates (ICGH, 2008), Vancouver, Canada, July 2008b, pp. 1-12.

Panda, M. N. and Morahan G. T. *An Integrated Reservoir Model Description for East Barrow and Walakpa Gas Fields*. Topical Report prepared under DoE Project No. DE-FC26-06NT42962 submitted to the USDOE, Morgantown, WV, [www.netl.doe.gov](http://www.netl.doe.gov), June 2008, 44p.

Pletcher, J. L. *Improvements to Reservoir Material Balance Methods*. SPE Paper No. 75354, SPE Reservoir Evaluation and Engineering, [www.spe.org](http://www.spe.org), 2001, pp. 49-59.



Selim, M. S. and Sloan, E. D. *Hydrate Dissociation in Sediments*. SPE Paper No. 16859, SPE Reservoir Engineering, May 1990, pp. 245-251.

Seol, Y., Kneafsey, T. J., Tomutsa, L., Moridis, G. J. *Preliminary Relative Permeability Estimates of Methane Hydrate-Bearing Sand*. Proceedings, TOUGH Symposium, LBNL, California, May 2006, pp. 1-6.

Sherrod, P. *Non Linear Regression Analysis Program (NLREG) User Manual*. Demonstration Copy, www.nlreg.com, 2007, 90p.

Sloan, E. D., Khoury, F. M., Kobayashi, R. *Water Content of Methane Gas in Equilibrium with Hydrates*. Industrial and Engineering Chemistry Fundamentals Journal, Vol. 15, No. 4, 1976, pp. 318-323.

Sloan, E. D. *Clathrate Hydrates of Natural Gases*. Second Edition, Marcel Dekker, New York, 1998, 705p.

Sloan, E. D. *Fundamental principles and applications of natural gas hydrates*. Nature Journal, Vol. 426, November 2003, pp. 353-359.

Sloan, E. D. and Koh, C. A. *Clathrate Hydrates of Natural Gases*. Third Edition, Taylor and Francis Inc., Boca Raton, FL, 2008, 721p.

Song, K. Y. and Kobayashi, R. *Measurement and Interpretation of the Water Content of a Methane-Propane Mixture in the Gaseous State in Equilibrium with Hydrate*. Industrial and Engineering Chemistry Fundamentals Journal, Vol. 21, 1982, pp. 391-395.

Stone, H. L. *Estimation of three-phase relative permeability and residual oil data*. Journal of Canadian Petroleum Technology, Vol. 12, No. 4, 1973, pp. 53-61.

Stokes, P. J., Walsh, T. P., Walsh, C. *Walakpa Field Reserve Study*. Technical Report Submitted to the NSB, Barrow Alaska, June 2005, 90p.

Stokes, P. J. and Walsh, T. P. *South and East Barrow Gas Fields Reserves Study*. Technical Report Submitted to the NSB, Barrow, Alaska, July 2007, 36p.

Stokes, P. J. and Walsh, T. P. *South and East Barrow Gas Fields Well Improvements Study*. Technical Report Submitted to the NSB, Barrow, Alaska, February 2006, 70p.

Swinkles, W. J. A. M. and Drenth, R. J. J. *Thermal Reservoir Simulation Model of Production from Naturally Occurring Gas Hydrate Accumulations*. SPE Reservoir Evaluation and Engineering, Vol. 3, No. 6, December 2000.

Takahashi, H. and Tsuji, Y. *Multi-Well Exploration Program in 2004 for Natural Hydrates in Nankai-Trough Offshore Japan*. Offshore Technology Conference (OTC) 17162, Houston, TX, U.S.A., May 2005, pp. 1-10.

Uddin, M., Coombe, D. A., Law, D. A., Gunter, D. W. *Numerical Studies of Gas-Hydrates Formation and Decomposition in a geologic reservoir*. SPE Paper No. 100460, www.spe.org, May 2006, pp. 1-20.

Ullerich, J. W., Selim, M. S., Sloan, E. D. *Theory and Measurement of Hydrate Dissociation*. AIChE Journal, May 1987, Vol. 33, No. 5, pp. 747-752.

*USDOE/NETL Methane Hydrate Reservoir Simulator Code Comparison Study*. National Methane Hydrate Research and Development Program, NETL Weblink: [http://www.netl.doe.gov/technologies/oilgas/FutureSupply/MethaneHydrates/MH\\_CodeCompare/MH\\_CodeCompare.html](http://www.netl.doe.gov/technologies/oilgas/FutureSupply/MethaneHydrates/MH_CodeCompare/MH_CodeCompare.html). 2007.

*USDOE/NETL and BPXA Resource Characterization and Quantification of Natural Gas-Hydrate and Associated Free Gas Accumulations in the Prudhoe Bay - Kuparuk River Area on the North Slope of Alaska*. National Methane Hydrate Research and Development Program, DE-FC26-01NT41332, NETL Weblink: <http://www.netl.doe.gov/technologies/oilgas/FutureSupply/MethaneHydrates/projects/DOEProjects/Alaska-41332.html>. September 2001.

*USDOE/NETL and NSB Characterization and Qualification of the Methane Hydrate Resource Potential Associated with the Barrow Gas Fields*. National Methane Hydrate Research and Development Program, DE-FC26-06NT42962. NETL Weblink: [http://www.netl.doe.gov/technologies/oilgas/FutureSupply/MethaneHydrates/projects/DOEProjects/MH\\_42962BarrowGas.html](http://www.netl.doe.gov/technologies/oilgas/FutureSupply/MethaneHydrates/projects/DOEProjects/MH_42962BarrowGas.html). October 2006.

Van der Waals, J. H. and Platteeuw, J. C. *Clathrate Solutions*. Advances in Chemical Physics, Vol. 2, 1959, pp. 1-57.

Walsh, T. P. *Characterization and Quantification of Methane Hydrate Resource Potential Associated with Barrow Gas Fields*. Quarterly Progress Report (January-March 2008) Submitted to the U.S. Department of Energy, Morgantown, WV, [www.netl.doe.gov](http://www.netl.doe.gov), April 2008, 19p.

Walsh, T. P. and Stokes, P. J. *Characterization and Quantification of the Methane Hydrate Resource Potential Associated with the Barrow Gas Fields*. "Fire In The Ice", NETL Methane Hydrates R and D Program Newsletter, Spring/Summer 2007, pp. 2-5.

Walsh, T. P., Stokes, P. J., Singh, P. *Characterization and Quantification of Methane Hydrate Resource Potential Associated with Barrow Gas Fields*. Phase 1-A Final Technical Report with Appendix Submitted to U.S. Department of Energy, Morgantown, WV, [www.netl.doe.gov](http://www.netl.doe.gov), May 2007, 30p.

West, S. L. and Chochrane, P. J. R. *Reserves Determination Using Type Curve Matching and EMB Methods in the Medicine Hat Shallow Gas Field*. SPE Paper No. 28609, [www.spe.org](http://www.spe.org), October 1994, pp. 82-87.

Westervelt, J. V. *Determination of Methane Hydrate Stability Zones in the Prudhoe Bay, Kuparuk River and Milne Point Units of the North Slope of Alaska*. M.S. Thesis, University of Alaska Fairbanks, Fairbanks, Alaska, May 2004, 85p.

Yousif, M.H. and Sloan, E.D. *Experimental Investigation of Hydrate Formation and Dissociation in Consolidated Porous Media*. SPE Reservoir Engineering, November 1991, pp. 452-458.

## GLOSSARY

### Symbols

<i>Notation</i>	<i>Description</i>	<i>Units</i>
$b(t)$	Hydrate-Cap Temperature Parameter	°K/sec
$g$	Methane Gas Molecule	-
$h$	Reservoir Pay Zone Thickness	ft
$k$	Reservoir Permeability	md
$k_d$	Reaction Rate Constant	lbmole/lb-day
$k_d^o$	Reaction Frequency Factor	-
$k_{rg}$	Gas Relative Permeability (End-Point, Gas-Hydrate System)	-
$k_{rw}$	Water Relative permeability (End-Point, Water-Hydrate System)	-
$k_{rgo}$	Gas Relative Permeability (at Irreducible Water Saturation)	-
$k_{rog}$	Hydrate Relative Permeability (End-Point, Gas-Hydrate System)	-
$k_{row}$	Hydrate Relative Permeability (End Point, Water-Hydrate system)-	-
$k_{rwo}$	Water Relative Permeability (at Residual Gas Saturation)	-
$m$	Slope	-
$n$	Flow Exponent	-
$n_H$	Hydration Number	-
$p_{co}$	Capillary Pressure at 100% Water Saturation	psi
$p_c$	Capillary Pressure at Current Water Saturation	psi
$p_g$	Pressure at Fluid-Hydrate Interface	psi
$p_o$	Reservoir Fluid Pressure	psi

$r_e$	Reservoir Radius	ft
$r_w$	Wellbore Radius	ft
$sI$	Cubic Structure I	-
$sII$	Cubic Structure II	-
$sH$	Hexagonal Structure H	-
$t$	Time	sec, mins, Day, Month, Year
$z_i$	Gas Deviation Factor at Initial Pressure	-
$z(t)$	Gas Deviation Factor (Time Dependent)	-
$A_d$	Surface Area per Unit Volume	ft <sup>-1</sup>
$B_g(t)$	Gas Formation Volume Factor (Time Dependent)	ft <sup>3</sup> (res)/scf
$B_{gi}(t)$	Gas Formation Volume Factor (at Initial Condition)	ft <sup>3</sup> (res)/scf
$B_w(t)$	Water Formation Volume Factor (Time Dependent)	bbl (res)/BBL
$C$	Deliverability Constant	-
$E_a$	Activation Energy	BTU/lbmole
$G$	Initial Gas In-Place	scf
$G_f$	Initial Free Gas In-Place	scf
$G_g(t)$	Cumulative Gas Generation (Time Dependent)	scf
$G_p(t)$	Cumulative Gas Production	scf
$H$	Hydrate Phase	-
$I$	Ice Phase	-
$K(t)$	Equilibrium Parameter	-
$L_w$	Water Phase	-
$P_i$	Initial Reservoir Pressure	psi
$P_{sc}$	Pressure at Standard Conditions	psi
$P(t)$	Reservoir Pressure (Time Dependent)	psi
$P_{avg}(t)$	Average Reservoir Pressure (Time Dependent)	psi

$P_{se}(t)$	Equilibrium Pressure (Time Dependent)	psi, kPa
$P_{wf}(t)$	Flowing Bottomhole Pressure (Time Dependent)	psi
$Q_g$	Gas Production Rate	scf/Day, scf/Month
$R$	Universal Gas Constant	BTU/lbmole-°R
$S_g$	Gas Saturation	-
$S_h$	Hydrate Saturation	-
$S_w$	Water Saturation	-
$S_{gr}$	Residual Gas Saturation	-
$S_{wr}$	Irreducible Water Saturation	-
$S_{orl}, S_{orw}$	Residual Hydrate Saturation	-
$S_{gcon}$	Connate Gas Saturation	-
$S_{lcon}$	Connate Hydrate Saturation	-
$S_{oirw}$	Irreducible Hydrate Saturation	-
$S_{wcon}$	Connate Water Saturation	-
$S_{gcrit}$	Critical Gas Saturation	-
$S_{wcrit}$	Critical Water Saturation	-
$T_i$	Initial Reservoir Temperature	°F
$T_s$	Hydrate Dissociation Temperature	°F
$T_{sc}$	Temperature at Standard Conditions	°R
$T(t)$	Reservoir Temperature (Time Dependent)	°F, °R
$T_{se}(t)$	Equilibrium Temperature (Time Dependent)	°F, K
$V$	Gas (Vapor) Phase	-
$W_e(t)$	Cumulative Water Influx	bbls

$W_p(t)$	Cumulative Water Production	bbls
$\mu_g$	Gas Viscosity	cp
$\Delta H$	Heat of Dissociation of Hydrates	BTU/lbmole
$\frac{dC_H}{dt}$	Rate of Hydrate Decomposition	lbmole/ft <sup>3</sup> -day

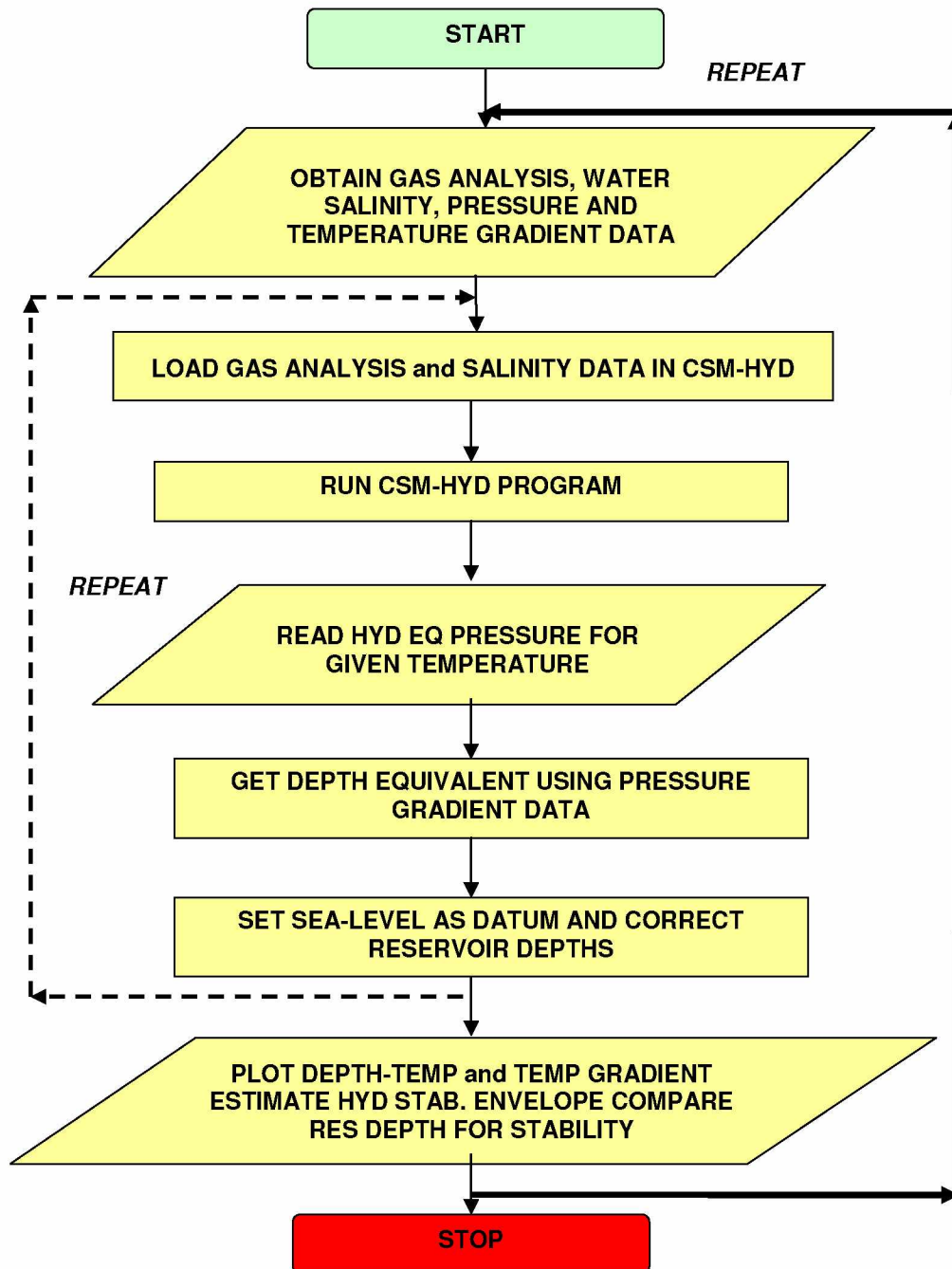
### Abbreviations

2D	two-dimensional
3D	three-dimensional
bbls	barrels of water (reservoir and standard conditions)
bcf	billion standard cubic feet
ft <sup>3</sup>	cubic feet
scf	standard cubic feet
tcf	trillion standard cubic feet
AOGCC	Alaska Oil and Gas Conservation Commission
ARSC	Arctic Region Supercomputing Center
BGF	Barrow Gas Fields
BPXA	BP Exploration Alaska
BS	Berea Sandstone
BSR	Bottom Simulating Reflector
CMG-STARS	Computer Modeling Group-Steam, Thermal, and Advanced Processes Reservoir Simulator
CORE	Core Holder
CSM-HYD	Colorado School of Mines Hydrate Program
CT	Computer Tomography
EB	East Barrow
ELEC BAL	Electrical Balance
EMB	Extended Material Balance

FBHP	Flowing Bottomhole Pressure
GFM	Gas Flow Meter
GOR	Free Gas-Oil Ratio
GWC	Free Gas-Water Contact
HGC	Hydrate-Free Gas Contact
HWC	Hydrate Water Contact
JBN	Johnson Bossler Naumann
KB	Kelly Bushing
LBNL	Lawrence Berkeley National Laboratory
MMbbls	Million Barrels
MMMbbls	Billion Barrels
MPU	Milne Point Unit
NETL	National Energy Technology Laboratory
NLREG	Non Linear Regression Program
NSB	North Slope Borough
NWE	North West Eileen
OGIP	Original Gas In-Place
PBU	Prudhoe Bay Unit
PC1	Gas Tank
PC2	Water Tank
PDL	Petroleum Development Laboratory
PG	Pressure Gauge
PNNL	Pacific Northwest National Laboratory
SB	South Barrow
STD	Standard Conditions
UAF	University of Alaska Fairbanks
U.S./U.S.A.	United States/United States of America
USDOE	U.S. Department of Energy
USGS	U.S. Geological Survey
UH-HYD	University of Houston-Hydrate Program
V#	Valve Numbers
WAL	Walakpa



## APPENDIX A. Flowchart - Hydrate Stability Model Development



## APPENDIX B. Volumetric Model

### B1. Theory

Tight-shallow gas reservoirs present a number of challenges in determining the reservoir drive mechanisms. Traditional material balance methods are inaccurate due to the formation's low permeability. Poor reservoir quality brings significant pressure changes within the reservoir; hence pressure data obtained from such wells may not represent the actual reservoir conditions. Wells within such formations undergoes long transient periods before they begin experiencing pseudosteady state flow that actually represents the decline portion of their lives. For such reservoirs initial production trend is not indicative of the long-term decline of the well. Conventional material balance techniques do not address this problem and should not be used while studying the tight gas reservoirs. To address this limitation, West and Cochrane (1994) developed an iterative technique, called the EMB (volumetric) method. The EMB is a shallow reservoir with poor reservoir permeabilities (Panda and Morahan, 2008). Scarcity of good quality pressure data and inconsistencies in downhole pressure measurements make this field a good candidate for volumetric model application. The essence of this technique lies in the fact that it can be applied to the entire reservoir by treating it as a single well system.

EMB method makes two fundamental assumptions.

- i. The gas pool depletes volumetrically (i.e., no water influx)
- ii. All wells behave like one average well with the same FBHP, deliverability constant, and turbulence constant.

The EMB technique is an iterative process for obtaining a suitable  $P(t)/z(t)$  vs. cumulative gas production,  $G_p(t)$ , relationship for the reservoir having inadequate pressure data. It combines the principles of volumetric gas depletion with the gas deliverability equation. The deliverability equation for radial flow of gas describes the relationship between the pressure differential in the wellbore and the gas flow rate.

$$Q_g(t) = C(P^2(t) - P_{wf}^2(t))^n \quad (\text{B.1})$$

where  $Q_g(t)$  - gas production rate, scf/Day;  $C$  - deliverability coefficient, scf/Day/psi<sup>2</sup>;  $P(t)$  - average reservoir pressure, psi;  $P_{wf}(t)$  - FBHP, psi; and  $n$  - flow exponent.

Considering low production rates from the wells, laminar flow regime can be considered for the reservoir. Mathematically, this condition can be described with the flow exponent,  $n = 1$ . The terms making up the coefficient  $C$  in Equation (B.1) are either fixed reservoir parameters ( $kh, r_e, r_w$  and  $T$ ) that do not vary with time or terms that fluctuate with pressure, temperature, and gas compositions (i.e.,  $\mu_g$  and  $z$ ). The performance coefficient  $C$  is given by (Craft and Hawkins, 1990):

$$C = kh1422T\mu_g z \left[ \ln\left(\frac{r_e}{r_w} - 0.5\right) \right] \quad (\text{B.2})$$

where  $k$  - reservoir permeability, md;  $h$  - reservoir pay zone thickness, ft;  $T$  - temperature, °F;  $z$  - gas deviation factor;  $\mu_g$  - gas viscosity, cp;  $r_e$  - drainage radius, ft; and  $r_w$  - wellbore radius, ft.

As the difference between the initial and current reservoir pressure is not significant, the variation in the pressure dependent properties are assumed to be negligible. Hence,  $C$  was considered constant over the production life of the reservoir. With these simplifications, the deliverability equation reduces to:

$$Q_g(t) = C(P^2(t) - P_{wf}^2(t)) \quad (\text{B.3})$$

The sum of the instantaneous production rates with time yields the relationship between  $G_p(t)$  and  $P(t)$ , similar to the material balance equation (Craft and Hawkins, 1990).

## APPENDIX C. Water Influx Model

### C1. Theory

The plot of  $P(t)/z(t)$  versus cumulative gas production,  $G_p(t)$ , is a widely accepted method for solving gas material balance under depletion drive conditions. The extrapolation of the plot to atmospheric (or abandonment) pressure provides a reliable estimate of the OGIP. If a waterdrive is present then the plot often appears to be linear, but its extrapolation gives an erroneously high value of OGIP. If the gas reservoir has a waterdrive, then there will be two unknowns in the material balance equation, even though the production data, pressure, temperature, and gas gravity are known. These two unknowns are OGIP,  $G$  and cumulative water influx,  $W_e(t)$ . In order to use the material balance equation to evaluate the contribution of water influx as potential drive mechanism of the EB reservoir, the Water Influx model was used (Pletcher 2001, Ahmed and McKinney, 2005).

Material balance equation for a volumetric reservoir was modified to include the effect of water influx. Assuming the EB type reservoir under active waterdrive, the material balance equation for an isothermal reservoir can be written as (Craft and Hawkins, 1990):

$$G(B_g(t) - B_{gi}) + W_e(t) = G_p(t)B_g(t) + W_p(t)B_w(t) \quad (C.1)$$

where  $G$  - OGIP, scf;  $W_e(t)$  - cumulative water influx, ft<sup>3</sup>;  $G_p(t)$  - cumulative gas production, scf;  $W_p(t)$  - cumulative water produced, ft<sup>3</sup>;  $B_g(t)$  - gas formation volume factor, ft<sup>3</sup>/scf at a given pressure;  $B_{gi}$  - gas formation volume factor, ft<sup>3</sup>/scf at initial pressure; and  $B_w(t)$  - water formation volume factor, ft<sup>3</sup>/scf at a given pressure. The above equation can be re-arranged and expressed as:

$$\frac{(G_p(t)B_g(t) + W_p(t)B_w(t))}{(B_g(t) - B_{gi})} = G + \frac{W_e(t)}{(B_g(t) - B_{gi})} \quad (C.2)$$

Pletcher (2001) and Ahmed et al. (2005) proposed plotting the mathematical expression  $\frac{(G_p(t)B_g(t) + W_p(t)B_w(t))}{(B_g(t) - B_{gi})}$  on the  $y$ -axis vs.  $G_p(t)$  on the  $x$ -axis (Equation C.2). If the reservoir is depletion drive (i.e., no water influx), the term  $W_e(t)$  becomes equal to zero, then the left hand side of Equation (C.3) becomes a horizontal line and the  $y$ -intercept becomes equal to OGIP (Figure C.1).

$$\frac{(G_p(t)B_g(t) + W_p(t)B_w(t))}{(B_g(t) - B_{gi})} = G + 0 \quad (C.3)$$

If a waterdrive is present, the water influx term is not zero, and the points will plot above the depletion drive line (above  $G$ ) with some degree of slope. In other words, the existence of a sloping line vs. horizontal line is a diagnostic tool for distinguishing between depletion drive and waterdrive mechanisms.

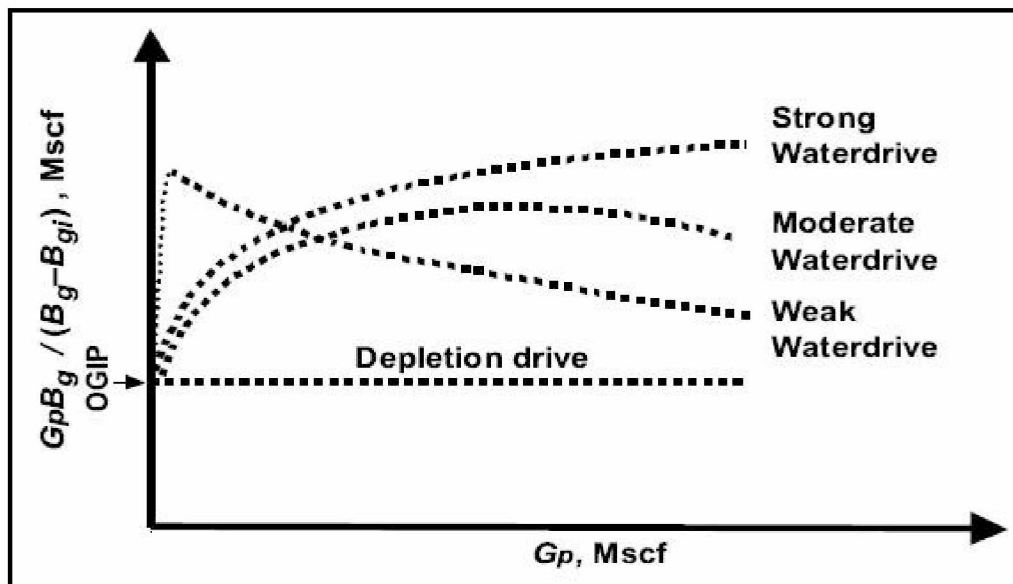


Figure C.1: Waterdrive Mechanisms (Pletcher, 2001)

Pletcher (2001) observed that the sloping waterdrive line can be extrapolated back to the y-intercept to obtain the OGIP (Figure C.1). However, the slope usually changes with each point; thus it is difficult to obtain the precise slope for the extrapolated section, if not impossible. Hence, this method is not recommended for estimating the OGIP.

The graphical technique can also be used to evaluate the value  $W_e(t)$ , because at any time the difference between the straight line  $\frac{(G_p(t)B_g(t) + W_p(t)B_w(t))}{(B_g(t) - B_{gi})}$  and horizontal line,  $G$ , will give the value of  $\frac{W_e(t)}{(B_g(t) - B_{gi})}$ . Moreover, the cumulative water influx,  $W_e(t)$ , estimates could be extended to estimate the size of associated aquifer.

The effectiveness of this method lies in its ability to provide qualitative information about the performance of gas reservoir producing under aquifer support. The nature of the slope also helps in identifying aquifer strength (Pletcher 2001). High positive slopes are associated with strong waterdrives, whereas weak waterdrive has negative slope (Figure C.1). The comparison although is purely qualitative, nevertheless provides crucial information about the aquifer size and type without quantifying.

## APPENDIX D. Hydrate Model

### D1. Theory

Gerami and Darvish (2006) developed a material balance model for studying hydrate-capped reservoirs. This model differs from conventional volumetric (depletion drive) and water influx models, because it includes the effect of gas recharge from hydrate decomposition and related cooling effect. The model is developed for a volumetric gas reservoir overlain with hydrate-cap (Class 1 type reservoir). The material balance equation has been developed by analytically solving mass and energy balance equations. The solution yields average reservoir pressure response and gas generated from hydrate decomposition as a function of cumulative gas production, for a reservoir that is produced at a constant rate.

Hydrate dissociation is an endothermic process, gas production reduces reservoir pressure and triggers hydrate dissociation leading to reduction in reservoir temperatures. During production, gas property changes continuously, due to the changes in pressure and temperature conditions. Gerami and Darvish (2006) considered these effects while developing material balance model for hydrate-capped systems. They assumed certain requirements for carrying out material balance analysis. These assumptions are mentioned below.

- i. Temperature and pressure within the reservoir were instantaneously uniform and were only the function of time.
- ii. Geothermal and hydrostatic gradients were ignored.
- iii. Kinetics of hydrate decomposition was neglected.
- iv. Reservoir was saturated with three fluid phases, hydrates, water, and gas.
- v. Reservoir was considered volumetric (no water influx).
- vi. Free gas temperature remained at the initial reservoir temperature.
- vii. The thermo-physical properties of hydrate, reservoir, and surrounding formations (cap and base rocks) remained constant during the production period.

viii. Reservoir was produced gas at a constant rate.

With these assumptions Gerami and Darvish (2006) modified the volumetric gas material balance equation and presented unique equation for hydrate-free gas system.

$$\frac{P_{avg}(t)}{z(t)} = \left(\frac{P_i}{z_i}\right) \left\{1 - \frac{(G_p(t) - G_g(t))}{G_f}\right\} \quad (D.1)$$

where  $P_{avg}(t)$  - average reservoir pressure at a given time, psi;  $P_i$  - initial reservoir pressure, psi;  $z_i$  - gas deviation factor at  $P_i$ ;  $z(t)$  - gas deviation factor at  $P_{avg}(t)$ ;  $G_p(t)$  - cumulative gas production, scf;  $G_g(t)$  - cumulative gas generation (from hydrate dissociation), scf; and  $G_f$  - initial free gas in-place, scf.

Hydrate block temperature is represented by a general equation given below.

$$T_{se}(t) = T_i - b(t)t \quad \text{for } T_{se}(t) \geq 273.15 \text{ °K} \quad (D.2)$$

where  $b(t)$  - hydrate-cap temperature parameter, °K/sec and  $t$  - time; sec. The term is obtained by performing heat and mass balance treatments to a 2D semi-infinite model.

The  $b(t)$  parameter combines the effect of hydrate dissociation and gas production rate to estimate the temperature profile. The hydrate-cap temperature parameter,  $b(t)$ , is a strong function of gas production rate, reservoir volume, thermophysical properties of hydrate-cap but weakly dependent on duration of gas production.

It is assumed that the slow dissociation rates causes hydrate zone pressure to be in equilibrium with reducing temperature. The changing temperature is related to the reservoir pressure by the empirical equation given by Kamath and Holder (1987) for estimating the hydrate equilibrium pressure and temperature (Equation 3.2). Thus, the



temperature profile obtained by estimating  $b(t)$  and Equation (D.2) could then be used to obtain equilibrium pressure (reservoir pressure) by using Equation (3.2).

Gerami and Darvish's (2006) hydrate model was used as an engineering tool to evaluate the role of hydrates in the EB gas field. After careful validation of the model with production history data, it can be used as a predictive tool to estimate OGIP (free gas) and hydrate thickness (hydrate-associated gas). However, the use of Kamath and Holder (1987) model for hydrate phase behavior predictions makes the hydrate model highly speculative and uncertain (as higher degree of deviations were observed between experimental data and model response, refer section 4.1.1).

### APPENDIX E. Summary of Displacement Experiments

Table E.1: Summary of Displacement Experiment (Hydrate Saturation 38%)

Initial Condition (Before Hydrate Formation)	
Sample Porosity (Determined Previously)	12.98%
Sample Pore Volume (Determined Previously)	20.67 ml
Volume of Water Removed from the Core (or Pore Volume Occupied by Gas)	10 ml
Pore Space Occupied by Water	10.67 ml
Desired Hydrate Saturation (Assuming 100% Hydrate Formation Gas Being the Limiting Component)	~48%
Waterflooding (After Hydrate Formation)	
Volume of Water Injected	49.23 ml
Volume of water Produced	47.08 ml
Volume of Gas Collected (Un-reacted)	2.15 ml
Total Volume of Water	12.82 ml
Water Saturation (Assuming No Trapped Gas Left After Waterflooding)	~62%
Volume of Hydrates Within the Pore Space	7.85 ml
Hydrate Saturation	~38%
% Hydrate Conversion	~78.5%
New Pore Volume (Assuming Hydrate to be Part of Rock System)	12.82 ml
New Porosity	8.05%
Effective Permeability to Water Flow ( $K_{ew}$ ) (At 100% Water Saturation based on New Porosity)	~1.97 md

Table E.1 contd.

Gasflooding (After Waterflooding)	
Mobile Water Displaced	4.95 ml
Irreducible Water (Based on New Pore Volume)	~61%
Effective Permeability to Gas Flow ( $K_{eg}$ ) (At 15% Irreducible Water Sat based on New Porosity)	0.021 md
Relative Permeability End-Points (Based on New Porosity)	
Effective Permeability to Water Flow (Base Permeability)	1.97 md
Water Relative Permeability at Initial Gas Saturation	1
Initial Gas Saturation	0%
Gas Relative Permeability at Irreducible Water Saturation	0.011
Irreducible Water Saturation	61%

Table E.2: Summary of Displacement Experiment (Hydrate Saturation 14%)

Initial Condition (Before Hydrate Formation)	
Sample Porosity (Determined Previously)	12.98%
Sample Pore Volume (Determined Previously)	20.67 ml
Volume of Water Removed from the Core (or Pore Volume Occupied by Gas)	6 ml
Pore Space Occupied by Water	14.67 ml
Desired Hydrate Saturation (Assuming 100% Hydrate Formation Gas Being the Limiting Component)	~30%
Waterflooding (After Hydrate Formation)	
Volume of Water Injected	141 ml

Table E.2 contd.

Volume of water Produced	137.9 ml
Volume of Gas Collected (Un-reacted)	3.1 ml
Total Volume of Water	17.77 ml
Water Saturation (Assuming No Trapped Gas Left After Waterflooding)	~86%
Volume of Hydrates Within the Pore Space	2.9 ml
Hydrate Saturation	~14%
% Hydrate Conversion	~50%
New Pore Volume (Assuming Hydrate to be Part of Rock System)	17.77 ml
New Porosity	11.16%
Effective Permeability to Water Flow (Kew) (At 100% Water Saturation based on New Porosity)	~8.5 md
Gasflooding (After Waterflooding)	
Mobile Water Displaced	14.73 ml
Irreducible Water (Based on New Pore Volume)	~17%
Effective Permeability to Gas Flow ( $K_{eg}$ ) (At 15% Irreducible Water Sat based on New Porosity)	0.8 md
Relative Permeability End-Points (Based on New Porosity)	
Effective Permeability to Water Flow (Base Permeability)	8.5 md
Water Relative Permeability at Initial Gas Saturation	1
Initial Gas Saturation	0%
Gas Relative Permeability at Irreducible Water Saturation	0.094
Irreducible Water Saturation	17%

Table E.3: Summary of Displacement Experiment (Hydrate Saturation 5%)

Initial Condition (Before Hydrate Formation)	
Sample Porosity (Determined Previously)	12.98%
Sample Pore Volume (Determined Previously)	20.67 ml
Volume of Water Removed from the Core (or Pore Volume Occupied by Gas)	4 ml
Pore Space Occupied by Water	16.67 ml
Desired Hydrate Saturation (Assuming 100% Hydrate Formation Gas Being the Limiting Component)	~19%
Waterflooding (After Hydrate Formation)	
Volume of Water Injected	52.91 ml
Volume of water Produced	49.99 ml
Volume of Gas Collected (Un-reacted)	2.92 ml
Total Volume of Water	19.59 ml
Water Saturation (Assuming No Trapped Gas Left After Waterflooding)	~95%
Volume of Hydrates Within the Pore Space	1.08 ml
Hydrate Saturation	~5%
% Hydrate Conversion	~27%
New Pore Volume (Assuming Hydrate to be Part of Rock System)	19.59 ml
New Porosity	12.30%
Effective Permeability to Water Flow ( $K_{ew}$ ) (At 100% Water Saturation based on New Porosity)	~26 md
Gasflooding (After Waterflooding)	
Mobile Water Displaced	16.50 ml

Table E.3 contd.

Irreducible Water (Based on New Pore Volume)	~15%
Effective Permeability to Gas Flow ( $K_{eg}$ ) (At 15% Irreducible Water Sat based on New Porosity)	0.84 md
Relative Permeability End-Points (Based on New Porosity)	
Effective Permeability to Water Flow (Base Permeability)	26 md
Water Relative Permeability at Initial Gas Saturation	1
Initial Gas Saturation	0%
Gas Relative Permeability at Irreducible Water Saturation	0.032
Irreducible Water Saturation	15%

## APPENDIX F. NLREG Programs

### F1. Program - Water Relative Permeability Model (Hydrate Saturation 5%)

Variables Swavg, Krw;

Parameter a;

$$\text{Function } k_{rw} = k_{rwo} S_w^{-0.5} [1 - (1 - S_w^{-1/m})^{0.45}]^a$$

Plot;

RPlot;

Data;

0.011240562	0.8709
0.009014708	0.06
0.006677562	0.043
0.005008171	0.0305
0.00289361	0.0295
0.000445171	0.0172

### F2. Program - Gas Relative Permeability Model (Hydrate Saturation 5%)

Variables Swavg, Sgavg, Krg;

Parameters a;

$$\text{Function } k_{rg} = k_{rgo} S_g^{-0.5} (1 - S_{wH}^{-1/m})^{0.45(a)}$$

Plot;

RPlot;

Data;

0.069815664	0.930184336	0.0069
0.06758981	0.93241019	0.008783
0.065252664	0.934747336	0.011701
0.063583273	0.936416727	0.012662
0.061468712	0.938531288	0.017581
0.059020273	0.940979727	0.031199

## APPENDIX G. Thermal and Fluid Component Properties

### G1. Thermal Properties

Table G.1 summarizes the thermal properties of rock and fluids initialized for the EB and WAL gas reservoir, these properties were taken from Howe (2004).

Table G.1: Thermal Properties of Rock and Fluids

Description	CMG-STARS Keyword	Value (Field Units)	
Reservoir Rock Type	*ROCKTYPE	1	
Vol Heat Capacity (rock)	*ROCKCP	34 BTU/(ft <sup>3</sup> -°F)	
Thermal Heat Conductivity			
Rock	*THCONR	24.01043 BTU/(ft-day-°F)	
Oil/Hydrate	*THCONO	265.30236 BTU/(ft-day-°F)	
Water	*THCONW	8.586616 BTU/(ft-day-°F)	
Gas	*THCONG	1.1876815 BTU/(ft-day-°F)	
Phase Mixing	*THCONMIX	SIMPLE	
Overburden and Underburden Temperature	*HLOSST	48°F	
Directional Heat Loss Property	*HLOSSPROP	Volumetric Heat Capacity BTU/(ft <sup>3</sup> -°F)	Thermal Conductivity BTU/(ft-day-°F)
		+I 34.99531654	+I 24.010425
		-I 34.99531654	-I 24.010425
		+J 34.99531654	+J 24.010425
		-J 34.99531654	-J 24.010425
		+K 34.99531654	+K 24.010425
		-K 34.99531654	-K 24.010425



## G2. Fluid-Component Properties

Table G.2 summarizes the fluid-component properties initialized for the EB and WAL Gas reservoir, these properties were taken from Howe (2004).

Table G.2: Fluid Properties for the EB and WAL Reservoir Model

<b>Description</b>	<b>CMG-STARS Keyword</b>	<b>Value (Field Units) Water/Hydrate/Methane</b>
Component Name/Definition	*COMPNAME	WATER / HYDRATE / CH4
Molecular Weight	*CMM	18 / 119.54408 / 16.043 (lb/lbmole)
Critical Pressure	*PRCIT	0 / 1450.377 / 667.174 (psi)
Critical Temperature	*TCRIT	32 / 1832 / -116.59 (°F)
Molar Density (Liquid)	*MOLDEN	3.46818 / 0.480455 / NA (lbmole/ft <sup>3</sup> )
Liquid Phase Viscosity (Using Temperature Dependent Correlation)	*AVISC  *BVISC	0 / 1000 / NA (cp)  32 / 32 / NA (°F)
Gas Phase Viscosity (Using correlation)	*AVG  *BVG	NA / NA / 0.00211 (cp/°F)  NA / NA / 0 (dimensionless)
Liquid Compressibility	*CP	0 / 0 / NA (1/psi)
Coefficient of thermal expansion		
First Coefficient	*CT1	0 / 0 / NA (1/°F)
Second Coefficient	*CT2	0 / 0 / NA (1/°F °F)

Table G.2 contd.

Description	CMG-STARS Keyword	Water/Hydrate/Methane Value (Field Units)
Heat Capacity in the Liquid Phase	*CPL1	0 / 45.6678 / 0 (BTU/lbmole-°F)
	*CPL2	0 / 0 / 0 (BTU/lbmole-°F°F)
	*CPL3	0 / 0 / 0 (BTU/lbmole-°F°F°F)
	*CPL4	0 / 0 / 0 (BTU/lbmole-°F°F°F°F)
Heat Capacity in the Gas Phase (Using Correlation)	*CPG1	0 / 0 / 4.59807 (BTU/lbmole-°F)
	*CPG2	0 / 0 / 0.00691333 (BTU/lbmole-°F°F)
	*CPG3	0 / 0 / 1.588e-6 (BTU/lbmole-°F°F°F)
	*CPG4	0 / 0 / -1.50209e-9 (BTU/lbmole-°F°F°F°F)
Note: 0 Denotes CMG Default Property will be Activated		
Reactant Stoichiometry	*STOREAC	0 / 1 / 0
Product Stocihometry	*STOPROD	5.7501 / 0 / 1
Component Reaction Order	*RORDER	0 / 1 / 0
Reaction Frequency Factor	*FREQFAC	1.35878e30
Reaction Enthalpy	*RENTH	-22295.1255 BTU/lbmole
Activation Energy	*EACT	64582.9213 BTU/lbmole
<i>K</i> values For Reactants Only (Using Correlation)	* <i>rxk</i> 1	NA / 6.3507334e15 / NA (psi)
	* <i>rxk</i> 2	NA / 0 / NA (1/psi)
	* <i>rxk</i> 3	NA / 0 / NA (dimensionless)
	* <i>rxk</i> 4	NA / -14967.7002 / NA (°K)
	* <i>rxk</i> 5	NA / -459.67 / NA (°F)

APPENDIX H. Wellbore Diagrams of the Existing EB Wells

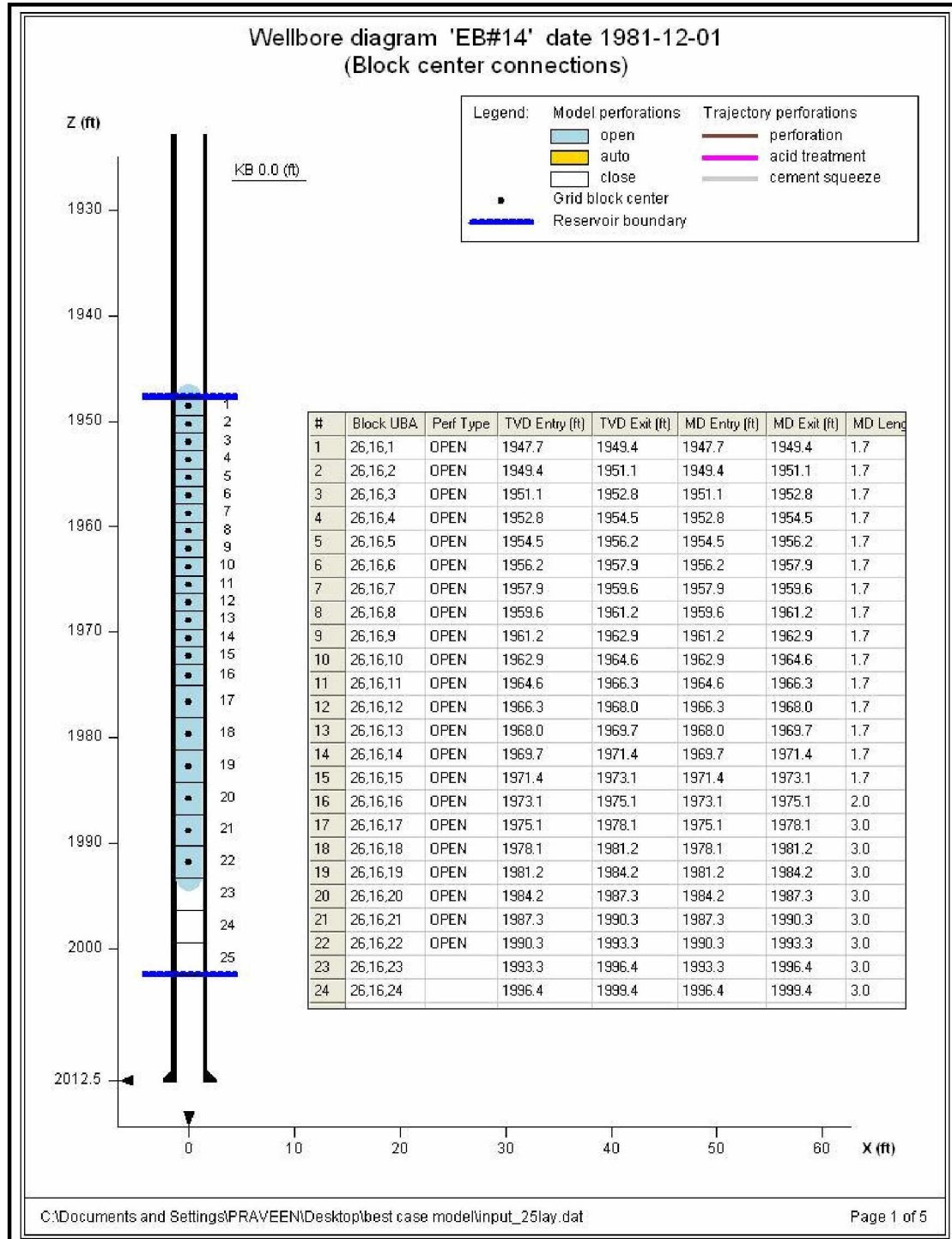


Figure H.1: Wellbore Diagram of EB #14

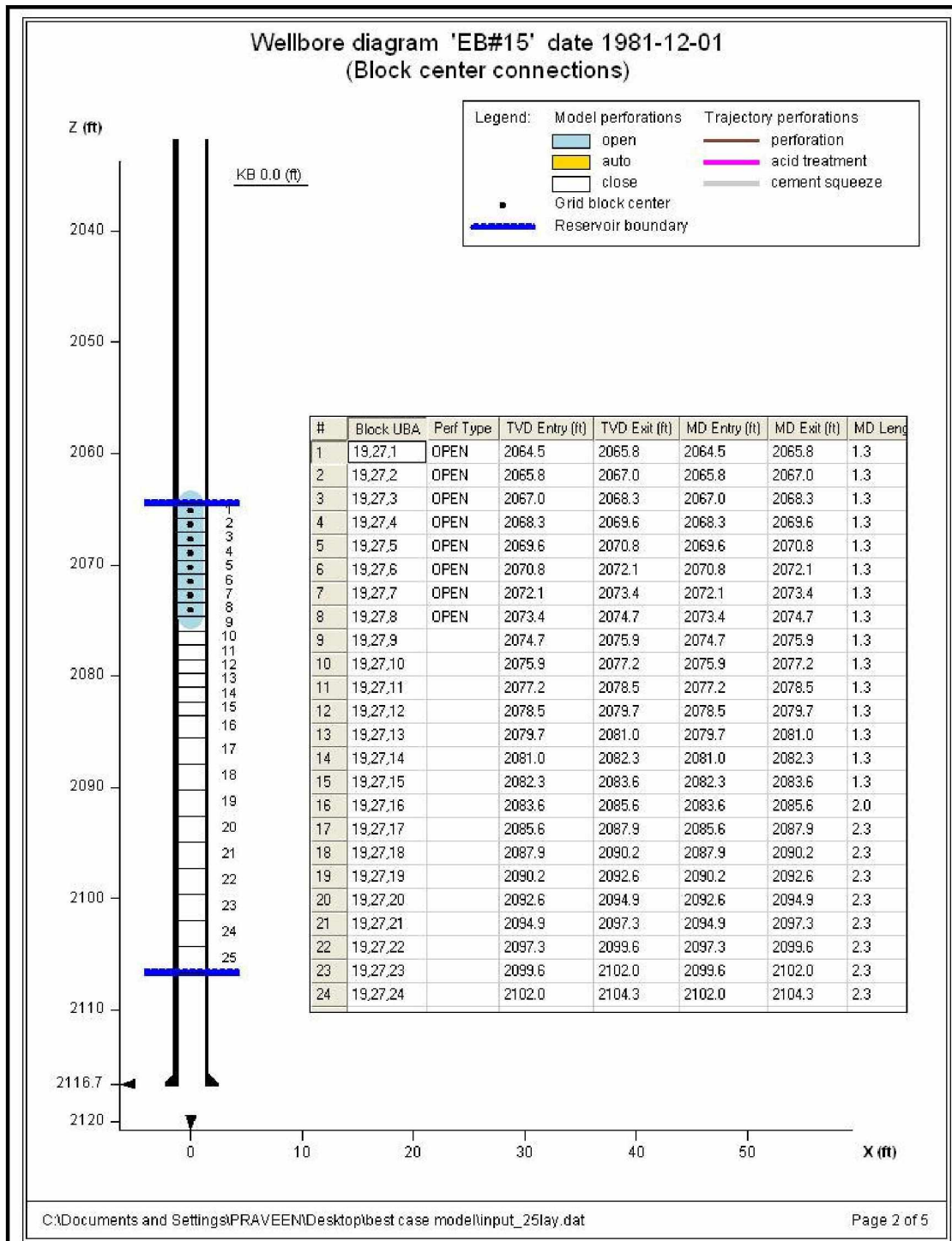


Figure H.2: Wellbore Diagram of EB #15

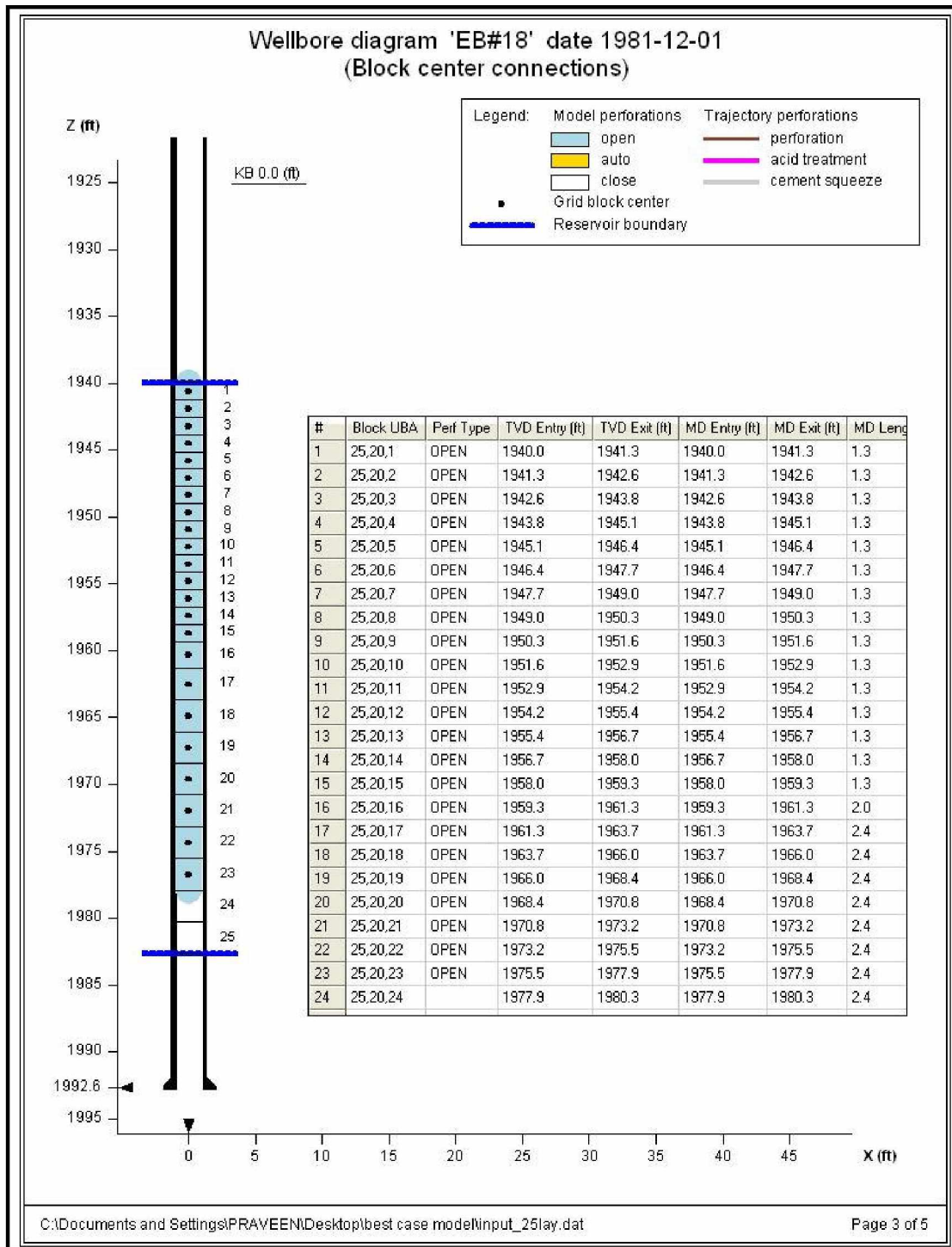


Figure H.3: Wellbore Diagram of EB #18

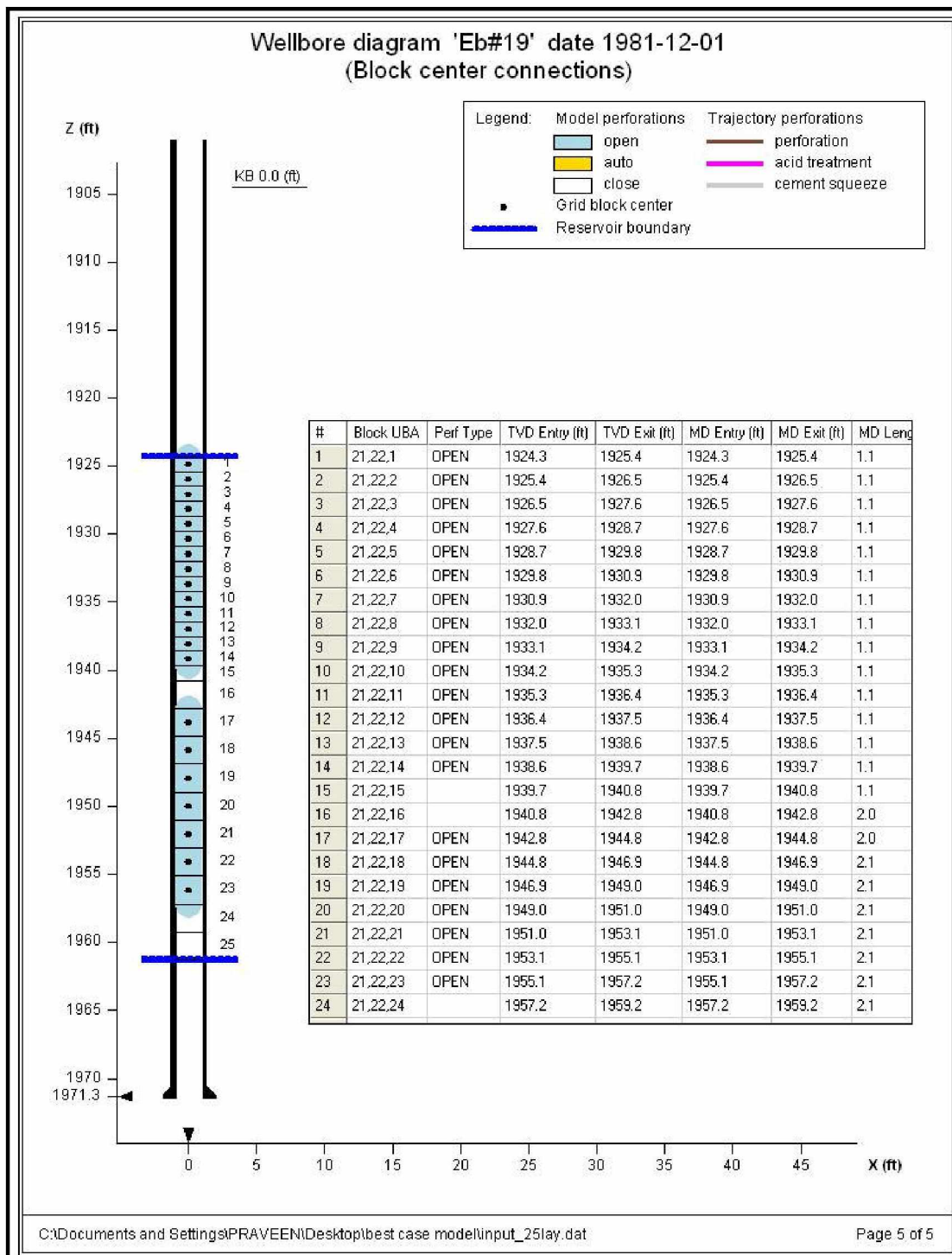


Figure H.4: Wellbore Diagram of EB #19



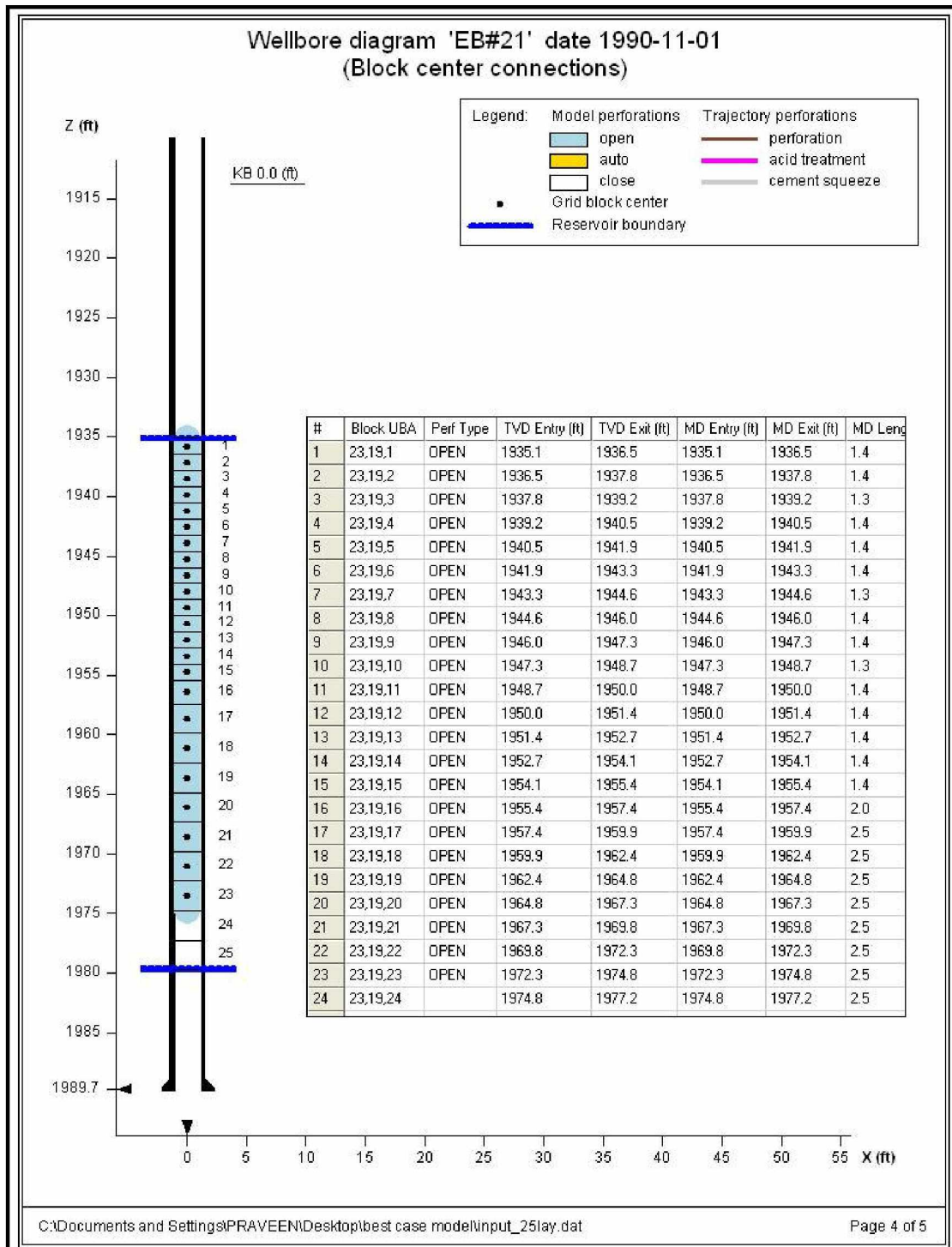


Figure H.5: Wellbore Diagram of EB #21

APPENDIX I. Wellbore Diagrams of the Future EB Wells (Forecast)

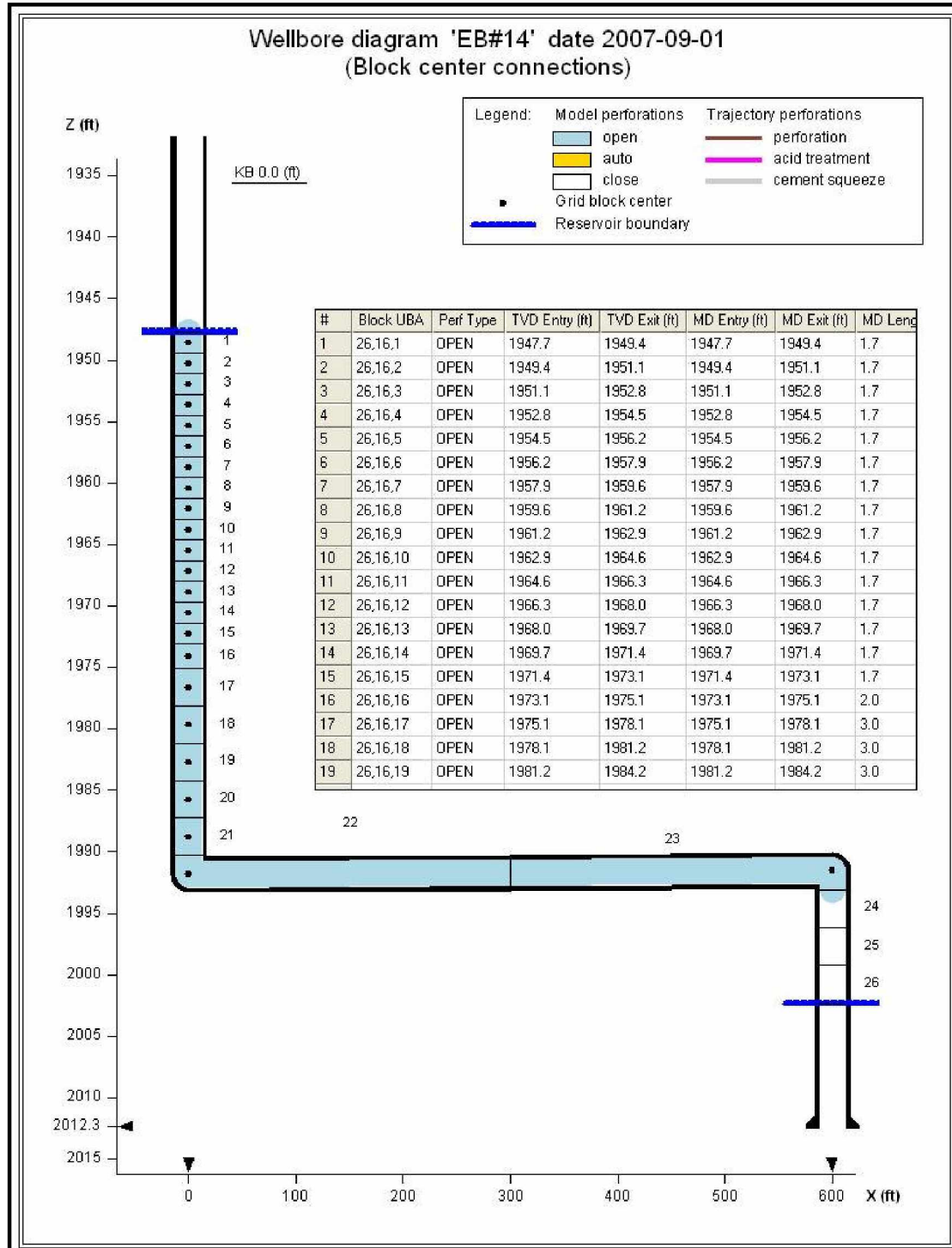


Figure I.1: Wellbore Diagram of EB #14 (Completed in Horizontal Section)



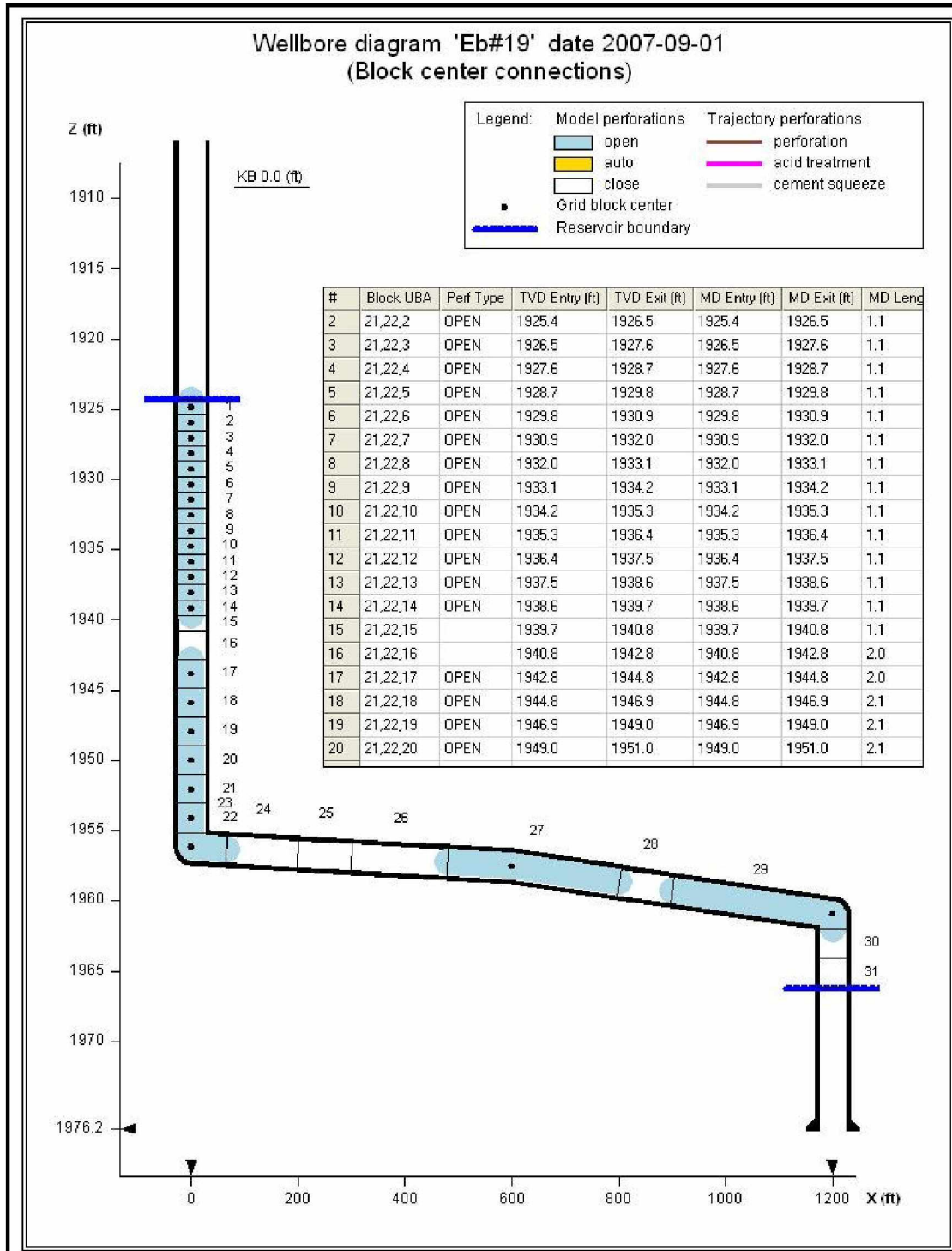


Figure I.2: Wellbore Diagram of EB #19 (Completed in Horizontal Section)

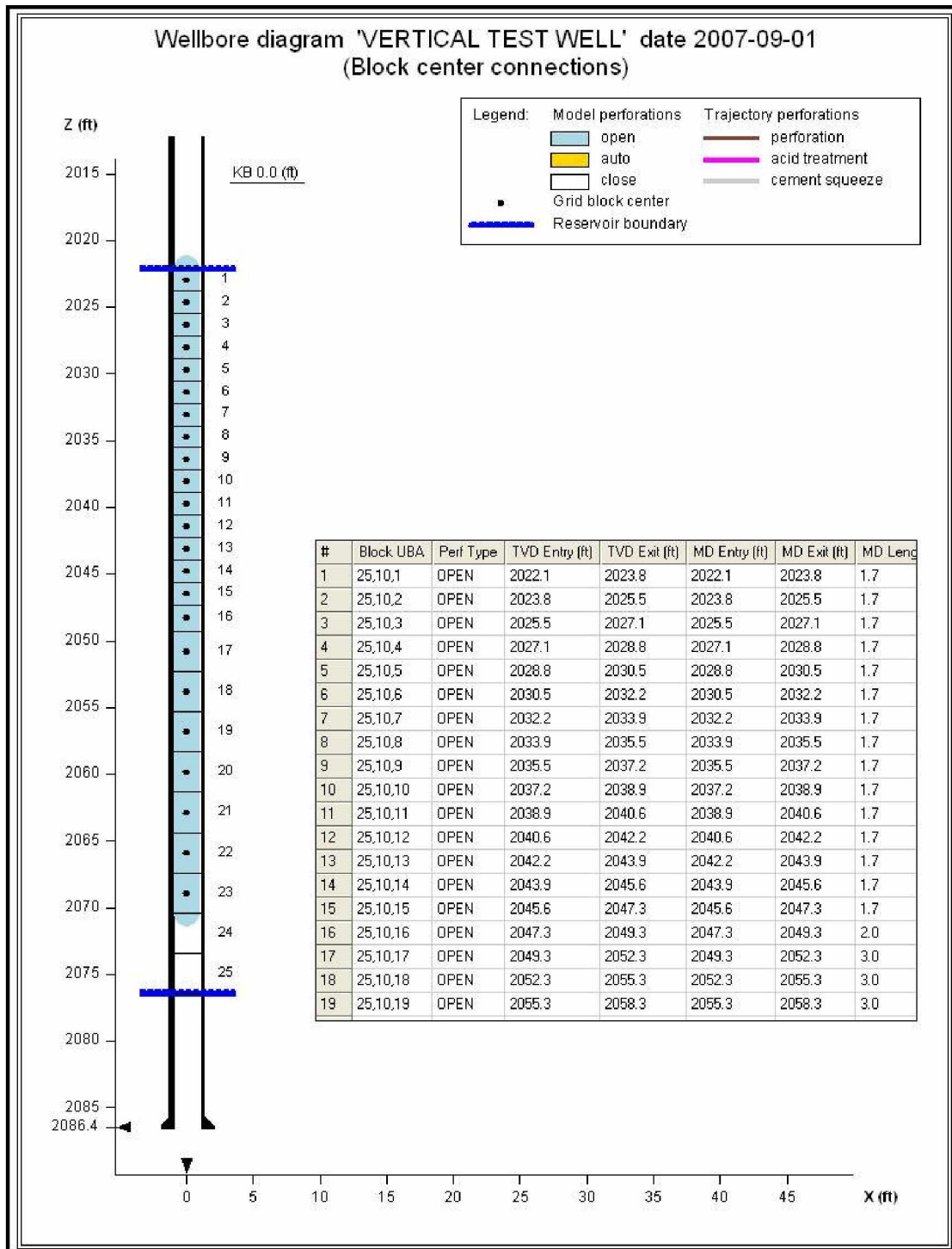


Figure I.3: Wellbore Diagram of Vertical Well (New Test Well)

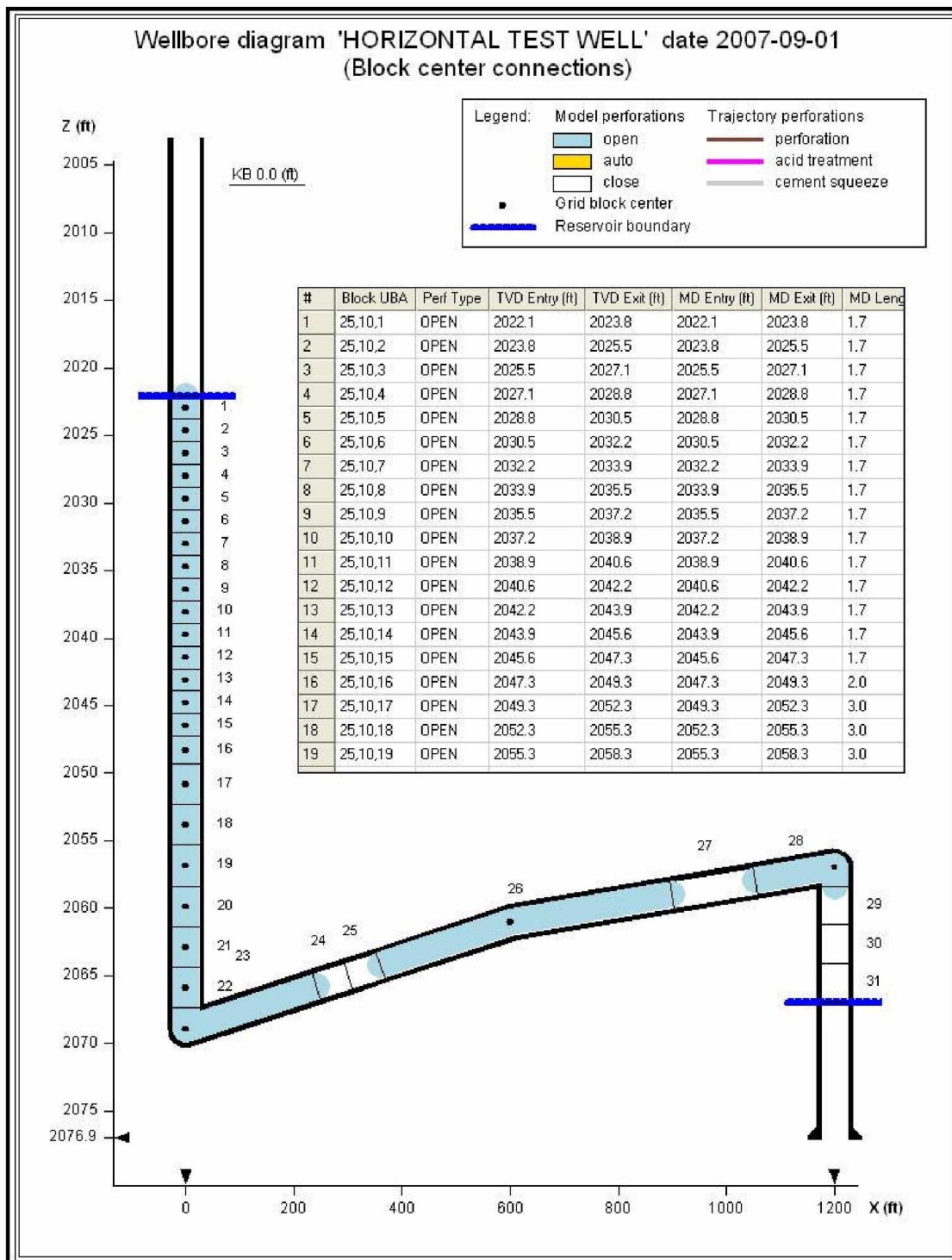


Figure I.4: Wellbore Diagram of Horizontal Well (New Test Well)

APPENDIX J. NLREG Regression Model Results

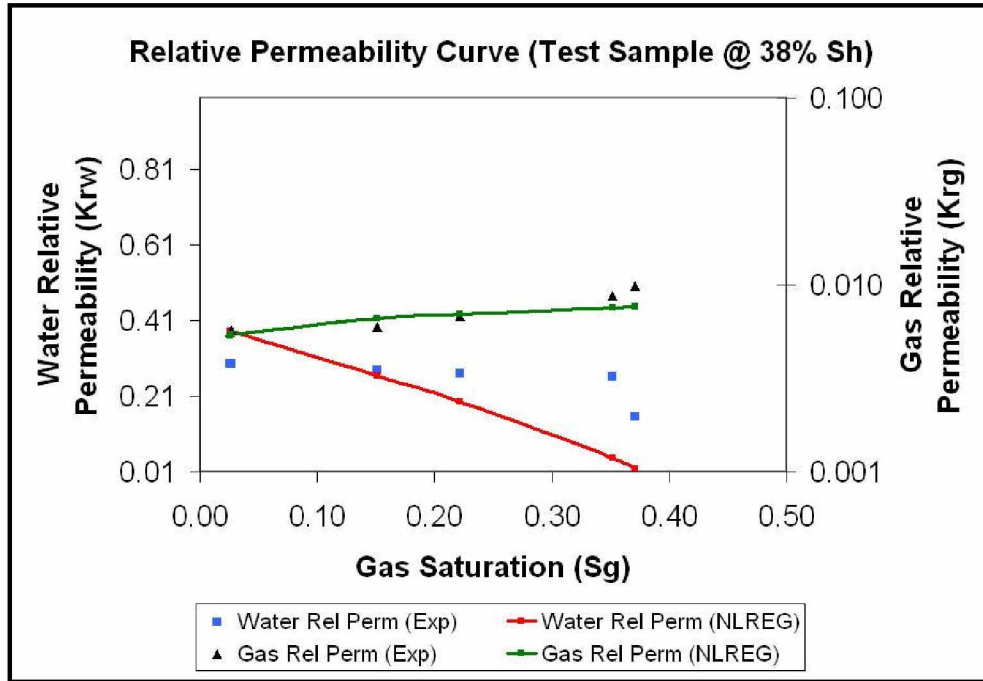


Figure J.1: Gas-Water Relative Permeability Curve (Hydrate Saturation 38%)

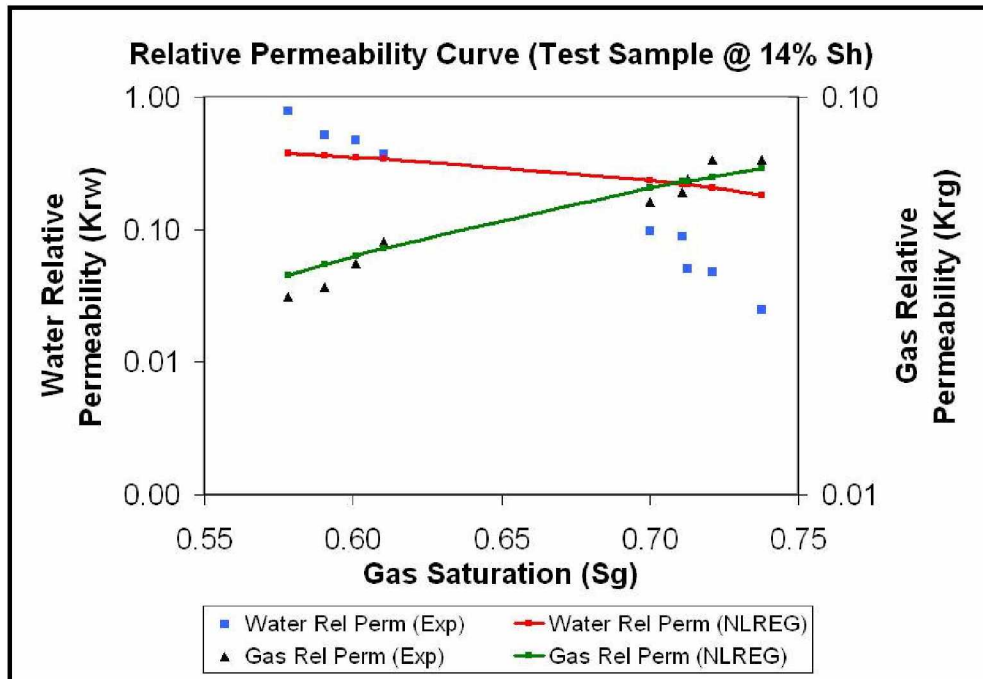


Figure J.2: Gas-Water Relative Permeability Curve (Hydrate Saturation 14%)

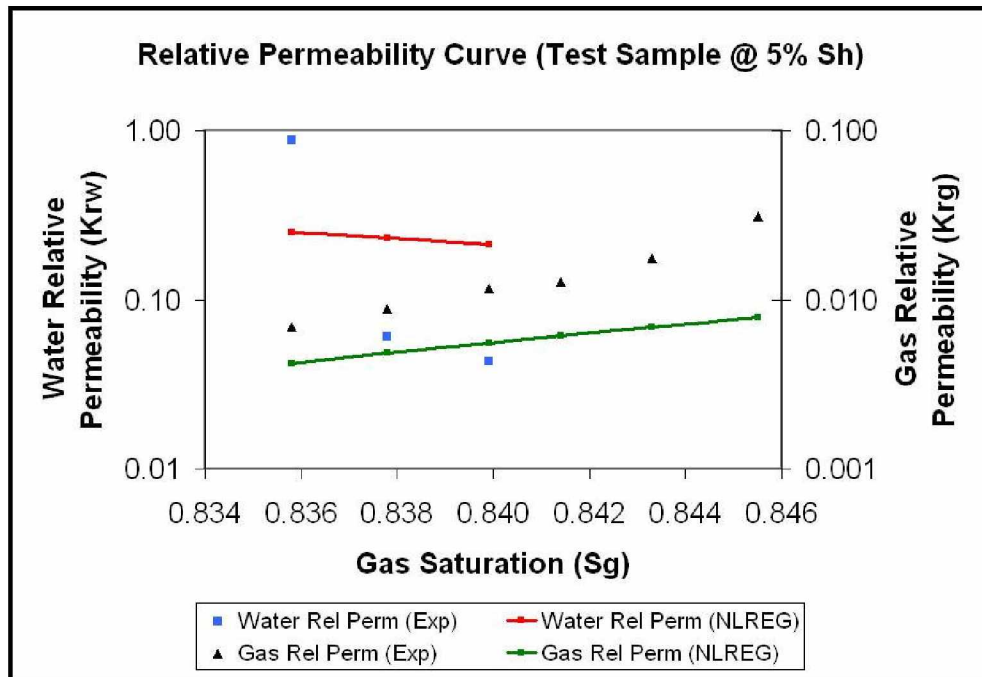


Figure J.3: Gas-Water Relative Permeability Curve (Hydrate Saturation 5%)